Cruising Towards Durability: Investigating Degradation in Polymer Electrolyte Fuel Cells (PEFCs) for Sustainable Vehicle Power

A Dissertation Presented for the

Doctor of Philosophy

Degree

The University of Tennessee, Knoxville

Preetam Sharma

August 2024

Copyright © 2024 by Preetam Sharma
All rights reserved

DEDICATION

Dedicated to my father, mother, and brother.

ACKNOWLEDGEMENTS

First and foremost, I would like to thank and extend my heartfelt appreciation to my advisor, Dr. Matthew M. Mench. His unwavering support, invaluable guidance, and wisdom have been instrumental in every aspect of my doctoral journey at the University of Tennessee, Knoxville. Dr. Mench's passion for research, his commitment to excellence, and his genuine concern for his students' well-being have been a constant source of inspiration. I am deeply grateful for his mentorship, which has left an indelible mark on my academic and professional trajectory. I am equally indebted to my co-advisor, Dr. Doug Aaron, whose expertise, encouragement, and support have been instrumental in shaping the trajectory of my research. Dr. Aaron's insightful guidance and constructive feedback have been invaluable assets throughout my doctoral studies. I would also like to thank my PhD committee members Dr. Kivanc Ekici and Dr. David J. Keffer for their valuable feedback and guidance in improving the quality of this dissertation.

I extend my sincere gratitude to Bosch Research and Technology Center, North America, Sunnyvale, CA for generously sponsoring the majority of my PhD work. My heartfelt thanks go to Dr. Lei Cheng and the entire team at Bosch for their collaborative spirit, invaluable resources, and unwavering support. The opportunity to work alongside such talented professionals has immensely enriched my research experience. I am also deeply grateful for the collaboration with Plug Power Inc., Rochester, NY and particularly indebted to Dr. Jon Owejan for his invaluable industry insights and academic expertise. Dr. Owejan's mentorship and guidance have broadened my perspective and enriched my understanding of real-world applications in the field of fuel cells and electrolyzers.

I would like to thank Dr. Pierre Boillat and Dirk Scheuble from Paul Scherrer Institut (PSI), Switzerland for helping me with the neutron imaging experiments.

I extend my heartfelt appreciation to my colleagues, past and present, at the Electrochemical Energy Storage and Conversion Lab at University of Tennessee, Knoxville. Their camaraderie, intellectual exchange, and support have been invaluable sources of strength and inspiration.

I would like to thank the University of Tennessee, Knoxville for granting me Tennessee Fellowship for Graduate Excellence, which supported first four years of my PhD.

I extend my deepest gratitude to my beloved family, whose love, encouragement, and support have been the cornerstone of my journey. Finally, to all those whose names may not grace these pages but whose contributions, support, and encouragement have played an integral role in shaping my journey, I offer my sincerest thanks. This milestone would not have been possible without the collective support of mentors, colleagues, friends, and loved ones who have stood by me through every step of this remarkable journey.

ABSTRACT

Energy production is central to the climate challenge, as a significant portion of greenhouse gases responsible for trapping heat in the Earth's atmosphere arises from burning fossil fuels to generate electricity and heat. To mitigate the adverse effects of climate change, emissions must be reduced by almost half by 2030 and achieve net-zero emissions by 2050. Polymer electrolyte fuel cells (PEFCs) offer numerous advantages compared to traditional internal combustion engines in vehicles. Fuel cell electric vehicles are known for their exceptional operating efficiency (over 60%), impressive driving range (more than 400 miles), and quick refueling times (under 5 minutes).

Automotive PEFCs undergo extensive load cycling, often reaching hundreds of thousands of cycles in regular use. However, the dissolution of platinum (Pt) catalyst and carbon-support oxidation under these conditions are significant barriers to their widespread adoption. The U.S. Department of Energy has set durability benchmarks at 8,000 hours for light-duty vehicles and 30,000 hours for heavy-duty vehicles. Consequently, PEFC catalyst degradation has received significant attention in the past decade. Still, our understanding of catalyst degradation remains incomplete, particularly regarding heterogeneity in catalyst growth and its localized performance impact.

This dissertation employs a combination of advanced characterization techniques to study the heterogeneous aging patterns in PEFCs and their localized impact. These techniques include synchrotron micro-X-ray diffraction, high-resolution neutron imaging, spatially and temporally resolved current and temperature measurements via a segmented cell, and a variety of electrochemical and analytical methods. This research presents a novel approach by providing a spatially-resolved comparison of current and Pt particle size distributions over a larger active area, relevant to fuel cell stack applications. Furthermore, these techniques have been utilized to identify interactions between different degradation modes in PEFCs and to elucidate path-dependent degradation. Finally, this research correlates heterogeneous catalyst growth with liquid water distribution within a PEFC, offering new insights into the factors influencing performance and durability.

A deeper understanding of local performance responses to aging and the interactions of different degradation mechanisms explored in this dissertation will enable the design of highly durable fuel cells capable of withstanding thousands of load/unload and start-up/shutdown cycles.

TABLE OF CONTENTS

Chapter 1: Introduction and Method of Approach 1

1.1 Motivation 1

1.2 Background 5

1.2.1 Polymer electrolyte fuel cells (PEFCs) 5

1.2.2 Voltage losses in PEFCs 19

1.2.3 Degradation in PEFCs 22

1.3 Method of Approach 32

1.3.1 In-situ localized current distribution measurements 33

1.3.2 Ex-situ synchrotron grazing incidence X-ray diffraction (GIXRD) 33

1.3.3 In-operando neutron imaging 37

1.4 Objectives 41

Chapter 2: Impact of Cathode Gas Flow Rate on Catalyst Degradation in Polymer Electrolyte Fuel Cells (PEFCs) 43

2.1 Abstract 44

2.2 Introduction 44

2.3 Method of approach 48

2.3.1 Materials and test equipment 48

2.3.2 Catalyst AST 48

2.3.3 Electrochemical characterization 49

2.3.4 Post-mortem analysis 49

2.4 Results and discussion 53

2.5 Conclusions 71

Chapter 3: Effects of Heterogeneous Catalyst Degradation on the Localized Electrochemical Performance Loss of Polymer Electrolyte Fuel Cells (PEFCs) 75

3.1 Abstract 76

3.2 Introduction 76

3.3 Method of approach 79
3.3.1 Materials and test equipment 79
3.3.2 Catalyst AST 81
3.3.3 In-situ electrochemical characterization 81
3.3.4 Post-mortem analysis 84
3.4 Results and Discussion 85
3.5 Conclusions 111
Chapter 4: Path-Dependent Degradation in High-Performance Polymer Electrolyte Fuel Cells (PEFCs) 113
4.1 Brief introduction/abstract 114
4.2 Method of approach 114
4.2.1 Materials and test equipment 114
4.2.2 AST combinations to explore path-dependence 115
4.2.3 In-situ electrochemical characterization 116
4.2.4 Ex-situ post-mortem characterization 118
4.3 Results and discussion 119
4.4 Conclusions 137
Chapter 5: Correlating Catalyst Growth with Liquid Water Distribution in Polymer Electrolyte Fuel Cells (PEFCs) 140
5.1 Abstract 141
5.2 Introduction 141
5.3 Method of Approach 144
5.3.1 Materials and test equipment 144
5.3.2 Catalyst AST and in-situ electrochemical characterization 146
5.3.3 In-situ neutron imaging 149
5.3.4 Post-mortem synchrotron micro-X-ray diffraction 150
5.4 Results and Discussion 151

5.5 Conclusions 166

Chapter 6: Conclusions and Future Work 168

6.1 Impact of cathode gas flow rate on catalyst degradation in polymer electrolyte fuel cells 168

6.2 Effects of heterogeneous catalyst degradation on the localized electrochemical performance loss of polymer electrolyte fuel cells 170

6.3 Path-dependent degradation in high-performance polymer electrolyte fuel cells 172

6.4 Correlating catalyst growth with liquid water distribution in polymer electrolyte fuel cells 174

6.5 Future work and recommendations 175

6.5.1 Novel catalyst layer architectures to mitigate degradation 175

6.5.2 Flow field architectures that eliminate land/channel bias (porous flow fields) 176

6.5.3 Polymer electrolyte membrane degradation under heavy-duty vehicle-relevant operating conditions 177

6.5.4 System level mitigation strategies 177

6.6 Broader impact of this dissertation 177

References 179

Appendices 191

Supporting Information for Chapter 2 192

Supporting Information for Chapter 3 194

Supporting Information for Chapter 4 207

Supporting Information for Chapter 5 210

Vita 213

LIST OF TABLES

Table 2-1. Test conditions for square-wave AST 50
Table 3-1. Test conditions for Pt AST – Wet, Pt AST – Dry, and CC AST..... 82
Table 4-1. Test conditions for PtfCC and CCfPt ASTs 117
Table S4.1. Fitted EIS parameters from the equivalent circuit for PtfCC and CCfPt ASTs at the BOL and EOL. 209

LIST OF FIGURES

Figure 1.1. Global average land-sea temperature anomaly relative to the 1961-1990 average temperature [1]. 2

Figure 1.2. Relative world energy consumption by source. The energy consumption (measured in TWh) is corrected for "inefficiency factor" for fossil fuels [3]. 2

Figure 1.3. U.S. DOE's H2@Scale initiative launched in 2016 to foster decarbonization of various sectors using clean hydrogen (Figure Courtesy: U.S. DOE's H2@Scale initiative [5]). 4

Figure 1.4. U.S. DOE's interim (2030) and ultimate (2050) targets for cost, system lifetime, and peak efficiency targets for automotive and trucks (Data for the figure is adapted from Cullen et al. [6]). 4

Figure 1.5. Schematics of a hydrogen polymer electrolyte fuel cell (PEFC) depicting critical components. In this figure, CL stands for catalyst layer, and GDL stands for gas diffusion layer. 6

Figure 1.6. Schematics of commonly used flow field/bipolar plate design patterns in PEFCs (Figure taken from Chapter 6 of *Fuel Cell Engines* [22]). 9

Figure 1.7. Scanning electron microscopy (SEM) images of (a) AvCarb EP40 carbon paper GDL without PTFE, (b) AvCarb EP40 carbon paper GDL with 13% PTFE treatment, (c) MPL on AvCarb EP40 substrate without PTFE, and (d) cross-sectional view of MPS (AvCarb EP40 without PTFE) + MPL (Vulcan XC-72R based). This figure is taken from Ozden et al. [23]. 11

Figure 1.8. X-ray computed tomography (X-ray CT) volume rendered images of Freudenberg H2315 C2 GDL showing the effect of compression on the MPS and MPL. The compression on the samples is (a) 0%, (b) 14%, and (c) 28%. This figure is taken from Atkinson et al. [30]. 13

Figure 1.9. General chemical structure of PFSA-based ionomers. Also, it depicts nano-phase-separation with water uptake (hydration). This figure is taken from Kusoglu et al. [33]. 15

Figure 1.10. Proton conduction mechanisms in PFSA-based membranes. This figure is taken from Kusoglu et al. [33]. 15

Figure 1.11. Transmission electron microscopy (TEM) images of a PEFC catalyst layer: Pt/C catalyst (40 wt.% Pt on Vulcan carbon). 17

Figure 1.12. Schematic of a triple phase boundary in a fuel cell catalyst layer [22]. 17

Figure 1.13. Various polarization losses in PEFCs [22]. 20
Figure 1.14. Stability of PGM catalyst (Pt/Pt^{2+}) in aqueous electrolyte. Dissolved Pt^{2+} concentration is 10^{-6} M. This figure is taken from a review paper by Zhu et al. [47]. 23
Figure 1.15. Different mechanisms of Pt degradation in PEFCs. This figure is adapted from the review paper by Josef C. Meier et al. [62]. 26
Figure 1.16. Schematics of (a) reverse current mechanism, (b) dual-cell mechanism under startup/shutdown cycling, and (d) potential profile along a gas channel in a fuel cell. This figure is taken from a review paper by P. Ren et al.[46]. Note that the original mechanism was proposed by Reiser et al.[75]. 30
Figure 1.17. Schematics of current mapping technique in PEFCs (Figure taken from Chapter 9 of *Fuel Cell Engines* [22]). 34
Figure 1.18 (a) Standard Bragg-Brentano XRD, (b) GIXRD 36
Figure 1.19 (a) Intensity vs. 2Theta (2θ) and (b) Attenuation length vs. Photon Energy (eV) 38
Figure 1.20. Difference between in-plane and through plane neutron imaging for water distribution mapping in fuel cells. 40
Figure 2.1. Illustration on the acquisition of micro-XRD. Samples were mounted as illustrated in panel (b) and measured as depicted in panel (c). Diffractograms of 500 μm x 500 μm spots were collected with a step size of 2.5 mm in the x-direction and 0.5 mm in the y-direction. No difference in the average Pt particle size was observed when resolving along or across the land and channels (see Figure S2.1, Supporting Information for Chapter 2). 52
Figure 2.2. Cyclic voltammograms of the hydrogen desorption region (corrected for capacitance) for the MEAs subjected to (a) 4 sccm/cm^2 N_2 flow, (b) 8 sccm/cm^2 N_2 flow, and (a) 16 sccm/cm^2 N_2 flow at the cathode during AST. The area under each curve was used for calculating ECSA at different stages during the AST. 54
Figure 2.3. (a) Absolute ECSA as a function of the number of AST cycles for different N_2 flow rate cases, and (b) normalized ECSA loss as a function of the number of AST cycles for different N_2 flow rate cases. Shaded regions indicate range of measured experimental error for each condition. 55
Figure 2.4. (a) Log of normalized ECSA versus number of AST cycles for the three N_2 flow rate cases. Corresponding linear fits along with R^2 values are also mentioned. (b) Rate constant

obtained from the slopes of best-fit straight lines in (a) versus the N_2 flow rate during the AST. 59
Figure 2.5. Polarization curves for the MEAs at the beginning of life (BOL) and after the AST subjected to different N_2 flow rates during the AST. (a) and (c) have 100% RH, H_2/air stoichiometry of 1.5/2, and an operating cell temperature of 60 °C and 80 °C, respectively. (b) and (d) have differential conditions, i.e., H_2/air stoichiometry of 10/10, 100% RH, and an operating cell temperature of 60 °C and 80 °C, respectively. 60
Figure 2.6. 2 cm x 2 cm micro-XRD maps for (a) pristine sample (synchrotron XRD) and aged samples with (b) 4 , (c) 8 and (d) 16 sccm/cm^2 N_2 flow showing Pt particle size distribution (lab-scale micro-XRD). The inlet and outlet regions are marked on the aged samples (color available online). 63
Figure 2.7. A possible explanation of the gradients formed inside the fuel cell that might be responsible for non-uniform Pt particle size growth during (a) regular operation with H_2/air [111], and (b) operation with H_2/N_2 during an AST 65
Figure 2.8. Pt particle size distribution of aged samples with (a) 4 sccm/cm^2 N_2 flow, (b) 8 sccm/cm^2 N_2 flow, and (c) 16 sccm/cm^2 N_2 flow. Micro-XRD maps are used as insets to serve as a guide to the eye. 70
Figure 2.9. TEM images of (a) pristine sample and aged samples with (b) 4, (c) 8, and (d) 16 sccm/cm^2 N_2 flow. Red circles in panel (b) highlight some of the “starlike” shaped Pt nanoparticles..... 72
Figure 3.1. U.S. DOE's (a) square-wave AST for catalyst durability, and (b) carbon corrosion AST for support durability used in the present study. Note that the square-wave AST was performed at two different RH conditions to simulate dry and wet operating conditions within a fixed potential window of 0.6 V to 0.95 V vs. RHE. 82
Figure 3.2. Absolute ECSA ($m^2/g_{\text{-Pt}}$) and normalized ECSA as a function of number of AST cycles for (a) CC AST and (b) Pt AST-Wet and Pt AST-Dry measured under H_2/N_2 atmosphere at $Tcell = 80$ °C, $RH\%\ A/C =$ 100/100 with no backpressure. The ECSA is obtained by integrating hydrogen desorption peaks in CVs (Figure S3.10, Supporting Information for Chapter 3). 86
Figure 3.3. (a) Polarization performance of the MEAs at the BOL and EOL for Pt AST-Wet, Pt AST-Dry, and CC AST. Polarization conditions include cell $Tcell$ of 80 °C, H_2/air

stoichiometry ($\lambda H2/\lambda Air$) of 1.5/2, inlet RH ($RH\%\ A/C$) of 100% on both the anode and cathode with a backpressure ($Pabs\ A/C$) of 150 kPa (absolute). In (b), the iR-free cell voltage is plotted vs. specific current density to assess the onset of mass transport limitations for different aging protocols. A Tafel slope of 70 mV/decade is plotted as a reference..... 88

Figure 3.4. EIS spectra (0.1 Hz to 10 kHz, 5 % DC amplitude, 7 points/decade) measured at the BOL and EOL for CC AST, Pt AST-Wet, and Pt AST-Dry at the current densities of (a) 0.2 A/cm^2, and (b) 0.5 A/cm^2. The spectra were recorded at $Tcell$ = 80 °C, $\lambda H2/\lambda Air$ = 1.5/2, and $RH\%\ A/C$ = 100/100 with $Pabs\ A/C$ = 150/150 kPa. The fitted equivalent circuit to derive the kinetic (K) and mass transport (MT) resistances at the BOL and EOL is shown in (c). The ratio of $(K+MT)EOL$ to $(K+MT)BOL$ can also be noted from (a) and (b). 91

Figure 3.5. CDD measured at the BOL ((a) to (e)) and EOL ((f) to (i)) for CC AST. (h) and (i) represent the EOL distributions with the flipped air inlet and outlet as compared to (f) and (g). All the distributions were recorded at $Tcell$ = 80 °C, $\lambda H2/\lambda Air$ = 1.5/2, and $RH\%\ A/C$ = 100/100 with $Pabs\ A/C$ = 150/150 kPa. The operating current densities and the corresponding cell voltages are mentioned at the bottom of each distribution. The color scale bar on the right represents the percentage deviation of the local current from the mean. 95

Figure 3.6. CDD measured at the BOL ((a) to (d)) and EOL ((e) and (f)) for CC AST under dry inlet conditions ($RH\%\ A/C$ = 50/50). All the distributions were recorded at $Tcell$ = 80 °C, $\lambda H2/\lambda Air$ = 1.5/2, and $RH\%\ A/C$ = 50/50 with $Pabs\ A/C$ = 150/150 kPa. The operating current densities and the corresponding cell voltages are mentioned at the bottom of each distribution. The color scale bar on the right represents percentage deviation of the local current from the mean. 97

Figure 3.7. CDD measured at the BOL ((a) to (e)) and EOL ((f) to (j)) for Pt AST-Wet. All the distributions were recorded at $Tcell$ = 80 °C, $\lambda H2/\lambda Air$ = 1.5/2, and $RH\%\ A/C$ = 100/100 with $Pabs\ A/C$ = 150/150 kPa. The operating current densities and the corresponding cell voltages are mentioned at the bottom of each distribution. The color scale bar on the right represents the percentage deviation of the local current from the mean. 99

Figure 3.8. CDD measured at the BOL ((a) to (e)) and EOL ((f) to (j)) for Pt AST-Dry. All the distributions were recorded at $Tcell$ = 80 °C, $\lambda H2/\lambda Air$ = 1.5/2, and $RH\%\ A/C$ = 100/100 with $Pabs\ A/C$ = 150/150 kPa. The operating current densities and the corresponding cell

voltages are mentioned at the bottom of each distribution. The color scale bar on the right represents the percentage deviation of the local current from the mean. 100
Figure 3.9. One-dimensional (1-D) current distributions at the BOL and EOL for CC AST, Pt AST-Wet and Pt AST-Dry at the average current density of 0.5 A/cm^2. All the distributions were recorded at $Tcell$ = 80 °C, $\lambda H2/\lambda Air$ = 1.5/2, and $RH\%\ A/C$ = 100/100 with $Pabs\ A/C$ = 150/150 kPa. Each point on the plot (row number vs. current) from the air inlet (top-right) to the outlet (bottom-left) is a row-wise average of 10 current segments as shown in the figure on the right. The cell voltages at the BOL and EOL for different ASTs at 0.5 A/cm^2 are marked with the arrows. 102
Figure 3.10. Cross-sectional SEM images for the (a) pristine and ((b) to (e)) aged samples for different ASTs along with their respective Pt EDS maps. The average cathode catalyst layer thickness ($tCCL$) is also mentioned for each case. (e) shows Pt-band formation in the polymer membrane for Pt AST-Wet. In all the images, the cathode catalyst layer (CCL) is on the left, and the anode catalyst layer (ACL) is on the right of the polymer membrane. 104
Figure 3.11. 5 cm x 5 cm micro-XRD maps for the (a) pristine and ((b) to (d)) aged samples for different ASTs. The average Pt particle size is also mentioned, along with the standard deviation. Each 5 cm x 5 cm micro-XRD map is stitched from individual 5 cm^2 quadrants. The inlet and outlet regions (superimposed 7-channel serpentine flow field) are marked on the maps along with the color scale bar for Pt particle size on the right. 106
Figure 3.12. Pt particle size distributions for the pristine and aged samples with different ASTs derived from micro-XRD maps. The inset micro-XRD maps serve as a guide to the eye. 109
Figure 3.13. Temperature distributions at the BOL (top panel) and EOL (bottom panel) for ((a) and (b)) Pt AST-Dry, ((c) and (d)) Pt AST-Wet, and ((e) to (f)) CC AST at 0.5 A/cm^2. All the distributions were recorded at $Tcell$ = 80 °C, $\lambda H2/\lambda Air$ = 1.5/2, and $RH\%\ A/C$ = 100/100 with $Pabs\ A/C$ = 150/150 kPa. (g) is the temperature distribution for CC AST with the flipped air inlet and outlet as compared to (f). The cell voltages at 0.5 A/cm^2 for different ASTs are also mentioned. The color scale bar on the right shows the measured temperature (°C) in the segments. 110

Figure 4.1. (a) PtfCC AST, and (b) CCfPt AST voltage profiles used in the present study. A total of 17,500 cycles were executed for each AST combination. 117
Figure 4.2. (a) Normalized ECSA versus number of AST cycles for PtfCC and CCfPt ASTs measured under fully humified ($RH\%\ A/C = 100/100$) H_2/N_2 (anode/cathode) atmosphere at a cell temperature ($Tcell$) of 80 °C with no backpressure. (b) Polarization curves of the MEAs at the BOL, MOL, and EOL for both the AST combinations used in this study. Panels (c) and (d) show the iR-free cell voltage as a function of specific current density at the geometric current densities of 0.1 A/cm^2 and 0.5 A/cm^2, respectively. Polarization conditions include $Tcell$ = 80 °C, H_2/air stoichiometry ($\lambda H2/\lambda Air$) of 1.5/2, $RH\%\ A/C$ = 100/100 and 50/50 with a backpressure ($Pabs\ A/C$) of 150 kPa (absolute) on both the anode and cathode. 120
Figure 4.3. EIS spectra measured at the BOL and EOL for PtfCC and CCfPt ASTs at the current densities of (a) 0.1 A/cm^2, and (b) 0.2 A/cm^2. A small current perturbation (5% of DC) was imposed, and the frequency was swept from 0.1 Hz to 10 kHz. Panel (c) shows the equivalent circuit used for fitting the EIS spectra. The ratio of $(K + MT)EOL$ to $(K + MT)BOL$ can be noted from (a) and (b). The EIS spectra were recorded at $Tcell$ = 80 °C, $\lambda H2/\lambda Air$ = 1.5/2, and $RH\%\ A/C$ = 100/100 with $Pabs\ A/C$ = 150/150 kPa. 126
Figure 4.4. CDDs measured for PtfCC AST at different stages during aging. Panels (a) to (e) represent CDDs at the BOL, panels (f) to (j) represent MOL, and panels (k) and (l) represent EOL. All the distributions were recorded at $Tcell$ = 80 °C, $\lambda H2/\lambda Air$ = 1.5/2, and $RH\%\ A/C = 100/100$ with $Pabs\ A/C$ = 150/150 kPa. The cell operating current densities and voltages are marked under each distribution. The color scale bar on the right represents the percentage deviation of the local current from the mean. 128
Figure 4.5. CDDs measured for CCfPt AST at different stages during aging. Panels (a) to (e) represent CDDs at the BOL, panels (f) to (i) represent MOL, and panels (j) and (k) represent EOL. All the distributions were recorded at $Tcell$ = 80 °C, $\lambda H2/\lambda Air$ = 1.5/2, and $RH\%\ A/C = 100/100$ with $Pabs\ A/C$ = 150/150 kPa. 130
Figure 4.6. One-dimensional (1-D) current distributions at the BOL, MOL, and EOL for PtfCC and CCfPt ASTs at the average current density of 0.5 A/cm^2. Each point on the figure is a row-wise average of 10 current segments on the CDD board. The cell voltages at the BOL and EOL for different ASTs at 0.5 A/cm^2 are marked with the arrows. All the distributions

were recorded at $Tcell$ = 80 °C, $\lambda H2/\lambda Air$ = 1.5/2, and $RH\%\ A/C$ = 100/100 with $Pabs\ A/C$ = 150/150 kPa. 132
Figure 4.7. Full active area (5 cm x 5 cm) micro-XRD maps for the (a) pristine, (b) EOL PtfCC AST, and (c) EOL CCfPt AST. The average Pt particle size is reported with the standard deviation. Each full active map is constructed by stitching individual 5 cm^2 quadrants that were raster scanned separately. (d) Violin plots of Pt particle size distributions for the pristine and aged samples with different ASTs derived from their respective micro-XRD maps. The data for CC AST, Pt AST-Dry, and Pt AST-Wet is extracted from Sharma et al. [153], and plotted for comparison with PtfCC and CCfPt ASTs studied in this work. The inset micro-XRD maps serve as a guide to the eye. 134
Figure 4.8. Cross-sectional SEM images for the (a) pristine, (b) EOL PtfCC AST, and (c) EOL CCfPt AST. The average CCL thickness is marked for each case. In all the images, CCL is on the left, and the anode catalyst layer (ACL) is on the right of the polymer membrane (PEM). 136
Figure 5.1. Schematics of the cell hardware to quantify in-plane liquid water distribution using neutron imaging. The complete field-of-view (FOV) is marked, along with the anode and cathode single-serpentine flow fields shown on the right. 145
Figure 5.2. U.S. DOE [55] voltage cycling profiles used in the present study for (a) N_2 AST, and (b) Air AST. 147
Figure 5.3. (a) Normalized ECSA versus number of AST cycles for N_2 and Air ASTs measured under fully humified ($RH\%\ A/C$ = 100/100). H_2/N_2 (anode/cathode) environment at $Tcell$ = 80 °C with no backpressure. (b) Polarization curves of the MEAs before and after aging for N_2 and Air AST at fully humidified cell inlets ($RH\%\ A/C$ = 100/100). (c) Polarization curves at partially humidified cell inlets ($RH\%\ A/C$ = 50/50). Other conditions during polarization curves include cell temperature ($Tcell$) of 80 °C, H_2/air stoichiometry ($\lambda H2/\lambda Air$) of 1.5/2 with a backpressure ($Pabs\ A/C$) of 150 kPa (absolute) on both the anode and cathode. (d) iR-free cell voltage versus specific current density for different ASTs used in the present study. A Tafel slope of 70 mV/decade is marked as a reference. This plot is generated by plotting the iR-free cell voltage from polarization curves collected at $Tcell$ = 80 °C, $RH\%\ A/C$ = 100/100, $\lambda H2/\lambda Air$ = 1.5/2 with $Pabs\ A/C$ = 150 kPa/150 kPa on both the anode and cathode. 152

Figure 5.4. Neutron images/radiographs (anisotropic scale) of the test cell with (a) pristine MEA, (b) MEA aged with Air AST, and (c) MEA aged with N_2 AST at a current density of 0.1 A/cm^2. In all the images, cathode is shown at the top and anode is at the bottom. The scale on the right shows the measured water thickness (mm) along in-plane direction. Other operating conditions include $Tcell$ = 80 °C, $RH\%\ A/C$ = 100/100, $\lambda H2/\lambda Air$ = 1.5/2 with $Pabs\ A/C$ = 150 kPa/150 kPa on both the anode and cathode. 156

Figure 5.5. Averaged water thickness (mm) in the MEA along the cell inlet to the outlet (from right to left) for the pristine and aged MEAs at a current density of 0.1 A/cm^2. In this image, cathode is shown at the top and anode is at the bottom. Other operating conditions include $Tcell$ = 80 °C, $RH\%\ A/C$ = 100/100, $\lambda H2/\lambda Air$ = 1.5/2 with $Pabs\ A/C$ = 150 kPa/150 kPa on both the anode and cathode. Note that the neutron radiograph is just a representative image to show where the liquid water distribution is calculated from..... 158

Figure 5.6. Neutron images/radiographs (anisotropic scale) of the test cell with (a) pristine MEA, (b) MEA aged with Air AST, and (c) MEA aged with N_2 AST at a current density of 0.5 A/cm^2. In all the images, cathode is shown at the top and anode is at the bottom. The scale on the right shows the measured water thickness (mm) along in-plane direction. Other operating conditions include $Tcell$ = 80 °C, $RH\%\ A/C$ = 100/100, $\lambda H2/\lambda Air$ = 1.5/2 with $Pabs\ A/C$ = 150 kPa/150 kPa on both the anode and cathode. 160

Figure 5.7. Averaged water thickness (mm) in the MEA along the cell inlet to the outlet (from right to left) for the pristine and aged MEAs at a current density of 0.5 A/cm^2. In this image, cathode is shown at the top and anode is at the bottom. Other operating conditions include $Tcell$ = 80 °C, $RH\%\ A/C$ = 100/100, $\lambda H2/\lambda Air$ = 1.5/2 with $Pabs\ A/C$ = 150 kPa/150 kPa on both the anode and cathode. Note that the neutron radiograph is just a representative image to show where the liquid water distribution is calculated from..... 161

Figure 5.8. Averaged water mass (mg) in the pristine and aged MEAs with different ASTs used in this study at (a) 0.1 A/cm^2, and (b) 0.5 A/cm^2. The water mass in the cathode or anode for a particular MEA is calculated by averaging water thickness from the cell inlet to the outlet in the diffusion media and catalyst layers alone. In all the images, cathode is shown at the top and anode is at the bottom. This calculation does not include water thickness in the flow field channels at the cathode or anode. Other operating conditions include $Tcell$ = 80 °C,

$RH\%\ A/C$ = 100/100, $\lambda H2/\lambda Air$ = 1.5/2 with $Pabs\ A/C$ = 150 kPa/150 kPa on both the anode and cathode. 162
Figure 5.9. Synchrotron micro-XRD maps for the pristine and aged samples with N_2 and Air ASTs at the (a) inlet and the (b) outlet of the cathode flow field. The color bars for the maps represent Pt particle sizes in nm. Panel (c) shows the particle size distributions derived from the spatial micro-XRD maps for the pristine and aged samples at the inlet and outlet. ... 164
Figure S2.1. No difference in the average Pt particle size was observed when measuring the sample in a different direction, i.e., when resolving along the land and channels as opposed to across. 192
Figure S2.2. Linear scan voltammograms (LSVs) of a sample MEA (subjected to 16 sccm/cm^2 N_2 flow rate during the AST) at the BOL and EOL, recorded in H_2/N_2 atmosphere at 2 mV/s, 80 °C cell temperature, 100 % relative humidity on both sides and at atmospheric backpressure. 193
Figure S3.3. (a) Schematic of Baltic cell fixture, (b) compression pressure on the gas diffusion layers (GDLs) (in MPa) vs. adjustable pneumatic pressure. In the present study, a pneumatic pressure of ~3.2 bars was applied to achieve a compression pressure of ~1 MPa on the GDLs. 194
Figure S3.4. Images of (a) current distribution board with current and temperature measurement segments, (b) cathode flow field bolted on top of the current distribution board. The air and fuel inlet/outlet are marked. The anode flow field is identical to the cathode flow field and the fuel i.e., hydrogen enters at the bottom and leaves at the top. The air enters at the top and leaves at the bottom. 195
Figure S3.5. Compression paper (Fujifilm Prescale® Super Low film) images showing uniform compression between (a) cathode flow field and the GDL, (b) anode flow field and the GDL, and (c) cathode flow field and the current density distribution (CDD) board. The yellow square in the images depicts the active area (25 cm^2). The impression of the flow fields can be clearly seen in (a) and (b). Also, the air inlet and the outlet O-rings can be identified in (c). 196
Figure S3.6. (a) Raw current (amps) in the 100 segments at the average cell current of 25 A (1 A/cm^2), (b) smoothed contours of percentage deviation from the mean current measured in (a), (c) raw temperature data (in °C) in the 25 segments at 25 A (1 A/cm^2), and (d) smoothed

contours of raw temperature data measured in (c). All the distributions were recorded at $Tcell$ = 80 °C, $\lambda H2/\lambda Air$ = 1.5/2, and $RH\%\ A/C$ = 100/100 with $Pabs\ A/C$ = 150/150 kPa. 198

Figure S3.7. Correction methodology for current density distributions (CDD). Raw current distributions plotted as the percentage deviation from mean at low geometric current densities (a) to (d) are averaged to obtain distribution in (e). This distribution is then subtracted from a distribution at high geometric current density (f) to obtain a corrected distribution in (h). All the distributions were recorded at $Tcell$ = 80 °C, $\lambda H2/\lambda Air$ = 1.5/2, and $RH\%\ A/C$ = 100/100 with $Pabs\ A/C$ = 150/150 kPa. 199

Figure S3.8. (b) to (d) are corrected distributions obtained from subtracting the averaged distribution in (a) at high geometric current densities. (f) to (h) are corrected distributions obtained from subtracting the averaged distribution in (e) at high geometric current densities with the flipped air inlet and outlet as compared to distributions in (a) to (d) to verify the robustness of the correction approach. All the distributions were recorded at $Tcell$ = 80 °C, $\lambda H2/\lambda Air$ = 1.5/2, and $RH\%\ A/C$ = 100/100 with $Pabs\ A/C$ = 150/150 kPa. 200

Figure S3.9. (b) and (c) are corrected distributions obtained from subtracting the averaged distribution in (a) at high geometric current densities under dry inlet conditions ($RH\%\ A/C$ = 50/50). (e) and (f) are corrected distributions obtained from subtracting the averaged distribution in (d) at high geometric current densities with the flipped air inlet and outlet as compared to distributions in (a) to (c), to test the robustness of the correction approach at dry inlet conditions ($RH\%\ A/C$ = 50/50). All the distributions were recorded at $Tcell$ = 80 °C, $\lambda H2/\lambda Air$ = 1.5/2, and $RH\%\ A/C$ = 50/50 with $Pabs\ A/C$ = 150/150 kPa. 201

Figure S3.10. Cyclic voltammograms (CVs) of the hydrogen desorption region after baseline correction for double-layer capacitance at the beginning-of-life (BOL) and different stages during the accelerated stress tests (ASTs) for (a) CC AST and (b) Pt AST-Wet, and (c) Pt AST-Dry measured under H_2/N_2 atmosphere at $Tcell$ = 80 °C, $RH\%\ A/C$ = 100/100 with no backpressure. 202

Figure S3.11. (a) Polarization performance of the membrane electrode assemblies (MEAs) at the BOL and different stages of the ASTs for (a) Pt AST-Dry, (b) Pt AST-Wet, and (c) CC AST.

Polarization curves were recorded at $Tcell$ = 80 °C, $\lambda H2/\lambda Air$ = 1.5/2, inlet $RH\%\ A/C$ = 100/100 and 50/50 with $Pabs\ A/C$ = 150/150 kPa. 203
Figure S3.12. Electrochemical impedance spectroscopy (EIS) spectra (0.1 Hz to 10 kHz, 5 % DC current amplitude, 7 points/decade) measured at the BOL and end-of-life (EOL) for (a) CC AST, (b) Pt AST-Wet, and (c) Pt AST-Dry at different geometric current densities. The spectra were recorded at $Tcell$ = 80 °C, $\lambda H2/\lambda Air$ = 1.5/2, and $RH\%\ A/C$ = 100/100 with $Pabs\ A/C$ = 150/150 kPa. 204
Figure S3.13. One dimensional (1-D) current distributions at the BOL and EOL for CC AST at the average current density of 0.5 A/cm^2. All the distributions were recorded at $Tcell$ = 80 °C, $\lambda H2/\lambda Air$ = 1.5/2, and $RH\%\ A/C$ = 100/100 with $Pabs\ A/C$ = 150/150 kPa. Each point on the plot (row number ss. current) from the air inlet (top-right) to outlet (bottom-left) is a row-wise average of 10 current segments. (b) to (e) are the CDD distributions at the EOL for CC AST. The cell voltages at the BOL and EOL at 0.5 A/cm^2 are marked with the arrows.. 205
Figure S3.14. (a) to (d) are the TEM images from different locations of the cathode catalyst layer of the pristine MEA sample. (e) Particle size distribution obtained by analyzing particles from the images in (a) to (d) using ImageJ along with a Gaussian fit to the distribution. 206
Figure S4.15. Absolute ECSA (m^2/g$_{\text{-Pt}}$) versus number of AST cycles for PtfCC and CCfPt ASTs measured under fully humified ($RH\%\ A/C$ = 100/100), H_2/N_2 (anode/cathode) atmosphere at a cell temperature ($Tcell$) of 80 °C with no backpressure. 207
Figure S4.16. Polarization curves for MEAs at different stages during aging for (a) PtfCC AST, and (b) CCfPt AST. Polarization conditions include $Tcell$ = 80 °C, H_2/air stoichiometry ($\lambda H2/\lambda Air$) of 1.5/2, $RH\%\ A/C$ = 100/100 and 50/50 with a backpressure ($Pabs\ A/C$) of 150 kPa (absolute) on both the anode and cathode. 208
Figure S4.17. Panels (a) and (b) represent CDDs measured at the BOL for PtfCC and CCfPt AST, respectively. Panels (c) and (d) represent CDDs measured at the EOL for PtfCC and CCfPt AST, respectively. All the distributions were recorded at $Tcell$ = 80 °C, $\lambda H2/\lambda Air$ = 1.5/2, and $RH\%\ A/C$ = 50/50 with $Pabs\ A/C$ = 150/150 kPa. 209
Figure S5.18. Hydrogen desorption regions of the cyclic voltammograms (CVs) collected under H_2/N_2 atmosphere at anode/cathode for the MEAs aged with (a) N_2 AST, and (b) Air AST. These CVs are corrected for the double-layer capacitance, and are used for calculating the electrochemically active surface area (ECSA) during different stages of the aging. Other

conditions during the CVs include a scan rate of 50 mV/s, $Tcell$ = 80 °C, and $RH\%\ A/C =$ 100/100 with no backpressure. Panel (c) shows the absolute ECSA ($m^2/g_{\text{-Pt}}$). 210
Figure S5.19. Polarization curves of the MEAs during different aging stages for (a) N_2 AST, and (b) Air AST. Polarization curves were collected $Tcell$ = 80 °C, $RH\%\ A/C =$ 100/100 or 50/50, $\lambda H2/\lambda Air$ = 1.5/2 with $Pabs\ A/C$ = 150 kPa/150 kPa on both the anode and cathode. 211
Figure S5.20. Linear sweep voltammograms (LSVs) collected under H_2/N_2 atmosphere at anode/cathode for the pristine and aged MEAs aged with N_2 and Air ASTs. These LSVs are used for calculating the hydrogen crossover currents for the pristine and aged sample. Other conditions during the LSVs include a scan rate of 2 mV/s, $Tcell$ = 80 °C, and $RH\%\ A/C =$ 100/100 with no backpressure. 212

Chapter 1: Introduction and Method of Approach

1.1 Motivation

The global response to the COVID-19 pandemic has underlined the importance of collective action when facing significant global challenges. Just as the pandemic required worldwide cooperation, the climate crisis, primarily driven by greenhouse gas emissions, demands a unified effort. Energy production is central to the climate challenge, as a significant portion of greenhouse gases responsible for trapping heat in the Earth's atmosphere arises from burning fossil fuels to generate electricity and heat. To get a sense of how the Earth has warmed up over the past century or so, Figure 1.1 represents change in global average temperature relative to the average of the baseline period between 1961 to 1990. Clearly, the last few decades have seen a sharp increase in the global temperatures, approximately 0.7 °C higher than the baseline [1]. Extending this analysis back to 1850, the overall increase in global average temperatures amounts to roughly between 1 to 1.2 °C. Fossil fuels, including coal, oil, and gas, contribute significantly to global climate change, responsible for over 75% of global greenhouse gas emissions and nearly 90% of carbon dioxide emissions [2]. To mitigate the adverse effects of climate change, emissions must be reduced by almost half by 2030 and achieve net-zero emissions by 2050. In simple terms, achieving net-zero emissions involves reducing greenhouse gas emissions to the lowest possible level and offsetting any remaining emissions by allowing oceans and forests, for example, to reabsorb these gases from the atmosphere.

Addressing the climate challenge requires a shift away from fossil fuels towards clean, accessible, affordable, sustainable, and reliable alternative energy sources. Renewable energy sources, derived from the sun, wind, water, and Earth's heat, are abundant and replenished naturally, emitting minimal greenhouse gases or air pollutants. Currently, fossil fuels still dominate global energy production, accounting for more than 80%, but cleaner energy sources are steadily gaining ground, with approximately 29% of electricity originating from renewables [3]. Figure 1.2 shows the relative energy consumption of the world from 1965 onwards. Clearly, we can see that usage of fossil fuels has declined slowly but surely and the usage of renewable energy sources have gained momentum, especially over the last decade. Accelerating this transition to renewable energy is imperative to meet emissions reduction targets and combat the climate crisis effectively. Fortunately, there is an active global effort to reach net-zero; over 70 countries, including major

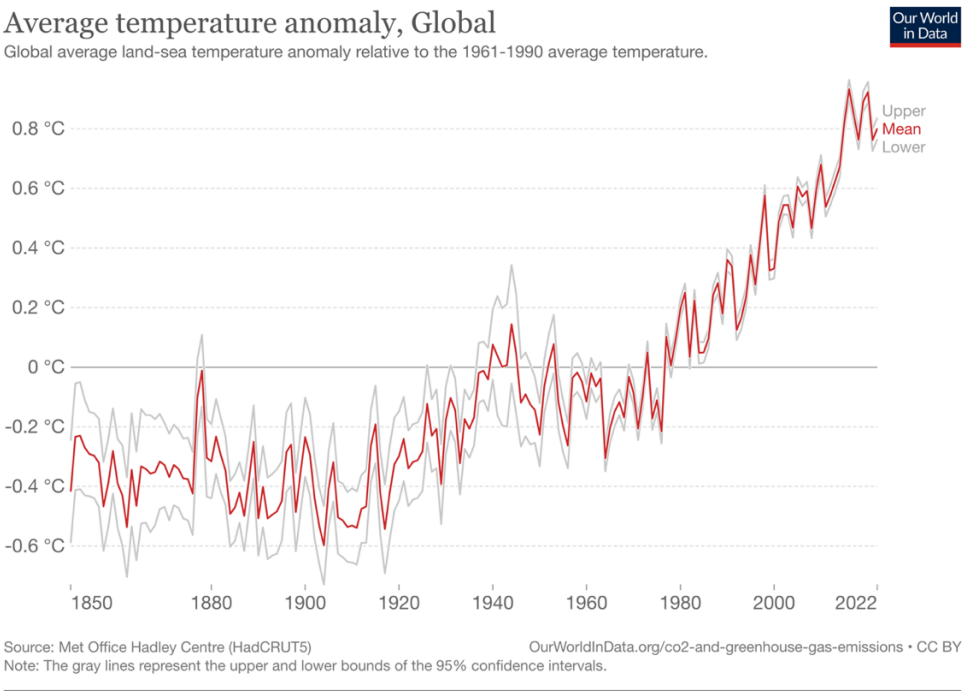


Figure 1.1. Global average land-sea temperature anomaly relative to the 1961-1990 average temperature [1].

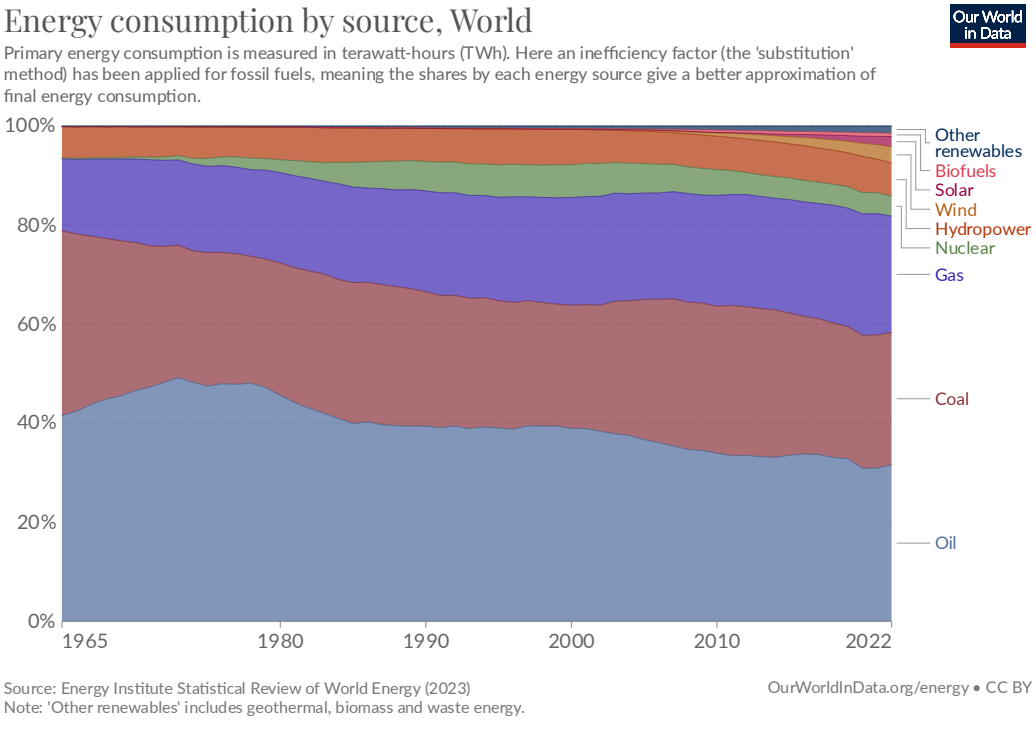


Figure 1.2. Relative world energy consumption by source. The energy consumption (measured in TWh) is corrected for “inefficiency factor” for fossil fuels [3].

polluters like China, the United States, and the European Union, have set net-zero targets, accounting for approximately 76% of global emissions [4].

Clean hydrogen has a vast potential to address the climate crisis along with other renewable resources. Lately, the interest in producing zero- and low-carbon hydrogen has spiked in the United States and other countries around the world. The U.S. Department of Energy (DOE) launched a H2@Scale initiative in 2016 to address the issues and challenges pertaining to affordable hydrogen production, transport, storage, and utilization across multiple sectors [5]. Figure 1.3 outlines DOE's vision under H2@Scale initiative. Clearly, hydrogen can be produced from a gamut of centralized or decentralized domestic resources. In addition, the production can be linked to the grid, offering versatility and can complement present day's conventional grid and natural gas infrastructure. Furthermore, as a part of U.S. National Clean Hydrogen Strategy and Roadmap, the DOE launched another initiative named "Hydrogen Shot" in June 2021. This initiative targets an 80% reduction in the production cost of clean hydrogen, bringing it down to $1 per kilogram in one decade (1 1 1) [6]. From the above discussion, it is obvious that as the green and clean hydrogen production gains momentum, its utilization in clean electrochemical energy conversion devices like hydrogen polymer electrolyte fuel cells (PEFCs) is bound to increase, especially in the transportation sector.

Hydrogen PEFCs offer numerous advantages compared to traditional internal combustion engines in vehicles. Fuel cell electric vehicles (FCEVs) are known for their exceptional operating efficiency (over 60%), impressive driving range (more than 400 miles), and quick refueling times (under 5 minutes) [6]. Low-duty FCEVs have been in the works for almost a decade now and have captured global attention. However, there are still significant hurdles to overcome, particularly regarding vehicle cost and durability, before we can see widespread adoption. Recently, the focus has shifted from the use of fuel cells in light-duty vehicles (LDVs) to heavy-duty vehicles (HDVs) due to the unique scalability of fuel cells in terms of both power and energy, as opposed to battery-operated electric vehicles (BEVs). However, this shift in focus comes with a demand for substantial improvements in cost (targeting $80 per kilowatt), durability (aiming for 25,000 hours of operation), and peak efficiency (targeting 68%) in HDVs, compared to their LDV counterparts, by 2030 [6]. Figure 1.4 shows the U.S. DOE's interim (2030) and ultimate (2050) targets for cost, system lifetime, and peak efficiency targets for automotive and trucks. The challenge of decarbonizing the heavy-duty transportation sector is formidable due to the unique weight and power requirements of these vehicles. These demands result from the different driving patterns

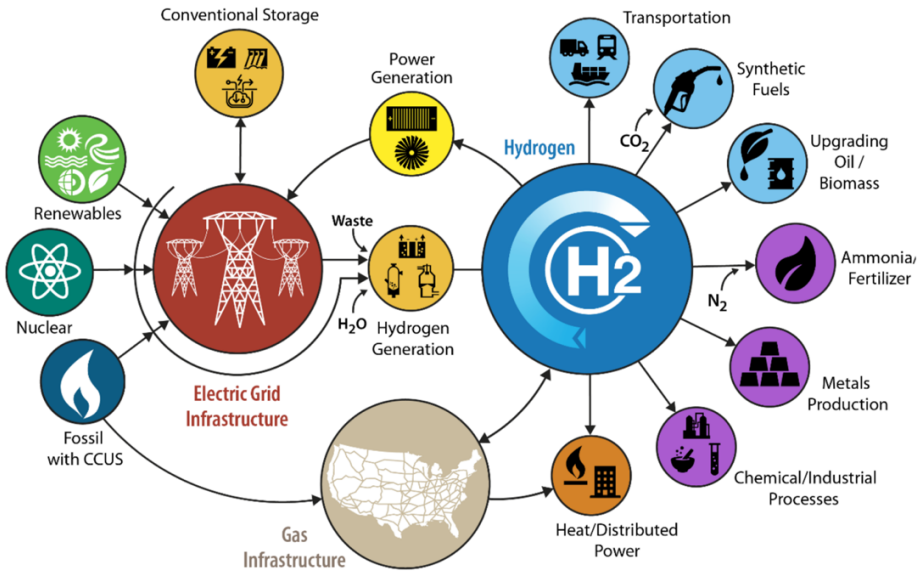


Figure 1.3. U.S. DOE's H2@Scale initiative launched in 2016 to foster decarbonization of various sectors using clean hydrogen (Figure Courtesy: U.S. DOE's H2@Scale initiative [5]).

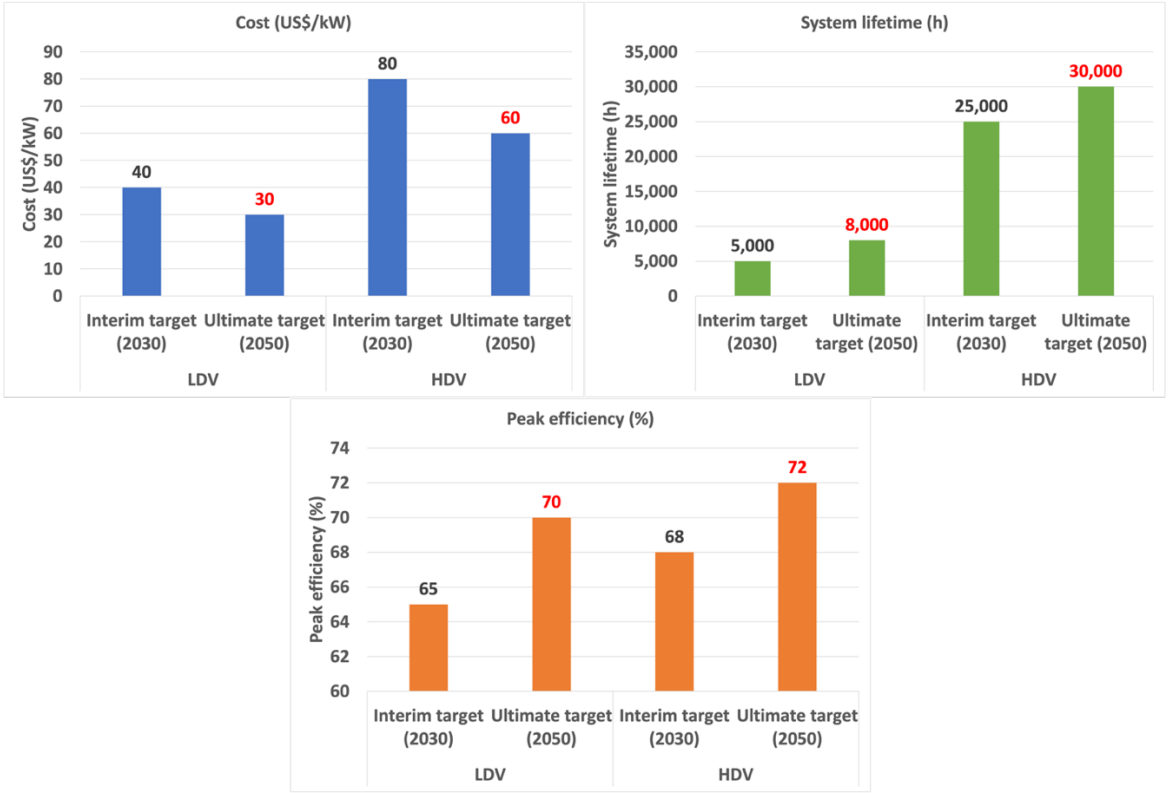


Figure 1.4. U.S. DOE's interim (2030) and ultimate (2050) targets for cost, system lifetime, and peak efficiency targets for automotive and trucks (Data for the figure is adapted from Cullen et al. [6]).

and operating conditions experienced by HDVs. To tackle these pressing challenges regarding the longevity of HDVs, the U.S. DOE has launched the Million Mile Fuel Cell Truck (M2FCT) consortium [7].

A critical aspect of hydrogen PEFCs is the degradation of electrocatalysts. PEFCs use platinum (Pt) or Pt-alloy catalysts, typically Pt nanoparticles dispersed on conductive carbon supports, to catalyze the oxygen reduction reaction (ORR) at the cathode. However, Pt nanoparticles are unstable under voltage cycling and lose catalytic activity over hundreds of thousands of cycles, conditions typically encountered in light and heavy-duty vehicles [8]. Therefore, gaining a deeper understanding of this electrocatalyst degradation in PEFCs is essential to ensure superior performance and longevity, and enable ubiquitous use of green hydrogen in clean electrochemical energy conversion devices like a PEFC.

1.2 Background

1.2.1 Polymer electrolyte fuel cells (PEFCs)

A fuel cell is an electrochemical device that directly converts chemical energy into electricity. In a typical hydrogen–air PEFC, protons produced at anode due to H_2 oxidation migrate through a polymer membrane and combine with oxygen (O_2) at the cathode to produce water. Compensating charge in the form of electrons flows through the external circuit and provides useful electrical work [9]. The electrochemical reactions at the anode and cathode, including the overall reaction are as follows:

At anode (Hydrogen oxidation reaction, HOR) : $H_2 \rightarrow 2H^+ + 2e^-$

At cathode (Oxygen reduction reaction, ORR) : $\frac{1}{2}O_2 + 2H^+ + 2e^- \rightarrow H_2O$

Overall reaction: $H_2 + \frac{1}{2}O_2 \rightarrow H_2O$

Figure 1.5 shows a schematic diagram of a typical fuel cell with its critical components. A single cell is a sandwich structure with several layers of different materials, each designed to accomplish a specific function. The flow fields or bipolar plates (BPP) facilitate liquid- or gas-phase reactant distribution, current collection, and thermal management. Reactant distribution to the catalyst layers (CLs) or electrodes happens through diffusion and/or convection. The electrodes are separated by a polymer electrolyte membrane (PEM). This membrane is ionically conductive and highly resistive to electron flow. A porous carbon paper or carbon cloth diffusion media is a contact layer between the flow fields and the electrodes. This gas diffusion layer (GDL) is

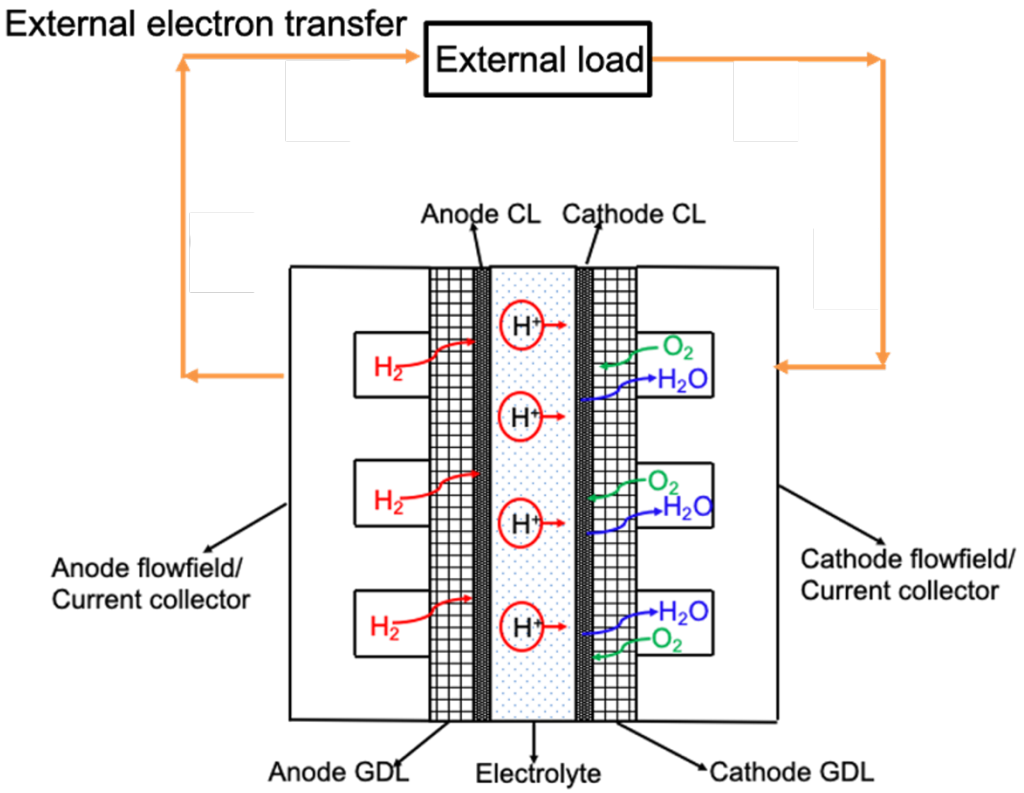


Figure 1.5. Schematics of a hydrogen polymer electrolyte fuel cell (PEFC) depicting critical components. In this figure, CL stands for catalyst layer, and GDL stands for gas diffusion layer.

electrically conductive and facilitates reactant/product species distribution to and from the electrodes. PEFC electrodes are usually 10 – 20 μm thick and consist of Pt/Pt-alloy nanoparticles (2 – 3 nm) dispersed on the surface of primary carbon particles (20 – 50 nm) for electrical contact and an impregnated ion conducting phase (ionomer), forming a highly porous three-dimensional (3D) structure. Electrochemical reactions happen at triple phase boundaries (TPB) with an open pore volume for reactant delivery and product removal, electrical contact with the support for electron transfer, and ionomer coverage for ion transport [10]. An ideal catalyst should have maximum TBPs available for electrochemical reactions. The anode and cathode GDLs, CLs, and the PEM assembly is known as the membrane electrode assembly (MEA).

Theoretically, a single fuel cell can produce the desired current and power by scaling the electrode active area and reactant flow rates. However, the voltage of a single cell has a thermodynamic limit and, under realistic operating conditions, is always less than 1 V. Therefore, if higher voltages are required, several individual cells can be connected in series or a series-parallel combination in a stack. For a series combination, the current is the same through all the cells and is proportional to the individual cell's active area. In this case, the total stack voltage is the sum of the individual cell voltages. For a parallel combination, the voltage across the cells is the same. However, the total current is the sum of individual cell currents. Typical automotive stacks have over 200 cells. Other components necessary for fuel cell system operation include fuel and oxidizer delivery subsystems, temperature and humidity regulators, gaskets for sealing, and voltage regulation and electronic control. The next section will describe some critical PEFC components in detail.

1.2.1.1 Flow fields/bipolar plates/current collectors

PEFCs utilize flow fields/bipolar plates to facilitate the delivery of reactants (hydrogen and oxygen) to the electrode and the removal of products (water) from the cell. Bipolar plates are typically made from graphite, carbon composites, or metal alloys such as stainless steel or titanium [11–15]. Graphite is commonly preferred due to its excellent electrical conductivity, corrosion resistance, and lightweight properties. Bipolar plates are designed to sandwich the MEAs and provide mechanical support to the cell stack. They feature intricate patterns of channels and ribs/lands to guide the flow of reactants and ensure uniform distribution across the electrodes. Flow fields also aid in the dissipation of heat generated during cell operation. Proper thermal management is essential to maintain optimal operating temperatures and prevent performance

degradation or cell damage. Several channel designs are possible in PEFCs [16]. Figure 1.6 shows schematics of some commonly used flow fields designs.

The flow field designs greatly influence the transport of reactants and the removal of product water to and from the electrode. For example,

Serpentine Design: This design offers high performance with fast channel velocities and effective water removal. However, it tends to have a high pressure drop.

Parallel Design: Unlike the serpentine design, this design has a lower overall pressure drop. However, it suffers from poor liquid water removal characteristics.

Interdigitated Design: In this design, there are no continuous channels. Instead, reactants are forced under the lands into the gas diffusion layer (GDL) through convection. This method helps remove product water from the GDL, improving performance, but it comes with a high pressure drop.

Combination Designs (Parallel-serpentine): Most practical fuel cell designs combine parallel and serpentine channels. This design allows tuning of the degree of parallelization and the size of channels/lands to balance high channel velocities and pressure drop [17–20].

Mesh Designs: Mesh designs reduce overall pressure losses. However, dead zones can occur, especially at corners, resulting in uneven reactant distribution and impacting overall performance.

Spiral Design: This design aims to exchange humidity between the inlet and outlet to reduce the humidity load. However, unintended bypass underneath the lands due to pressure mismatch can result in areas without sufficient reactant supply.

Foam Design: This design uses highly porous and electrically conductive metal foam as the flow field, eliminating conventional channel/land architecture. While it can achieve high performance [19,20], it suffers from high pressure loss and uneven reactant distribution. Additionally, metal foams are usually costly. An excellent review of the porous flow fields can be found elsewhere [21].

Recently, there has been an increasing interest in biomimetic or bio-inspired flow fields that mimic natural circulatory systems found in plants and animals [16]. These designs aim to enhance fuel cell performance by achieving a more uniform reactant distribution and lower pressure loss than conventional designs. In summary, the design and optimization of flow fields are critical for enhancing the performance, durability, and efficiency of polymer electrolyte fuel cells (PEFCs). As a note, the flow fields used in the present dissertation for various studies are described in detail in relevant chapters.

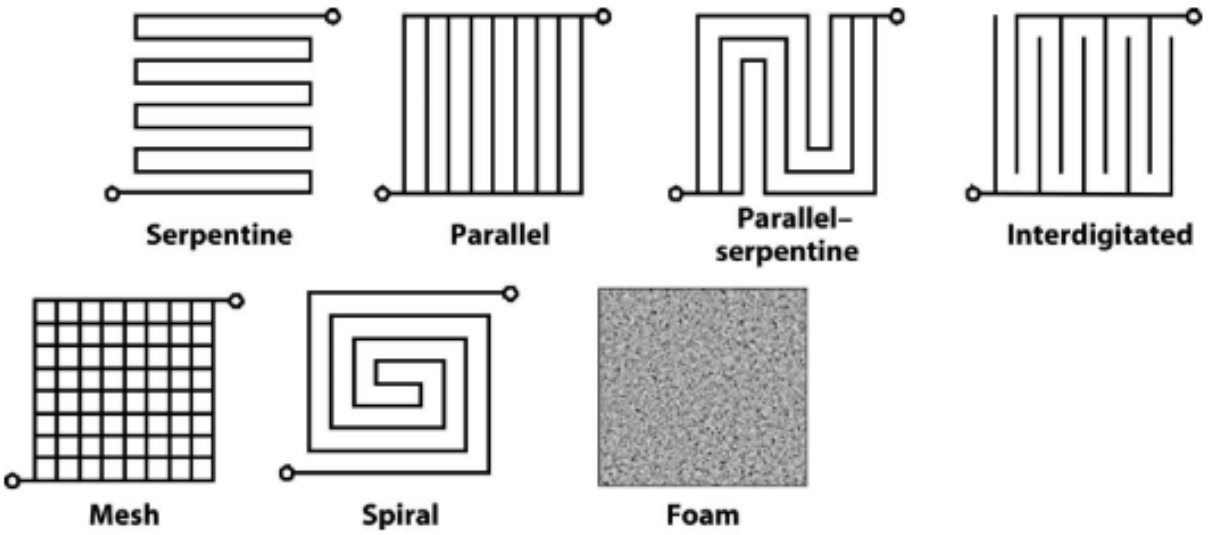


Figure 1.6. Schematics of commonly used flow field/bipolar plate design patterns in PEFCs (Figure taken from Chapter 6 of *Fuel Cell Engines* [22]).

1.2.1.2 Gas diffusion layers (GDLs)

A PEFC gas diffusion layer (GDL) is primarily composed of two sub-layers: a macroporous layer/substrate (MPS) made of carbon fibers or woven carbon cloth and a microporous layer (MPL). The total thickness of this bi-layered structure typically ranges from 200 to 400 μm [23]. The MPS consists of carbon fibers (5 – 10 μm in diameter) stacked randomly and horizontally, bound together with an electrically conductive polymer binder. It is highly porous, with a porosity ranging from 70 to 90% and an average pore diameter ranging from 10 to 50 μm [23]. The MPS undergoes carbonization and graphitization stages at high temperatures, followed by hydrophobic treatment with polytetrafluoroethylene (PTFE). Both the MPS and the MPL are treated with PTFE in varying weight percentages, usually between 5 to 50 wt. %, with the MPL being more hydrophobic than the MPS [23].

The MPL is a composite of carbon powder and a hydrophobic agent (PTFE). Its microstructure comprises agglomerates of carbon powder/hydrophobic agent. The pore sizes in an MPL can vary between 100 to 500 nm. MPL manufacturing involves slurry preparation, deposition, and sintering. In slurry preparation and deposition, carbon powder and hydrophobic agent are dispersed in water or organic solvents and deposited onto the MPS. After deposition, the GDL undergoes heat treatment at around 250 ºC for 30 to 50 minutes to remove any solvent. Subsequently, it is further heat-treated at around 350 ºC for 30 to 60 minutes to ensure uniform distribution of the hydrophobic agent as the GDL dries out [23]. The MPL can either be embedded into the substrate or it can be a standalone structure. Figure 1.7 shows the scanning electron microscopy images of a commercially available GDL (AvCarb EP40 carbon paper). Note the differences in microstructures of the MPS and MPL.

A GDL in a PEFC serves the following functions:

Gas distribution: GDLs provide pathways for distributing reactant gases to the catalyst layers within the MEA. The porous structure of GDLs facilitates the distribution of gases across the electrode surfaces, ensuring mostly uniform reaction rates and minimizing concentration gradients to an extent.

Water management: Water is produced as a byproduct during the electrochemical reactions in a PEFC. GDLs play a crucial role in managing this water by allowing it to migrate away from the electrode surfaces. The porous structure of GDLs helps transport excess water to the flow channels, where it can be removed from the cell. Effective water management is essential for preventing

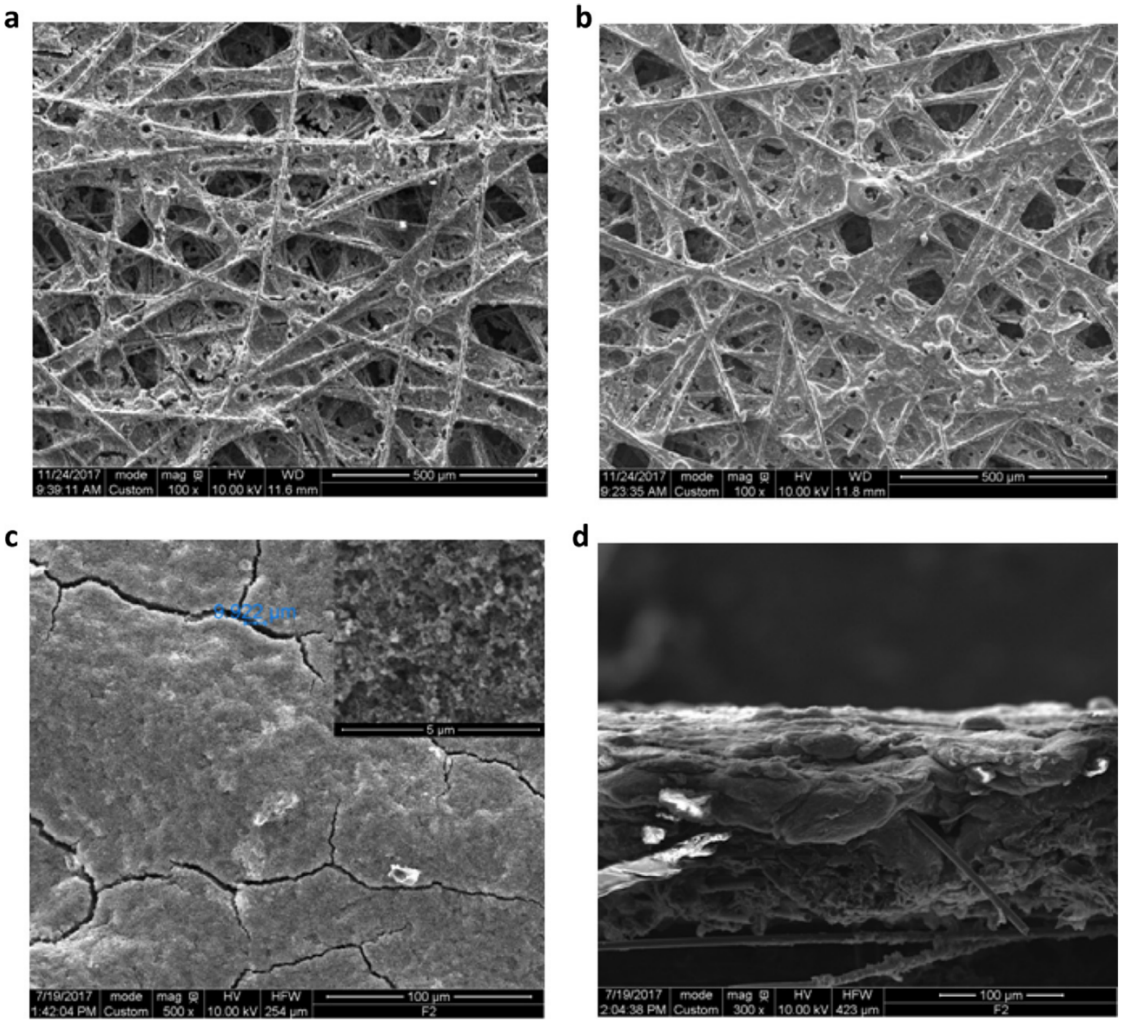


Figure 1.7. Scanning electron microscopy (SEM) images of (a) AvCarb EP40 carbon paper GDL without PTFE, (b) AvCarb EP40 carbon paper GDL with 13% PTFE treatment, (c) MPL on AvCarb EP40 substrate without PTFE, and (d) cross-sectional view of MPS (AvCarb EP40 without PTFE) + MPL (Vulcan XC-72R based). This figure is taken from Ozden et al. [23].

flooding of the electrode surfaces, which can impede gas diffusion and reduce cell performance [17,24–26].

Heat transport: GLDs facilitate heat transport from the electrodes to the current collector. The thermal conductivity of GDLs varies with PTFE content, but it is typically between 0.2 to 1.8 W/m-K [27]. With such low thermal conductivity, it acts as an insulator between the catalyst layers and current collector. The thermal conductivity of a GDL is a crucial property for water removal from a PEFC through phase-change-induced flow [28,29].

Electron conduction: GDLs provide electrical conductivity between the catalyst layers and the bipolar plates in the fuel cell stack. As discussed earlier, carbon-based materials, such as carbon fibers or carbon cloth, are commonly used in GDLs due to their high electrical conductivity. This property allows for the efficient transfer of electrons generated during the electrochemical reactions, enabling the flow of electrical current through the fuel cell stack and to the external circuit.

Mechanical support: GDLs also serve as mechanical support for the catalyst layers and the MEA. They help to maintain the structural integrity of the fuel cell stack during assembly and operation, preventing deformation or damage to the electrode components. This mechanical support is essential for ensuring the long-term durability and reliability of the fuel cell system.

During the assembly of a PEFC, compression is applied to ensure proper contact between different layers. This compression causes deformation in the diffusion media, particularly the GDLs, due to the compressive strain. Typically, GDLs experience compressive strains ranging from 5% to 20% under compression pressures of 1 to 2 MPa. As GDLs are highly porous structures, compression, especially under the flow field lands, reduces porosity. Volume-rendered X-ray CT images of a commercially available GDL (Freudenberg H2315 C2) under various compressive strains illustrate this phenomenon in Figure 1.8. In the case of Freudenberg GDL, compression primarily affects both the substrate and the MPL, causing strain perpendicular to the plane of the GDL [30]. However, this behavior varies depending on the nature of the substrate and the MPL (whether embedded or standalone). For instance, with Sigracet SGL 29BC GDL, compressive strain mainly occurs in the substrate as the voids between the fibers collapse [30]. Further insights into the stress-strain behavior of commercially used GDLs in PEFCs are available in previous publications [31]. Understanding these changes in GDL morphologies is crucial for enhancing the high-power performance of PEFCs.

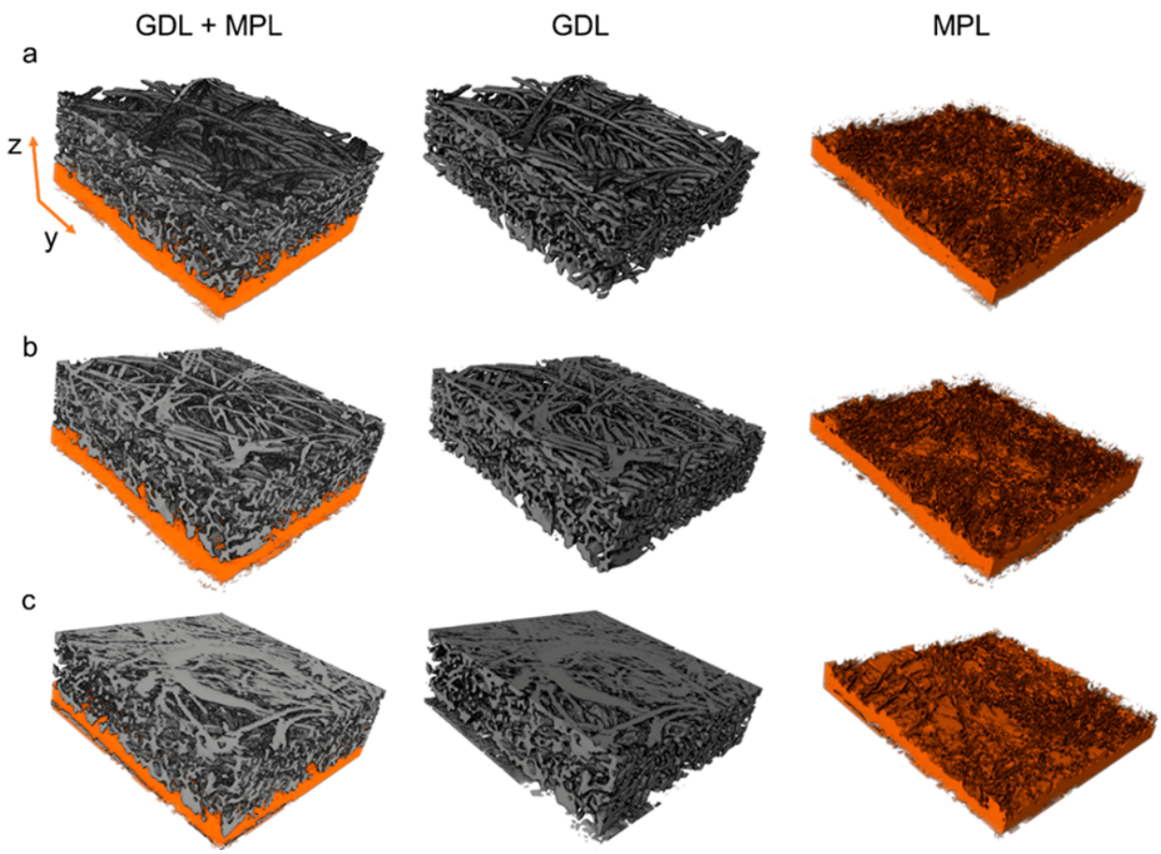


Figure 1.8. X-ray computed tomography (X-ray CT) volume rendered images of Freudenberg H2315 C2 GDL showing the effect of compression on the MPS and MPL. The compression on the samples is (a) 0%, (b) 14%, and (c) 28%. This figure is taken from Atkinson et al. [30].

1.2.1.3 Polymer electrolyte membrane (PEM)

In PEFCs, perfluorinated sulfonic acid (PFSA) based ionomers are commonly employed as solid polymer electrolytes. These ionomers exhibit exceptional ion conductivity and chemical-mechanical stability. Among them, Nafion, developed by DuPont in the 1970s, stands out as the most widely used PEM in PEFCs. Nafion is a copolymer consisting of a chemically inert and stable polytetrafluoroethylene (PTFE) backbone, to which sulphonic acid groups (SO_3^-) are randomly tethered (covalently bonded) as side chains [22]. This structure gives Nafion dual characteristics: 1) hydrophilic and ionically conductive sulphonic acid side chains that absorb water and facilitate proton conduction, and 2) a hydrophobic and chemically inert backbone that provides stability. As the ionomer absorbs water, a natural phase separation occurs, with the hydrated sulphonic acid side chains (H_3O^+-SO_3^-) enabling proton conduction. The general chemical structure of a typical PFSA-based ionomer, along with the phase separation between the hydrophilic and hydrophobic domains, is illustrated in Figure 1.9. In the literature, two modes of proton conduction in PFSA-based ionomers are proposed [32]: 1) At low relative humidity or water content, the ionically conductive side chains behave as isolated clusters, and proton transport occurs purely by diffusion and physical means. This mechanism is known as the vehicular mechanism. 2) Under high relative humidity or water content, proton conduction happens through the Grotthuss or proton hopping mechanism. Here, protons hop from one ion cluster to another, increasing effective conductivity. Figure 1.10 illustrates the vehicular and Grotthuss mechanisms of proton conduction in PFSA-based membranes.

The ionic conductivity of electrolyte membranes relies on the clustering of conductive side chains and water uptake. A polymer membrane's equivalent weight (EW) is a critical parameter that quantifies the relationship between conductive and non-conductive domains in the ionomer. EW represents the weight of dry polymer per ionic group (SO_3^-). For fuel cell electrolytes, EW typically falls between 800-1200 and is calculated as follows [22]:

$$EW\left(\frac{g}{eq}\right) = 100 \times k + MW_{side-chain}$$

Here, k represents the number of tetrafluoroethylene (TFE) groups, and MW (side-chain) is the molecular weight of the side-chain. PEMs are typically 8 to 50 μm thick in fuel cell applications. Several companies, including W. L. Gore and Associates, 3M, Asahi Glass Co. Ltd., and Dow Chemical, manufacture PEMs for fuel cells. For a comprehensive understanding of PFSA-based

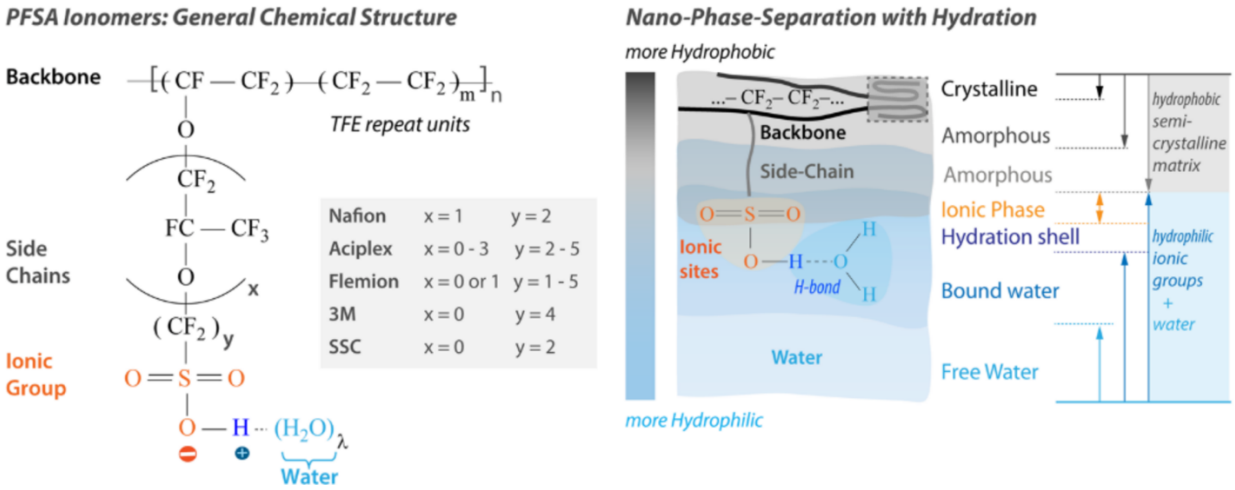


Figure 1.9. General chemical structure of PFSA-based ionomers. Also, it depicts nano-phase-separation with water uptake (hydration). This figure is taken from Kusoglu et al. [33].

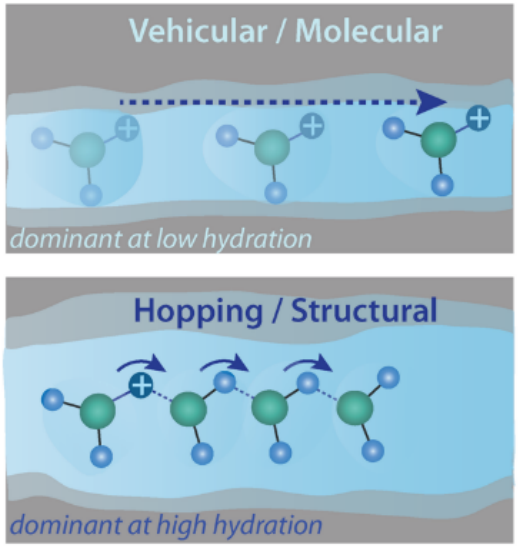


Figure 1.10. Proton conduction mechanisms in PFSA-based membranes. This figure is taken from Kusoglu et al. [33].

ionomers, a detailed review by Kusoglu et al. [33] is recommended. In the present dissertation, for most of the studies, a Nafion XL membrane is used, which is approximately 27.5 μm thick.

1.2.1.4 Catalyst layers

PEFC electrodes or catalyst layers are usually 10 – 20 μm thick and consist of Pt/Pt-alloy nanoparticles (2 – 5 nm) dispersed on the surface of primary carbon particles (40 – 90 nm) for electrical contact and an impregnated ion conducting phase (ionomer), forming a highly porous three-dimensional structure [22]. Figure 1.11 shows a typical PEFC catalyst layer with highly dispersed Pt nanoparticles on carbon particles. Electrochemical reactions happen at triple phase boundaries (TPB) with an open pore volume for reactant delivery and product removal, electrical contact with the support for electron transfer, and ionomer coverage for ion transport [10]. An ideal catalyst should have maximum TBPs available for electrochemical reactions i.e., high ECSA, where reactant gases delivery, protons, and electron conduction can be facilitated. Figure 1.12 shows the concept of a TBP in a fuel cell catalyst layer. PEFC catalyst layers can have considerable ionomer fraction (up to 30 wt.%) to enable proton transport [22]. Some PTFE treatment is also possible for water removal but it is not completely hydrophobic.

The quantity of catalyst dispersed within the catalyst layer plays a vital role in determining the catalytic activity and overall efficiency of the fuel cell. Achieving an optimal catalyst loading involves finding the right balance between maximizing the catalytic surface area and minimizing the cost of the catalyst material. In a PEFC, the amount of catalyst loaded onto the anode typically ranges from 0.01 to 0.1 $mg_{\text{-Pt}}/cm^2$ [34]. This relatively low loading is feasible at the anode due to the favorable kinetics of the hydrogen oxidation reaction. On the other hand, at the cathode, the catalyst loading is typically higher, ranging from 0.1 to 0.4 $mg_{\text{-Pt}}/cm^2$. Efforts to reduce Pt loading in fuel cells have been actively pursued. For instance, the U.S. DOE set a 2020 target for the total Pt group metal loading (including both anode and cathode) in a PEFC to be around 0.125 mg-Pt/cm² [34]. However, this target may evolve significantly in the future, particularly with the transition to HDV applications. A major challenge associated with reducing Pt loading at the cathode is the increase in oxygen mass transport resistance of the electrodes with low Pt loading. This increase in resistance is primarily attributed to the diffusion of oxygen through the thin ionomer film covering the Pt catalyst [35–38]. At ultra-low loadings or roughness factor, oxygen transport resistance becomes the dominant factor contributing to performance degradation. Therefore, overcoming this transport resistance is essential for achieving high performance with

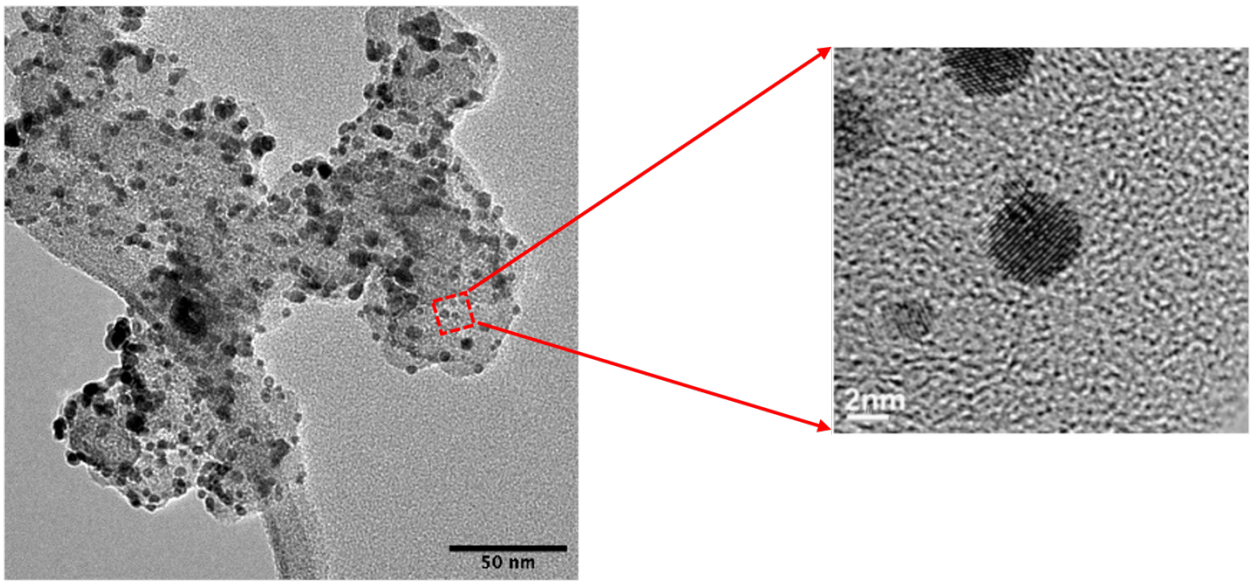


Figure 1.11. Transmission electron microscopy (TEM) images of a PEFC catalyst layer: Pt/C catalyst (40 wt.% Pt on Vulcan carbon).

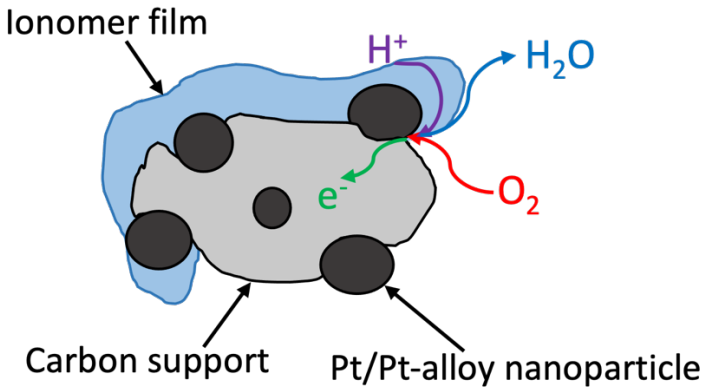


Figure 1.12. Schematic of a triple phase boundary in a fuel cell catalyst layer [22].

low-loaded electrodes in fuel cells. Addressing this challenge will be crucial for realizing the full potential of low-Pt-loading catalyst layers and increasing the efficiency and affordability of fuel cell technology.

The size and distribution of catalyst particles within the catalyst layer influence the accessibility of reactants to catalytic sites and the overall reaction kinetics. Fine-tuning the particle size and distribution can enhance mass transport and reaction rates. The choice of support materials for catalyst particles, such as carbon black or carbon nanotubes, affects the stability, conductivity, and durability of catalyst layers. Support materials provide a high surface area for catalyst dispersion and facilitate electron transport. More details on the supports used in fuel cell catalyst layers can be found in previous publications [39–42].

PEFC catalyst layers are manufactured using several techniques, including physical spray deposition on diffusion media or the PEM, slurry tape casting, and the decal transfer method [22]. In physical spray deposition, a catalyst slurry consisting of catalyst powder, ionomer, and solvents such as water and alcohols is prepared. This slurry is then directly sprayed onto the diffusion media or PEM using a simple nozzle or other methods like electrodeposition or sputter deposition. Subsequently, the solvents are dried out by subjecting the slurry to high temperatures. In slurry tape casting, a doctor blade spreads the catalyst ink directly onto the diffusion media or PEM. This method allows for precise control over the thickness and uniformity of the catalyst layer. The decal transfer method involves spreading the catalyst slurry onto a non-adhesive medium and then transferring the decal onto the electrolyte by hot-pressing. This method is suitable for the mass production of fuel cell catalyst layers with tight tolerances and batch processing capabilities. Each of these manufacturing methods offers distinct advantages and may be chosen based on factors such as scalability, precision, and cost-effectiveness. Detailed descriptions can be found in previous publications [34] for a more comprehensive understanding of the various catalyst layer manufacturing techniques.

Recent research efforts have focused on the development of Pt group metal-free (PGM-free) catalysts based on earth-abundant metals (such as iron) or alternative materials to reduce dependency on expensive and scarce Pt-based catalysts [43,44]. Advanced catalyst layer architectures have been proposed for improving mass transport, reduce catalyst loading requirements, and enhance overall fuel cell performance [45].

1.2.2 Voltage losses in PEFCs

A polarization curve for a PEFC represents the cell voltage as a function of the current density (scaled by geometric electrode area), typically obtained through experimental testing under various operating conditions. The curve exhibits a characteristic shape with voltage decreasing as current density increases, reflecting the performance characteristics of the fuel cell. Figure 1.13 shows a typical polarization curve for a PEFC. The polarization curve begins at the open circuit voltage (OCV), representing the maximum voltage output of the fuel cell when no current is drawn. The OCV is established by the thermodynamic potential of the electrochemical reactions taking place at the anode and cathode. In practical hydrogen fuel cells, the OCV typically falls within the range of 0.92 V to 1.0 V. This value is lower than the thermodynamic voltage due to reactant gas crossover and short circuit. The thermodynamic voltage or Nernst voltage (E_N) can be written as [22,46]:

$$E_N = E^{\circ}_{rev}(T) - \frac{RT}{2F} ln\left(\frac{a_{H_2O}}{a_{H_2} a_{O_2}^{1/2}}\right), a_j = \frac{P_j}{P^o}$$

In the above equation, $E^{\circ}_{rev}(T)$ is the reversible cell voltage at standard pressure (P^o) and temperature (T), R is the gas constant, F is the Faraday constant, a_j is the activity of species j, and P_j is the partial pressure of species j.

The expression for the OCV accounting for the leakage current is:

$$OCV = E_N - \eta_{loss}$$

where η_{loss} is given as [22,46]:

$$\eta_{loss} = \frac{RT}{\alpha nF} ln\left(\frac{i_{loss}}{i_o}\right)$$

In the above equation, α is the charge transfer coefficient, n is the number of electrons transferred, i_{loss} is the leakage current due to the reactant crossover and short circuit, and i_o is the exchange current density. Other symbols have their usual meaning.

Various losses due to polarization of a fuel cell away from the equilibrium state are as follows:

Activation/Kinetic losses: As current is drawn from the fuel cell, the voltage drops due to activation losses associated with the kinetics of the electrochemical reactions. This region of the curve, known as the activation region, represents the voltage losses due to the activation overpotential at both the anode and cathode. Activation losses result from the energy barrier that

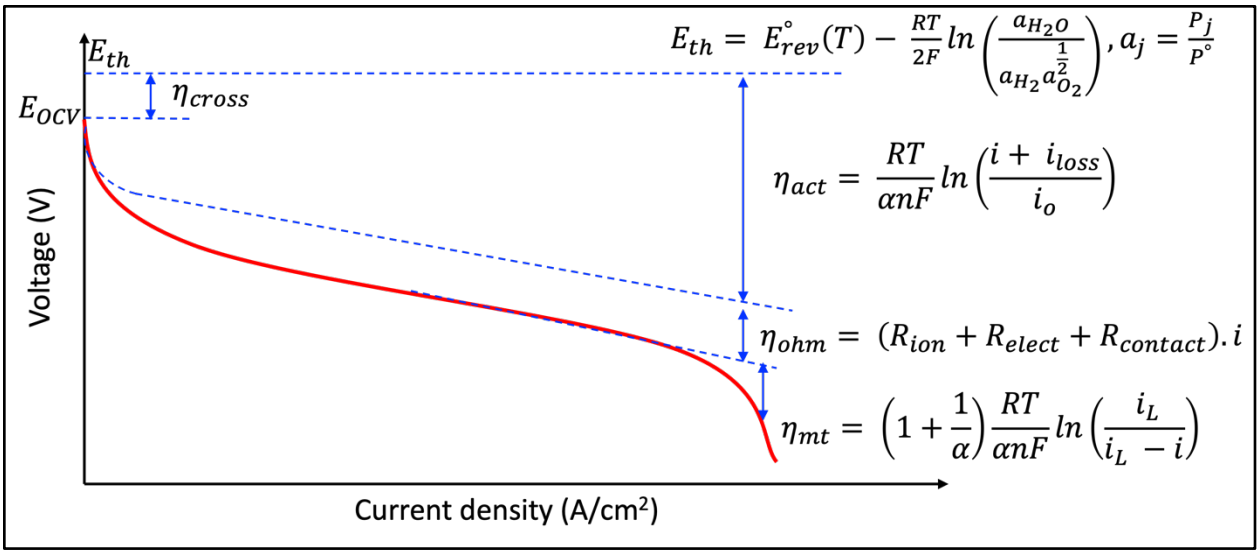


Figure 1.13. Various polarization losses in PEFCs [22].

must be overcome for the electrochemical reactions to occur at the catalyst sites. Assuming that the activation losses at the anode (HOR) are relatively small compared to those at the cathode (ORR) and that the Tafel kinetics (approximation of Butler-Volmer equation) applies, we can express the activation overpotential (η_{act}) as follows [22,46]:

$$\eta_{act} = \frac{RT}{\alpha nF} ln\left(\frac{i + i_{loss}}{i_o}\right)$$

In the above equation, α is the charge transfer coefficient, n is the number of electrons transferred, i is the operating current density, i_{loss} is the leakage current due to the reactant crossover and short circuit, i_o is the exchange current density, and other symbols have their usual meaning.

Ohmic losses: Following the activation region, the curve transitions into the ohmic region, characterized by a linear decrease in voltage with increasing current density. Ohmic losses occur due to the electrical/ionic resistance encountered by ions and electrons as they traverse through the electrolyte membrane, catalyst layers, and current collectors, including the contact resistances. The ohmic overpotential (η_{ohm}) can be written as follows [22,46]:

$$\eta_{ohm} = (R_{ion} + R_{elec} + R_{contact}).\, i$$

In the above equation, R_{ion} is the ionic resistance in the cell, R_{elec} is the electronic resistance, and $R_{contact}$ is the contact resistance.

Concentration/Mass transport losses: At higher current densities, the voltage drop becomes more pronounced, indicating concentration/mass transport losses associated with the depletion of reactants near the catalyst sites. The rate of reactant transport to the catalyst sites becomes limiting, with the removal of products from the electrode surfaces becoming inefficient. This region, known as the concentration/mass transport region, reflects the voltage losses due to concentration overpotential at both the anode and cathode. The mass transport overpotential (η_{mt}) can be written as [22,46]:

$$\eta_{mt} = \left(1 + \frac{1}{\alpha}\right)\frac{RT}{\alpha nF} ln\left(\frac{i_L}{i_L - i}\right)$$

In the above equation, i_L is the limiting current density and the other symbols represent quantities discussed earlier.

In general, the operating voltage of a fuel cell can be written as [22,46]:

$$E_{cell} = E_N - \eta_{loss} - \eta_{act} - \eta_{ohm} - \eta_{mt}$$

Note that the activation and mass transport overpotential equations can be individually formulated for both the anode and the cathode. In a PEFC, the losses at the anode are much smaller compared to those at the cathode [22]. Comparing and analyzing polarization performance is a fundamental method for evaluating degradation in fuel cells. Over time, PEFC aging results in performance degradation due to changes in the key parameters mentioned above.

1.2.3 Degradation in PEFCs

1.2.3.1 Catalyst degradation in PEFCs

In typical automotive fuel cells, extensive load cycling occurs during regular operation, leading to the dissolution of Pt catalysts and posing a significant hurdle for commercialization. Multiple studies in the literature have delved into the factors influencing the durability of the cathode catalyst layer (CCL) under various operating conditions. We can assess the stability of Pt species in an aqueous electrolyte by examining a pH-potential diagram, also known as a Pourbaix diagram. Figure 1.14 illustrates the thermodynamic stability windows for planar Pt and nanoparticles with diameters of 3 nm and 1 nm [47].

Planar Pt exhibits a wide stability window and only dissolves within a narrow potential range (1 to 1.25 V versus reversible hydrogen electrode, RHE) and pH range (-2 to 0). However, Pt nanoparticles have a broader dissolution window, with the equilibrium dissolution potential strongly dependent on the nanoparticle radius.

This relationship is defined by the Gibbs-Thomson equation, which relates the equilibrium dissolution potential to the particle size [47] :

$$\Delta E = \frac{2\gamma\Omega}{nFr}$$

In the above equation, ΔE is the change in equilibrium dissolution potential, γ is the surface tension, Ω is the molar volume, F is the Faraday's constant, r is the radius of spherical nanoparticle, and n is the electrons transferred per metal cation. The Gibbs-Thomson equation highlights the significant influence of particle size and surface energy on the dissolution potential. As nanoparticle size decreases, surface tension increases due to lower coordination and exposure of high-index facets, leading to a rapid decrease in the dissolution potential. The morphology of nanoparticles are more prone to dissolution than those on the flat surface. Previous studies have extensively investigated the size and shape dependency of Pt nanoparticles [8,48–52]. In PEFC studies, the electrocatalyst activity and durability are assessed using rotating disk electrodes

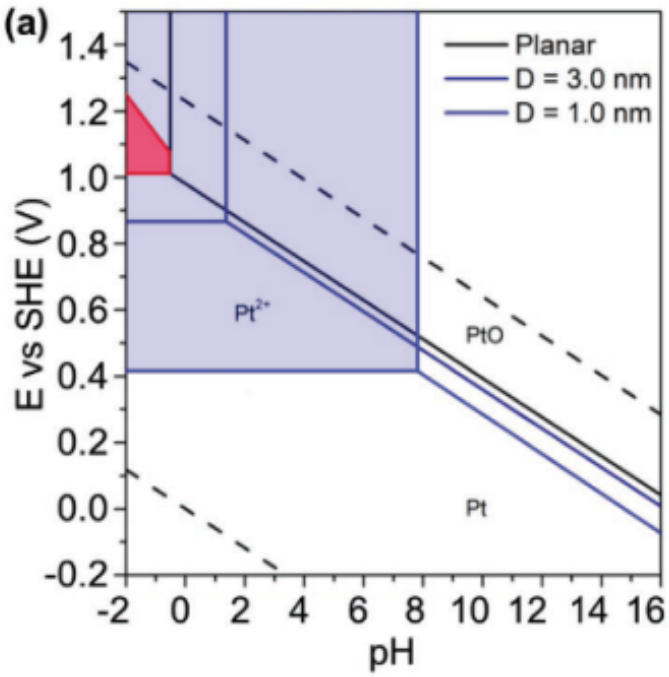


Figure 1.14. Stability of PGM catalyst (Pt/Pt^{2+}) in aqueous electrolyte. Dissolved Pt^{2+} concentration is 10^{-6} M. This figure is taken from a review paper by Zhu et al. [47].

(RDEs) or MEAs. Though an RDE is a quick and easily accessible tool, the results might not match those of MEA testing, which closely resembles the actual application [53]. So, a careful interpretation of results is required to avoid errors related to the determination of catalyst activity and durability.

As mentioned earlier, catalyst cost is projected to be the largest single component of stack cost. For example, in a 275-kW_{net} HDV PEFC system, catalyst cost amounts to approximately 59% of the stack cost, with a system cost of \$112/kW_{net} at 50,000 systems produced per year [54]. Therefore, further improvements and significant research and development is required, especially in terms of durability of both the PGM and PGM-free catalyst materials proposed for HDV applications.

In vehicles equipped with PEFCs, power output needs to adapt to various driving conditions, often resulting in rapid changes in load. These transient load fluctuations can significantly impact fuel cell durability due to changes in local conditions such as gas stoichiometry, temperature, humidity, pressure, water distribution, and electrode potential [46]. Accelerated stress tests (ASTs) are commonly employed to replicate the degradation experienced by catalysts, catalyst supports, and other components during dynamic fuel cell operation. These tests typically involve exposing the fuel cell to controlled conditions, often using air or nitrogen at the cathode and pure hydrogen at the anode. Different potential limits are selected to simulate specific types of degradation. For example, the U.S. Department of Energy (DOE) recommends voltage cycling within certain ranges to mimic catalyst or catalyst support corrosion. For catalyst corrosion, a square-wave pattern cycling between 0.6 and 0.95 V versus RHE is often utilized, with a hold time of typically three seconds at each voltage setting [41,55]. On the other hand, for catalyst support corrosion, a triangular-wave pattern cycling between voltage limits of 1.0 and 1.5 V versus RHE is recommended, with a voltage ramp rate of 500 mV/s or greater [41,55]. It is important to note that the chosen voltage limits, ramp rates, and hold times during these tests can significantly affect catalyst degradation. Previous research has extensively explored the impact of these parameters on the degradation of the catalyst layer in PEFCs [56–58].

Extensive literature is available on different mechanisms responsible for catalyst degradation in PEFCs subjected to load cycling. Pt degradation leads to loss in ECSA and hence, loss in polarization performance. Significant Pt dissolution can occur at high cathode potentials due to oxidizing conditions. The Pt dissolution process in PEFC can be described as [46]:

Pt dissolution: $Pt - 2e^- \rightarrow Pt^{2+},\ E_o = 1.18\,V\ vs.\,RHE\ at\ 25\ ℃$

Pt oxide formation: $Pt + H_2O - 2e^- \rightarrow PtO + 2H^+,\ E_o = 0.98\,V\ vs.\,RHE\ at\ 25\ ℃$

Pt oxide dissolution: $PtO + 2H^+ \rightarrow Pt^{2+} + H_2O$

Note that as nanoparticle size decreases, surface tension increases due to lower coordination and exposure of high-index facets, leading to a rapid decrease in the dissolution potentials mentioned in the above equations. Pt oxides are formed on the surface of nanoparticles, followed by reduction and chemical dissolution. Other Pt oxides such as PtO_2 and $Pt(OH)_2$ have also been reported to be formed along with PtO [46,51]. More details on Pt oxide formation and dissolution under typical fuel cell operating conditions can be found in previous studies [51,59,60].

In general, four mechanisms (shown schematically in Figure 1.15) contribute to the loss of the ECSA through Pt degradation in fuel cells [61]:

1. **Modified (electrochemical) Ostwald ripening** leads to Pt growth, where Pt ions from smaller particles diffuse through the ionomer, redepositing on larger particles, resulting in a decrease in smaller particle size and an increase in larger particle size. The particles move from a higher chemical potential to a lower chemical potential. This mechanism dominates at cathode potentials above 0.8 V vs. RHE and can be described using the Gibbs-Thomson equation. Due to Pt dissolution, the solute concentration around small particles exceeds that of large particles. As a result, Pt ions are transported from smaller to larger particles via diffusion, as per Fick's law. The transport of Pt ions happens over nanometer length scales. In the electrochemical Ostwald ripening, the transport of Pt ions and electrons is coupled. Therefore, the electrical connection of Pt particles with the carbon support is necessary. This mechanism is usually responsible for a rapid ECSA decline in the early phases of potential cycling, as the Pt particles have high surface tension. Furthermore, the electrochemical Ostwald ripening is intensified at high relative humidity conditions (>90%) at the cathode.
2. **Pt crystal migration and coalescence** cause Pt nanoparticles to migrate on the carbon support and coalesce, responsible for ECSA loss at cathode potentials below 0.7 V vs. RHE. Typically, crystal migration and coalescence is observed in gas phase sintering without an electrolyte for Pt/C catalysts. However, unique experimental evidence of this mechanism is yet to be reported. Most voltage cycling ASTs typically recommend cycling above 0.6 V vs. RHE. So, ECSA loss through Pt crystal migration and coalescence is likely

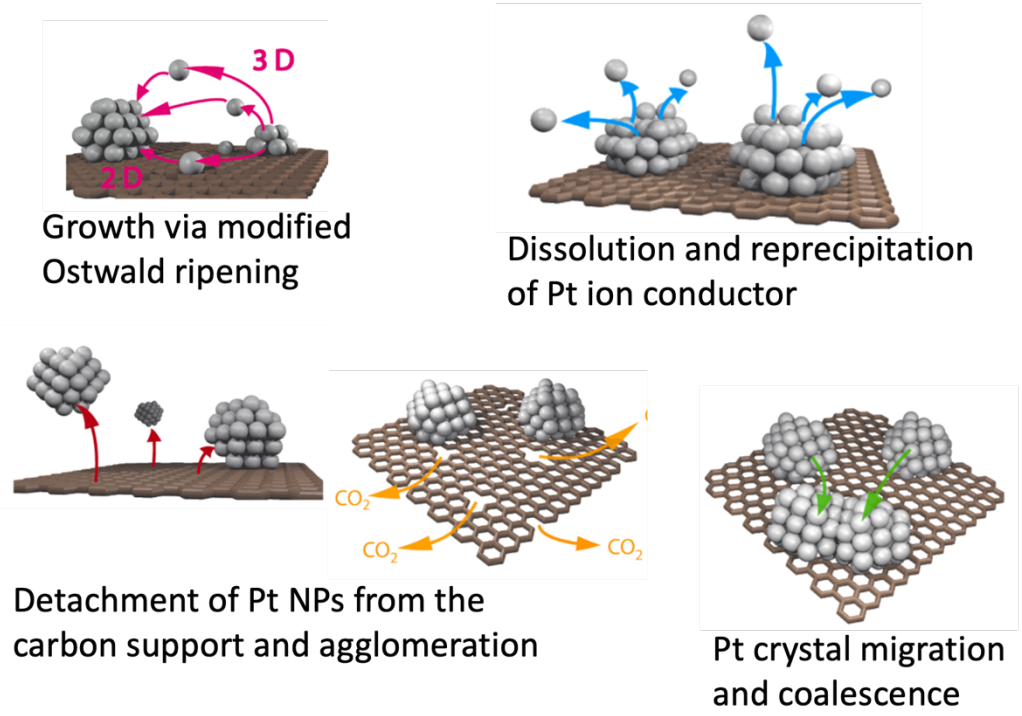


Figure 1.15. Different mechanisms of Pt degradation in PEFCs. This figure is adapted from the review paper by Josef C. Meier et al. [62].

not predominant under typical PEFC operating conditions. Also, the solubility of Pt below 0.7 V vs. RHE has been reported to be negligible. Note that this mechanism does not result in a loss of electrical contact of Pt particles from the carbon support. The migration and coalescence happen at a nanometer length scale.

3. **Detachment of Pt nanoparticles from the carbon support and agglomeration**, typically due to carbon corrosion, occurs at cathode potentials exceeding 1.1 V vs. RHE, resulting in a loss of electrical contact. Carbon corrosion occurs due to high potential excursion in a PEFC during startup/shutdown, fuel/air starvation, and cell reversal. Due to the rapid oxidation of the carbon support at voltages exceeding 1.1 V vs. RHE, Pt particles detach from the support, rendering them electrically isolated. With continued cycling, open pore volume for reactant and product transport in the catalyst layer decreases, resulting in severe mass transport losses. Carbon corrosion depends on the nature of the support (low, medium, and high surface area), interactions between the Pt particles and the support, voltage cycling limits, and the presence of water (relative humidity). Carbon corrosion is discussed in detail in the following section. This mechanism occurs at a nanometer length scale.
4. **Pt dissolution and reprecipitation** in the ion conductor occur when soluble Pt species from the cathode are reduced and precipitated within the ionomer and the polymer membrane through chemical reduction by hydrogen molecules from the anode. Due to a high concentration of dissolved Pt ions at the cathode and a low concentration at the anode, there is a diffusion-driven transport of Pt ions from the cathode towards the anode. However, due to the hydrogen crossover from the anode, these Pt ions get reduced into microcrystalline form and precipitate into the ionomer or membrane. As a result of it, a well-defined Pt band is observed in the membrane. This mechanism is typically active for cycling above 0.6 V vs. RHE. The extent to which this mechanism contributes to the ECSA loss depends on the relative humidity, partial pressures of oxygen and hydrogen, membrane thickness, and voltage limits. This mechanism is primarily diffusion or concentration-driven as the effect of migration under the potential gradient under typical fuel cell operating conditions is negligible in the membrane. This process occurs at the micrometer length scale.

During OCV or idling conditions, Pt catalysts in PEFCs can experience accelerated degradation through Pt growth and precipitation. However, under these conditions, membrane degradation can be particularly severe [63–68]. PFSA-based membranes, commonly used in PEFCs, undergo chemical degradation when attacked by free radicals such as hydroxyl radical (*OH), hydroperoxyl radical (*OOH), and hydrogen radical (*H). One significant factor contributing to membrane degradation is the generation of hydrogen peroxide (H_2O_2) within the fuel cell. Hydrogen peroxide (H_2O_2) is generated in a fuel cell due to a two-electron ORR reaction as follows [46]:

$$O_2 + 2H^+ + 2e^- \rightarrow H_2O_2, E_o = 0.695\, V\ vs.\ RHE\ at\ 75\ ℃$$

The generation of hydrogen peroxide is somewhat suppressed at the cathode during OCV or idling conditions due to the high potential (>0.9 V). However, the anode of the fuel cell is typically considered the primary source of peroxide generation due to its lower potential. It is important to note that gas permeation plays a crucial role in membrane durability because the reactants for peroxide generation, hydrogen and oxygen, can crossover from their respective electrodes. This crossover of reactants contributes to the chemical degradation of the membrane. Besides chemical degradation, mechanical degradation of the membrane can also occur due to humidity cycling.

1.2.3.2 Catalyst support corrosion in PEFCs

In PEFCs, the MEAs and GDLs are commonly made from carbon-based materials. These materials, particularly on the cathode, are subjected to oxidizing conditions. Under these conditions, both the catalyst and catalyst support are prone to degradation, leading to reduced ORR activity and increased mass transport losses. Carbon support degradation mainly occurs during startup and shutdown cycling, especially at high cathode potentials (> 1.0 V vs. RHE). The primary oxidant responsible for electrochemical carbon corrosion is water, with carbon dioxide (CO_2) being the end product. This oxidation reaction can be represented as [41]:

$$C + 2H_2O \rightarrow CO_2 + 4H^+ + 4e^-, E_o = 0.207\, V\ vs.\ RHE$$

Although carbon corrosion kinetics are typically slow under normal PEFC operating conditions, the presence of Pt can catalyze this reaction. Carbon support oxidation leads to loss in ECSA due to particle detachment, decreased electrical conductivity of the support, pore structure collapse, and reduced open pore volume for reactant and product transport [41,42,46,69–74]. Carbon corrosion typically occurs during the startup/shutdown phases in a PEFC. During startup, the air present at the anode is replaced by hydrogen, and conversely, during shutdown, the hydrogen at the anode is

replaced by air. This transition creates a local boundary between hydrogen and air at the anode, if not mitigated by using an inert gas like nitrogen. Reiser et al. [75] elucidated this phenomenon through a reverse current mechanism.

In the left region of Figure 1.16, regular fuel cell operation occurs, with the HOR taking place at the anode and the ORR at the cathode. Due to the high in-plane electrical conductivity of the GDLs and bipolar plate, both the left and right regions are at a potential close to the HOR potential, neglecting any in-plane potential drops. However, the ORR occurring in the right region at the anode further decreases the ionomer potential, leading to a substantial increase in the interfacial potential difference in the right cathode region to approximately 1.5 V [46,75]. This increased potential difference intensifies the carbon oxidation reaction (COR) and oxygen evolution reaction (OER) at the cathode, causing significant corrosion in the local cathode region. During regular fuel cell operation, carbon corrosion can also occur if localized regions are deprived of fuel and air due to flooding at the anode or cathode. To simulate carbon corrosion encountered during startup/shutdown cycling, the U.S. Department of Energy (DOE) recommends a triangular-wave pattern cycling between voltage limits of 1.0 and 1.5 V versus RHE, with a voltage ramp rate of 500 mV/s or greater.

While the abovementioned mechanisms of Pt degradation and carbon corrosion have been proposed, the nature of Pt dissolution remains poorly understood within the context of operational fuel cells, as they depend on various operating conditions such as cell temperature, relative humidity, water content, reactant partial pressure, and operating potential. In summary, higher upper potential limits (>1 V vs. RHE), elevated temperatures (>90 °C), and increased RH levels exacerbate degradation [76].

Since the focus of this dissertation is the catalyst and catalyst support degradation in PEFCs, the degradation of other components such as the GDLs, membrane, and bipolar plates is not discussed in detail. Thorough studies can be found in the relevant literature [77–85].

While numerous studies have explored the impact of operating conditions on the degradation of PEFCs, there remains a dearth of studies investigating the heterogeneity of degradation, both in-plane and through plane, and its quantification under various operating conditions. Fairweather et al.[86] studied the effects of cathode corrosion on through-plane water transport in PEFCs using neutron imaging. They observed a significant decrease in water retention in all cell designs after severe cathode corrosion. This decrease was attributed to increased internal

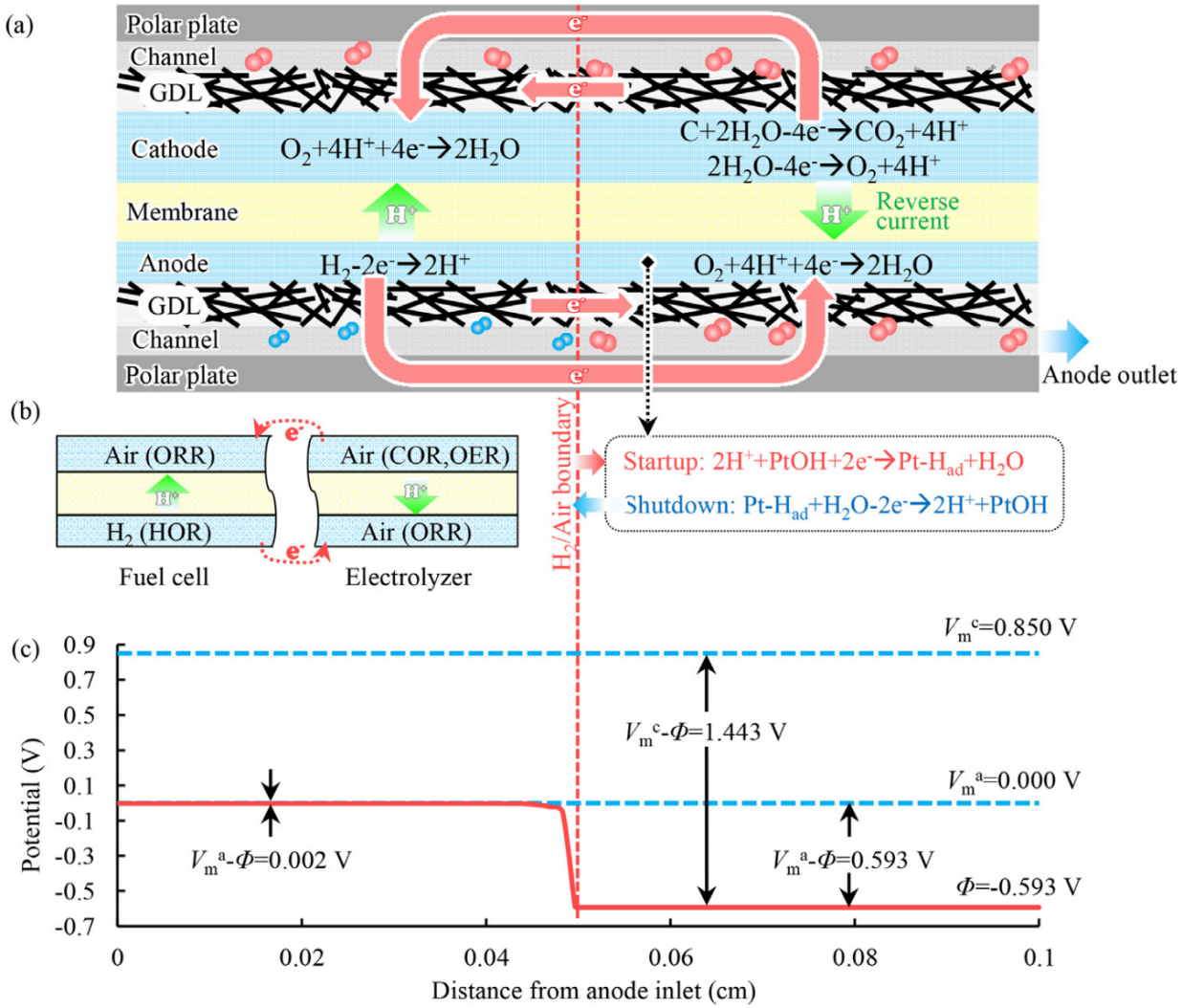


Figure 1.16. Schematics of (a) reverse current mechanism, (b) dual-cell mechanism under startup/shutdown cycling, and (d) potential profile along a gas channel in a fuel cell. This figure is taken from a review paper by P. Ren et al.[46]. Note that the original mechanism was proposed by Reiser et al.[75].

heat generation in the degraded cell, causing a drying effect. The collapse and compaction of the catalyst layer were identified as the primary limitations to cell performance, rather than lower amounts of ECSA. Higher temperature gradients were found to contribute to cell drying. Lin et al. [87] investigated the impact of dynamic driving cycles on catalyst layer degradation using segmented cell technology in real time. They observed a faster decline in current density at the exit and inlet regions compared to other areas in the MEA during drive cycles. This degradation was characterized by catalyst layer thinning, an increase in platinum particle size, and a loss of ECSA, consistent with typical drive cycle degradation patterns. In another study, Lochner et al. [88] examined the operation of an automotive-sized single cell under realistic operating conditions. They found that the current density distribution (CDD) was influenced by the partial pressure of hydrogen, particularly during transitions from high to low current densities, leading to flooding of the anode catalyst layer near the anode outlet. Ex-situ characterization revealed significant cathode corrosion in areas associated with low current densities.

White et al. [89] conducted a study aiming to connect water distribution to electrode degradation in PEFCs. They utilized four-dimensional joint visualization, incorporating three spatial dimensions and time, to observe liquid water distribution inside an operating PEFC during potential cycling. This study marked the first attempt, as claimed by the authors, to obtain time-resolved data on local degradation using identical-location operando X-ray computed tomography (X-ray CT). Similar to the findings of Fairweather et al. [86], White et al. observed that at the end-of-life stage, liquid water in the GDL was nearly absent at moderate to high current densities, likely due to evaporation from excessive heat generation. Additionally, they noted an increase in catalyst layer movement attributed to stresses from membrane swelling during advanced stages of cathode degradation. The porosity of the CCL was initially found to increase before experiencing a sudden collapse at end-of-life. Hack et al. [90] utilized identical-location X-ray CT imaging to investigate local degradation of a MEA at various locations along the channel of a serpentine flow field. They conducted carbon corrosion ASTs and found that degradation occurred in the order of outlet > middle > inlet, with the outlet CCL being thinner than the middle and inlet regions and exhibiting more extensive cracking. Furthermore, they observed that land regions were less degraded than channel regions.

In another study, Cheng et al. [91] attempted to map heterogeneity in the CCL using synchrotron X-ray microdiffraction. They demonstrated that Pt particle size growth was non-

uniform, with greater growth observed under lands than channels. Additionally, Pt particle size increased more at the outlet region than the inlet region of the MEA. Furthermore, it has been shown that ASTs conducted under fully humidified conditions resulted in more pronounced Pt particle size growth and ECSA loss compared to underhumidified conditions for the same number of cycles [92]. Despite identifying these heterogeneities in Pt particle size growth, there remains a gap in understanding how these non-uniform distributions impact localized performance loss in PEFCs following an AST. There is a dearth of studies investigating the effects of heterogeneous catalyst degradation on localized electrochemical performance.

Comprehending the local effects is crucial, particularly for automotive-sized PEFC stacks, where species, temperature, RH, and pressure distributions are mostly heterogeneous. Deeper understanding of local performance responses to aging must be incorporated in the design of highly durable fuel cells capable of withstanding thousands of load/unload, start-up/shutdown cycles. It is also important to understand the interactions between different degradation mechanisms and quantify any path-dependent degradation in PEFCs.

From the discussion above, it is apparent that heterogeneity in CCL degradation is catching the attention of the researchers and only recently, a few studies have emerged. There is significant room for developing new diagnostic methods and get novel insights into local degradation effects and link important factors such as water distribution to it. This dissertation is an attempt to advance the current understanding of local degradation effects with a unique combination of in-situ and ex-situ techniques. Results from this study would certainly pave the way for better design of automotive fuel cell catalyst layers with maximum utilization and durability to achieve DOE's target [6].

1.3 Method of Approach

This section briefly discusses major in-situ and ex-situ characterization techniques used in the present study. A variety of other in-situ electrochemical techniques such as cyclic voltammograms (CVs), linear sweep voltammograms (LSVs), polarization curves, electrochemical impedance spectroscopy (EIS), and Tafel analysis were also employed to elucidate electrocatalyst degradation. For details on these in-situ electrochemical techniques and other experimental methods, including different materials used, please refer to Chapters 2 through 5.

1.3.1 In-situ localized current distribution measurements

Determining the localized current density distribution (CDD) is crucial for understanding and resolving heterogeneities in degradation within fuel cells. Over the years, various approaches have been developed for in-situ CDD measurements. Most of these techniques involve dividing the cell current into discrete in-plane segments and measuring the current in these electrically isolated segments. One such method is the partial MEA approach, where different areas of the MEA are either masked or partially catalyzed to determine local CDD [93]. However, this method may only partially capture inherent variations in electrical, transport, and kinetic properties between different MEAs. Another approach is the segmented cell method, where flow fields, bipolar plates, current collectors, and GDLs are separated by insulated segments. This approach can be further categorized into the sub-cell method, segmented plates approach, and the printed circuit board (PCB) technique [94],[95]. The segmented cell approach includes two additional categories [96] in terms of design and construction: the resistor network methodology and magnetic loop (Hall effect) sensors. Hall effect sensors allow for high spatial and time-resolution measurements without the need to modify MEAs [97]. In other words, the resistor network and magnetic loop sensors differ in how they measure the current generated by the MEA.

In this study, the PCB technique is used. The basic premise of this technique relies on measuring a voltage drop across shunt resistors in each segment and using Ohm's law, current in each segment can be calculated [94],[95]. Figure 1.17 shows the principle of PCB technique. Segments 1 through 9 have individual shunt resistances. This technique requires modification of one or both current collectors and flow fields i.e., they need to be segmented to minimize the lateral current spread and obtain spatially resolved measurements. Several authors have pioneered this technique for PEFCs and have done extensive performance characterization at various operating conditions. Perez et al. [98] provide an excellent review of such studies. Few of the recent studies [88,99] utilizing this technique for understanding spatial degradation in automotive size PEFCs have already been discussed in the previous section.

1.3.2 Ex-situ synchrotron grazing incidence X-ray diffraction (GIXRD)

X-ray is a form of electromagnetic radiation characterized by a wavelength (λ) typically ranging from 0.5 to 2.5 Å. In a standard X-ray diffraction (XRD) experiment, monochromatic X-rays emitted from a source are directed towards the sample at a specific angle, denoted as θ. The extent of X-ray penetration into the sample is determined by this angle, θ.

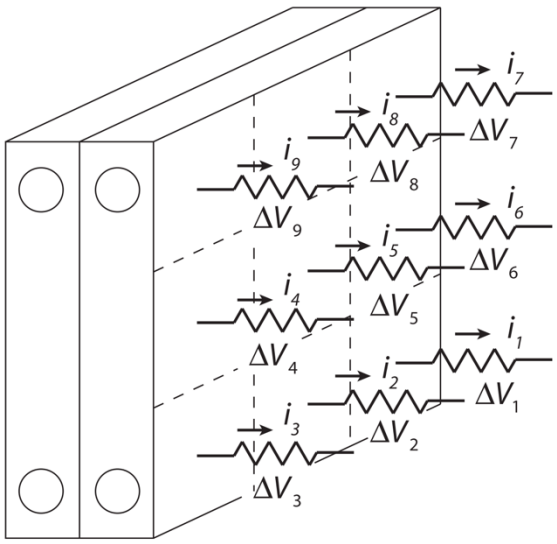


Figure 1.17. Schematics of current mapping technique in PEFCs (Figure taken from Chapter 9 of *Fuel Cell Engines* [22]).

The X-rays that are diffracted by the sample emerge at an angle of 2θ relative to the incident beam and are then collected by a detector. Typically, both the X-ray source and the detector are mounted on a goniometer, which ensures precise angular positioning of θ. This setup is known as Bragg-Brenton θ-θ geometry. Alternatively, there is another configuration known as Bragg-Brentano θ-2θ geometry, where the X-ray tube remains stationary while the sample and detector move. In this setup, the sample and detector are positioned horizontally, and the angular position of the diffracted beam is adjusted to twice the angle of the incident beam. The resulting diffraction pattern comprises intensity peaks at specific 2θ angles, which depend on the lattice parameters of the sample [100]. The relationship between the wavelength (λ) of the incident X-ray beam and the lattice spacing (denoted as d) is described by Bragg's law, which forms the fundamental principle of XRD techniques. It is expressed as:

$$n\lambda = 2d \sin \theta$$

where n (an integer) is the "order" of reflection, λ is the wavelength of the incident X-rays, d is the interplanar spacing of the crystal and θ is the incident angle of the X-rays. The peak positions correspond to crystallite type and the shape of the peak gives information about crystallite size.

XRD is widely utilized in fuel cell research to analyze catalyst powders and determine the size of Pt nanoparticles, representing a common practice in the field. However, conventional XRD techniques suffer due to their significant penetration depth into the sample, especially in PEFC MEAs. This limitation hampers the ability to distinguish between particle size growth at the cathode and the anode in fuel cell degradation studies. To address this issue, grazing incidence X-ray diffraction (GIXRD) techniques are employed. GIXRD utilizes very shallow incident angles, typically ranging from 0.3 to 3 degrees, to maximize the signal from thin surface layers [100]. Figure 1.18 illustrates the schematic difference between conventional XRD and GIXRD setups. In GIXRD, only the detector rotates through the angular range, while the incident angle, beam path length, and irradiated area remain constant during the diffraction spectrum collection. By employing a narrow beam spot, GIXRD allows the active area in a fuel cell MEA to be divided into several measurement volumes. The average particle size within these volumes can then be determined using the classical Scherrer's equation, which relates crystallite size (t) to the wavelength of incident X-rays (λ), incident angle (θ), and the full width at half-maximum (FWHM) of the diffraction peak. The equation is expressed as:

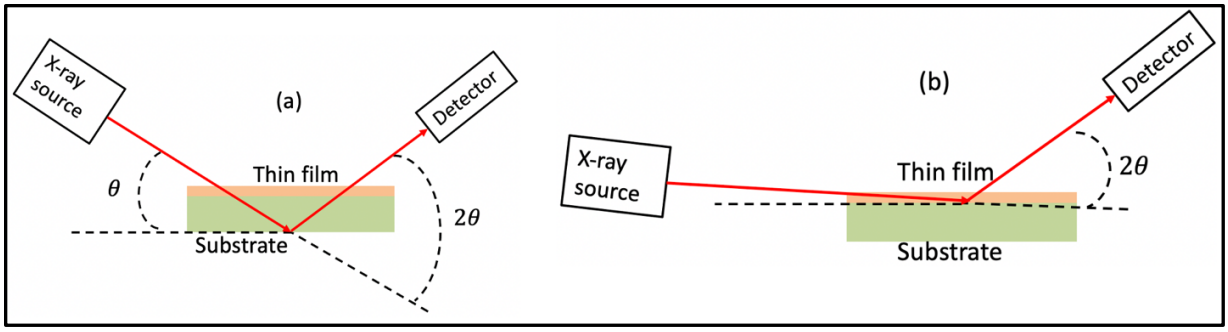


Figure 1.18 (a) Standard Bragg-Brentano XRD, (b) GIXRD

$$t = \frac{K\lambda}{B\cos\theta}$$

Here, t represents the crystallite size, K is the shape or structure factor, λ is the wavelength of the incident X-rays, θ is the incident angle of the X-rays, and B is the FWHM.

Cheng et al. [91] used GIXRD for mapping heterogeneous catalyst degradation in PEFCs. In the present dissertation, aged samples were analyzed using the technique developed by Cheng et al. [91]. All the measurements were performed at Stanford Synchrotron Radiation Lightsource (SSRL), Beam line 2-1. Beam line 2-1 is a dedicated thin film/powder diffraction and reflectivity station. It has an energy range (5500 – 17500 eV), resolution $\frac{\Delta E}{E}$ ~ 5x10^{-4}, spot size of 0.2x0.45 mm^2 and angular acceptance of 1.5 mrad. Such a small beam spot size allows for resolving channel-land particle sizes in heterogeneous degradation. Huber 2-circle goniometer and several types of sample stages are available to allow for easy sample mounting and analysis. As GIXRD allows for a shallow angle probing, the derived signal is from Pt particles within the CCL. Probing depth can be controlled by tweaking incident angle and beam energy. Figure 1.19(a) shows intensity peaks of Pt vs 2θ and Figure 1.19(b) shows X-ray attenuation length (penetration) vs beam energy used in the present study. Data acquisition was performed using SPEC, with SPECPlot GUI interface (in-house diffractometer control, peak fitting, and plotting software). Note that some of the Pt particle size mapping was performed using in-house XRD equipment at Bosch Research and Technology Centre, Sunnyvale, CA. More details on these can be found in Chapters 2 through 5.

1.3.3 In-operando neutron imaging

Neutron radiography (NR) or neutron imaging is a technique in which neutrons pass through the sample to determine internal structures. This technique relies on a microscopic cross-section of a material, which is essentially the probability of neutron interaction with a single atom, independent of the concentration of atoms in the concerned material. Attenuation coefficient which is the product of the microscopic cross-section and the atomic density of material towards a neutron beam gives a quantitative way to use this technique for calculating water thickness in fuel cells.

Neutron imaging was first used by Mosdale et al. [101] to determine water profile across the electrolyte membrane in a running PEFC. Bellows et al. [102] also used the neutron imaging technique for in-situ measurement of water transport gradients within the Nafion membrane in PEFCs. However, neutron facility at NIST was first used by Satija et al. [103] to estimate water

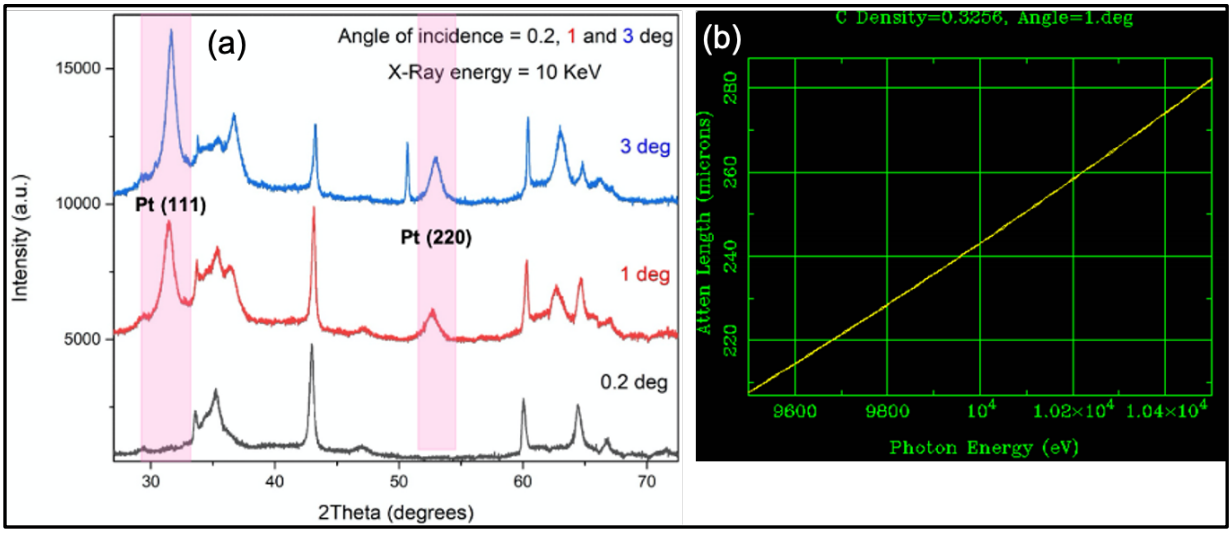


Figure 1.19 (a) Intensity vs. 2Theta (2θ) and (b) Attenuation length vs. Photon Energy (eV)

distribution in the fuel cell diffusion media. The limitations in detector resolution at NIST confined majority of the initial research to in-plane direction [104–112]. An in-plane image is essentially an integration of two halves of the cell and hence, separation of water distribution in the cathode from the anode is not feasible. High-resolution through plane imaging of PEFCs started in mid 2000s with the detector resolution reaching ~25 μm [113]. Figure 1.20 shows the difference between the in-plane and through plane neutron imaging in fuel cells. An excellent review on neutron imaging of PEFCs is provided by Boillat et al. [113].

While the first paper on neutron imaging of fuel cells emerged more than a couple of decades ago, there is still ample potential for further advancements in this field, offering unique solutions to issues such as the distributed or heterogeneous degradation of PEFCs. Understanding water management in PEFCs is crucial as materials age with successive potential cycling, leading to water redistribution within the cell. Fuel cell materials possess varying heat and mass transport properties that evolve depending on the degradation cycle applied. These changes in properties drive particle size growth in the CCL. Therefore, comprehending water management and monitoring how thermal and mass transport evolve in an aged cell could contribute to enhancing the current understanding of degradation pathways and the loss of ECSA. While most neutron imaging studies have focused on characterizing and improving the performance of operational PEFCs, more research is needed to utilize neutron imaging to quantify and characterize degradation in PEFCs. Thus, the present dissertation aims to provide novel insights into PEFC degradation by leveraging neutron imaging techniques.

All the neutron imaging experiments in the present dissertation were performed at the SINQ-NEUTRA beam-line at Paul Scherrer Institute (PSI), Switzerland. A spatial resolution of 25 μm was achieved with an exposure time of 30 seconds. The images were acquired at a specific condition after the cell was run at steady-state for at least 10 to 15 minutes. A referencing method is used to distinguish between the beam attenuation caused by the water and the other materials in the sample. This is done by acquiring a reference image without liquid water, typically, by flowing dry N_2 through the cell [100]. By dividing the image of the operating cell by the image of the dry cell (pixel-wise), beam attenuation caused by the water alone can be obtained. In some cases, structural changes can be induced by the change in relative humidity as the polymer membrane swells and shrinks. This problem is alleviated by using other referencing methods, such as humidifying the membrane with heavy water. The water thickness is computed using the

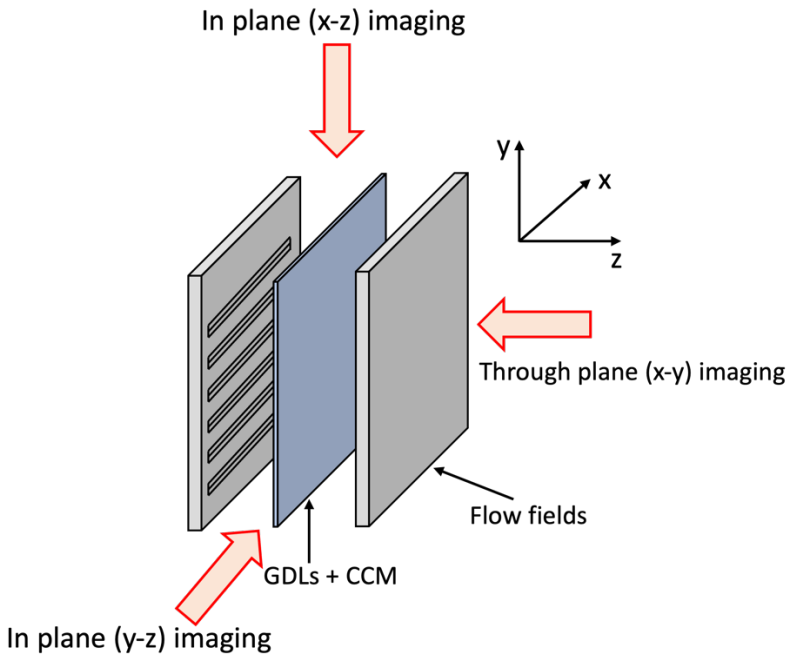


Figure 1.20. Difference between in-plane and through plane neutron imaging for water distribution mapping in fuel cells.

attenuation-based quantification [100], where all the attenuation is considered to originate from a single material i.e., water. The accumulated thickness of water (δ) is then computed from the attenuation coefficient of water (Σ) using Lambert-Beer relation [100]:

$$\frac{I}{I_o} = e^{-\Sigma x \delta}$$

Where I_o is the incident beam intensity, I the outgoing intensity, and δ the thickness of water. As Σ depends on neutron energy, the effective value of the attenuation coefficient is affected by beam spectrum and the sensitivity spectrum of the detector system. Hence, for a given setup, an empirical value of Σ is used based on the measurement of water layers of known thicknesses. More details on the neutron imaging setup can be found in a previous study [114] and Chapter 5 of this dissertation.

1.4 Objectives

Automotive PEFCs undergo extensive load cycling, often reaching hundreds of thousands of cycles in regular use. However, the dissolution of platinum (Pt) catalyst and carbon-support oxidation under these conditions are significant barriers to their widespread adoption. The U.S. Department of Energy (DOE) has set durability benchmarks at 8,000 hours for light-duty vehicles and 30,000 hours for heavy-duty vehicles. Consequently, PEFC electrocatalyst degradation has received significant attention in the past decade. Still, our understanding of electrocatalyst degradation remains incomplete, particularly regarding heterogeneity in catalyst growth and its localized performance impact. Based on these gaps in the literature, the objectives of this dissertation are:

1. Investigate the impact of cathode gas flow rate on electrocatalyst degradation during an accelerated stress test, a parameter often overlooked in PEFC degradation research.
2. Investigate the effects of heterogeneous catalyst degradation on localized electrochemical performance loss.
3. Identify the interactions between various degradation modes in PEFCs and investigate path-dependent degradation.
4. Determine and investigate the relationship between heterogeneous water distribution and catalyst growth in PEFCs.

A deeper understanding of local performance responses to aging and the interactions of different degradation mechanisms explored in this study will enable the design of highly durable fuel cells capable of withstanding thousands of load/unload, start-up/shutdown cycles.

NOTE: In Chapter 2, Objective 1 has been thoroughly investigated and is now a published journal article. Objective 2 has been addressed in Chapter 3 and is also a published article in the journal Small. Objectives 3 and 4 are explored in chapters 4 and 5, respectively. These chapters will be submitted to relevant journals at a later stage after the submission of this dissertation to TRACE portal.

Chapter 2: Impact of Cathode Gas Flow Rate on Catalyst Degradation in Polymer Electrolyte Fuel Cells (PEFCs)

This chapter is revised based on the published paper [115]:

Preetam Sharma, Bapi Bera, Douglas Aaron, Muenir Mustafa Besli, Saravanan Kuppan, Lei Cheng, Jonathan Braaten, Nathan Craig, Sarah Stewart, Michael Metzger, Christina Johnston, Matthew M. Mench, "Spatially Resolved Heterogeneous Electrocatalyst Degradation in Polymer Electrolyte Fuel Cells (PEFCs) Subjected to Accelerated Aging Conditions", Journal of the Electrochemical Society, no. 11, vol. 169, pp. 114506, 2022 (DOI: 10.1149/1945-7111/ac9ee5)

My contributions to this work include conceptualization of the idea, collection, reduction, and analysis of the data and manuscript preparation. Bapi assisted in electrochemical measurements. Lei and Saravanan helped with in-house and synchrotron micro-XRD measurements. Other authors assisted with data curation, review and editing of the manuscript.

Note on copyright: The Electrochemical Society (ECS) and IOP Publishing grant the "Named Authors" the right to "include the Final Published Version (all or part) in a research thesis or dissertation provided it is not then published commercially" in Paragraph 2, bullet point 2 of the Named Authors' Rights (ECS hybrid journals) – Version dated 19 March 2021.

2.1 Abstract

This work quantifies in-plane spatial heterogeneity (polymer electrolyte fuel cell cathode inlet versus outlet) in Pt particle size growth and distribution as a function of nitrogen (N_2) flow rate during a square-wave accelerated stress test (AST). The average Pt particle sizes for membrane electrode assemblies (MEAs) subjected to N_2 flow rates ranging from 4 – 16 sccm/cm^2 are in the range 9-10.5 nm at the end-of-life (EOL) with similar electrochemically active surface area (ECSA) loss (~65%). However, Pt particle size at EOL exhibits spatial heterogeneity: greater Pt particle size growth occurs near the flow field outlet than the inlet. The spatial heterogeneity for a fully-humidified N_2 flow is believed to originate from non-uniform humidification (outlet is more humidified than the inlet) across the cell for a co-flow arrangement. A first-order rate model for ECSA loss predicts linear increase of the rate constant with N_2 flow rate. The polarization losses of the aged MEAs over a wide range of operating conditions increase with N_2 flow rate. From the results of this work, for holistically assessing durability of Pt catalysts in fuel cells at high humidity conditions, it is recommended to include purge gas flow rate as a stressor during an AST.

2.2 Introduction

Polymer electrolyte fuel cells (PEFCs) can be subjected to an enormous number of cycles depending on application, for example, an automotive PEFC is typically subjected to hundreds of

thousands of load cycles during regular operation [116]. Pt catalyst dissolves under such potential cycling conditions and this is a major roadblock to commercialization. Pt loadings below 0.125 mg_{-Pt}/cm^2 are required to meet the stringent cost targets ($30/kW) set by the U.S. Department of Energy (DOE) by 2025 [117]. Many studies have been published to describe the factors influencing load cycle durability of the cathode catalyst layer subject to various operating conditions. PEFC electrodes are usually 10 - 20 μm thick and consist of Pt/Pt-alloy nanoparticles (2 - 3 nm) dispersed on the surface of primary carbon particles (20 - 50 nm) and an impregnated proton-conducting phase (ionomer), forming a highly porous three-dimensional (3D) structure [10].

In general, four mechanisms contribute to the loss of electrochemically active surface area (ECSA) [8]. One mechanism is growth via modified Ostwald ripening; Pt species from smaller particles dissolve into hydrated ionomer and then diffuse through it (at nanometer length scale), redepositing on the surface of larger particles, primarily due to the concentration gradient. This mechanism results in decreased size for smaller particles and increased size of larger particles. This mode usually dominates at cathode potentials > 0.8 V vs. reversible hydrogen electrode (RHE). Another mechanism is Pt crystal migration and coalescence. In this mode, Pt nanoparticles migrate (at nanometer length scale) on the carbon support and coalesce to minimize surface energy. This mechanism is proposed to be responsible for ECSA loss at cathode potentials < 0.7 V vs. RHE [8]. The third mechanism is detachment of Pt nanoparticles from the carbon support and agglomeration due to carbon corrosion at cathode potentials > 1.1 V vs. RHE. This agglomeration also happens at a nanometer length scale and results in loss of electrical contact between Pt nanoparticles and the carbon support. In the fourth known mode of electrochemically based Pt catalyst degradation, soluble Pt species from the cathode are reduced and precipitate into the ionomer; this precipitation usually occurs via chemical reduction by permeated hydrogen molecules from the anode and over a micrometer length scale. Even though these mechanisms are proposed, the nature of Pt dissolution is still poorly understood in the context of an operational fuel cell as it depends on several operating conditions such as cell temperature, relative humidity (RH), water content, reactant partial pressure, local overpotential, etc. In general, high upper potential limit (>1 V vs. RHE), high temperature (>90 °C), and high RH are known to exacerbate degradation [76]. Other factors such as high mass transport resistance and low Pt utilization also limit the performance and durability of cathode catalyst layers (CCLs). These issues are convoluted as they operate over a wide range of length scales and involve the complex interplay

of thermal and mass transport [34,118]. Therefore, a thorough mechanistic understanding of degradation phenomena is still incomplete.

A plethora of literature describe the interplay between operating conditions and PEFC degradation, however, there is a relative paucity of studies elucidating any heterogeneity in degradation and its functionality with various operating conditions. Fairweather et al. [86] studied the effects of cathode corrosion on through-plane water transport in PEFCs using neutron imaging. A dramatic decrease in water retention was observed in each cell design after the cathode corrosion. This was associated with the drying effect of increased internal heat generation in the degraded cell. Collapse and compaction of the CCL were identified as limitations to cell performance, not loss of Pt ECSA. Lin et al. [99] investigated the effect of dynamic driving cycles on CCL degradation using segmented cell technology in real-time. It was observed that the current density at the exit and inlet regions declined faster than other areas in the membrane electrode assembly (MEA) during drive cycles. CCL thinning, Pt particle size increase, and ECSA loss were observed consistent with typical drive cycle degradation. In another study, Lochner et al. [88] studied an automotive-size single cell under realistic operative conditions. Hydrogen partial pressure dominated the current distribution (CD) due to flooding of the anode catalyst layer closer to the anode outlet, especially when switching the operation from high to low current densities. Ex-situ characterization revealed severe cathode corrosion in areas associated with low current density.

White et al. [89] performed four-dimensional (geometric and temporal) visualization of liquid water inside an operating PEFC during potential cycling. Similar to the findings of Fairweather et al. [86], they found that, at the end-of-life (EOL), liquid water in the cathode gas diffusion layer (GDL) was almost absent at moderate to high current densities, possibly caused by evaporation due to excessive heat generation. Also, an increase in catalyst layer movement (local separation of CCL from microporous layer) was observed due to stress applied by membrane swelling at advanced stages of cathode degradation. Hack et al.[119] used identical-location X-ray computed tomography (XCT) imaging to study along-the-channel (serpentine flow field) degradation of an MEA. A Carbon corrosion accelerated stress test (AST) was used and it was found that degradation was worst at the outlet and least at the inlet; the CCL near the outlet was thinner than the middle and inlet regions, and land regions were found to be less degraded than channel regions. Recently, Cheng et al. [91] mapped heterogeneity in CCL using synchrotron X-ray

microdiffraction (micro-XRD) and showed that the Pt particle size growth was non-uniform and greater under the flow field lands than channels when the MEAs were subjected to a hydrogen (H_2) and air AST. Similar observations were made by Khedekar et al. [92] under varied humidity conditions using multimodal techniques. The average EOL Pt particle size was larger for the wet conditions than the dry conditions and, in general, larger under the flow field lands than channels. More recently, Martens et al. [120] used operando X-ray diffraction computed tomography (XRD-CT) and small-angle X-ray scattering computed tomography (SAXS-CT) to elucidate the heterogeneous nature of Pt degradation. They observed more extreme degradation in the operating cell compared to less, and more uniform, degradation in the rotating disc electrode (RDE) system typically used for screening fuel cell catalysts. The heterogeneous nature of degradation was linked to the flow field design and water distribution inside the cell.

From a review of the literature, it is apparent that there is increasing impetus to understand and quantify heterogeneity in CCL degradation. Typically, ASTs are used to evaluate catalyst durability in PEFCs, and there is a persistent need to develop ASTs that simulate material component degradation (Pt dissolution, membrane degradation, and carbon corrosion) precisely and rapidly [55], [121]. The ASTs used for studying Pt dissolution in PEFCs with nitrogen (N_2) are intended to achieve nearly homogenous Pt particle size growth throughout the CCL. This is done to correlate Pt particle size growth to other operating conditions (temperature, RH, potential limits, cycle profiles, and dwell time) rather than the effects of the cell or architecture [119]. Stariha et al. [55] evaluated the effect of different voltage cycle profiles on the durability of state-of-the-art Pt and Pt-alloy catalysts and found that a square-wave catalyst AST induced more degradation than both a triangular wave AST and modified wet drive-cycle AST. For the first time, it was suggested that a square-wave AST (0.6 V to 0.95 V vs. RHE), high N_2 flow rate (4 sccm/cm^2), and 4-serpentine flow field in a 50 cm^2 cell had the most rapid ECSA loss. This square-wave resulted in non-uniform degradation rates as compared to low N_2 flow rate (1.5 sccm/cm^2) in the same flow field architecture. However, this phenomenon was not studied in greater detail. Our previous work [122] attempted to quantify heterogeneity in Pt particle size growth as a function of N_2 flow rate during a square-wave AST (0.6 V to 0.95 V vs. RHE) in a 5 cm^2, parallel flow field architecture using the novel micro-XRD technique developed by Cheng et al. [91].

The present study builds upon the previous work and investigates the topical theme of spatially heterogenous Pt particle size growth and distribution as a function of N_2 flow rate during

a US DOE square-wave AST and its plausible causes. Overall, the current study highlights the impact of purge gas (N_2) flow rate during an AST and challenges the inherent assumption of homogenous Pt particle size growth and distribution at CCL during aging. It also supports the inclusion of the purge gas flow rate as a stressor for Pt degradation in AST protocols.

2.3 Method of approach

2.3.1 Materials and test equipment

The fuel cell used in the current study consisted of single-channel serpentine flow fields on both electrodes, an active area of 5 cm^2, and was manufactured by Fuel Cell Technologies (Albuquerque, NM). It was operated in a co-flow arrangement with the inlets to the flow fields located at a higher elevation than the outlets. The MEAs consisted of Nafion XL (27.5 μm thick) membrane (manufactured by DuPont) sandwiched between Sigracet SGL 22BB gas diffusion electrodes (GDE) with a nominal catalyst loading of 0.3 mg-Pt/cm^2. The cell was assembled at a torque of 11.0 N-m to achieve uniform compression. A Scribner Associates, Inc. (Southern Pines, NC) fuel cell test station was used to control the operating conditions. All the MEAs were subjected to a consistent conditioning procedure involving cycling with H_2/Air; ~320 cycles involving constant cell voltage holds for 30 seconds at each of 0.8 V, 0.6 V, and 0.3 V were conducted over 8 hours. The cell temperature was held at 60 °C during conditioning with the inlet relative humidity of 100 % on each side. A constant stoichiometry (H_2/air) of 1.2/2 at atmospheric pressure was maintained throughout the conditioning procedure.

2.3.2 Catalyst AST

A DOE square-wave cycling protocol was executed [55] : H_2/N_2 flows at anode/cathode, voltage cycling between 0.6 V and 0.95 V, with 3 second holds at each voltage. 30,000 cycles (total test time of 50 hours) were performed at 100 % RH, 80 °C, and atmospheric pressure. Voltage was applied using a Biologic potentiostat (SP-240). The anode with fully humidified H_2 flow served as the reference electrode and the counter electrode, and the cathode served as the working electrode. To investigate the effect of N_2 flow rate on the heterogeneity of Pt particle size growth, three different cathode N_2 flow rates (normalized by the geometric active area) of 20 sccm (4 sccm/cm^2), 40 sccm (8 sccm/cm^2), and 80 sccm (16 sccm/cm^2) were used during the AST with a fixed H_2 flow of 40 sccm (8 sccm/cm^2) at the anode. The range of N_2 flow rates chosen in the current study (4 sccm/cm^2 to 16 sccm/cm^2) is higher than the range (1.5 sccm/cm^2 to 4 sccm/cm^2) used by Stariha et al. [55], limited by the ability of the fuel cell test station to reliably control the

flow rate, especially at the lower end (4 sccm/cm^2). Table 2-1 summarizes the test conditions used in this study. Each sample's EOL stage is defined as the end of 30,000 voltage cycles. For reproducibility and error estimation, at least three different MEA samples of each test case were tested.

2.3.3 Electrochemical characterization

ECSA was measured periodically by integrating hydrogen desorption peaks in cyclic voltammograms (CVs) during the AST cycles for all the cell builds. CVs were performed from 0.1 V to 0.9 V at a scan rate of 20 mV/s with fully humidified H_2/N_2 flows at anode/cathode. Carter et al. [123] showed that H_2 evolution during a CV could lead to artifacts in the hydrogen adsorption/desorption (HAD) region, and hence, it can induce error in ECSA calculation. This artifact relates to the mass transfer rate of H_2 away from the working electrode and it primarily depends on the purge gas flow rate used during a CV. Increased purge gas flow rate at the working electrode rapidly removed evolved H_2, decreasing the partial pressure of H_2 in the vicinity of the catalyst, and enabling rapid H_2 evolution. For the purge gas flow rates lower than 1 sccm/cm^2 (normalized by the geometric active area), ECSA measured for an MEA was within 10-15% of ECSA measured for the same catalyst in an RDE. [123] Similar findings were also reported by Garrick et al.[124] for aged Pt-alloy catalysts in PEFCs. Hence, for this study, a low flow rate (4 sccm/cm^2) of the N_2 purge gas was used to record CVs for all the test cases at 80 °C with no backpressure. To measure H_2 crossover current, linear sweep voltammograms (LSVs) were recorded at similar conditions as CVs but with a scan rate of 2 mV/s. Polarization curves were recorded at various operating conditions by holding the cell at constant currents for 3 minutes and averaging the cell voltage during this interval. Before every polarization curve, the cell was at identical starting conditions to obtain repeatable performance and avoid the effects of hysteresis.

2.3.4 Post-mortem analysis

2.3.4.1 Transmission electron microscopy (TEM)

Post-AST transmission electron microscopy (TEM) was conducted at the Institute for Advanced Materials and Manufacturing (IAMM), University of Tennessee, Knoxville. Catalyst particles were carefully scraped from the GDEs of aged samples and dispersed in dilute isopropyl alcohol (IPA). The solution was then sonicated to achieve uniform dispersion and drop-cast onto a 200-mesh Cu grid with Lacey carbon film. The average hole size on the grid was 50 μm.

Table 2-1. Test conditions for square-wave AST

Test case	Inlet RH at the anode and cathode (%)	Cell temperature (°C)	Anode H_2 flow rate (sccm/cm^2)	Cathode N_2 flow rate (sccm/cm^2)	AST (3 seconds hold at each potential)	Gauge Backpressure (atm)
1	100	80	8	4	Square-wave (0.6 V – 0.95V)	0
2	100	80	8	8	Square-wave (0.6 V – 0.95V)	0
3	100	80	8	16	Square-wave (0.6 V – 0.95V)	0

The samples were then dried in air at room temperature and TEM was performed on a Zeiss Libra 200 HT electron microscope operated at 200 kV. Several micrographs were collected at different resolutions and processed using Fiji/ImageJ software and standard image processing techniques to determine the average Pt particle sizes for different samples. At least 100 Pt particles from each micrograph of different samples were considered for averaging. Note that highly irregularly shaped particles were not included in the averaging.

2.3.4.2 Synchrotron X-ray diffraction

Synchrotron X-ray diffraction patterns were collected at the Stanford Synchrotron Radiation Lightsource (SSRL) at experimental Beam Station 2-1, a dedicated reflectivity station for thin film and powder diffraction; this station is equipped with a Huber 2-circle goniometer, Pilatus 100K detector, and a Si (111) monochromator. Samples were mounted on a motorized *xyz* stage for exact positioning; samples were scanned with a step size of 2 mm in the x-direction and 0.5 mm in the z-direction. At each position, X-ray patterns were collected with a beam energy of 10 keV (1.2398 Å) at an incident angle of 1° and a 2 second exposure time for a range of 25 – 70° (2θ); a vertical beam slit of 0.1 mm and a horizontal beam slit of 0.2 mm resulted in a 0.5 x 3 mm beam size on the sample. Data acquisition was performed using SPEC (software for diffraction); data were processed using GSAS-II v.3957 [125].

2.3.4.3 In-house lab-scale micro-X-ray diffraction

Micro-XRD patterns were collected with the in-house (Bosch Research and Technology Center, North America, Sunnyvale, CA) Bruker D8 Advance X-ray diffractometer equipped with a Cu K_α radiation source (1.5406 Å), a Bruker LYNXEYE XE detector, custom 0.3 mm and 0.1 mm collimators, and an *xyz* stage along with a double-laser unit for accurate alignment of samples; samples were scanned with a step size of 2.5 mm in the x-direction, 0.5 mm in the y-direction, and a 500 μm x 500 μm spot size (see Figure 2.1(c)). This way, data were acquired across lands and channels, thus not resolving the differences between lands and channels. However, as indicated in Figure S2.1 of Supporting Information for Chapter 2, no difference in Pt size was obtained when measuring the sample in a different direction, i.e., when resolving along land and channels. For all measurements, the accelerating voltage and current were set to 40 kV and 40 mA, respectively. Scans were collected between 37.5° and 42° (2θ) at a step size of 0.03°and 2.5 seconds time per step. Data were processed using GSAS-II v.3957 [125]. More details about the technique are given in a previous publication. [91].

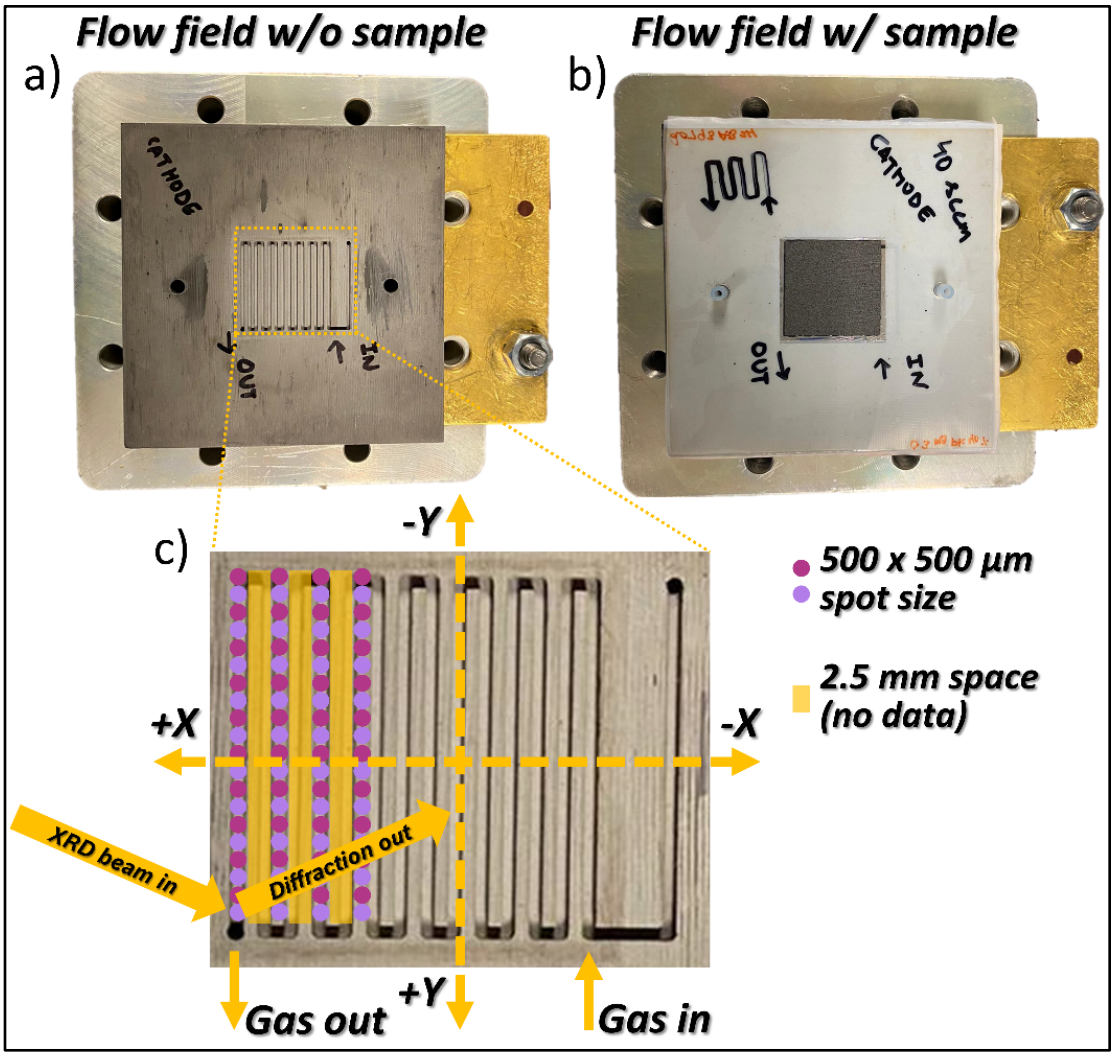


Figure 2.1. Illustration on the acquisition of micro-XRD. Samples were mounted as illustrated in panel (b) and measured as depicted in panel (c). Diffractograms of 500 µm x 500 µm spots were collected with a step size of 2.5 mm in the x-direction and 0.5 mm in the y-direction. No difference in the average Pt particle size was observed when resolving along or across the land and channels (see Figure S2.1, Supporting Information for Chapter 2).

2.4 Results and discussion

As a general note, the error bars in the Results and Discussion section plots are drawn as lines with filled areas. The transparency of the error bars shows overlapping regions where performance for two different conditions (e.g., different ASTs) was similar. The filled area is thus an envelope of errors for each data point.

Figure 2.2 shows the hydrogen desorption region CVs for three different MEAs from the beginning to the end of life, i.e., 30,000 voltage cycles subjected to different N_2 flow rates at the cathode during the AST. These CVs are corrected for capacitance, and the area under each curve is used for calculating ECSA. It is evident from the figure that the hydrogen desorption region for all MEAs, irrespective of the aging condition, decreased from the beginning-of-life (BOL) to EOL at 30,000 cycles. However, the shape of this region varies with N_2 flow conditions, highlighting possible changes in the Pt crystal structure with aging. Different peaks in the hydrogen desorption region are usually associated with different facets of carbon-supported polycrystalline Pt nanoparticles; for example, the peaks in region 0.1 V ~ 0.15 V vs. RHE and 0.2 V ~ 0.3 V vs. RHE are usually associated with Pt (110) and Pt (100), respectively [8,49,51,126–128]. For all the MEAs tested in this study, these peaks can be seen at the BOL. However, with cycling under different N_2 flow rates, these peaks progressively disappear, albeit at different rates. For an N_2 flow rate of 4 sccm/cm^2, the disappearance of the peak in the 0.1 V ~ 0.15 V vs. RHE region is rather gradual, i.e., it can be observed through 24,000 AST cycles. However, for 8 sccm/cm^2 and 16 sccm/cm^2 N_2 flow cases, the peak in this region disappeared completely after 6000 and 3000 AST cycles, respectively. For ideal face-centered-cubic metals such as Pt, the surface energy (γ) of atomic planes follows the order $\gamma\ \{111\} < \gamma\ \{100\} < \gamma\ \{110\}$ [8]. Hence, it is not surprising that Pt (110) is least stable and surface roughening of Pt nanoparticles is expected with potential cycling. Dynamic roughening of other Pt facets such as Pt (111) with potential cycling has been directly observed in previous studies [51]. Different fully humidified N_2 flow rates used in this study might cause heterogeneous degradation of the catalyst nanostructure due to non-uniform chemical potential conditions (non-uniform hydration) developed at the local level around the catalyst particles [120].

Figure 2.3(a) shows the variation of calculated ECSA obtained from the integration of hydrogen desorption peaks with the number of AST cycles and Figure 2.3(b) shows the percentage ECSA loss. At the BOL, ECSA varies between 18 to 22 $m^2/g_{\text{-Pt}}$ and this difference can be attributed

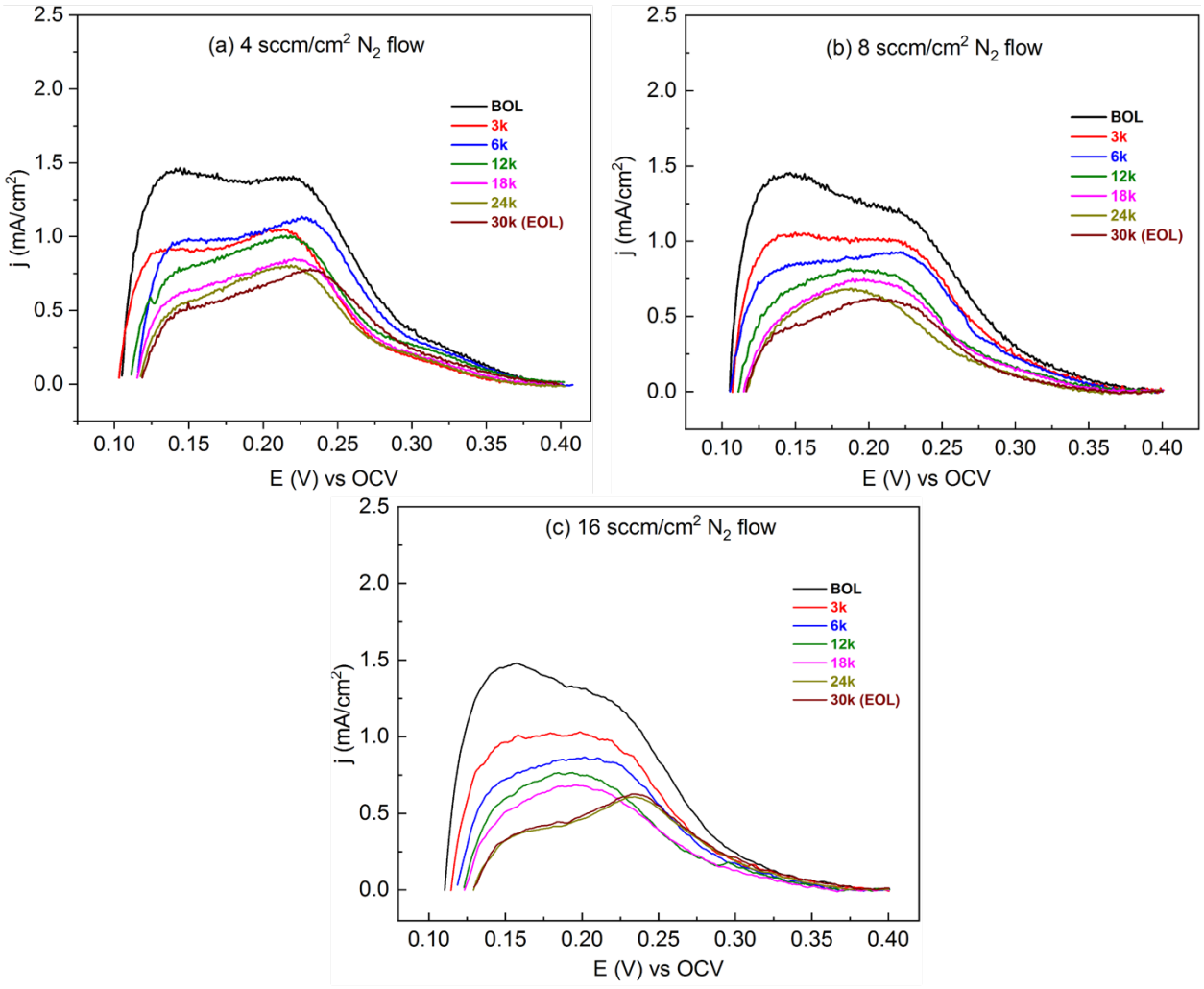


Figure 2.2. Cyclic voltammograms of the hydrogen desorption region (corrected for capacitance) for the MEAs subjected to (a) 4 sccm/cm^2 N_2 flow, (b) 8 sccm/cm^2 N_2 flow, and (a) 16 sccm/cm^2 N_2 flow at the cathode during AST. The area under each curve was used for calculating ECSA at different stages during the AST.

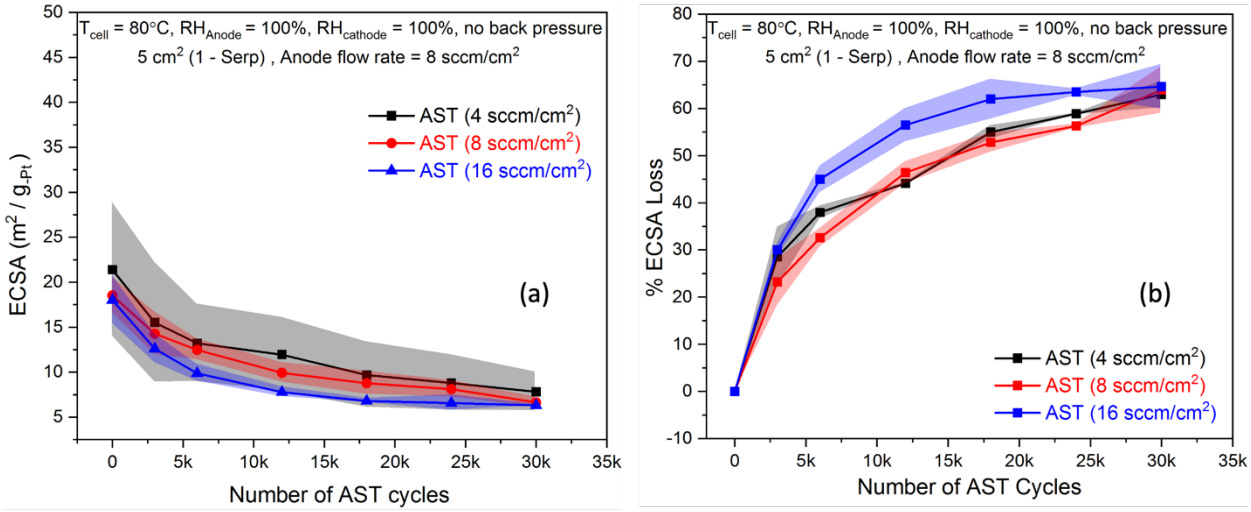


Figure 2.3. (a) Absolute ECSA as a function of the number of AST cycles for different N_2 flow rate cases, and (b) normalized ECSA loss as a function of the number of AST cycles for different N_2 flow rate cases. Shaded regions indicate range of measured experimental error for each condition.

to sample-to-sample variability during manufacturing. For a similar set of materials, Khedekar et al. [92] also obtained BOL ECSA between 25 to 43 m^2/g_{-Pt}. For all N_2 flow rate cases at the cathode, ECSA dropped rapidly for the first 10,000 – 12,000 AST cycles. This rapid ECSA drop (40 – 50% from the initial value) can be linked to electrochemical Ostwald ripening, which is more prevalent for the MEAs with initial Pt particle sizes between 2.2 – 3.5 nm [50,129]. The average Pt particle size at the BOL for the MEAs used in this study was about 3.5 nm and 3.7 nm, determined from TEM, respectively. Horn et al. [8] have also pointed out the dramatic increase in the chemical potential driving the dissolution of Pt nanoparticles via the Gibbs-Thomson effect for particles smaller than 5 nm.

From Figure 2.3(a), a trend can be observed: the average ECSA remaining at each sampling interval during the AST roughly follows the order, ECSA (4 sccm/cm^2 N_2) > ECSA (8 sccm/cm^2 N_2) > ECSA (16 sccm/cm^2 N_2). However, at 30,000 cycles (EOL), irrespective of the N_2 flow rates, the differences in ECSA are modest. The EOL values of ECSA are 7.8 m^2/g_{-Pt}, 6.6 $m^2/g_{-Pt,}$ and 6.3 m^2/g_{-Pt} for 4, 8, and 16 sccm/cm^2 N_2, respectively; the samples lost about 65% ECSA from the BOL to EOL, seen in Figure 2.3(b). This loss can be attributed to the fact that Pt particles attain a "quasi" stable average size which resists further dissolution; hence, Pt degradation rate slows as particles approach that quasi-stable size [8]. Figure 2.3(a) supports this observation, where the ECSA flattens out around 20,000 cycles for all the samples. Similar observations have also been made in previous studies [130,131]. It should be noted that such "quasi" stable average size is strongly dependent on the stressors during an AST. In summary, though the average Pt particle sizes and the cumulative ECSA loss are similar at the EOL for different N_2 flow rates used during AST, the decay rates to the EOL are non-uniform depending on N_2 flow rates. Once the average Pt particle size reaches a quasi-stable state after a certain number of AST cycles, it resists further change for a given set of AST conditions.

The fact that the MEAs subjected to different N_2 flow rates during the AST end up having similar ECSA loss (~65%) at EOL in this study is somewhat contrary to the observations made by Stariha et al. [55], where the square-wave AST run at a high N_2 flow rate (4 sccm/cm^2) resulted in ~70% ECSA loss compared to the AST run at a low N_2 flow rate (1.5 sccm/cm^2), which resulted in ~50% ECSA loss at EOL. This difference between the two studies can be attributed to a different BOL average Pt particle size (2 nm[55] vs. 3.7 nm in the present study) and vastly different architecture (4-serpentine, 50 cm^2 flow field [55] vs. 1-serpentine, 5 cm^2 flow field in the present

study). Also, the range of N_2 flow rates chosen in the present study (4 sccm/cm^2 to 16 sccm/cm^2) was higher than the range (1.5 sccm/cm^2 to 4 sccm/cm^2) reported earlier [55]. However, the effect of N_2 flow rates during an AST on non-uniform Pt particle size growth is confirmed and quantified in the present study. Even though the MEAs subjected to different N_2 flow rates end up with similar ECSA and average Pt particle size, the spatial distribution of Pt particle sizes is vastly different for these MEAs, i.e., the Pt particle size growth is spatially heterogeneous. This heterogeneity is discussed in detail in the sections to follow.

Many studies have used a first-order rate model to describe ECSA loss [56,57,132–135]. According to this model, the normalized platinum surface area $S(N)$ is a function of the number of AST cycles in a durability test. The Pt degradation rate is expressed as,

$$\frac{dS}{dN} = -kS(N) \tag{1}$$

where N is the number of AST cycles, $\frac{dS}{dN}$ is the rate of Pt surface area loss, and k is the first-order reaction rate constant. Debe et al. [132] introduced a concept of minimum ECSA (S_{min}) based on the observation that ECSA loss stabilizes to non-zero values after a certain number of AST cycles. This stable ECSA indicates that the Pt particles resist further dissolution and growth due to Ostwald ripening and reach a stable average particle size.[8] The ECSA loss in Figure 2.3(b) supports the concept of a stable S_{min}; ECSA loss for all three flow rates stabilized around 35 % (remaining ECSA) at the end of 30,000 AST cycles. Integrating Equation 1 between (1 - S_{min}) and ($S(N)$ - S_{min}) yields [132],

$$ln\left(\frac{S(N)-S_{min}}{1-S_{min}}\right) = -kN \tag{2}$$

$$S(N) = S_{min} + (1 - S_{min})e^{-kN} \tag{3}$$

Equation 3 represents the exponential decay of ECSA with cycling. Furthermore, $(1 - S_{min})$ represents the maximum, normalized, lost surface area for a given catalyst type subjected to an AST under various stressors. Debe et al. [132] chose different S_{min} for different catalysts to improve the quality of fit to their experimental data. Kneer et al. [56] also pointed out that S_{min} should be a function of the stressors during an AST and not a constant.

An advantage of this simple first-order rate loss model is that the ECSA decay with cycling is solely dependent on the rate constant k, which can be determined from the fit to the experimental data. Different stressors during an AST like temperature, RH, dwell time, and scan rate induce different rate constants. However, Moein-Jahromi et al. [135] proposed combining the rate constants

for different operating conditions to obtain the overall degradation rate. In the present study, parameters like temperature, RH, number of AST cycles, and the cycle profile remained identical for all flow rate cases. Hence, the rate constant in this study (Equation 1) is solely associated with the ECSA loss as a function of N_2 flow rate. Messing et al. [134] have also demonstrated this approach. As mentioned earlier, S_{min} is empirically found to be 0.35 in the current study. For a similar set of materials used in this study, Khedekar et al. [92] also obtained a value close to 0.3 of the normalized ECSA loss for the N_2-wet case at the end of 30,000 AST cycles. Using S_{min} as 0.35, the first-order rate model fits results in this work well. Figure 2.4(a) shows the best-fit straight lines (through least squares regression) for all the flow rate cases along with the equations and R^2 values. From the slopes of linear fits in Figure 2.4(a), the values of rate constants k, are extracted and plotted as a function of N_2 flow rate at the cathode during the AST in Figure 2.4(b).

From Figure 2.4(b), we see that the rate constant has a linear dependence on N_2 flow rate at the cathode during the AST with R^2 value of 0.97. The rate constant increased by ~57% for an increase in N_2 flow rate from 4 sccm/cm^2 to 16 sccm/cm^2. For most of the duration of AST before the normalized ECSA loss stabilized to S_{min}, higher N_2 flow rate induced more rapid ECSA loss. Thus, if the AST stopped before the Pt particle sizes reached a "quasi" stable state, greater N_2 flow rate would have resulted in higher ECSA loss. This simple first-order analysis confirms the exponential decay of ECSA with the number of AST cycles, as discussed in the literature. Also, for the studies utilizing a similar set of test conditions and the materials used in the present case, the k values obtained in Figure 2.4(b) can be incorporated in semi-empirical or empirical models for Pt catalyst layer degradation as described in previous studies [56,57,134,135]. In this study, for the sake of simplicity, a linear fit is used for describing the variation of k with N_2 flow rate. A more complex fitting function would improve fit quality; however, it would also add complexity.

Figure 2.5 shows iR-corrected polarization curves recorded at various operating conditions at the BOL and the EOL with three different N_2 flow rates. The performance loss of the aged samples after 30,000 AST cycles can be observed with a clear trend; across all operating conditions and a majority of the geometric current densities, the voltage loss (ΔV) is greater for higher N_2 flow rates. For example, in Figure 2.5(c), at the geometric current density of 0.1 A/cm^2, ΔV after AST (or EOL) for 4, 8, and 16 sccm/cm^2 N_2 cases are 29 mV, 32 mV, and 61 mV, respectively; this voltage loss is primarily associated to oxygen reduction reaction (ORR) kinetics due to loss in ECSA (~65% loss at the EOL for all three N_2 flow rates) [58,130,136]. Similar values of ΔV were also

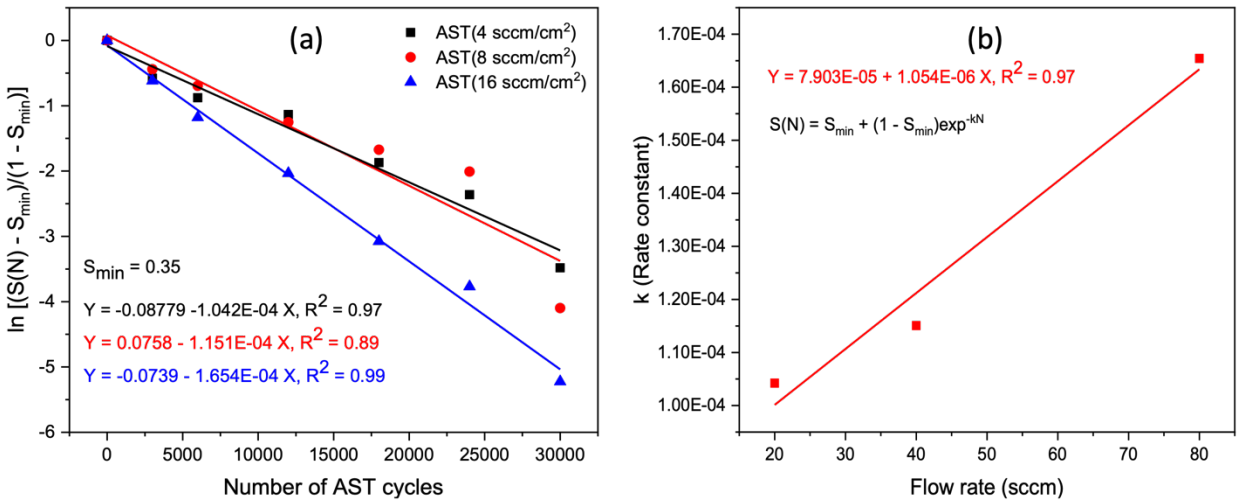


Figure 2.4. (a) Log of normalized ECSA versus number of AST cycles for the three N_2 flow rate cases. Corresponding linear fits along with R^2 values are also mentioned. (b) Rate constant obtained from the slopes of best-fit straight lines in (a) versus the N_2 flow rate during the AST.

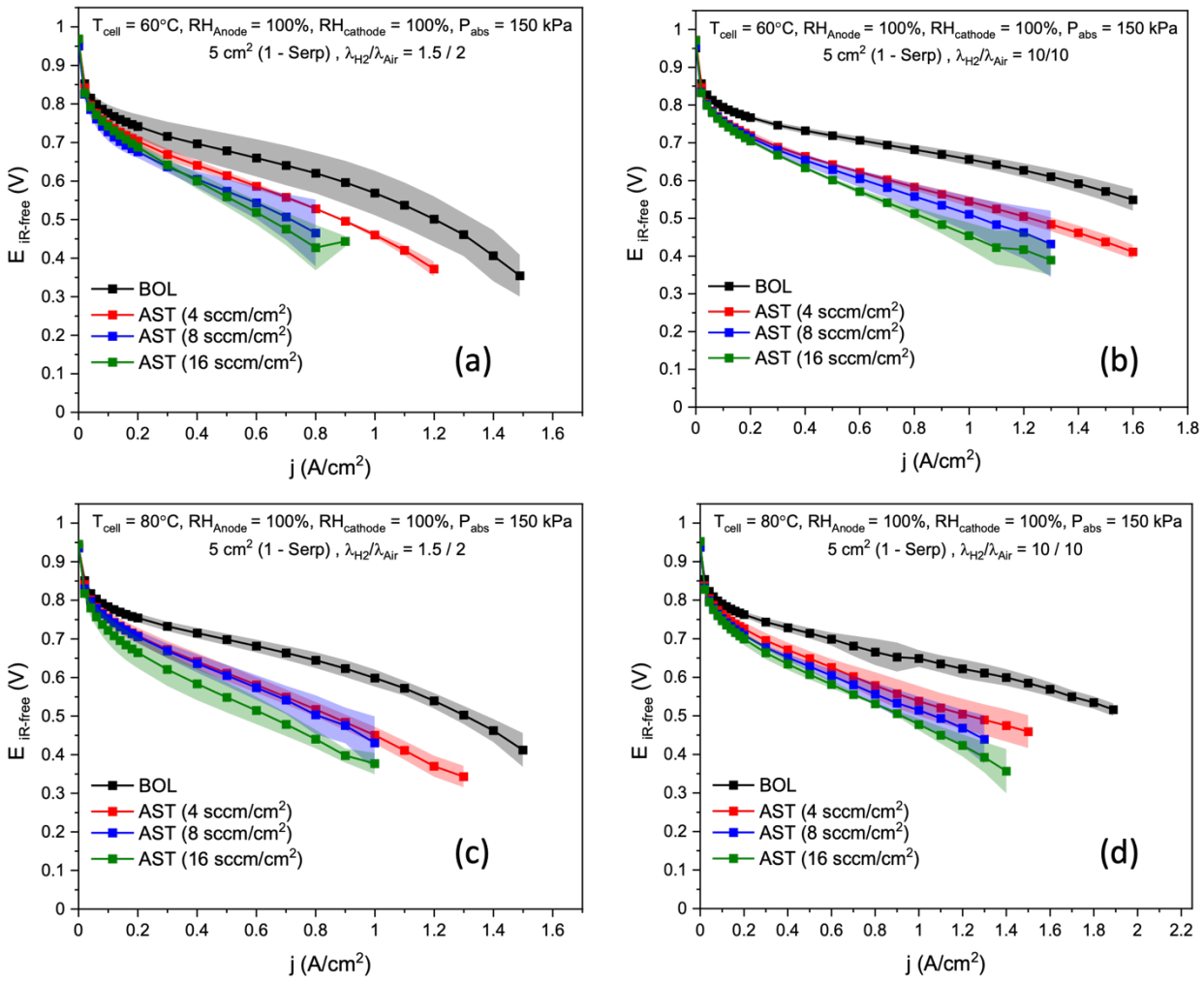


Figure 2.5. Polarization curves for the MEAs at the beginning of life (BOL) and after the AST subjected to different N_2 flow rates during the AST. (a) and (c) have 100% RH, H_2/air stoichiometry of 1.5/2, and an operating cell temperature of 60 °C and 80 °C, respectively. (b) and (d) have differential conditions, i.e., H_2/air stoichiometry of 10/10, 100% RH, and an operating cell temperature of 60 °C and 80 °C, respectively.

obtained at the end of 30,000 AST cycles for the N_2 Wet case by Khedekar et al. [92]. However, some mass transport and other losses still occur at this low current density. The influence of mass transport overpotential can be verified by isolating the voltage loss purely due to the increase in ORR overpotential (loss of ECSA) after correcting the ohmic losses. Furthermore, from Figure 2.5 (b) and (d), at differential operating conditions (H_2/air stoichiometry of 10/10), the performance of the aged samples in the high geometric current density regions significantly improves but the trend of the performance loss still holds i.e., the voltage loss (ΔV) is greater for higher N_2 flow rates.

The change in ORR overpotential ($\Delta\eta_{ORR}$) due to voltage cycling can be estimated by assuming Tafel kinetics and ignoring minor changes in exchange current density and Pt loading with aging. It is given by [130]:

$$\Delta\eta_{ORR} = \frac{2.303*RT}{\alpha F} * log\left\{\frac{(i_o*ECSA)_{BOL}}{(i_o*ECSA)_{EOL}}\right\} \quad (4)$$

where α is the cathodic charge transfer coefficient, R is the universal gas constant, T is the temperature, F is Faraday's constant, and i_o is the exchange current density. Equation 4 predicts ~70 mV ORR kinetic loss at 80 °C for a 10-fold decrease in ECSA due to aging. Assuming that the performance loss is purely kinetic (Tafel slope of ~70 mV/decade), using Equation 4, we get a voltage loss of ~30 mV due to aging for all N_2 flow rates at a low geometric current density of 0.1 A/cm^2. The experimentally measured voltage loss (from Figure 2.5(c)) for 4 and 8 sccm/cm^2 N_2 case is closer to the calculated value of ~30 mV; for the 16 sccm/cm^2 case, it is 61 mV. The higher-than-expected value of voltage loss for 16 sccm/cm^2 N_2 case indicates additional polarization losses, most likely due to mass transport. Furthermore, higher voltage losses are incurred at moderate-to-high current densities at EOL for all N_2 flow rate cases, possibly due to additional transport losses resulting from spatially non-uniform Pt degradation [91,120,137]. Zihrul et al. [130] have also reported an increase in local oxygen transport resistance through the ionomer film covering Pt surface in aged samples at moderate-to-high current densities. Though the oxygen transport resistance was not measured and quantified in the present study, it is reasonable to assume that such transport losses are possible after an AST in the range 0.6 V to 0.95 V vs RHE. It is important to note that for voltage cycling above 1 V vs. RHE, significant carbon-support corrosion can occur during the AST, exacerbating mass transport losses [71,74,138,139]. Carbon-support corrosion is not expected to be severely limiting in the present study as the voltage cycling range was from 0.6 to 0.95 V vs. RHE. Also, the degradation of the polymer electrolyte membrane

(PEM) in the present study is negligible (for all N_2 flow rate cases), as there was no appreciable increase in H_2 crossover after the AST, measured via LSV (see Figure S2.2, Supporting Information for Chapter 2). The PEM, however, can be severely damaged by prolonged holds at potentials closer to open circuit; membrane thinning or pin-hole formation are common near open circuit [140,141].

Overall, the performance of the MEAs subjected to the AST with different N_2 flow rates decreased from the BOL to the EOL at all current densities, with higher losses related to mass transport at moderate-to-high-current densities, possibly due to heterogeneous Pt particle size growth from the inlet to the outlet.

Figure 2.6 shows the 2D micro-XRD maps (2 cm x 2 cm) of Pt particle size distribution for the MEAs. The air inlet and the outlet regions are marked on the aged samples. It should be noted that the pristine samples were analyzed using Synchrotron XRD at experimental Beam Station 2-1, Stanford Synchrotron Radiation Lightsource (SSRL), and the aged samples were analyzed using an in-house lab-scale micro-XRD at Bosch Research and Technology Center, North America, Sunnyvale, CA.

The pristine sample mostly has a uniform Pt particle size distribution with an average of 3.7 nm over the entire imaged area; consistent with the TEM measurements (average Pt size is 3.5 nm), and previously reported values using similar techniques [91,137]. After aging, the Pt particle size is non-uniform and varies with N_2 flow rates from the inlet to the outlet. There is a substantial increase in Pt particle size (averaged over the entire imaged area) for all N_2 flow rates from the BOL to EOL: roughly 181% growth for 4 sccm/cm^2 N_2 flow, 173% for 8 sccm/cm^2 N_2 flow, and 154% for 16 sccm/cm^2 N_2 flow. Furthermore, on average, greater Pt particle size growth is seen near the outlet for all ASTs, albeit the degree of growth is different for different N_2 flow rates. This trend is consistent with previous studies on Pt degradation [55,91,119,120,137]. In particular, Stariha et al. [55] reported an increase of 145% and 170% in average Pt particle size near the inlet and the outlet (measured via TEM), respectively, for the MEAs subjected to the square-wave AST with high flow (4 sccm/cm^2) of N_2 at the cathode. The absolute Pt particle sizes, however, are very different from the present study. Also, in the previous study[122], we reported similar non-uniformity in Pt particle size growth in a different flow field architecture (5 cm^2, parallel). Furthermore, the range (difference between the maximum and the minimum Pt particle size in the imaged area) is 7.7 nm, 3.5 nm, and 1.7 nm for 4, 8, and 16 sccm/cm^2 N_2 flow rates, respectively.

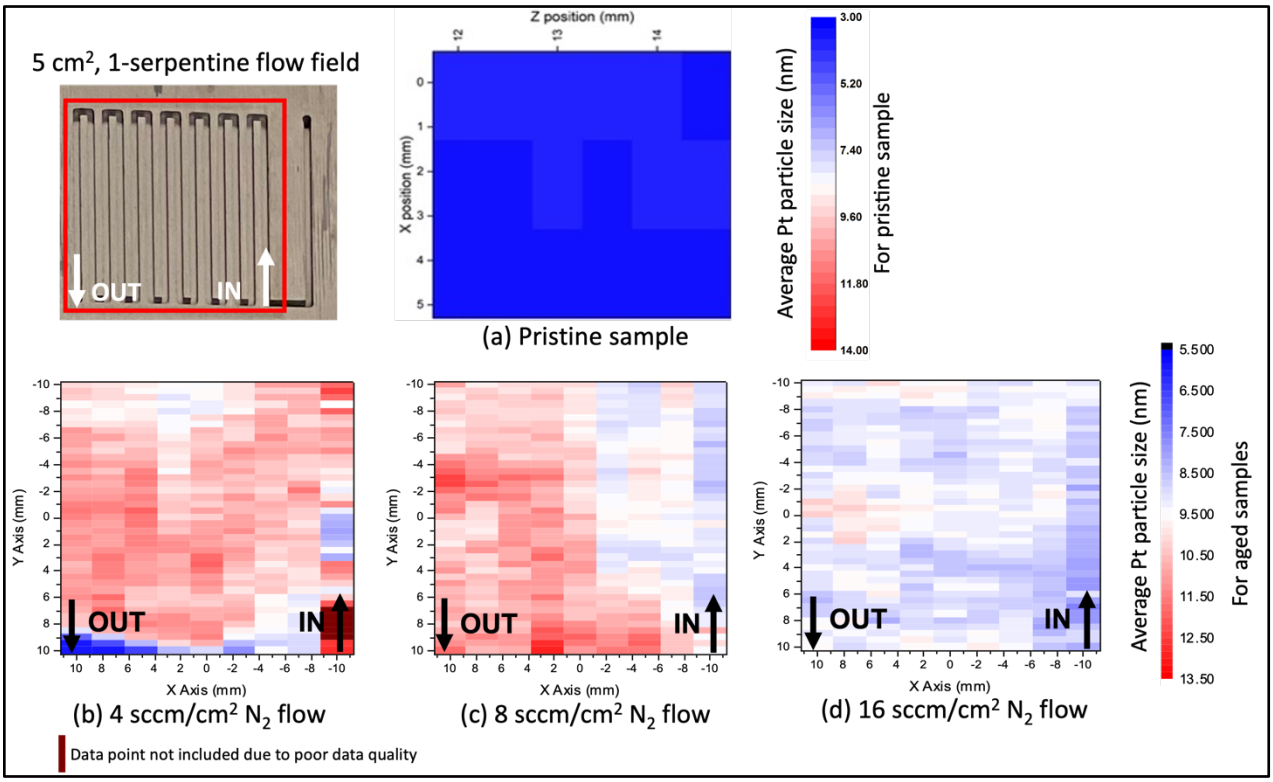


Figure 2.6. 2 cm x 2 cm micro-XRD maps for (a) pristine sample (synchrotron XRD) and aged samples with (b) 4 , (c) 8 and (d) 16 sccm/cm^2 N_2 flow showing Pt particle size distribution (lab-scale micro-XRD). The inlet and outlet regions are marked on the aged samples (color available online).

It should be noted that resolving channel-land bias in Pt particle size growth was not possible with the in-house micro-XRD. However, it was sufficient to resolve the heterogeneity in Pt particle size from the air inlet to the outlet, seen for the first time with varying N_2 flow rates at the cathode during a square-wave AST. For 8 sccm/cm^2 N_2 flow case (see Figure 2.6(c)), a distinct pattern in Pt particle growth is observed; almost half of the active area (X = 0 mm to X = -10 mm) near the inlet is seen to have a mean Pt particle size of ~9 nm; the other half of the area (X = 0 mm to X = 10 mm) near the outlet has a mean of ~11 nm. No such clear distinction is observed for 4 sccm/cm^2 and 16 sccm/cm^2 N_2 flow rates. Interestingly, they all end up losing ~65% ECSA after 30k AST cycles, as discussed earlier. However, the performance is very different (see Figure 2.4), likely due to the heterogeneous nature of Pt particle size growth.

To elucidate the functional dependence of heterogeneity in Pt particle size growth on N_2 flow rate, it is important to understand various gradients that can develop inside a PEFC. In the study of PEFCs, some naively assume that the thermal, mass, and current profiles are uniform across the active area and that a nearly homogeneous distribution of these operational parameters exists. However, the accurate picture is that few properties are uniform for in-plane and through-plane directions [9]. During the normal operation/cycling of a PEFC with H_2/air, complex interactions of thermal and mass transport can result in liquid water build-up/accumulation under the flow field lands (contact points between the flow field plates and porous media), channel switchbacks, and other over-saturated locations in the cell [109–111,142–147]. This is a result of greater effective thermal resistance under the channels than lands, as shown in Figure 2.7(a); the normal direction of heat flow is generally from the catalyst layers to the flow field/coolant plates. Therefore, there is a non-uniform temperature distribution (both in-plane and through-plane) in an operating PEFC. This temperature gradient is further exacerbated at higher current, lower efficiency operation. In large PEFC plates, there can easily be 8 - 10 °C gradient from the inlet to the outlet [148]. Furthermore, the temperature gradient can lead to the heterogeneous membrane and electrode humidification, leading to membrane stresses and localized flooding. Flow field land and channel size or land-to-channel ratio (L/C) also plays a crucial role in liquid water accumulation in the diffusion media. In general, a higher L/C ratio results in greater accumulation of liquid water in the cell at similar operating conditions [111]. For a narrow channel design, liquid water will accumulate under the land until there is sufficient capillary pressure build-up to initiate lateral in-plane transport, either into the channel or merging with the water from the adjacent channel [111].

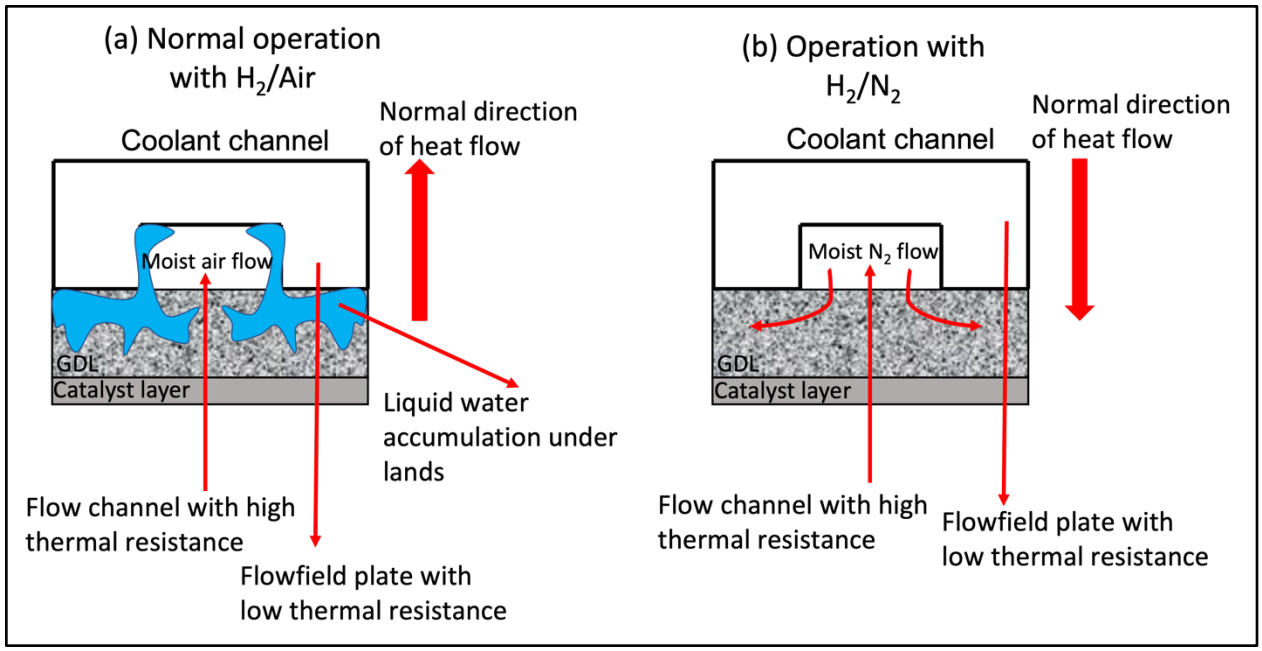


Figure 2.7. A possible explanation of the gradients formed inside the fuel cell that might be responsible for non-uniform Pt particle size growth during (a) regular operation with H_2/air [111], and (b) operation with H_2/N_2 during an AST

If this water is not removed in the form of droplets from the channels, it can lead to severe mass transport limitations and related degradation. On the other hand, for wider channels, this lateral connection of liquid water in the diffusion media is prevented to a greater extent, as the water is removed via droplets from the channels [111]. Santamaria et al. [149] have investigated the effect of cross-flow (as a result of pressure differential in the adjacent channels of flow field configurations like the interdigitated and serpentine) on PEFC liquid water distribution. They reported a strong correlation between the saturation level in the diffusion media and the cross-flow rates; membrane hydration was found to decrease at elevated cross-flow rates. Thus, we expect that degradation, if related to temperature, water, and gradients of the same, will also be a strong function of the thermal and transport properties of the materials and architectural design of the cell itself, as well as the conventionally considered degradation parameters such as voltage, etc.

One can expect the accumulation of liquid water to impact Pt particle size growth during long-term cycling with H_2/air, as it would lead to increased mobility of the dissolved Pt species, accelerating redeposition onto larger Pt particles via the mechanisms presented earlier [150]. This has partly been shown in previous studies [91,120,137], where the Pt particle size growth mimicked flow field architecture. Furthermore, one would expect negligible liquid water and heat generation when cycling with H_2/N_2; hence, Pt particle size growth related to any mechanism affected by hydration of the ionomer should not be impacted by the architecture during H_2/N_2 AST. However, as shown in Figure 2.6 and the previous study [122], Pt particle size growth is spatially heterogeneous and responds to flow field architecture when cycled with H_2/N_2. We hypothesize that non-uniform humidification from the flow field inlet to the outlet (co-flow arrangement) could be responsible for the heterogeneous Pt particle size growth (see Figure 2.6). This non-uniform humidification could be the result of the small temperature gradient between the nitrogen gas at the inlet and cell temperature. It is conventional in fuel cell research to heat the cell inlet lines (supply of moist hydrogen and air/nitrogen) by 5-10 °C above the dew-point point temperature of the gases. Usually, the external humidifiers are set at temperatures corresponding to the desired RH at the cell inlets. If the inlet lines are not heated above the dew-point temperature of the reactant gases, moisture condenses at cold spots and causes instability in cell performance. Though this practice of heating the cell inlets above the dew point temperature prevents condensation in the inlet lines, it also heats up the reactant gases. This local heating of the gas stream in the inlet line increases its bulk/mean temperature and, hence, its effective water-carrying capacity

(dehumidification) near the cell inlet also increases. This further allows the gas stream to absorb more water as it flows downstream, thus drying the cell inlet. Furthermore, at higher operating temperatures (> 60 °C) and RH (> 90 %) , this problem can be exacerbated as the saturation pressure of water vapor varies non-linearly with temperature [9]. For instance, a 1 °C rise in bulk temperature of the reactant gas (e.g. from 80 °C to 81 °C) at the cell inlet results in RH drop to 96 % from 100 % for a cell operating temperature of 80 °C. It should be noted that the effect of this dehumidification is expected to be balanced out by generation of water when the cell operates with H_2/air and a complex water balance is established. It also depends on the flow arrangement of the reactant gases (co-flow vs. counter-flow). This phenomenon was partly explained in a previous publication [122].

In the present study, during the ASTs, cell inlet lines were heated by 10 °C more than the dew-point temperature of the gases and the cell temperature was maintained at 80 °C. As a result of this local heating and increase in bulk/mean temperature of the inlet N_2 stream, it is expected to absorb moisture as it travels downstream in the flow field channels (1 mm wide and 1 mm deep) until it becomes fully humidified and equilibrium is reached. Thus, a gradient in humidification likely develops from the cell inlet to the outlet which could possibly explain higher Pt particle size growth (Pt growth is supported by water content, as discussed earlier) at the flow field outlet than the inlet due to higher humidification at the outlet. With increasing N_2 flow rate, the gradient in humidification could be smaller; for increasing flow rate, the effect of relatively drier inlet might be offset by the overall higher water removal from the cell [122]. Thus, a “tighter” particle size distribution and smaller average Pt particle size is expected for high N_2 flow rate. Performing ASTs at high RH conditions, especially at 100 % (as is the case in the present study), is thus highly sensitive to testing conditions and test stand stability. Water accumulation in the cell diffusion media even when there is no net generation of water due to the absence of Faradaic reactions at 80 °C and 100 % RH is not surprising, due to the water-carrying capacity of N_2 at such high temperatures and RH [122] conditions. Even the slightest decrease in the local temperature in the diffusion media would allow water vapor to condense. Though there is a lack of evidence of net water accumulation for operation with N_2 instead of air, one can still observe accumulation by leaving a fuel cell at open circuit (no water generation due to zero cell current). So, whatever water mass accumulates in the cell, it primarily comes from the humidified gas streams (H_2/air), ignoring evaporation due to small heat generation at open circuit from hydrogen crossover. Hickner et al.

[122] used high-resolution neutron radiography to understand liquid water distribution in an operating fuel cell as a function of temperature and reported ~ 8.2 mg/cm^2 of liquid water mass at open circuit (zero current density). The cell operated at 80 °C, 100 % RH with stoichiometric flow of 2 at the cathode and had 50 cm^2 active area with 4-serpentine flow channels. Surprisingly, this water mass at open circuit was comparable to the operation at 1.5 A/cm^2, where ~9.0 mg/cm^2 of water mass was reported. Drier cell inlet region was also observed at open circuit, which supports our hypothesis. Thus, liquid water can accumulate in the cell for high temperature and humidity operation when no current is generated. Further studies are underway to better quantify this gradient in humidification from the cell inlet to the outlet during an AST.

As stated earlier, resolving channel-land bias in Pt particle size growth was not possible with the in-house micro-XRD. However, we could still expect higher Pt particle size growth under the flow field lands than channels as observed in previous studies, [91,120,137] due to the large land width (1 mm) used in the present study. One possible explanation of such channel-land bias in Pt particle size growth with N_2 could be the temperature gradients between the lands and the channels of the flow field due to different thermal resistance when cycled with H_2/N_2. Moist N_2 flow in the channels offers higher thermal resistance to heat transfer than the lands, as depicted in Figure 2.7(b). However, the direction of net heat flow is from the coolant channel to the catalyst layer (to maintain the applied cell temperature) due to the negligible heat generation when cycling with H_2/N_2 between the potential limits of 0.6 to 0.95 V vs. RHE [151]. Also, the magnitude of this temperature gradient (in H_2/N_2) is expected to be smaller than in the case of H_2/air. It should be noted that experimental measurement of such local temperature gradients is extremely difficult. However, multiscale 3-D modeling approaches [152] predict temperature gradients of 2-3 °C between channels and lands with H_2/air. Even though the temperature gradient seems to be small, at fully humidified conditions, condensation under the lands in the diffusion media can still occur, especially at higher operating temperatures as the saturation pressure of water vapor varies non-linearly with temperature [9]. For a fully humidified N_2 flow in the channels, as is the case in the present study, the temperature gradient developed due to the difference in thermal resistance can result in non-uniform hydration of the membrane and the ionomer in the catalyst layer [120]. This can impact the chemical gradients (concentration and the mobility of the soluble Pt species [150]) inside the cell, leading to a patterned or heterogenous Pt particle size growth.

Furthermore, as a serpentine flow field is used in the present study, one can expect the heterogeneity in Pt particle size growth to respond to increased N_2 flow rate as it would impact the amount of cross-flow in adjacent channels, leading to non-uniform membrane and ionomer hydration [149]. Interestingly, as discussed earlier, we also observed the heterogeneity in Pt particle size growth for a 5 cm^2 parallel flow field [122], where cross-flow between the adjacent channels can be assumed to be negligible. However, the temperature gradient still exists; this temperature gradient can impact Pt particle size growth. Overall, heterogeneous catalyst degradation (higher Pt particle size growth at the outlet than inlet) can be associated with non-uniform humidification (unequal distribution of water from inlet to the outlet) resulting from the increase in mean/bulk temperature of gases closer to the cell inlet and, hence, water-carrying capacity. Furthermore, for a high N_2 flow (16 sccm/cm^2), the effect of drier inlet relative to the outlet is likely offset by its higher overall water removal capacity from the cell, and hence, the gradient in humification would consequently be smaller from the inlet to the outlet, resulting in overall smaller average Pt particle size growth and narrower distribution. It can be concluded that N_2 flow rate effect on Pt particle size growth is coupled to non-uniform humidification from inlet to the outlet at high operating temperature and humidity. This effect is expected to be smaller at lower RH and cell operating temperatures [122]. It is worth mentioning that other purge gases like argon (Ar) at the cathode during an AST are expected to impact heterogeneity in Pt particle size growth; the diffusivities of water vapor and oxygen are different in Ar than in N_2 atmosphere. However, in most PEFC degradation studies using ASTs, N_2 is used because of the operating cost and similarity in molecular weight to air [55].

Figure 2.8 shows the quantitative comparison of the Pt particle size distributions for the aged samples. The data are extracted from Figure 2.6 and plotted as histograms with corresponding Gaussian fits. Micro-XRD maps are used as insets to serve as a guide to the eye. The mean Pt particle sizes are 10.4 nm, 10.1 nm, and 9.1 nm for 4, 8, and 16 sccm/cm^2 N_2 flow rates, respectively. These values are in good agreement with previous studies [91,137] utilizing similar aging protocols and material sets. Also, the standard deviation (σ), signifying uniformity in size or "tightness" of the fit, follows the order, σ(16 sccm/cm^2 N_2) < σ(8 sccm/cm^2 N_2) < σ(4 sccm/cm^2 N_2). The histograms for 4 and 8 sccm/cm^2 N_2 flow rates (Figure 2.8(a) and (b)) exhibit a larger fraction of Pt particles having sizes greater than 11 nm as compared to 16 sccm/cm^2 N_2 flow (Figure 2.8(a)).

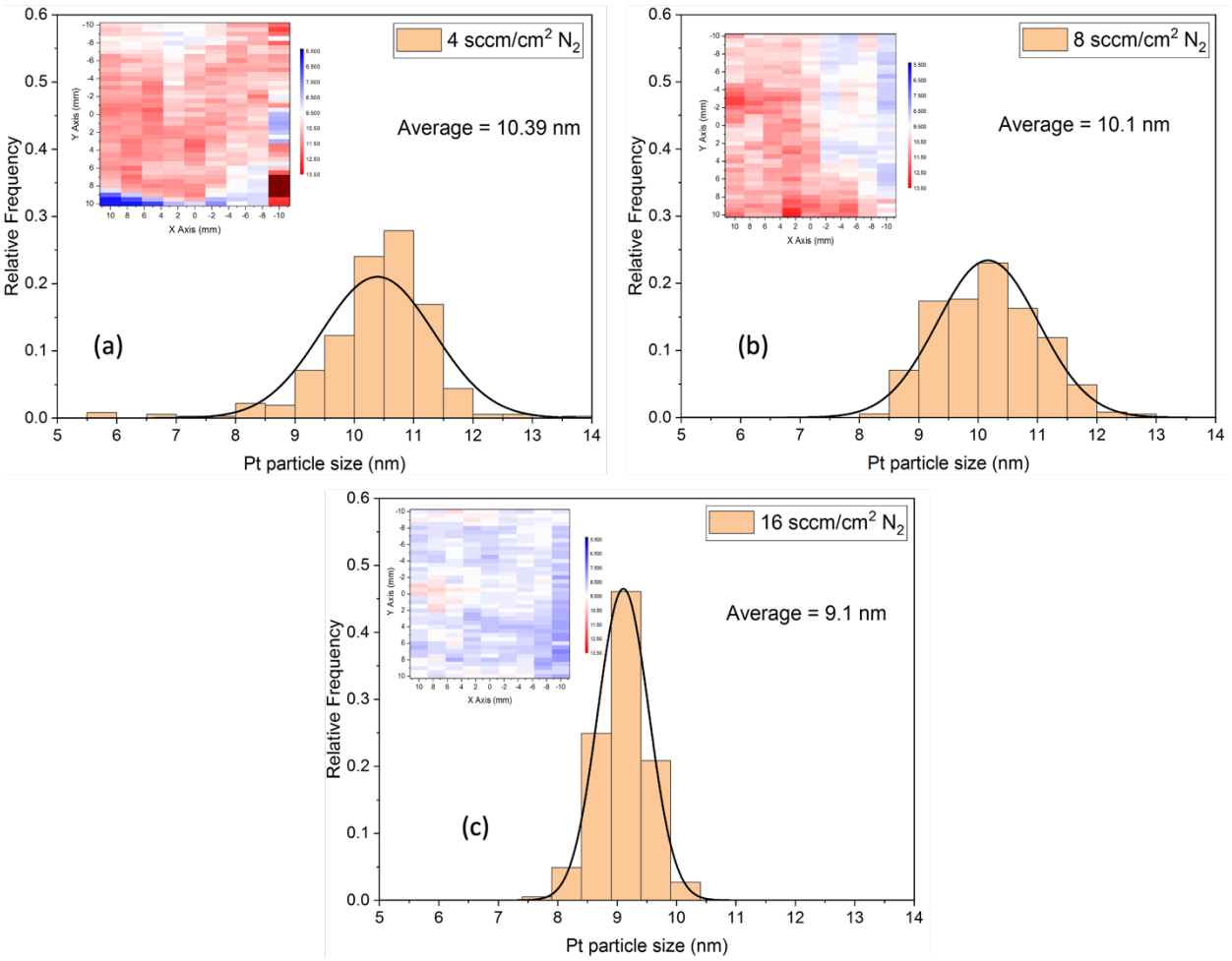


Figure 2.8. Pt particle size distribution of aged samples with (a) 4 sccm/cm^2 N_2 flow, (b) 8 sccm/cm^2 N_2 flow, and (c) 16 sccm/cm^2 N_2 flow. Micro-XRD maps are used as insets to serve as a guide to the eye.

This can also be verified from the TEM images in Figure 2.9, where 4 and 8 sccm/cm^2 N_2 flow rates have large non-spherical Pt agglomerates compared to nearly spherical Pt particles for 16 sccm/cm^2 N_2 flow. Furthermore, in Figure 2.9(b), some "starlike" shaped Pt nanoparticles can be observed. Such shapes of Pt nanoparticles have also been reported previously for potential cycling with H_2/N_2 from 0.6 V to 1 V vs. RHE [49]. The formation of such particles is attributed to non-uniform supersaturation (concentration of the Pt species in the electrolyte phase exceeds the value permissible at equilibrium) of soluble Pt species at the growing nanoparticle surface [49]. As these non-spherical particles generally have a higher number of defect sites, they can exhibit a higher area-specific activity towards ORR [126]. Yano et al. [50] have shown that the kinetically-controlled area-specific ORR activity of Pt is independent of particle size growth from the BOL to EOL for an AST in O_2 saturated 0.1 M $HClO_4$ at 65 °C. In other words, larger Pt particles (>9 nm) can exhibit higher area-specific activity towards ORR if they have optimum interparticle distance and are electrically connected to the carbon support. We speculate this could be the reason for lower voltage losses (at EOL) for 4 sccm/cm^2 N_2 flow compared to 8 and 16 sccm/cm^2 N_2 flow at low-to-moderate geometric current densities, as shown in Figure 2.5. However, a deeper understanding of how the gradient in Pt particle sizes from the air inlet to the outlet (as quantified in Figure 2.6) impacts the performance after aging is required to decouple such effects.

2.5 Conclusions

In this study, we quantified spatially heterogeneous electrocatalyst degradation at the cathode (Pt particle size growth and distribution) in a PEFC as a function of fully humidified N_2 flow rate during a DOE square-wave AST (0.6 V to 0.95 V vs. RHE, 30,000 cycles) with H_2/N_2 on the anode/cathode, respectively. The current density peaks associated with different facets of polycrystalline Pt nanoparticles in the hydrogen desorption region of the CVs of low (4 sccm/cm^2), medium (8 sccm/cm^2), and high (16 sccm/cm^2) N_2 flow rates decreased at different rates, highlighting possible changes in Pt crystal structure with aging. As the AST progressed, the ECSA loss at each sampling interval was inversely proportional to N_2 flow rate. Interestingly, at the EOL, irrespective of the N_2 flow rates and influence on ECSA loss rate, the MEAs ended up having similar overall ECSA loss (~65 % from the BOL). This can be attributed to the fact that Pt particles attain a "quasi" stable average size which resists further dissolution and impedes Pt degradation rate. A first-order rate model for ECSA loss predicted a linear dependence of the rate constant on N_2 flow rate. The rate constant increased by ~57% for an increase in N_2 flow rate from 4 sccm/cm^2

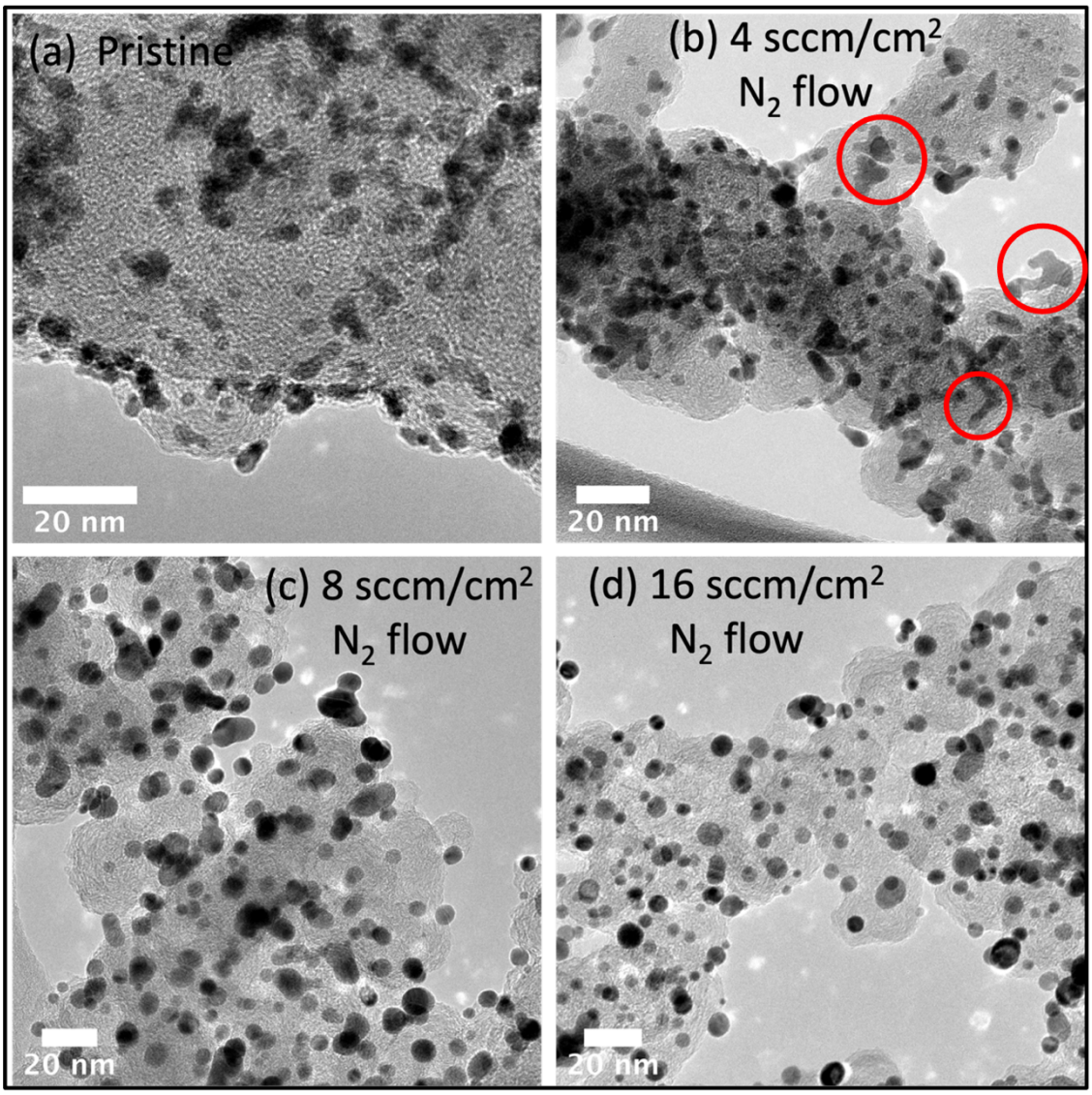


Figure 2.9. TEM images of (a) pristine sample and aged samples with (b) 4, (c) 8, and (d) 16 sccm/cm^2 N_2 flow. Red circles in panel (b) highlight some of the "starlike" shaped Pt nanoparticles.

to 16 sccm/cm^2 at the CCL during the AST. The 2D (2 cm x 2 cm) micro-XRD maps of the pristine and the aged MEAs revealed striking differences; Pt particle size distribution for the pristine MEA sample was largely uniform with an average of 3.5 nm, whereas the MEAs aged with different N_2 flow rates exhibited spatial heterogeneity in Pt particle size growth and distribution. In general, a higher Pt particle size growth was observed near the flow field outlet than the inlet. Although micro-XRD could not resolve channel-land differences in Pt particle sizes, this is an important finding as the ASTs used for studying Pt dissolution in PEFCs with N_2 are usually intended to achieve nearly homogenous Pt particle size growth throughout the CCL. However, an implicit assumption that Pt particle size growth is homogeneous is not supported by this work. We hypothesize that non-uniform humidification from the flow field inlet to the outlet (outlet more humidified than the inlet) could be responsible for heterogeneous Pt particle size growth at high temperature and humidity AST conditions. This non-uniform humidification across the cell active area results from the increase in water-carrying capacity of N_2 due to the local heating in the inlet lines to the cell. This humidity gradient is expected to be smaller for higher N_2 flow rate, likely offset by its overall increase in water removal capacity from the cell. Thus, overall humidification in the cell (in the absence of Faradaic reactions) is a delicate balance between the humidity gradient at the cell inlet and water removal capacity of the purge gas which directly depends on its flow rate in the channels. Since the humidity gradient and overall water mass is expected to be smaller for high N_2 flow rate, we would expect smaller average Pt particle size and "tighter" Pt particle size distribution compared to low N_2 flow rate as Pt particle size growth is supported by water content. This hypothesis is supported by our data. Furthermore, the non-uniform humidification impacts local chemical gradients (concentration and the mobility of the soluble Pt species) inside the cell, leading to the patterned or heterogenous Pt particle size growth. The hydration levels are further exacerbated by increased strength of cross-flow under the lands for higher N_2 flow rates in a serpentine flow field.

The histograms of Pt particle sizes followed a Gaussian distribution with the mean Pt particle sizes of 10.4 nm, 10.1 nm, and 9.1 nm for 4, 8, and 16 sccm/cm^2 N_2 flow rates, respectively. The histograms for 4 and 8 sccm/cm^2 N_2 flow rates, however, exhibited a larger fraction of Pt particles with sizes greater than 11 nm compared to 16 sccm/cm^2 N_2 flow, corroborated by the TEM measurements. The voltage loss (ΔV) analysis with H_2/air revealed greater losses for higher N_2 flow rates at most of the operating current densities; higher polarization losses occurred at

moderate-to-high current densities, most likely due to the heterogeneous nature of the Pt particle size growth.

Overall, it can be concluded that the catalyst aging inside the cell with fully humidified N_2 flow subjected to an AST is spatially heterogeneous, even though there is negligible heat and water generation (absence of Faradaic currents). The flow field architecture cannot be neglected as it strongly influences thermal and mass transport inside the cell due to the channel-land bias. An important outcome of this study is the call for inclusion of N_2 flow rate as a stressor for Pt degradation along with the usual ones during an AST for a holistic assessment of the performance and durability of the state-of-the-art Pt catalysts in PEFCs. Determination of the role of architecture is critical in understanding local degradation behavior.

Chapter 3: Effects of Heterogeneous Catalyst Degradation on the Localized Electrochemical Performance Loss of Polymer Electrolyte Fuel Cells (PEFCs)

This chapter is revised based on the published paper [153]:

Preetam Sharma, Lei Cheng, Douglas Aaron, Shirin Mehrazi, Jonathan Braaten, Nathan Craig, Christina Johnston, and Matthew M. Mench, "Unveiling Local Aging Patterns Following Accelerated Stress Testing of High-Performance Polymer Electrolyte Fuel Cells", Small, 2306433, 2023 (https://doi.org/10.1002/smll.202306433).

My contributions to this work include conceptualization of the idea, collection, reduction, and analysis of the data and manuscript preparation. Lei and Shirin helped with in-house micro-XRD and SEM measurements. Other authors assisted with data curation, review and editing of the manuscript.

Note on copyright: Under "How to Clear Permissions for a Thesis or Dissertation" on Wiley's website (dated November 16, 2020) it is clearly stated that, "If you are the author of a published Wiley article, you have the right to reuse the full text of your published article as part of your thesis or dissertation, you do not need to request permission from Wiley for this use."

3.1 Abstract

This study presents an in-depth analysis of heterogeneous aging patterns in membrane electrode assemblies (MEAs) subjected to diverse accelerated stress test (AST) conditions, simulating carbon corrosion (CC AST) and Pt particle size growth in fully humidified (Pt AST-Wet) and underhumidified (Pt AST-Dry) H_2/N_2 atmospheres. Multimodal characterization techniques are used to focus on heterogeneous aging patterns, primarily examining the variations in current distributions and Pt particle size maps. The findings reveal distinct characteristics of current distributions for all the AST cases, with substantial changes and strong current gradients in the CC AST case, indicative of severe performance degradation. Notably, despite significant differences in Pt particle size growth at the end-of-life (EOL), the Pt AST-Wet and Pt AST-Dry cases show minor changes in spatial current distributions. Moreover, a preferential growth of Pt particles under serpentine flow field bends in the Pt AST-Wet case is observed for the first time. This study provides crucial insights into the role of mass transport properties in shaping fuel cell performance, and highlights the need to consider factors beyond electrochemically-active surface area (ECSA) when assessing fuel cell durability.

3.2 Introduction

Automotive polymer electrolyte fuel cells (PEFCs) commonly experience a vast number of load cycles in their regular use, often in the hundreds of thousands. However, the dissolution of

platinum (Pt) catalyst and oxidation of carbon support under these cycling conditions poses a significant obstacle to their widespread commercial adoption. The durability benchmarks set by the U.S. Department of Energy (DOE) stipulate 8,000 hours and 30,000 hours of operation for light- and heavy-duty vehicles, respectively [6]. Numerous studies [8,41,46,48,57,78,79,130,154] have been conducted to investigate and understand the factors that influence durability of PEFCs and develop either materials- or systems engineering-based mitigation strategies [34].

In a typical PEFC, catalyst layers consist of Pt or Pt-alloy nanoparticles on carbon supports such as high surface area carbon (HSAC), low surface area carbon (LSAC), and medium surface area carbon (Vulcan®). HSAC supports are favored due to their high Pt nanoparticle dispersion ability, enhancing the electrochemically active surface area (ECSA). However, their higher defect rates make them more prone to corrosion [41,70]. Carbon corrosion can occur when high potentials (> 1.1 V vs. reversible hydrogen electrode, RHE) are reached during start-up/shutdown cycling. These high potential excursions result in carbon support oxidation to carbon dioxide (CO_2). Carbon corrosion can also occur under anode fuel starvation due to blockage or flooding, resulting in cell reversal [75]. Carbon corrosion at the cathode can orphan Pt nanoparticles, making them electrochemically inactive. Additionally, the gradual oxidation of amorphous carbon can lead to a pore structure collapse and consequent compaction [42]. Other mechanisms contributing to the loss of ECSA during standard operation (0.6 to 0.95 vs. RHE) of a PEFC encompass Pt dissolution and redeposition, Pt migration, and coalescence/agglomeration, along with the precipitation of dissolved Pt species (Pt^{n+}) into the ionomer phase [8]. The high surface energy of Pt nanoparticles and concentration gradients mainly drive these mechanisms. Degradation of other PEFC components, such as the polymer membrane [63,78,79], gas diffusion layers (GDLs) [77,81–83], and bipolar plates [13], is well-documented in the literature.

Accelerated stress tests (ASTs) are typically employed to evaluate the durability of various components in PEFCs [55]. Pt catalyst durability is usually assessed by cycling between voltage limits of 0.6 and 0.95 vs. RHE, while carbon corrosion is evaluated by cycling between voltage limits of 1.0 and 1.5 vs. RHE. A square-wave (SW) voltage profile with voltage holds (~3 seconds) is preferred for Pt catalyst durability, and a triangular-wave (TW) profile is used for carbon corrosion [41]. These ASTs are performed under a hydrogen (H_2) and nitrogen (N_2) atmosphere at the anode and cathode.

Recently, there has been a surge of interest in ASTs due to the need for robust protocols that can rapidly simulate the different degradation modes in PEFCs. During the tests, conditions are tailored to induce nearly homogeneous degradation, directly linking the applied stressors (e.g., relative humidity (RH), temperature, reactant flow rates, voltage cycling profiles) to performance loss. However, it is now understood that catalyst degradation in a PEFC is a highly heterogeneous process. The complexity arises from intricate interactions between the flow field architecture, materials, and local transport [92,115,155,156]. Recent studies have revealed heterogeneous growth in Pt particle size under the flow field channels and lands and from the cathode inlet to the outlet [92]. The particle size growth is notably more significant under the cathode flow field lands than channels and towards the outlet. It is believed that these heterogeneities stem primarily from local variations in water content at the catalyst layer. Due to the cooler conditions under the flow field lands during PEFC operation, liquid water tends to accumulate under the lands. This preferential accumulation promotes Pt particle size growth through intensified electrochemical Ostwald ripening. Higher humidity levels enhance ionic conductivity due to increased ionomer water uptake and thin water film formation, resulting in rapid Pt particle agglomeration and subsequent ECSA loss.

Furthermore, it has been demonstrated that the ASTs performed under fully humidified conditions cause more pronounced Pt particle size growth and ECSA loss than in underhumidified conditions for the same number of cycles [92]. Despite identifying these Pt particle size growth heterogeneities, there remains a gap in understanding how these non-uniform Pt particle size distributions impact a PEFC's localized performance following an AST. There is a dearth of studies investigating the effects of heterogeneous catalyst degradation on localized electrochemical performance loss.

Comprehending these local effects is crucial, particularly for automotive-sized PEFC stacks, where species, temperature, RH, and pressure distributions are mostly heterogeneous. Deeper understanding of local performance responses to aging must be incorporated in the design of highly durable fuel cells capable of withstanding thousands of load/unload, start-up/shutdown cycles.

In this investigation, multimodal characterization techniques are used to study the heterogeneous aging patterns in PEFCs, focusing on variations in current distributions and Pt particle size maps. Specialized segmented cell hardware was used to capture the local current and

temperature distributions at the beginning-of-life (BOL) and end-of-life (EOL) stages. These measurements were carried out on membrane electrode assemblies (MEAs) subjected to diverse AST conditions as prescribed by the U.S. DOE [55]. These conditions were designed to emulate carbon corrosion and Pt particle size growth in fully humidified and under-humidified H_2/N_2 environments. The segmented cell approach is an excellent tool for studying the spatially distributed electrochemical response of an operating PEFC, given that local current distributions are primarily influenced by species concentration, relative humidity conditions, and reactant flow rates [98,157–160]. Following the aging process, Pt particle size distributions for the aged MEAs were mapped using micro-X-ray diffraction (micro-XRD) at Bosch Research and Technology Center, North America, Sunnyvale, CA. Concurrently, scanning electron microscopy (SEM) cross-sectional images were utilized to quantify the post-aging morphological changes in the MEAs. Full active area (25 cm^2) current and Pt particle size maps were directly compared to understand how heterogeneous aging patterns affect local performance. This spatially-resolved comparison of the current and Pt particle size distributions, particularly across a larger active area, represents a novel approach not documented in previous studies.

3.3 Method of approach

3.3.1 Materials and test equipment

Single-cell tests were conducted using a fuel cell quick connect fixture (qCf) provided by balticFuelCells GmbH (Hagenower, Germany). The fixture included identical 7-channel serpentine flow fields on both the anode and cathode, with an active area of 25 cm^2. The flow channels were machined into 3 mm thick graphite plates. The cell compression was pneumatically regulated (see Figure S3.3 in Supporting Information for Chapter 3) to achieve a uniform pressure of approximately 1.0 MPa on the active area, resulting in a compression of the GDLs by about 20%. The test cell featured separate coolant plates for the anode and cathode, supplied with deionized (DI) water from precisely temperature-controlled refrigerated/heating circulating baths (VWR International, USA). The baths ensured accurate temperature control (with an accuracy of ± 0.01°C) and allowed for a maximum coolant flow rate of 22 L/min. This high coolant flow rate enabled precise cell temperature control across the active area.

The MEAs used in the tests consisted of Nafion™ XL membranes (27.5 µm thick) coated with Pt/C catalyst (40 wt.% Pt on Vulcan® carbon). The MEAs were sandwiched between Sigracet® SGL 22BB gas diffusion layers, each 215 µm thick (uncompressed). A nominal catalyst

loading of 0.3 mg_{-Pt}/cm^2 was used on both the anode and cathode. A fuel cell test station from Scribner Associates, Inc. (Southern Pines, NC) was utilized to control the cell operating conditions. During electrochemical characterization with nitrogen, an external potentiostat (Biologic SP-240) was employed to regulate the cell voltage.

The current and temperature distributions at the cathode were recorded using a printed circuit board known as the current scan shunt provided by S++® Simulation Services (Murnau-Westried, Germany). This current density distribution (CDD) board consisted of 100 current measurement segments and 25 temperature measurement segments (see Figure S3.4, Supporting Information for Chapter 3). Each temperature measurement segment represented four current distribution segments, resulting in a spatial resolution of approximately 5 mm for current measurements and 10 mm for temperature measurements. The CDD board, or cathode current collector, was the only segmented component in the cell; the flow field was not segmented. As a result, there is a slight smearing in the current distribution data (lateral current spread). However, due to the thin (3 mm) flow field plates, this effect is expected to be minimal while maintaining sufficient resolution to identify variations [98,161,162]. It should be noted that the measured temperature distribution is closer to the temperature in the cathode flow field rather than the catalyst layer since the sensor plate is positioned between the cathode flow field and the backing plate.

Uniform cell compression is crucial for accurate CDD measurements. Uneven compression or pressure distribution in the cell can result in artificial current distributions, which may be mistaken for variations in reactant distribution. A Fujifilm Prescale® Super Low pressure measurement film was used between each layer of the cell assembly to ensure uniform compression across the active area. The resulting pressure distribution and the uniform contact between the cathode flow field and the segmented current collector plate were verified, as shown in Figure S3.5, Supporting Information for Chapter 3. The CDD board was connected to a computer using data acquisition cables and a custom LabVIEW™ program to collect the current and temperature distribution data. The data were simultaneously gathered with the polarization curves at a sampling frequency of 2 points/s (sampling interval of 500 ms). The collected data were averaged over a minimum period of 60 seconds for each current setting at the specified operating condition. The CDD board can reliably measure geometric current densities up to 2.1 A/cm^2 and temperatures up to 100 °C.

3.3.2 Catalyst AST

The ASTs were carried out under specific conditions to evaluate the performance and durability of the fuel cell. All ASTs were conducted at a cell temperature of 80 °C with atmospheric back pressure, using a H_2/N_2 (anode/cathode) environment. Three different ASTs recommended by the U.S. DOE [55] were performed, each with different RH and voltage cycling windows.

The first AST, referred to as Pt AST-Wet, involved subjecting the cell to 30,000 cycles of a square-wave voltage profile ranging from 0.6 to 0.95 V vs. RHE at 100% RH. Each potential step lasted for 3 seconds. The second AST, referred to as Pt AST-Dry, subjected the cell to 30,000 cycles of a square-wave voltage profile ranging from 0.6 to 0.95 V vs. RHE at 50% RH, again with a dwell time of 3 seconds at each potential. The third AST, referred to as CC AST, involved subjecting the cell to 5,000 cycles of a triangular-wave voltage profile ranging from 1.0 to 1.5 V vs. RHE at 100% RH. During all ASTs, constant flow rates of H_2 and N_2 gases were maintained at 4 and 8 sccm/cm^2, respectively. It is worth noting that recent studies have indicated that varying N_2 flow rates during long-term AST cycling can lead to non-uniform aging effects in the cell [115]. Therefore, consistent flow rates were maintained throughout the tests to minimize such variations. In the square-wave and triangular-wave ASTs, a voltage step-up/down ramp rate of 500 mV/s was employed. These specific test conditions are summarized in Table 3-1, and Figure 3.1 illustrates the waveforms utilized for the ASTs. The square-wave AST conditions were selected to simulate Pt particle size growth in a fully humidified and underhumidified H_2/N_2 atmosphere [92,155], while the triangular-wave AST induced carbon support corrosion [41].

3.3.3 In-situ electrochemical characterization

Cathode cyclic voltammograms (CVs) were recorded from 0.1 V to 0.9 V vs. RHE at a scan rate of 50 mV/s in a fully humidified (100% RH) H_2/N_2 (anode/cathode) atmosphere at 80 °C. Hydrogen desorption peaks in CVs were numerically integrated to compute ECSA after correcting for double-layer capacitance using Equation 1 [163]:

$$ECSA = \frac{Q_H}{210 \times L_{Pt} \times \upsilon} \quad (1)$$

where, Q_H is the hydrogen desorption charge, L_{Pt} is the Pt loading, $210\ \mu C/cm^2_{Pt}$ is the unit charge, and υ is the scan rate. During CVs, low H_2/N_2 flow rates of 4/8 sccm/cm^2 were used to avoid errors in ECSA calculation related to the artifacts in the hydrogen adsorption/desorption region [124,164]. Linear sweep voltammograms (LSVs) were collected to measure H_2 crossover from 0.05 V – 0.7 V vs. RHE at a scan rate of 2 mV/s in a fully humidified H_2/N_2 (anode/cathode) atmosphere at

Table 3-1. Test conditions for Pt AST – Wet, Pt AST – Dry, and CC AST

Test case	Inlet RH at the anode and cathode (%)	Cell temperature (°C)	H_2/N_2 flow rate (sccm/cm^2)	AST waveform and potential limits	No. of AST cycles	Gauge Back-pressure (atm)
Pt AST - Wet	100	80	4/8	SW (0.6 V – 0.95V)	30,000	0
Pt AST - Dry	50	80	4/8	SW (0.6 V – 0.95V)	30,000	0
CC AST	100	80	4/8	TW (1.0 V – 1.5V)	5,000	0

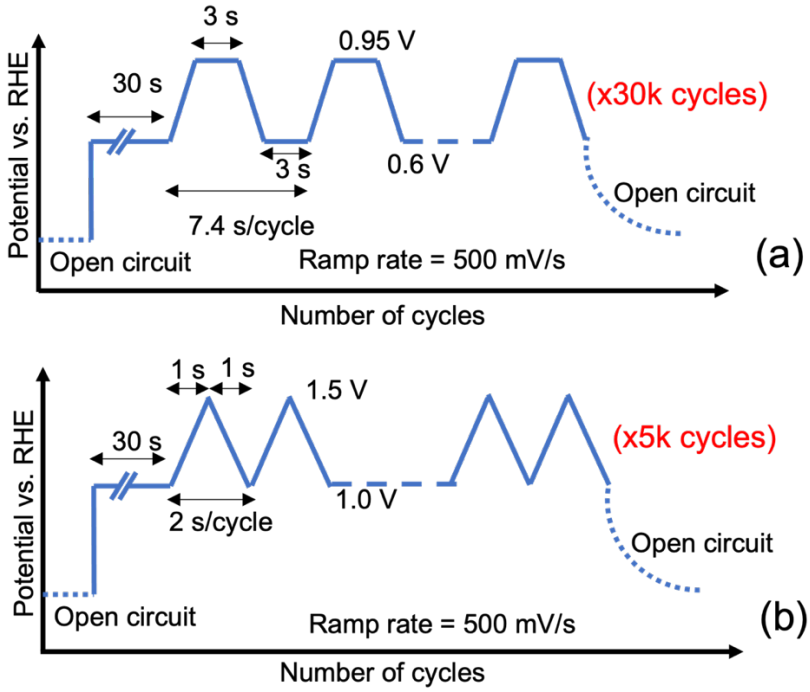


Figure 3.1. U.S. DOE's (a) square-wave AST for catalyst durability, and (b) carbon corrosion AST for support durability used in the present study. Note that the square-wave AST was performed at two different RH conditions to simulate dry and wet operating conditions within a fixed potential window of 0.6 V to 0.95 V vs. RHE.

80 °C. The H_2/N_2 flow rates during the LSVs were similar to that of the CVs. The galvanostatic electrochemical impedance spectroscopy (EIS) measurements were recorded in H_2/air atmosphere at 80 °C, 100 % RH, and 150 kPa (absolute) backpressure on both the anode and cathode. A small DC current perturbation (5% of the applied current) was imposed during EIS, and the frequency was swept from 0.1 Hz to 10 kHz at 7 points/decade. An equivalent circuit model (discussed later in detail) [72] was used to fit the EIS data and extract high-frequency resistance (HFR), kinetic, and mass transport resistance at the BOL and EOL of each AST.

Before subjecting the MEAs to different ASTs, a consistent break-in/conditioning procedure was performed to ensure that the MEAs exhibited peak performance at the BOL [165]. The procedure involved voltage cycling between 0.8, 0.6, and 0.3 V with 30 seconds hold at each potential in H_2/air atmosphere at 80 °C, 100% RH, and 150 kPa (absolute) backpressure on both the anode and cathode. A total of 160 cycles were performed. The H_2/air stoichiometry was held constant at 1.5/2. Polarization curves were recorded in the H_2/air atmosphere by holding the cell at constant current densities (from ~ 2 A/cm^2 to 0 A/cm^2) for 4 minutes at wet (100% RH) and dry (50% RH) conditions to gauge the impact of ASTs on flooding/drying behavior at the EOL. The cell temperature and the H_2/air stoichiometry were held constant at 80 °C and 1.5/2, respectively. The cell was kept at identical starting conditions to avoid the effects of hysteresis and to ensure repeatable performance and measurement consistency. At least three different MEA samples were tested for each AST case; average performance is reported with one standard deviation ($\pm \sigma_{error}$) representing variability about the mean.

The current and temperature distribution data were collected in parallel with the polarization curves and processed using an in-house MATLAB® code. As mentioned earlier, the sampling interval was 500 ms, and the data were averaged over the final 60 seconds for each operating condition. The detailed data reduction procedure is explained in the Supporting Information for Chapter 3. In summary, the time-averaged raw current data (10 × 10 matrix) at a given operating condition was smoothed and plotted as a contour map of the percentage deviation from the mean current to identify localized regions of low/high current relative to the mean [162]. The contour map was then corrected for minor ohmic variations (likely due to variations in interlayer contact resistance). For the temperature distributions, time-averaged temperature data (5 × 5 matrix) at a given operating condition was smoothed to obtain a contour map, and no further normalization or correction was carried out. Therefore, in the sections to follow, all current

distributions are represented as the corrected contours of percentage deviation from the mean operating current, and the temperature distributions are presented as the smoothed contours of the time-averaged raw data.

3.3.4 Post-mortem analysis

3.3.4.1 Transmission electron microscopy (TEM)

Transmission electron microscopy (TEM) imaging was performed at the Institute for Advanced Materials and Manufacturing (IAMM), University of Tennessee, Knoxville. A diluted mixture of isopropyl alcohol (IPA) and catalyst particles collected from catalyst-coated membranes (CCMs) was subjected to sonication and later delicately placed onto a copper grid with Lacey carbon film. The grid, which had 200-mesh size and an average pore dimension of 50 μm, was then examined with a Zeiss Libra 200 HT electron microscope running at 200 kV. The resultant images' features were processed and analyzed using the Fiji/ImageJ software platform. At least 100 Pt particles from each micrograph of different samples were considered for averaging. Note that highly irregularly shaped particles were not included in the averaging.

3.3.4.2 Scanning electron microscopy (SEM) with energy dispersive spectroscopy (EDS)

MEAs were mounted in epoxy for cross-sectional scanning electron microscopy (SEM, JEOL JSM-7200F). Epoxy-mounted MEAs were successively sanded using low to high-grit sandpaper from 320-1200 grit. Energy dispersive spectroscopy (EDS, Oxford) was employed to map the elemental distribution and, in particular Pt band across the MEA. Both SEM and EDS were performed at 15 KeV accelerating voltage.

3.3.4.3 In-house lab-scale micro-X-ray diffraction (micro-XRD)

Micro-diffraction measurements were carried out using a Bruker D8 Advance X-ray diffractometer equipped with a Cu Kα radiation source (1.5406 A) and a Bruker LYNXEYE XE detector. Alignment of the samples was done using a *xyz* moving sample stage with a double-laser unit. For the measurement, the accelerating voltage and current were set at 40 kV and 40 mA. XRD scans were collected between 37.5 and 42 degrees (2θ) at a step size of 0.03 degrees and 2.5 seconds time per step. Data were processed and analyzed using GSAS-II [125]. The 25 cm^2 active area MEAs were sliced into four 5 cm^2 size quadrant pieces. Each of the 5 cm^2 was individually raster scanned with a step size of 2 mm in both *x* and *y* directions with a 500 μm × 500 μm spot size. After the measurement of the four quadrants, the XRD mappings were stitched together to represent the entire 25 cm^2 active area.

3.4 Results and Discussion

As a general note, the error bars ($\pm \sigma_{error}$) in the Results and Discussion section figures are plotted as lines with filled areas. Figure 3.2 shows the absolute ECSA ($m^2/g_{\text{-Pt}}$) and normalized ECSA as a function of the number of AST cycles for different AST types used in this study. The ECSA was obtained by numerically integrating hydrogen desorption peaks in the CVs shown in Figure S3.10, Supporting Information for Chapter 3. The CVs in Figure S3.10, Supporting Information for Chapter 3, show a clear trend of decreasing hydrogen desorption charge (area under the curve) with aging irrespective of the type of AST used, highlighting possible changes in Pt crystal structure. This loss of peaks in the region 0.1 ~ 0.3 V vs. RHE for carbon-supported polycrystalline Pt nanoparticles with aging is well-documented in the literature [8,49,50,121,129,166]. However, an interesting observation can be made regarding the loss of desorption charge in the early phases of cycling (BOL to ~6,000) for Pt AST-Wet and Pt AST-Dry (Figure S3.10 (b) and (c), Supporting Information for Chapter 3); the decline is faster for Pt AST-Wet as compared to Pt AST-Dry. This rapid loss in the early phases of cycling could be due to higher net water content for Pt AST-Wet compared to Pt AST-Dry at the catalyst layer leading to the intensification of electrochemical Ostwald ripening. This observation has also been recorded in other recent studies [92,155,156]. The chemical potential for Pt dissolution and subsequent agglomeration in the early phases of cycling is inversely related to Pt particle size, i.e., smaller particles dissolve more rapidly due to high surface energy via the Gibbs-Thomson effect and redeposit onto larger Pt particles [8]. However, for this dissolution and redeposition to proceed, the particles should be electrically connected through the porous carbon support and must have ionically conductive pathways (ionomer coverage or thin water film) for Pt ions to transport. At higher humidity levels (as is the case for Pt AST-Wet), the ionic conductivity is enhanced due to increased water uptake by ionomer and thin water films, leading to rapid agglomeration of Pt particles and loss of ECSA.

Figure 3.2 shows that the MEAs have BOL ECSA between 20 to 25 $m^2/g_{\text{-Pt}}$, attributed to sample-to-sample variability. Similar values have been reported in earlier studies with identical materials [92,115]. From Figure 3.2(a), it is observed that the CC AST MEAs lost ~52% ECSA at the EOL. The most significant drop in the ECSA is observed for the first ~1000 cycles, likely due to Pt particle detachment from the support. In a recent study, Saha et al. [42] made similar observations where rapid oxidation of amorphous carbon support in early cycling phases (~500 cycles) led to a drastic reduction in the ECSA. Furthermore, it is observed from Figure 3.2(a) that

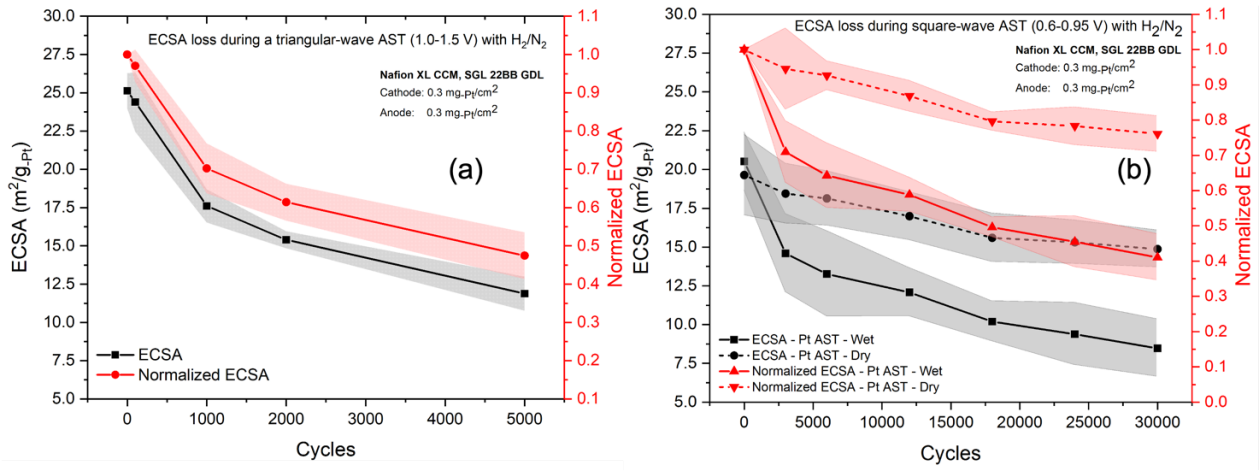


Figure 3.2. Absolute ECSA (m^2/g_{-Pt}) and normalized ECSA as a function of number of AST cycles for (a) CC AST and (b) Pt AST-Wet and Pt AST-Dry measured under H_2/N_2 atmosphere at $T_{cell} =$ 80 °C, $RH\%_{A/C} = 100/100$ with no backpressure. The ECSA is obtained by integrating hydrogen desorption peaks in CVs (Figure S3.10, Supporting Information for Chapter 3).

the ECSA loss stabilized after ~2000 cycles. This stabilization of the ECSA loss is in line with the findings in ref. [42] where carbon loss slowed down during the second cycling phase (~1500 cycles), but a sudden collapse of the pore structure was observed.

The ECSA loss for Pt AST-Wet and Pt AST-Dry at the EOL is ~60% and ~25%, respectively (Figure 3.2(b)). This drastic difference in the ECSA loss for the square-wave cycling under identical conditions except for the inlet RH% can solely be attributed to higher water content at the catalyst layer for Pt AST-Wet as compared to Pt AST-Dry, leading to intensified Ostwald ripening and particle dissolution (repeated oxidation and reduction of Pt particles). Similar ECSA loss values have been reported in the literature [92,115,155] with identical materials used in the present study. A well-defined Pt band is also observed for Pt AST-Wet in the membrane near the CCL interface (discussed later in the section). This band is formed due to the reduction of dissolved Pt ions by H_2 crossover from the anode [49]. As discussed by Ferreira et al. [49], the crossover H_2 flux significantly exceeds the estimated flux (~8 x 10^{-9} mol/s-cm^2 for a typical crossover current density of ~1.5 mA/cm^2) of dissolved Pt species (~ 5 x 10^{-14} mol/s-cm^2) during voltage cycling (0.6 V to 1.0 V vs. RHE) at typical PEFC operating conditions with Pt catalyst. Consequently, the Pt ionic species are almost entirely reduced at the CCL-membrane interface. This permanent loss of Pt in the membrane could further explain such high ECSA loss for Pt AST-Wet. Interestingly, no Pt band is observed for other AST cases. Furthermore, the ECSA loss slows down for both the Pt AST-Wet and Pt AST-Dry towards the tail-end of cycling (~20,000 to 30,000 cycles), owing to Pt particles attaining a "quasi" stable average size, resisting further dissolution [56–58,130]. Overall, ECSA loss is observed for all the MEAs, albeit at different rates and through different mechanisms with the maximum and minimum values at the EOL for Pt AST-Wet (~60%) and Pt AST-Wet (~25%), respectively.

Figure 3.3(a) shows the H_2/air polarization curves at the BOL and EOL for different AST cases (detailed polarization curves during several aging stages are shown in Figure S3.11, Supporting Information for Chapter 3). The tight error bars at the BOL and EOL indicate excellent reproducibility of H_2/air performance across different MEAs. For all the ASTs, a clear performance loss is observed at the EOL. For Pt AST-Wet and Pt AST-Dry, higher voltage loss is observed at moderate-to-high geometric current densities; for example, at 1.5 A/cm^2, Pt AST-Wet lost ~150 mV as compared to ~50 mV for Pt AST-Dry. This performance loss can be attributed to the reduction in ECSA caused by voltage cycling [130,136]. Pt AST-Dry demonstrates a reduced

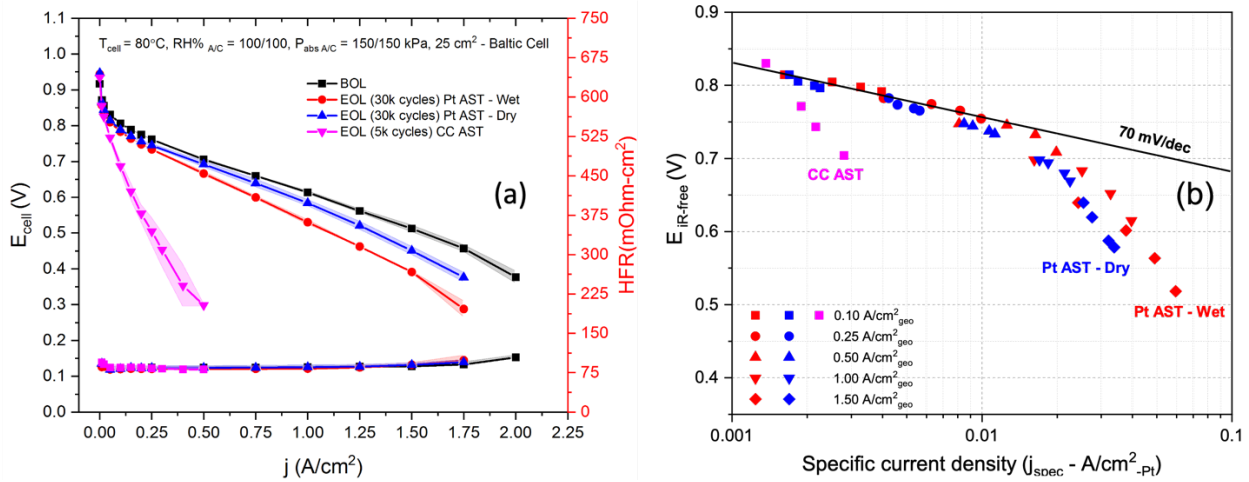


Figure 3.3. (a) Polarization performance of the MEAs at the BOL and EOL for Pt AST-Wet, Pt AST-Dry, and CC AST. Polarization conditions include cell T_{cell} of 80 °C, H_2/air stoichiometry ($\lambda_{H_2}/\lambda_{Air}$) of 1.5/2, inlet RH ($RH\%_{\,A/C}$) of 100% on both the anode and cathode with a backpressure ($P_{abs\ A/C}$) of 150 kPa (absolute). In (b), the iR-free cell voltage is plotted vs. specific current density to assess the onset of mass transport limitations for different aging protocols. A Tafel slope of 70 mV/decade is plotted as a reference.

performance loss compared to Pt AST-Wet, likely due to smaller cumulative ECSA decrease. At higher geometric current densities (> 1 A/cm^2), the voltage losses are exacerbated for both Pt AST-Wet and Pt AST-Dry, most likely due to an increase in Pt area-specific mass transport overpotential [136]. The voltage loss for CC AST case is rather dramatic, with almost ~250 mV loss at a low geometric current density of 0.25 A/cm^2. This severe voltage loss is most likely due to poor mass transport, and can be attributed to flooding in the catalyst layer caused by pore structure collapse and decreased hydrophobicity [42]. The improved polarization performance (see Figure S3.11 (c), Supporting Information for Chapter 3) of the CC AST case at the EOL under dry inlet conditions ($RH\%_{A/C}$ = 50/50) supports the flooding argument; the cell voltage is ~100 mV higher compared to wet inlet conditions ($RH\%_{A/C}$ = 100/100) at 0.25 A/cm^2. The HFR remains relatively unchanged for all the AST cases compared to BOL. This stability is because the polymer membrane is the main contributor to the HFR, and given the specific AST conditions in this study, it is anticipated that there would be minimal degradation of the membrane [63].

To further understand the impact of voltage cycling on the polarization performance of different AST cases, the iR-free cell voltage for various geometric current densities is plotted as a function of the specific current density (j_{spec}) in Figure 3.3(b). The specific current density is defined as the following [130]:

$$j_{spec}\,(A/cm^2_{Pt}) = \frac{j_{geo}(A/cm^2)}{ECSA\,(m^2_{Pt}/g_{Pt})\times L_{Pt}(mg_{Pt}/cm^2)\times 10} \tag{2}$$

where j_{geo} is the geometric current density, ECSA is the electrochemically active surface area, and L_{Pt} is the Pt loading in the cathode. The denominator in Equation 2 is also termed as the roughness factor. Assuming that the performance loss at the EOL for a particular MEA is solely due to ECSA loss and follows Tafel kinetics, the change in ORR overpotential ($\Delta\eta_{ORR}$) at any given geometric current density can be estimated as [130],

$$\Delta\eta_{ORR} = \frac{2.303\times RT}{\alpha F} \times log\left\{\frac{(i_o\times ECSA)_{BOL}}{(i_o\times ECSA)_{EOL}}\right\} \tag{3}$$

where α is the cathodic charge transfer coefficient, R is the universal gas constant, T is the temperature, F is Faraday's constant, and i_o is the exchange current density. According to Equation 3, a 10-fold decrease in ECSA predicts a kinetic voltage loss of approximately 70 mV at 80 °C. However, when additional losses such as mass transport are present, the slope of iR-corrected voltage vs. j_{spec} deviates significantly from the theoretical value of 70 mV/decade, especially at higher geometric current densities. These additional mass transport losses can occur due to local

oxygen transport resistance at the catalyst site or proton conduction through the ionomer films on catalyst particles [130]. Moreover, if carbon corrosion occurs during an AST, the voltage loss would be further aggravated.

From Figure 3.3(b), it is evident that both Pt AST-Wet and Pt AST-Dry exhibit a slope of around 70 mV/decade up to a j_{spec} of approximately 0.02 A/cm^2_{Pt}. However, for j_{spec} > 0.02 A/cm^2_{Pt}, significant deviation from the 70 mV/decade slope can be observed, indicating the presence of additional mass transport losses. Interestingly, these losses resemble those seen in the electrodes with very low Pt loading or roughness factor [35,36], where there is a high influx of oxygen to the Pt catalyst surface. In other words, when oxygen consumption is high, there is a "crowding" of oxygen molecules at the catalyst/ionomer interface. Similar values of j_{spec} (around 0.02 A/cm^2_{Pt}) where the voltage loss behavior deviates from the Tafel prediction of 70 mV/decade have been reported in the literature [92,130,136,167,168]. For the CC AST case, the slope strongly deviates from the Tafel prediction at a low geometric current density of 0.1 A/cm^2. This substantial deviation indicates severe mass transport losses as a result of pore structure collapse, rather than purely kinetic losses. Similar observations have been made by other researchers [42,136,169]. In summary, Pt AST-Wet and Pt AST-Dry exhibit voltage loss behavior that aligns with the Tafel prediction up to a geometric current density of approximately 1 A/cm^2. Beyond this point, mass transport losses become dominant. However, the losses observed for CC AST case deviate significantly from the Tafel prediction, even at low geometric current densities. It is worth mentioning that correcting the voltage losses for oxygen mass transport resistance in Figure 3.3(b) through limiting current measurements [37] would yield a more accurate comparison. The oxygen transport resistance was not measured in this study and hence, no such correction was applied.

To delve deeper into the different mechanisms responsible for polarization performance loss caused by voltage cycling, EIS measurements were employed. Figure S3.12, Supporting Information for Chapter 3, shows the complete Nyquist-impedance spectra for Pt AST-Wet, Pt AST-Dry, and CC AST. These spectra span a range of geometric current densities from low to high (0.1 to 1.0 A/cm^2) at both the BOL and EOL. Comparing the EIS spectra across different samples at the BOL confirms the reproducibility of performance. It is important to note that the EIS spectra are qualitatively responsive to variations in ECSA, Pt utilization, and morphological changes that occur during the aging process. To quantify various losses, an equivalent circuit was fitted (see Figure 3.4(c)) to the EIS spectra at the geometric current densities of 0.2 A/cm^2 and

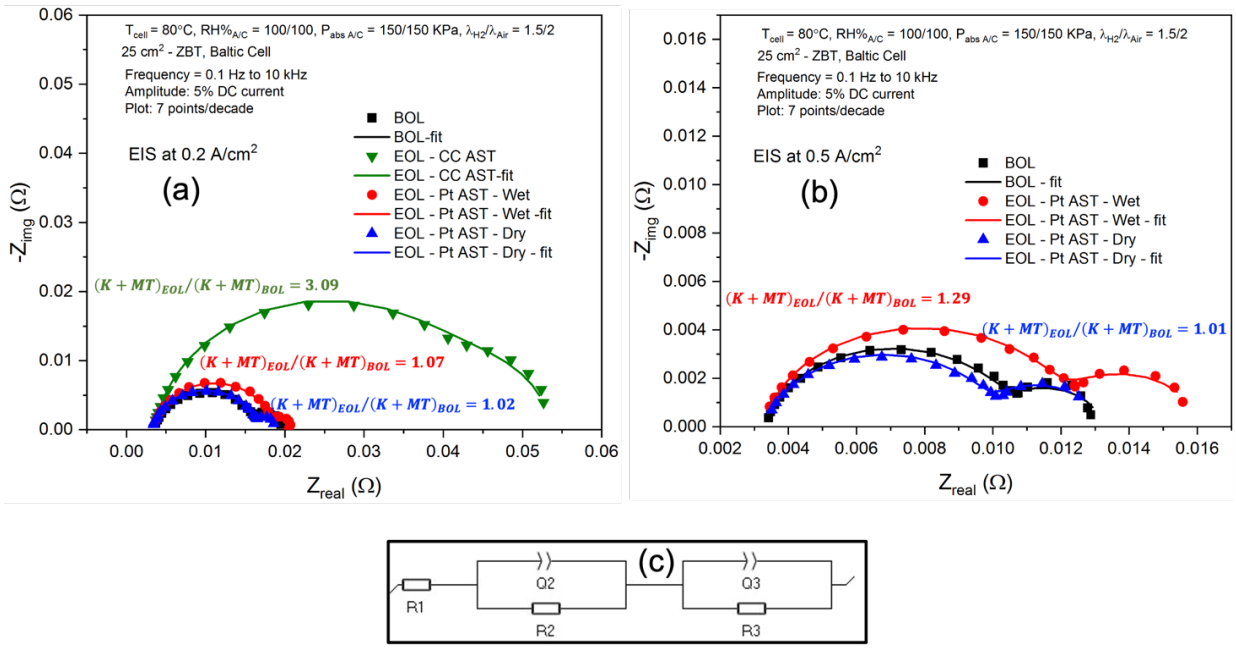


Figure 3.4. EIS spectra (0.1 Hz to 10 kHz, 5 % DC amplitude, 7 points/decade) measured at the BOL and EOL for CC AST, Pt AST-Wet, and Pt AST-Dry at the current densities of (a) 0.2 A/cm^2, and (b) 0.5 A/cm^2. The spectra were recorded at T_{cell} = 80 °C, $\lambda_{H_2}/\lambda_{Air}$ = 1.5/2, and $RH\%_{A/C}$ = 100/100 with $P_{abs\ A/C}$ = 150/150 kPa. The fitted equivalent circuit to derive the kinetic (K) and mass transport (MT) resistances at the BOL and EOL is shown in (c). The ratio of $(K+MT)_{EOL}$ to $(K+MT)_{BOL}$ can also be noted from (a) and (b).

0.5 A/cm^2 . The fitting involved resistances (R1, R2, and R3) and constant phase elements (Q2 and Q3), with the constant phase element accounting for heterogeneous electrochemical reactions in the fuel cell's porous electrodes. Other researchers have used similar equivalent circuits to quantify various losses [72,80,81]. The ohmic resistance of a specific cell build is represented by R1 and the lumped kinetic (K) and mass transport (MT) resistances (predominantly at the cathode), i.e., (K+MT) are represented by (R2+R3). Hence, the total cell impedance becomes R1+(K+MT). By lumping the kinetic and mass transport resistances, we can compare the relative increase in cell impedance across different AST cases with respect to BOL. This increase in impedance is quantified using the ratio $(K + MT)_{EOL}/(K + MT)_{BOL}$.

Figure 3.4(a) and (b) reveal negligible change in HFR for all the AST cases compared to BOL. This aligns with our observations in Figure 3.3(a), confirming negligible membrane degradation from the ASTs. At a geometric current density of 0.2 A/cm^2 (Figure 3.4(a)), where the kinetics likely dominate, the change in lumped kinetic and mass transport impedance (K+MT) is approximately 3.1 times higher at the EOL compared to BOL for the CC AST case. As discussed earlier, MEAs subjected to CC AST experience significant voltage loss and exhibit severe mass transport limitations at the EOL, even at low geometric current densities. These mass transport losses primarily arise from the progressive oxidation of the porous carbon support, ultimately resulting in the collapse of the pore structure. This collapse leads to flooding by liquid water, hindering gas phase reactant transport to the catalyst particles. Furthermore, there is a concomitant increase in kinetic resistance due to the electrical isolation of Pt particles from the support (~52% ECSA loss compared to BOL), and agglomeration. This electrical isolation hampers Pt utilization, further exacerbating the performance loss. In the case of CC AST, a significant deviation of the fitted slope (see Figure 3.3(b)) from the Tafel prediction at 0.1 A/cm^2 agrees with the substantial increase in (K+MT) impedance observed in Figure 3.4(a). The change in (K+MT) impedance for Pt AST-Dry is more modest, approximately 1.02 times that of the BOL. This finding can be attributed to a lower cumulative ECSA loss (~25% compared to BOL) and negligible change in the CCL structure. However, for Pt AST-Wet, where the cumulative ECSA loss reached around ~60% compared to the BOL, along with the migration of Pt particles within the ionomer, the increase in (K+MT) impedance is approximately 1.07 times higher than the BOL. This increase in (K+MT) impedance is greater than that of Pt AST-Dry. Note that there is negligible change in CCL structure at the EOL for Pt AST-Wet case.

At a higher geometric current density of 0.5 A/cm^2 (Figure 3.4(b)), where the mass transport losses likely dominate (kinetic component is lower than at 0.2 A/cm^2 due to higher overpotential), the (K+MT) impedance for Pt AST-Wet increases to approximately 1.29 times that of the BOL. This increase is likely due to elevated Pt area-specific mass transport overpotential [136]. In contrast, the ratio remains unchanged for Pt AST-Dry, despite experiencing higher total losses than at 0.1 A/cm^2. Similar observations have been made in a study by Spernjak et al. [72]. Unfortunately, due to unstable performance at the EOL, the CC AST case could not provide reliable EIS data at 0.5 A/cm^2, resulting in its absence from Figure 3.4(b) for comparison.

In summary, the CC AST case exhibits the highest increase in (K+MT) impedance at 0.2 A/cm^2, while the Pt AST-Dry case shows the lowest increase. This trend of (K+MT) impedance increase is consistent at 0.5 A/cm^2. Therefore, the EIS measurements support the identification of different performance loss mechanisms, as demonstrated by the simplified voltage loss analysis in Figure 3.3(b).

The changes in CDD during aging were tracked using segmented cell hardware. Before connecting these changes to degradation, it is crucial to understand the factors influencing local current distributions in a fuel cell. At a given voltage, local current distributions are mainly influenced by local relative humidity, reactant concentration, and liquid water distribution [95,159,170]. Temperature gradients (~15 to 20 °C) exist at the cathode [148] and between flow field channels and lands (~2 to 3 °C), with lands being cooler due to direct contact with the diffusion media [152]. However, the impact of temperature gradients on reaction kinetics is relatively small compared to interactions with liquid water and relative humidity. The ionic conductivity of the polymer membrane and ionomer in the catalyst layers is closely coupled to relative humidity, meaning that humidity and liquid water distribution changes can dramatically impact current distributions. For underhumidified or unsaturated inlet conditions, local current distributions are typically controlled by relative humidity at the anode [171]. Electroosmotic drag can exacerbate anode dryout if back diffusion is insufficient, resulting in significant gradients in local current distribution and a decline in fuel cell performance. Conversely, the oxygen partial pressure governs the local current distributions for fully humidified inlets [171]. In areas where flooding occurs (mainly at the cathode exit or colder spots), the local currents decrease due to the blockage of oxygen supply to the reaction sites. This blockage substantially impacts the fuel cell performance, leading to pronounced gradients in current density. It is worth mentioning that factors such as

reactant flow orientation, stoichiometry, and the thermal and mechanical properties of the MEA can also influence local current distributions [98]. In this study, the CDDs are compared at equivalent geometric current densities, where the amount of electrochemically generated water is the same and other parameters are held constant.

Figure 3.5, panels (a) to (e), illustrates the CDD measured at the BOL for the CC AST case with fully humidified air and H_2 inlets. A notable trend of increasing non-uniformity in CDD at BOL is observed as the geometric current densities increase from low (0.2 A/cm^2) to high (1.5 A/cm^2) values. Specifically, as the current density increases, local regions with higher and lower currents are observed at the air inlet and outlet, respectively. This observation aligns with the understanding that oxygen partial pressure governs the local current distributions for fully humidified inlets. In essence, the current distributions follow the path of oxygen depletion at the cathode. As the operating current density increases, higher oxygen depletion near the cathode outlet and accumulation of excess liquid water impede oxygen supply to the reaction sites, significantly impacting performance and local current distributions. Similar findings have been reported in other studies that utilized segmented cell hardware [95,159,170].

At the EOL, strong current gradients are observed in panels (f) and (g) of Figure 3.5 for geometric current densities of 0.2 A/cm^2 and 0.5 A/cm^2, respectively. For instance, at 0.2 A/cm^2, the local current deviation from the mean current increases from around ± 2.5% (relatively uniform) at the BOL to over ± 15% at the EOL. These substantial current gradients indicate significant performance degradation and severe limitations in mass transport, primarily caused by flooding in the catalyst layer due to the collapse of its pore structure and loss of hydrophobicity. The pore structure collapse occurs due to the progressive oxidation of the porous carbon support, ultimately leading to the compaction of the catalyst layer. The observed current gradients at EOL (panels (f) and (g) in Figure 3.5) can be closely linked to the significant deviation observed in the Tafel behavior (Figure 3.3(b)) and the increase in (K+MT) impedance (Figure 3.4(a)) for the CC AST case. Other researchers [72,88,99,172] have also corroborated the presence of spatial heterogeneity in current distributions with various materials, aging conditions, and flow arrangements.

During the CC AST, fully humidified H_2/N_2 streams were utilized at 80 °C. The purpose of voltage cycling within the range of 1 to 1.5 V vs. RHE was to induce degradation in the carbon

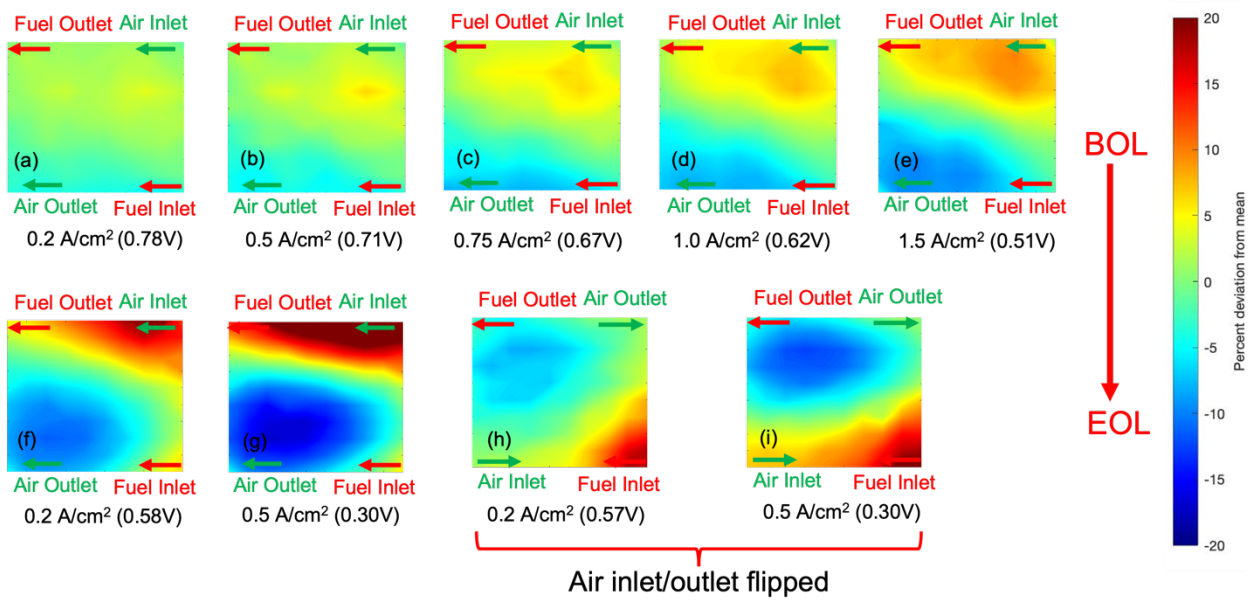


Figure 3.5. CDD measured at the BOL ((a) to (e)) and EOL ((f) to (i)) for CC AST. (h) and (i) represent the EOL distributions with the flipped air inlet and outlet as compared to (f) and (g). All the distributions were recorded at T_{cell} = 80 °C, $\lambda_{H_2}/\lambda_{Air}$ = 1.5/2, and $RH\%_{\,A/C}$ = 100/100 with $P_{abs\,A/C}$ = 150/150 kPa. The operating current densities and the corresponding cell voltages are mentioned at the bottom of each distribution. The color scale bar on the right represents the percentage deviation of the local current from the mean.

support. Due to the presence of N_2 at the cathode during voltage cycling, heat and water generation were expected to be absent. However, slight variations in humidity could arise due to differences in liquid water saturation (for fully humidified inlets) within the diffusion media from the cathode inlet to the outlet [86]. This non-uniform humidification has the potential to cause spatial heterogeneity in carbon corrosion of the support, as water plays a key role as an oxidant in the electrochemical oxidation of carbon [41]. To investigate this hypothesis, the CDDs were recorded with the air inlet and outlet flipped while keeping the fuel inlet and outlet unchanged. Flipping the fuel inlet and outlet is expected to have minimal impact on the spatial current distributions, as the fully humidified pure H_2 flow at the anode is unlikely to affect them significantly. The resulting configuration is depicted in panels (h) and (i) of Figure 3.5. Interestingly, the polarization performance remained consistent; however, the current distributions flipped and aligned with the oxygen depletion path. Specifically, higher current regions were observed closer to the air inlet, while lower current regions appeared near the outlet. These sharp current gradients confirm severe mass transport limitations caused by flooding in the catalyst layer due to pore structure collapse and loss of hydrophobicity. Based on the evidence that the current distributions followed the oxygen depletion path even with the flipped air inlet and outlet locations, while exhibiting only slight spatial variation compared to the unflipped configuration, it can be concluded that carbon corrosion in a fully humidified H_2/N_2 environment proceeds more or less uniformly.

To gain further insights into the flooding behavior and mass transport limitations associated with the CC AST case, current distributions were recorded using underhumidified or unsaturated inlet reactant streams. Figure 3.6 presents these CDDs at the BOL and EOL stages. At the BOL, the maximum local current region was observed in the middle portion of the active area, where the hydration of the ionomer and membrane is optimal (panels (a) and (d) in Figure 3.6), due to the balance of electroosmotic drag and back diffusion of water. Interestingly, at the EOL, the current distributions aligned with the oxygen depletion path (panels (e) and (f) in Figure 3.6). The physical degradation of the CCL, characterized by porosity loss, compaction, and loss of hydrophobicity due to carbon corrosion, renders it more susceptible to flooding and mass transport losses. Even a small amount of water, only a few hundredths of a milligram per square centimeter of the active area in the catalyst layer, can severely limit polarization performance and result in steep current gradients [171]. Comparing the EOL performance between Figure 3.5 and 6, it is apparent that the

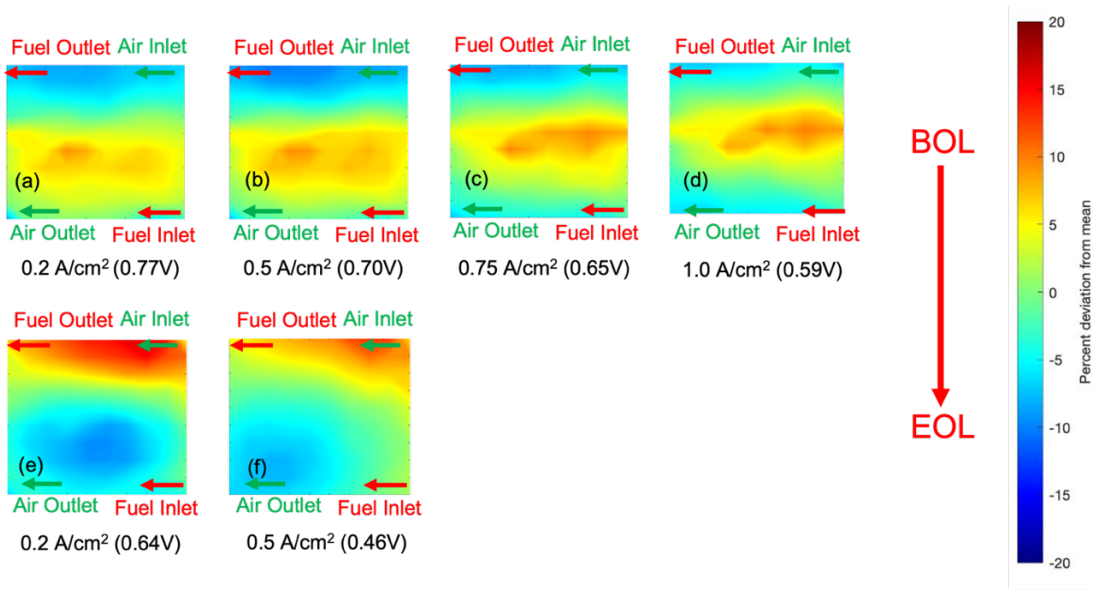


Figure 3.6. CDD measured at the BOL ((a) to (d)) and EOL ((e) and (f)) for CC AST under dry inlet conditions ($RH\%_{\,A/C} = 50/50$). All the distributions were recorded at T_{cell} = 80 °C, $\lambda_{H_2}/\lambda_{Air}$ = 1.5/2, and $RH\%_{\,A/C} = 50/50$ with $P_{abs\,A/C}$ = 150/150 kPa. The operating current densities and the corresponding cell voltages are mentioned at the bottom of each distribution. The color scale bar on the right represents percentage deviation of the local current from the mean.

current gradients are smaller for underhumidified inlets than fully humidified inlets, leading to improved polarization performance. The reduction in open pore volume for liquid water removal from the catalyst layer exacerbates mass transport limitations. However, some of these limitations are mitigated when there is less overall water content in the cell, as indicated by the preceding discussion.

The panels (a) to (e) in Figure 3.7 and 8 illustrate the CDD measured at the BOL (fully humidified air and H_2 inlets) for the Pt AST-Wet and Pt AST-Dry cases, respectively. These distributions are comparable to those presented in Figure 3.6. Across both the AST cases, a consistent trend of increasing non-uniformity in CDD at the BOL is observed as the geometric current densities increase from low (0.2 A/cm^2) to high (1.5 A/cm^2) values. Similar to the CC AST case, local regions with higher and lower currents are identified at the air inlet and outlet, respectively. Interestingly, at the EOL (panels (f) to (j) in Figure 3.7 and Figure 3.8), only minor variations are observed in the spatial current distributions for both the Pt AST-Wet and Pt AST-Dry cases, despite the higher voltage losses observed in Pt AST-Wet. Specifically, at higher current densities (0.75 A/cm^2 to 1.5 A/cm^2), the current gradients slightly intensify at the air inlet and outlet compared to the BOL for both AST cases. This finding contrasts with the behavior observed in the CC AST case at the EOL, where steep current gradients were observed. The minor variations observed in the spatial current distributions for both the Pt AST-Wet and Pt AST-Dry cases can be attributed to negligible changes in the physical properties of the CCL, owing to the voltage range (0.6 to 0.95 V vs. RHE) chosen for cycling. The performance decay is primarily due to the ECSA loss through Pt dissolution and redeposition in the ionomer phase.

When comparing the current distributions at equivalent geometric current densities, where the amount of electrochemically generated water is the same and other parameters are held constant, any changes observed at the EOL across different AST cases primarily reflect alterations in the mass transport properties of the catalyst layers. In essence, the CDDs can be utilized as a quantitative measure to assess how the distribution of reactants and the ability to remove excess water from the catalyst layers have evolved with aging. Notably, despite a significant difference in the loss of ECSA between the Pt AST-Wet (approximately 60% ECSA loss) and Pt AST-Dry (around 25% ECSA loss) cases, there is only a minor variation in the current distributions at the EOL. This finding challenges the conventional notion that ECSA alone is a reliable indicator of

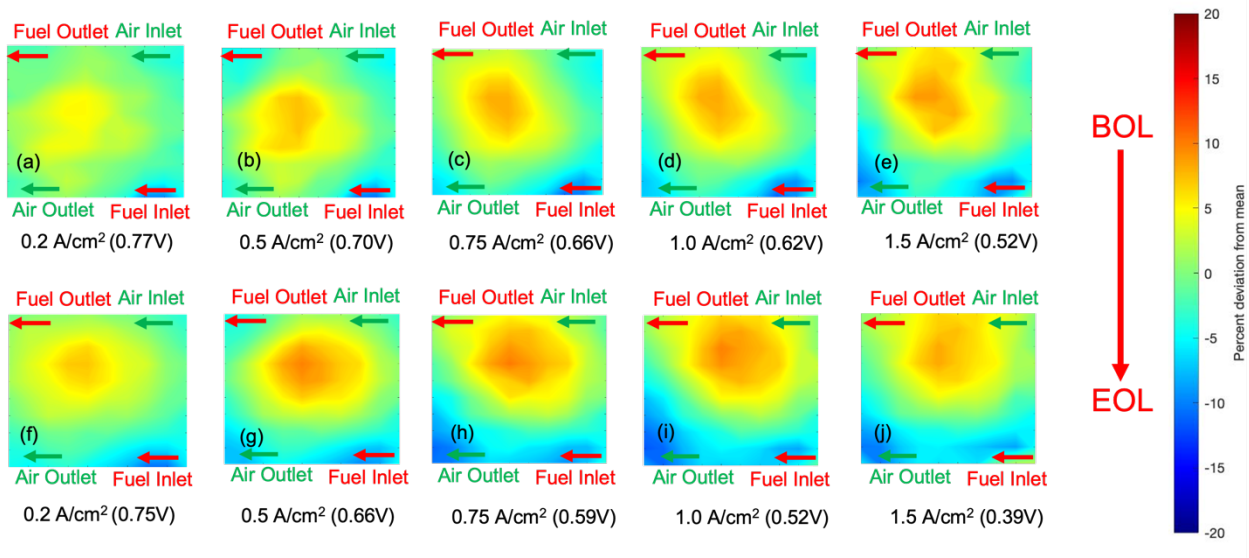


Figure 3.7. CDD measured at the BOL ((a) to (e)) and EOL ((f) to (j)) for Pt AST-Wet. All the distributions were recorded at T_{cell} = 80 °C, $\lambda_{H_2}/\lambda_{Air}$ = 1.5/2, and $RH\%_{\,A/C} = 100/100$ with $P_{abs\,A/C}$ = 150/150 kPa. The operating current densities and the corresponding cell voltages are mentioned at the bottom of each distribution. The color scale bar on the right represents the percentage deviation of the local current from the mean.

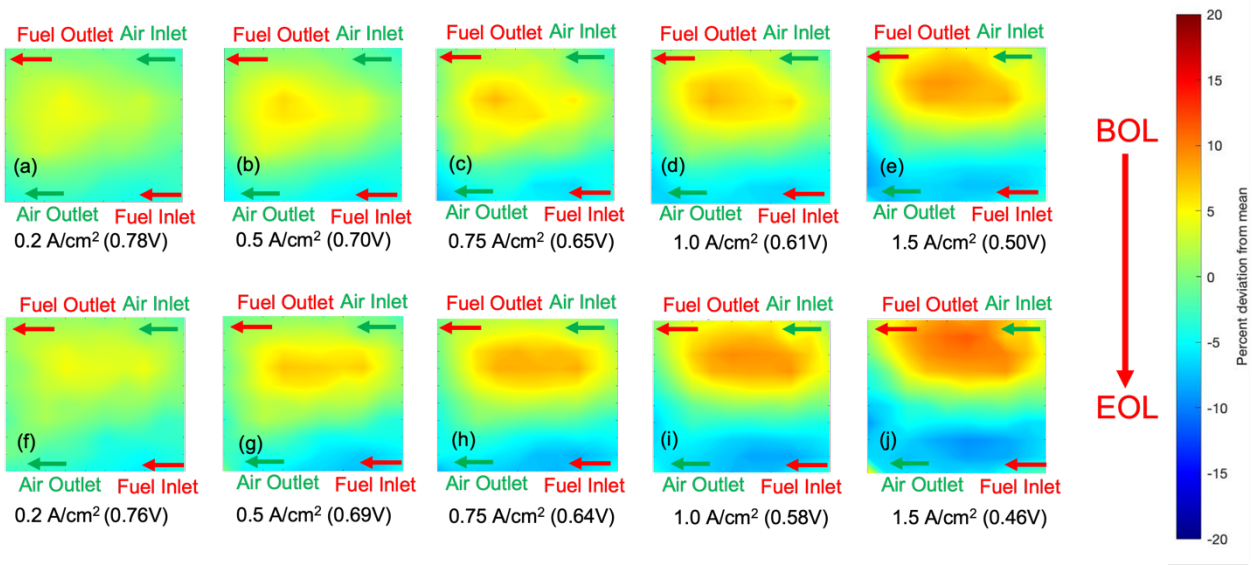


Figure 3.8. CDD measured at the BOL ((a) to (e)) and EOL ((f) to (j)) for Pt AST-Dry. All the distributions were recorded at T_{cell} = 80 °C, $\lambda_{H_2}/\lambda_{Air}$ = 1.5/2, and $RH\%_{\,A/C}$ = 100/100 with $P_{abs\,A/C}$ = 150/150 kPa. The operating current densities and the corresponding cell voltages are mentioned at the bottom of each distribution. The color scale bar on the right represents the percentage deviation of the local current from the mean.

the fuel cell's health during aging as determined by ASTs. Instead, it highlights the crucial role of mass transport properties in shaping the local current distributions after an AST. Gaining a comprehensive understanding of these local distributions is a major step toward enhancing our knowledge of the various degradation mechanisms that can impact fuel cell durability. It also enables the evaluation of different fuel cell operational strategies and the identification of "benign" operating conditions. The attainment of a more uniform current distribution can serve as a marker for assessing durability since steep current gradients may indicate membrane thinning and/or reaction starvation. This enhanced understanding will contribute to designing and developing robust materials for highly durable fuel cells.

In summary, the CDDs for the CC AST, Pt AST-Wet, and Pt AST-Dry cases demonstrate distinct characteristics. While CC AST shows significant changes in current distributions and strong current gradients at the EOL, the Pt AST-Wet and Pt AST-Dry cases exhibit relatively minor variations in the spatial current distributions despite substantial ECSA loss. These findings emphasize the importance of reactant and water distribution in influencing local current distributions and underscore the need to consider additional factors beyond ECSA as indicators of fuel cell health during aging.

For a more comprehensive comparison of the current distributions at the EOL for different AST cases, the 2-D raw current distributions are converted into 1-D distributions. These 1-D distributions are obtained by averaging the currents in ten segments in a specific row, and the row-wise average is then plotted from the air inlet to the outlet. The data presented in Figure 3.9 illustrate the 1-D distributions at a geometric current density of 0.5 A/cm^2 (total current of 12.5 A). Figure 3.9 shows that the Pt AST-Wet and Pt AST-Dry cases exhibit only minor deviations from the profile at the BOL from the air inlet to the outlet. The row-wise averages of segment currents vary between approximately 0.11 A and 0.13 A for both Pt AST-Wet and Pt AST-Dry cases. In contrast, the CC AST case shows significant deviations from the BOL profile, with row-wise averages of segment currents ranging from approximately 0.155 A to 0.093 A along the path from the air inlet to the outlet. Notably, the region of the lowest current aligns with the gradients observed in panel (g) of Figure 3.5. As discussed earlier, these strong current gradients in the CC AST case result from severe mass transport limitations. Similar deviations in current distributions at the EOL were observed by Spernjak et al. [72] in a cell subjected to carbon corrosion AST with a microporous layer.

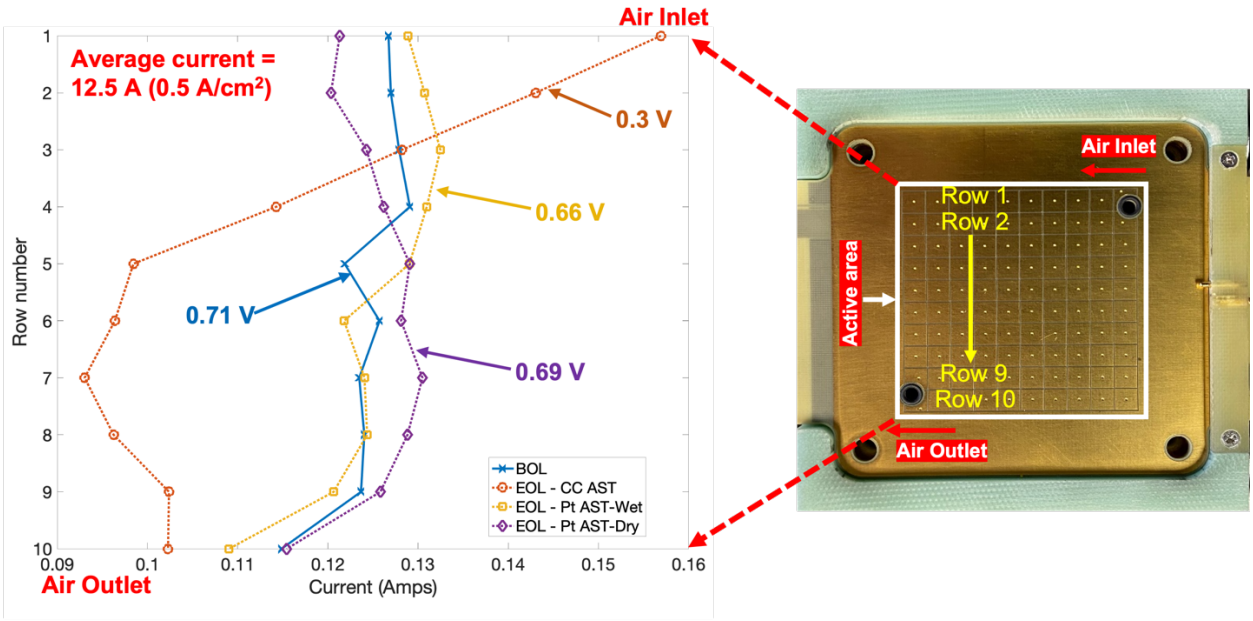


Figure 3.9. One-dimensional (1-D) current distributions at the BOL and EOL for CC AST, Pt AST-Wet and Pt AST-Dry at the average current density of 0.5 A/cm^2. All the distributions were recorded at T_{cell} = 80 °C, $\lambda_{H_2}/\lambda_{Air}$ = 1.5/2, and $RH\%_{\,A/C}$ = 100/100 with $P_{abs\ A/C}$ = 150/150 kPa. Each point on the plot (row number vs. current) from the air inlet (top-right) to the outlet (bottom-left) is a row-wise average of 10 current segments as shown in the figure on the right. The cell voltages at the BOL and EOL for different ASTs at 0.5 A/cm^2 are marked with the arrows.

Furthermore, Figure S3.13 in the Supporting Information for Chapter 3 presents similar 1-D distributions for the CC AST case, comparing the case where the air inlet and outlet are flipped at the EOL. The row-wise averages of segment currents range from approximately 0.105 A to 0.158 A for both the flipped and unflipped cases. Interestingly, the transition from low current to high (or vice versa) occurs around row 5 for both cases, highlighting the uniformity with which carbon corrosion progresses in the H_2/N_2 atmosphere. Overall, the 1-D distributions offer deeper insights into the current deviations observed at the EOL for different AST cases.

Figure 3.10 presents SEM cross-sectional images and corresponding Pt EDS spectra to quantify the morphological changes at the EOL resulting from different ASTs. Panel (a) shows the pristine sample, while panels (b) to (e) depict the aged MEAs. A reinforced polymer membrane, approximately 27 μm thick, with the cathode and anode catalyst layers on the left and right sides, respectively, can be identified in all the cases.

The measurements from SEM cross-sectional images reveal that the thickness of the CCL at the BOL is approximately 6.98 μm ± 0.81 μm. Interestingly, the Pt AST-Wet and Pt AST-Dry cases show negligible changes in CCL thickness within the measurement accuracy, indicating that carbon corrosion was insignificant in the voltage cycling window of 0.6 to 0.95 V vs. RHE. In contrast, the CC AST case (1.0 to 1.5 V vs. RHE) demonstrates significant CCL thinning at the EOL, with a thickness reduction of approximately 25%. This thinning is attributed to the progressive oxidation of amorphous carbon support, leading to the collapse and compaction of the pore structure. Other researchers have reported similar observations investigating carbon support corrosion in fuel cells [41,42,70,72,73,173].

Furthermore, the distribution of Pt in the catalyst layer and membrane exhibits heterogeneity after aging. In the pristine MEA, Pt is uniformly distributed in the cathode and anode catalyst layers. However, at the EOL, apparent variations in Pt distribution are observed among the different AST cases. Specifically, a distinct Pt band near the CCL-membrane interface is visible for the Pt AST-Wet case (panels (d) and (e) in Figure 3.10). The position of this Pt band in the membrane depends on the partial pressure of oxygen and hydrogen streams at the cathode and anode, respectively [174]. As the Pt AST-Wet was conducted in a fully humidified H_2/N_2 environment, the partial pressure of oxygen at the cathode was 0 kPa during the AST, resulting in the Pt band located adjacent to the CCL-membrane interface. This Pt band formation is attributed to the reduction of dissolved Pt ions by the crossover H_2 from the anode.

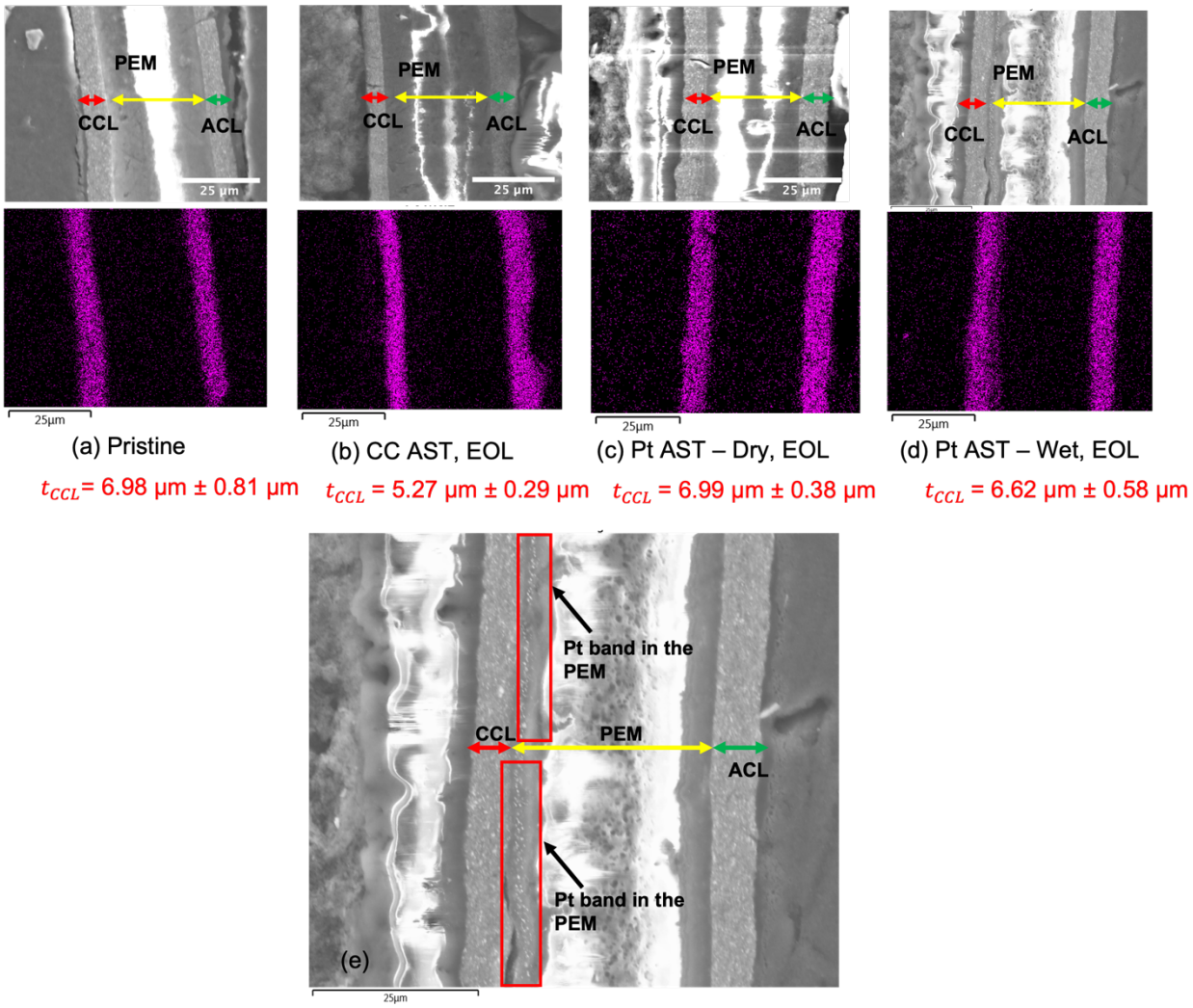


Figure 3.10. Cross-sectional SEM images for the (a) pristine and ((b) to (e)) aged samples for different ASTs along with their respective Pt EDS maps. The average cathode catalyst layer thickness (t_{CCL}) is also mentioned for each case. (e) shows Pt-band formation in the polymer membrane for Pt AST-Wet. In all the images, the cathode catalyst layer (CCL) is on the left, and the anode catalyst layer (ACL) is on the right of the polymer membrane.

The high flux of H_2 crossover, exceeding the flux of dissolved Pt species, leads to an almost complete reduction of Pt ionic species at the CCL-membrane interface [49]. This loss of Pt in the membrane explains the highest ECSA loss at the EOL compared to other AST cases. In contrast, no such Pt band is observed for the CC AST and Pt AST-Dry cases, indicating different mechanisms of ECSA loss. Additionally, within the measurement accuracy, the thickness of the anode catalyst layer (ACL) remains unchanged in the aged samples compared to the pristine sample.

In summary, the SEM cross-sectional measurements align with the observed current gradients in the current distributions for different AST cases. Notably, significant CCL thinning is observed in the MEAs aged with CC AST, while the other AST cases show negligible thinning. A distinct Pt band near the CCL-membrane interface is evident in the Pt AST-Wet case, whereas no such band is observed in other AST cases.

Figure 3.11 presents micro-XRD maps of the 5 cm × 5 cm Pt particle size distribution following various ASTs. Panel (a) represents the pristine sample, while panels (b) to (d) illustrate the aged MEAs. Owing to the MEAs' large active area, they were divided into four 5 cm^2 sections for the micro-XRD measurements. Each section was scanned independently in a 2 mm grid pattern using a 500 μm × 500 μm spot size. These parts were combined to create the complete active area maps depicted in Figure 3.11. A 7-channel serpentine flow field pattern is superimposed on the maps to highlight areas of non-uniform particle growth. Although the 2 mm × 2 mm resolution could not differentiate between the Pt particle growth in the flow field channels and lands, it was adequate to detect variations from the cathode inlet to the outlet across the extensive active area.

The pristine sample has an average particle size of 5.53 nm, corroborated by TEM measurements across various CCL locations (Figure S3.14, Supporting Information for Chapter 3). This pristine sample exhibits a mostly uniform particle size distribution, with slight spatial variations likely from the conditioning process [165]. Post-aging, all AST cases show an increase in average particle size. Notably, the CC AST case exhibits a particle size growth of approximately 35% compared to the pristine sample, probably due to particle coalescence or agglomeration. The Pt particle detachment resulting from the oxidation of the carbon support renders these particles inactive, as indicated by only ~10% ECSA decrease after ~2,000 CC AST cycles (Figure 3.2(a)). It suggests that the remaining Pt particles stayed attached to the graphitic carbon [42]. Pt particle size distribution also remains uniform from the air inlet to the outlet with a standard deviation of

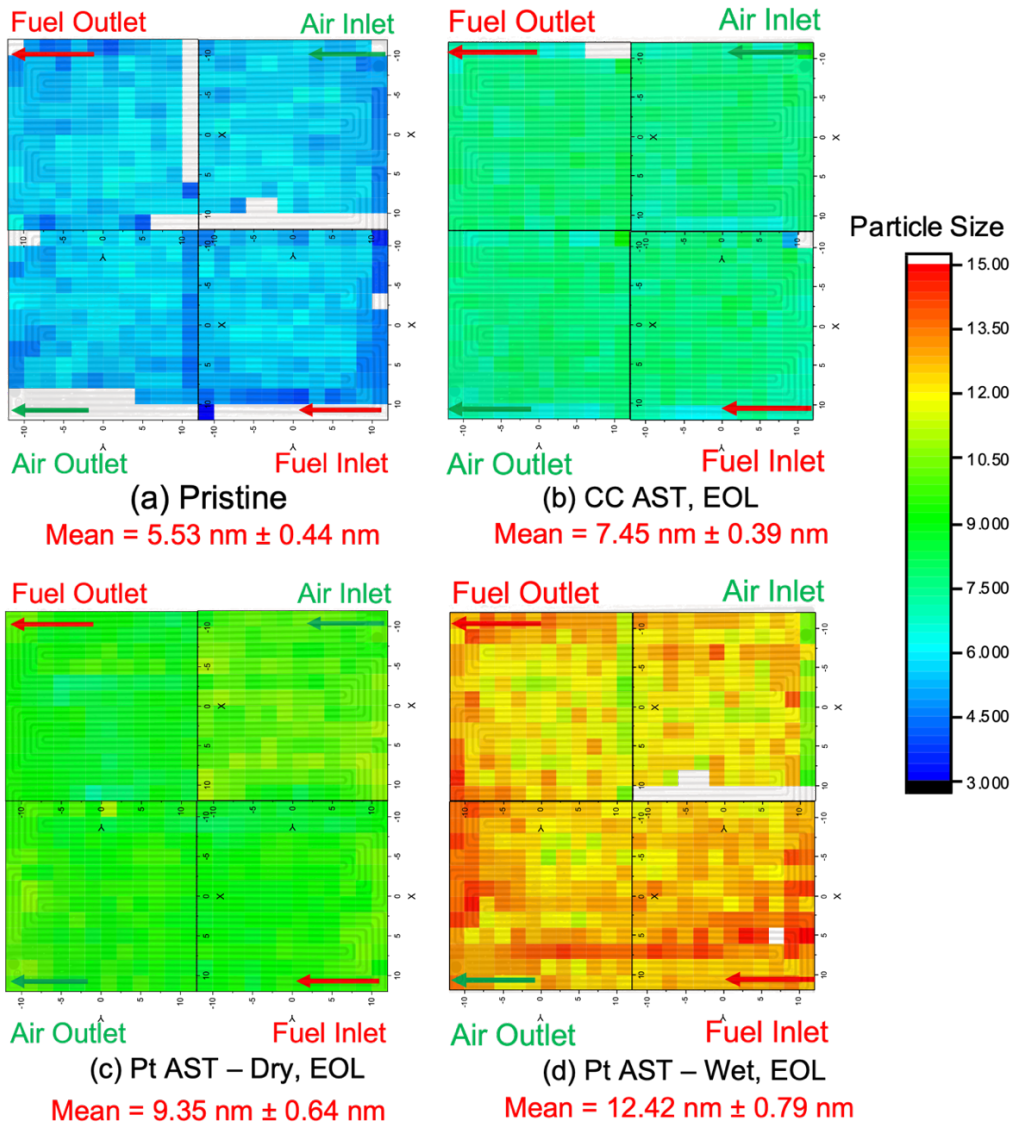


Figure 3.11. 5 cm x 5 cm micro-XRD maps for the (a) pristine and ((b) to (d)) aged samples for different ASTs. The average Pt particle size is also mentioned, along with the standard deviation. Each 5 cm x 5 cm micro-XRD map is stitched from individual 5 cm^2 quadrants. The inlet and outlet regions (superimposed 7-channel serpentine flow field) are marked on the maps along with the color scale bar for Pt particle size on the right.

about 0.39 nm. This consistency at the EOL aligns with observations in Figure 3.5 (panels (h) and (i)), reflecting the uniform carbon corrosion in a fully humidified H_2/N_2 environment.

Figure 3.11 (c) and (d) illustrate the Pt particle size distributions for Pt AST-Dry and Pt AST-Wet cases, respectively. The Pt AST-Dry case shows a 69% average Pt particle size increase from the original case, while the Pt AST-Wet case experiences a dramatic increase of 124%. These significant differences at the EOL are attributed to the higher net water content in the Pt AST-Wet case, intensifying electrochemical Ostwald ripening. Under higher humidity (Pt AST-Wet case), the enhanced ionic conductivity and thin water films promote rapid Pt particle agglomeration and ECSA loss. This difference in particle size growth aligns with the cumulative ECSA loss seen in Figure 3.2. For instance, Pt AST-Dry, with a 69% particle size increase, retains about 75% ECSA at the EOL, whereas Pt AST-Wet, with a 124% increase, retains only 40% ECSA. Khedekar et al. [92] made similar observations where particle size growth for the N_2 Dry case was significantly less than for the N_2 Wet case. Spatial heterogeneity in Pt particle size growth also increases with net water content. Notably, for the Pt AST-Wet case, the particle size growth is higher at the air outlet than at the inlet. This heterogeneity in Pt particle size growth is most likely due to non-uniform humidification from the flow field inlet to the outlet [109]. Recently, Sharma et al. [115] have demonstrated that local humidity variations due to temperature gradients can occur during an AST in a H_2/N_2 atmosphere, resulting in heterogeneous Pt particle size growth.

The Pt AST-Wet case also shows higher particle size growth under the serpentine flow field bends, likely due to liquid water accumulation in these areas. This preferential accumulation of liquid water has been previously confirmed using neutron imaging for similar serpentine flow field architectures [17,109,112,175,176]. Even though water is not electrochemically generated during H_2/N_2 cycling, liquid water saturation can still occur in the diffusion media, especially under the flow field lands [86,109]. The present study is the first to report such preferential growth of Pt particles under the bends for large active areas. Previous studies [92,115,155,156] have shown heterogeneity related to Pt particle size growth but for relatively small active areas (~1 to 5 cm^2).

An advantage of having comprehensive maps of Pt particle size across the full active area is that they can be associated with EOL current distributions. Despite having the smallest average Pt particle size at the EOL in the CC AST case, significant changes and strong gradients in current distributions are observed compared to Pt AST-Wet and Pt AST-Dry cases.

Conversely, despite their larger average Pt particle size and pronounced heterogeneity, the Pt AST-Wet and Pt AST-Dry cases exhibit relatively minor variations in spatial current distributions. These findings demonstrate that EOL current distributions are primarily influenced by the distribution of reactants and water within the cell. They also highlight the importance of considering additional factors beyond ECSA when assessing fuel cell health during aging.

Figure 3.12 summarizes the data from Figure 3.11 for the pristine and aged samples, using kernel-smooth fitting in violin plots to analyze the particle size distributions. The pristine sample shows a mostly unimodal distribution with an average of 5.53 nm. The CC AST retains this unimodal pattern at the EOL, albeit with a higher mean of 7.45 nm. However, the Pt AST-Dry and Pt AST-Wet cases display multimodal distributions due to the variability in Pt particle growth from the air inlet to the outlet, a factor explained earlier. This multimodal pattern results from electrochemical Ostwald ripening, where smaller particles dissolve and reattach to larger ones. Similar multimodal distributions have been reported in previous studies [92,155]. Overall, distinct differences in Pt particle size distribution after aging are evident across the various AST cases.

Figure 3.13 illustrates the temperature distribution maps at the BOL and EOL for different AST cases at a geometric current density of 0.5 A/cm^2. It should be noted that the measured temperature is more representative of the cathode flow field than the catalyst layer since the sensor plate is located between the cathode flow field and the backing plate. A comparison of the BOL temperature distributions in panels (a), (c), and (e) highlights the superior temperature control achieved in this study via independent coolant baths. The temperature remains within a close ~1°C range of the set value of 80°C. Interestingly, the center of the active area is slightly warmer than the edges, a finding also reported by Peng et al. [160] in a study on a commercial-size PEFC plate.

At the EOL, the Pt AST-Wet and Pt AST-Dry cases show only minor changes in their spatial temperature distributions compared to the BOL. However, the CC AST case exhibits a noticeably different spatial temperature distribution at the EOL, with the hotter region shifting closer to the air inlet rather than the center of the active area. Despite this change, the absolute temperature variation remains within ~2°C of the set value of 80°C. This shift in temperature distribution aligns with the high current density region observed near the air inlet at the EOL for the CC AST case in Figure 3.5 (g). Moreover, the warmer area continues to correspond with the high current region, even when the air inlet and outlet were swapped, while the fuel inlet and outlet positions remained unchanged (refer to Figure 3.13 (g)).

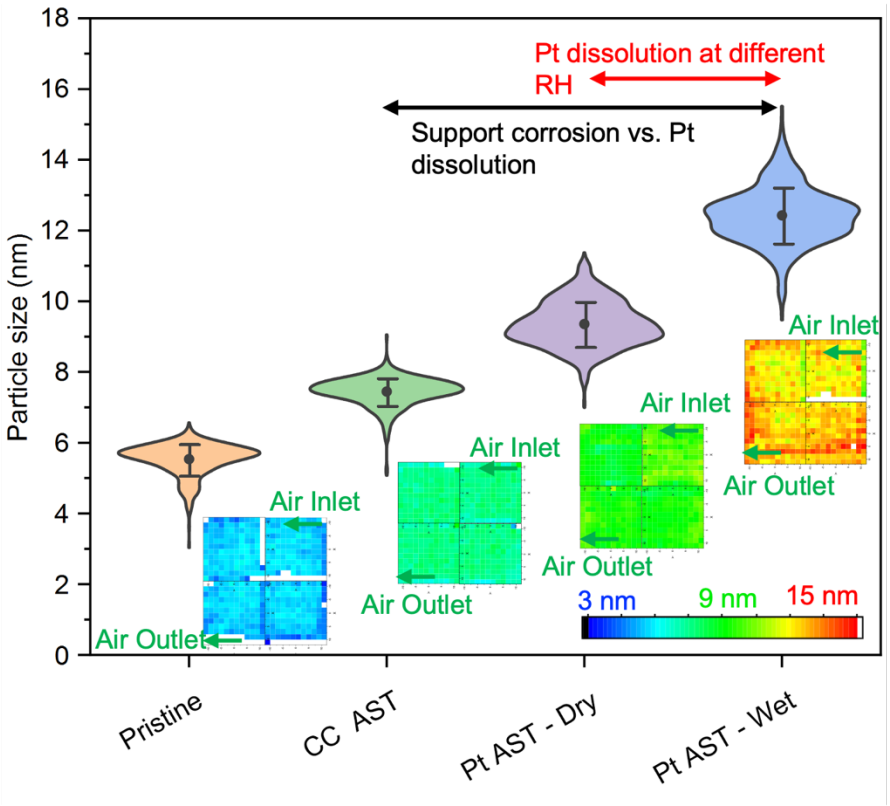


Figure 3.12. Pt particle size distributions for the pristine and aged samples with different ASTs derived from micro-XRD maps. The inset micro-XRD maps serve as a guide to the eye.

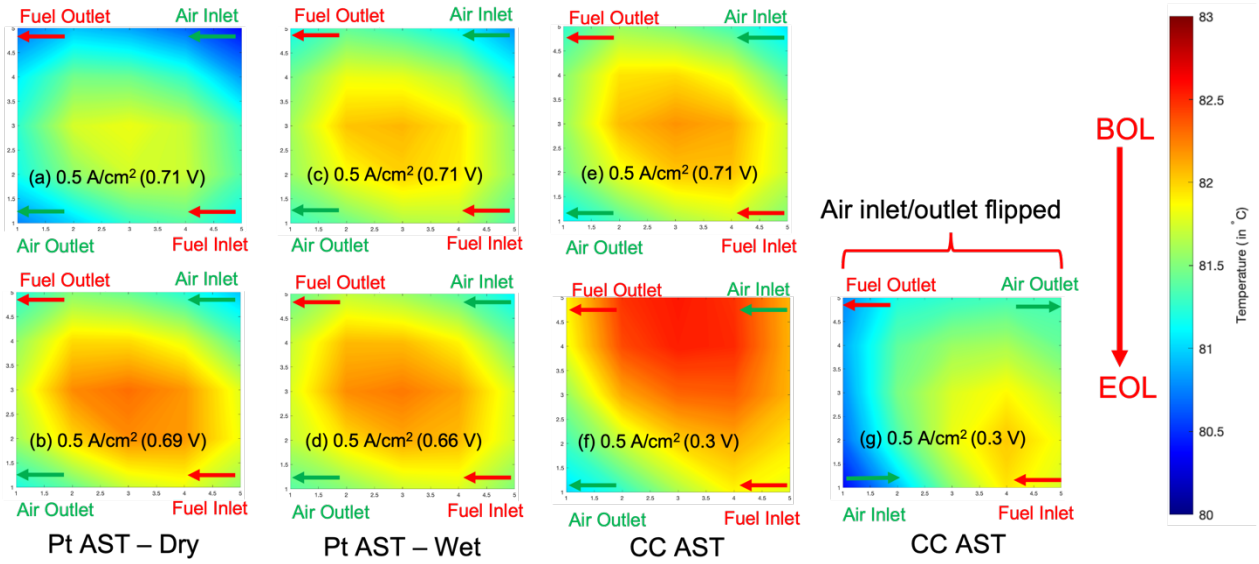


Figure 3.13. Temperature distributions at the BOL (top panel) and EOL (bottom panel) for ((a) and (b)) Pt AST-Dry, ((c) and (d)) Pt AST-Wet, and ((e) to (f)) CC AST at 0.5 A/cm^2. All the distributions were recorded at T_{cell} = 80 °C, $\lambda_{H_2}/\lambda_{Air}$ = 1.5/2, and $RH\%_{\,A/C}$ = 100/100 with $P_{abs\,A/C}$ = 150/150 kPa. (g) is the temperature distribution for CC AST with the flipped air inlet and outlet as compared to (f). The cell voltages at 0.5 A/cm^2 for different ASTs are also mentioned. The color scale bar on the right shows the measured temperature (°C) in the segments.

The changes in temperature distributions for the CC AST case at the EOL are likely due to much higher overpotential (higher waste heat generation) compared to Pt AST-Wet and Pt AST-Dry cases.

3.5 Conclusions

The present study examined heterogeneous aging patterns in current, Pt particle size, and temperature distributions after different accelerated stress tests (ASTs). The chosen conditions simulated carbon corrosion (CC AST) and Pt particle size growth in both fully humidified (Pt AST-Wet) and underhumidified (Pt AST-Dry) H_2/N_2 environments. Multimodal characterization techniques such as in-situ current and temperature mapping, along with full active area micro-XRD maps, enabled the study of the impact of accelerated aging on local cell performance and morphological changes.

At the EOL, ECSA losses occurred in all MEAs, with differing rates and mechanisms. The ECSA losses ranged from about 25% for Pt AST-Dry to roughly 60% for Pt AST-Wet. With regard to polarization performance loss at EOL, the most significant performance degradation was evident in the CC AST case, where nearly ~250 mV loss at a low geometric current density of 0.25 A/cm^2 occurred, mainly due to mass transport restrictions. The Pt AST-Dry case experienced a lower performance loss than the Pt AST-Wet case, likely owing to a smaller cumulative ECSA loss.

Interestingly, while the CC AST demonstrated considerable changes in current distributions and strong current gradients, the Pt AST-Wet and Pt AST-Dry cases showed only minor variations, despite substantial ECSA loss. This finding challenges the conventional belief that ECSA alone can indicate fuel cell health. This investigation also revealed that carbon corrosion in a fully humidified H_2/N_2 environment proceeds relatively uniformly, and mass transport properties significantly shape the local current distributions post-AST. Furthermore, supporting these observations, SEM cross-sectional measurements revealed substantial catalyst layer thinning in the MEAs exposed to CC AST, while others showed negligible thinning. A distinct Pt band near the CCL-membrane interface was visible in the Pt AST-Wet case but absent in the other AST cases. The average Pt particle size after aging for CC AST, Pt AST-Dry, and Pt AST-Wet increased by around 35%, 69%, and 124%, respectively, as determined from the full active area micro-XRD maps. Notably, the larger average Pt particle size in the Pt AST-Wet and Pt AST-Dry cases did not result in significant variations in current distributions. This finding re-emphasizes the need to consider additional factors beyond ECSA for fuel cell health assessment.

Moreover, a higher particle size growth under the serpentine flow field bends in the Pt AST-Wet case was observed, possibly due to liquid water accumulation. This study is the first to report such a preferential growth of Pt particles under bends for large active areas. Despite the smallest average Pt particle size at EOL in the CC AST case, this case demonstrated strong gradients in current distributions compared to the other cases.

Lastly, at EOL, the Pt AST-Wet and Pt AST-Dry cases showed only minor changes in spatial temperature distributions compared to the BOL. The CC AST case presented a shift in the hotter region closer to the air inlet. However, the absolute temperature variation stayed within ~2°C of the set value of 80°C.

Overall, this study provides critical insights into the heterogeneous aging patterns of a PEFC under different ASTs. It is evident that mass transport properties, morphological changes, and humidity conditions significantly influence fuel cell performance following the ASTs. Our research indicates that the degradation in the performance of aged MEAs is more closely tied to species distribution than to the growth of Pt particle size. While the ECSA loss has been recognized as an important contributor to fuel cell aging, this study underscores that ECSA loss is not the sole determinant of fuel cell health; instead, a complex interplay of several aspects shapes a PEFC's overall performance and durability. For enhanced durability and uniform current distributions in a PEFC, it is crucial to avoid high potential excursions (>1 V vs. RHE).

Chapter 4: Path-Dependent Degradation in High-Performance Polymer Electrolyte Fuel Cells (PEFCs)

This chapter will not be published as a stand-alone article prior to submission of my ETD; therefore, a publication statement is not included. The content of this chapter (full or in part) will be submitted for a publication authored by Preetam Sharma, Lei Cheng, Douglas Aaron, Shirin Mehrazi, Jonathan Braaten, Nathan Craig, Christina Johnston, and Matthew M. Mench.

My contributions to this work include conceptualization of the idea, collection, reduction, and analysis of the data and manuscript preparation. Lei and Shirin helped with in-house micro-XRD and SEM measurements. Other authors assisted with data curation, review and editing of the manuscript.

4.1 Brief introduction/abstract

This study investigates the path-dependent degradation in polymer electrolyte fuel cells (PEFCs) using two accelerated stress test (AST) protocols derived from the U.S. Department of Energy (DOE) guidelines. The first protocol, PtfCC AST, involved 15,000 cycles of square-wave voltage cycling (0.6 - 0.95 V vs. reversible hydrogen electrode, RHE) followed by 2,500 cycles of triangular-wave voltage cycling (1.0 - 1.5 V vs. RHE). The second protocol, CCfPt AST reversed the order of execution of triangular- and square-wave cycling. The tests were conducted in a fully humidified nitrogen environment at the cathode. Multimodal characterization techniques, including spatially resolved current distribution and post-mortem micro-X-ray diffraction (micro-XRD) platinum (Pt) particle size mapping, revealed significant differences in degradation patterns. Different polarization performance (spatially distributed and averaged), electrochemically-active surface area (ECSA) loss, morphological changes, and Pt particle size maps of the active area at the end-of-life (EOL) for the same cumulative stress cycles indicate path dependency of degradation in PEFCs for the two tested protocols and the set of materials. The findings from this study highlight the complex interplay of degradation mechanisms, which are crucial for improving PEFC durability and predictive health monitoring in real-world applications with irregular cycling patterns.

4.2 Method of approach

4.2.1 Materials and test equipment

A test cell with 25 cm^2 active area, supplied by balticFuelCells GmbH (Hagenower, Germany) was utilized for this study. The quick connect fixture (qCf) composed of identical 7-channel serpentine flow fields on both the anode and the cathode, with a pneumatically-controlled cell compression mechanism. A pneumatically-controlled cell pressure of approximately 1.0 MPa

provided a GDL compression of roughly 20%. The cell temperature was controlled using two independent cooling loops, supplied with deionized water from two precisely temperature-controlled refrigerated water-baths (VWR International, USA). The coolant flow rate was set to a maximum value of 22 L/min for maintaining temperature uniformity. The materials used in this study comprised of catalyst-coated (Pt/C, 40 wt.% Pt on Vulcan carbon) Nafion XL membranes (manufactured by DuPont) and Sigracet SGL 22BB GDLs. The catalyst layers at the anode and cathode had a nominal Pt loading of 0.3 mg_{-Pt}/cm^2. All the catalyst coated membranes (CCMs) and the gas diffusion layers (GDLs) were purchased from the Fuel Cell Store, Bryan, Texas. A Scribner Associates, Inc. (Southern Pines, NC) fuel cell test station and a Biologic SP-240 potentiostat were used to control the operating conditions, including cell voltage and current.

A printed circuit board manufactured by S++® Simulation Services (Germany) was used for measuring the current density distributions (CDD). The CDD board consisted of 100 electrically isolated current measurement segments, each measuring 5 mm × 5 mm. This segmented CDD board was positioned between the cathode flow field and the backing plate. It is important to mention that the only segmented component in the cell assembly was the CDD board. Consequently, a minor lateral current spread is expected in the CDD data. However, due to very thin flow fields (each 3 mm) used in this study, smearing of the CDDs is expected to be minimal [98,161,162].

Furthermore, uniform cell compression was verified using a Fujifilm Prescale® Super Low pressure measurement film. Uniform cell compression is a crucial factor for accurate CDD measurements. The CDDs were acquired in parallel with the polarization data at a sampling frequency of 2 Hz, and averaged over a minimum period of 60 seconds for each operating condition once a steady state was established. More details regarding the CDD hardware, data acquisition system, and data reduction procedure employed in this study can be found in a previous publication by the authors [153]. For brevity, the CDD maps in this study are presented as the smoothed contours of the percentage deviation from the mean current to identify local regions of high or low current than the mean. These smoothed CDD maps are corrected for minor ohmic variations, following the procedure outlined in a previous publication [153].

4.2.2 AST combinations to explore path-dependence

To explore the path-dependence of degradation modes in PEFCs, two distinct AST combinations derived from the U.S. DOE aging protocols were executed in a fully humidified (100

% RH) H_2/N_2 (anode/cathode) environment [55]. The cell temperature was held at 80 °C with atmospheric back pressure for both the AST combinations.

The first AST combination, referred to as PtfCC AST, involved subjecting the cell to 15,000 cycles of a square-wave voltage profile AST ranging from 0.6 to 0.95 V vs. RHE, followed by 2,500 cycles of a triangular-wave voltage profile AST ranging from 1.0 to 1.5 V vs. RHE. Each potential step was held for 3 seconds during the square-wave voltage profile AST. In the second AST combination, referred to as CCfPt AST, the execution sequence of the square-wave and triangular-wave ASTs was reversed, starting with 2,500 cycles of triangular-wave AST, followed by 15,000 cycles of the square-wave AST. The total number of voltage cycles for both AST combinations was 17,500. All other conditions were kept identical for both the AST combinations, including constant flow rates of H_2 (4 sccm/cm^2) and N_2 (8 sccm/cm^2) at the anode and cathode, respectively. The voltage was ramped at 500 mV/s between the potential steps. The test conditions are summarized in Table 4-1 and Figure 4.1 illustrates the voltage profiles utilized for the AST combinations. The square-wave voltage profile AST induces Pt particle size growth through Pt dissolution and redeposition (electrochemical Ostwald ripening), and the triangular-wave AST leads to carbon support corrosion. Combining these two ASTs is expected to yield any interaction or accelerating factors between different modes of Pt loss in an operating PEFC. The selection of the number of cycles for each AST type used in this study aligns with the recommendations from the U.S. DOE. To evaluate cathode electrocatalyst durability in a PEFC, the DOE suggests 30,000 cycles of square-wave AST, and roughly 5,000 cycles of triangular-wave AST for assessing catalyst support durability. To investigate the path-dependent degradation and interactions of different modes, we start with a combination of ASTs using half the number of cycles suggested by the DOE for electrocatalyst and support durability protocols. A vital consideration in studying the path-dependence is to ensure that the cumulative number of cycles remains the same for each AST combination tested.

4.2.3 In-situ electrochemical characterization

Before testing, all the MEAs were subjected to an identical break-in/conditioning protocol involving 160 voltage cycles in an H_2/air atmosphere at 80°C, 100% RH, and 150 kPa (absolute) backpressure at both the anode and cathode. The cell voltage cycled between 0.8, 0.6, and 0.3 V with a 30-second hold at each potential. Throughout this conditioning procedure, H_2/air

Table 4-1. Test conditions for PtfCC and CCfPt ASTs

Test case	Inlet RH at the anode and cathode (%)	Cell temperature (°C)	H_2/N_2 flow rate (sccm/cm^2)	AST waveform and potential limits	AST cycles	Gauge Backpressure (atm)
PtfCC AST	100	80	4/8	SW (0.6 V – 0.95 V) followed by TW (1.0 V – 1.5 V)	17.5k	0
CCfPt AST	100	80	4/8	TW (1.0 V – 1.5 V) followed by SW (1.0 V – 1.5 V)	17.5k	0

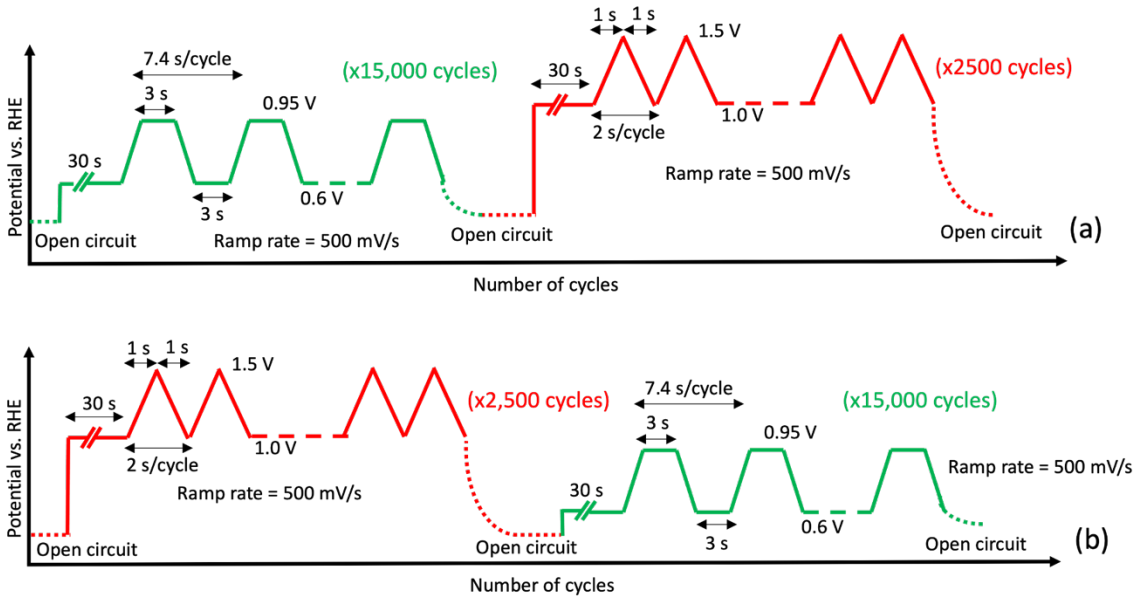


Figure 4.1. (a) PtfCC AST, and (b) CCfPt AST voltage profiles used in the present study. A total of 17,500 cycles were executed for each AST combination.

stoichiometry was maintained at 1.5/2 with minimum flow rates of 100 and 350 sccm at the anode and cathode, respectively. Cyclic voltammograms (CVs) and linear sweep voltammograms (LSVs) were conducted in a fully humidified H_2/N_2 (anode/cathode) environment at 80°C under atmospheric backpressure. CVs were recorded within the range of 0.1 V to 0.9 V vs. RHE at a scan rate of 50 mV/s. The hydrogen desorption region in the CVs was integrated numerically to estimate ECSA. For H_2 crossover current estimation, LSVs were carried out in the voltage range of 0.05 V to 0.7 V vs. RHE at a scan rate of 2 mV/s. The average limiting current density within the voltage range of 0.3 V to 0.35 V was used to estimate H_2 crossover current. During both CV and LSV measurements, H_2 and N_2 flow rates were maintained at 4 and 8 sccm/cm², respectively.

Polarization curves and galvanostatic electrochemical impedance spectroscopy (EIS) measurements were performed in an H_2/air atmosphere at 80°C, 100% RH, and 150 kPa (absolute) backpressure at both the anode and cathode. Polarization curves were also recorded under relatively dry inlet conditions, i.e., with an inlet RH of 50% at both the anode and cathode. During these measurements, H_2/air stoichiometry was maintained at 1.5/2 with minimum flow rates of 100 and 350 sccm at the anode and cathode, respectively. For the electrochemical impedance spectroscopy (EIS) measurements, a perturbation with an amplitude equal to 5% of the DC was applied, and the frequency was swept from 0.1 Hz to 10 kHz at a rate of 7 points per decade. The EIS data were fitted using an equivalent circuit model described in previous publications [72,153] to extract different voltage losses. The polarization curves were obtained by sweeping the cell current from approximately 2 A/cm^2 to 0 A/cm^2, with a 4-minute hold time for each current density. The high frequency resistance (HFR) was measured at a single frequency (3,800 Hz) for each current hold. To ensure consistent and repeatable measurements, the cell was maintained under identical starting conditions before recording a polarization curve. Each AST combination, i.e., PtfCC AST and CCfPt AST case, was tested with at least three different MEA samples, and the reported average performance includes one standard deviation as the error about the mean. The error bars are plotted as lines with filled areas about the mean.

4.2.4 Ex-situ post-mortem characterization

To obtain cross-sectional scanning electron microscopy (SEM, JEOL JSM-7200F) images after aging, an area of about 1 cm × 1 cm was carefully cut from the inlet and outlet regions of each 25 cm^2 MEA.

These 1 cm × 1 cm MEA sections were then sandwiched between a flat aluminum plate and conductive carbon tape. This assembly was mounted in an epoxy (EpoxiCure™ 2 Epoxy Resin (20-3430-128) with Epoxy Hardener (20-3432-032) from Buehler) and successively polished/sanded to expose the cross-sections using low to high-grit sandpaper from 320 to 1200 grit. Energy dispersive spectroscopy (EDS, Oxford) was employed to map the elemental distribution, particularly the Pt band in the ionomer. Both SEM and EDS analysis were conducted at 15 KeV accelerating voltage.

For the post-mortem micro-X-Ray diffraction (micro-XRD) measurements, a Bruker D8 Advance X-ray diffractometer equipped with a Cu K_α radiation source (1.5406 Å) and a Bruker LYNXEYE XE detector was utilized. Alignment of the samples was achieved with an *xyz* moving sample stage featuring a double-laser unit. The measurements were conducted with an accelerating voltage and current set at 40 kV and 40 mA, respectively. XRD scans spanned a range between 37.5° and 42° (2θ), with a step size of 0.03° and a 2.5-second duration per step. Data processing and analysis were carried out using GSAS-II [125]. The 25 cm^2 active area MEAs were cut into four 5 cm^2 quadrant pieces to fit on to the XRD sample stage. Each of these 5 cm^2 sections was raster scanned with a step size of 2 mm in both the *x* and *y* directions, utilizing a spot size of 500 µm × 500 µm. Following mapping of all four quadrants, the XRD mappings were combined to represent the entire 25 cm^2 active area. It is important to mention that the micro-XRD maps include Pt particles from the anode. However, after an AST, overall particle size growth is dominated by the cathode and not the anode, as the potential of the anode is maintained close to 0 V vs. RHE. Therefore, the changes in Pt particle size for the anode in all the AST cases are expected to be minimal. More details on the micro-XRD can be found in a previous publication [155].

4.3 Results and discussion

As a note, the error bars are presented as the filled areas about the mean in the plots to follow in this section. Figure 4.2(a) shows the normalized ECSA loss in PtfCC and CCfPt AST cases as a function of AST cycles. Absolute ECSA values for both cases are provided in Figure S4.15 in the Supporting Information for Chapter 4. The hydrogen desorption region in the CVs was integrated numerically to estimate ECSA. It can be seen from Figure 4.2(a) that PtfCC AST results in approximately 74% ECSA loss compared to BOL at EOL, while CCfPt AST shows around 61% ECSA loss for the same number of cumulative AST cycles (17,500 cycles).

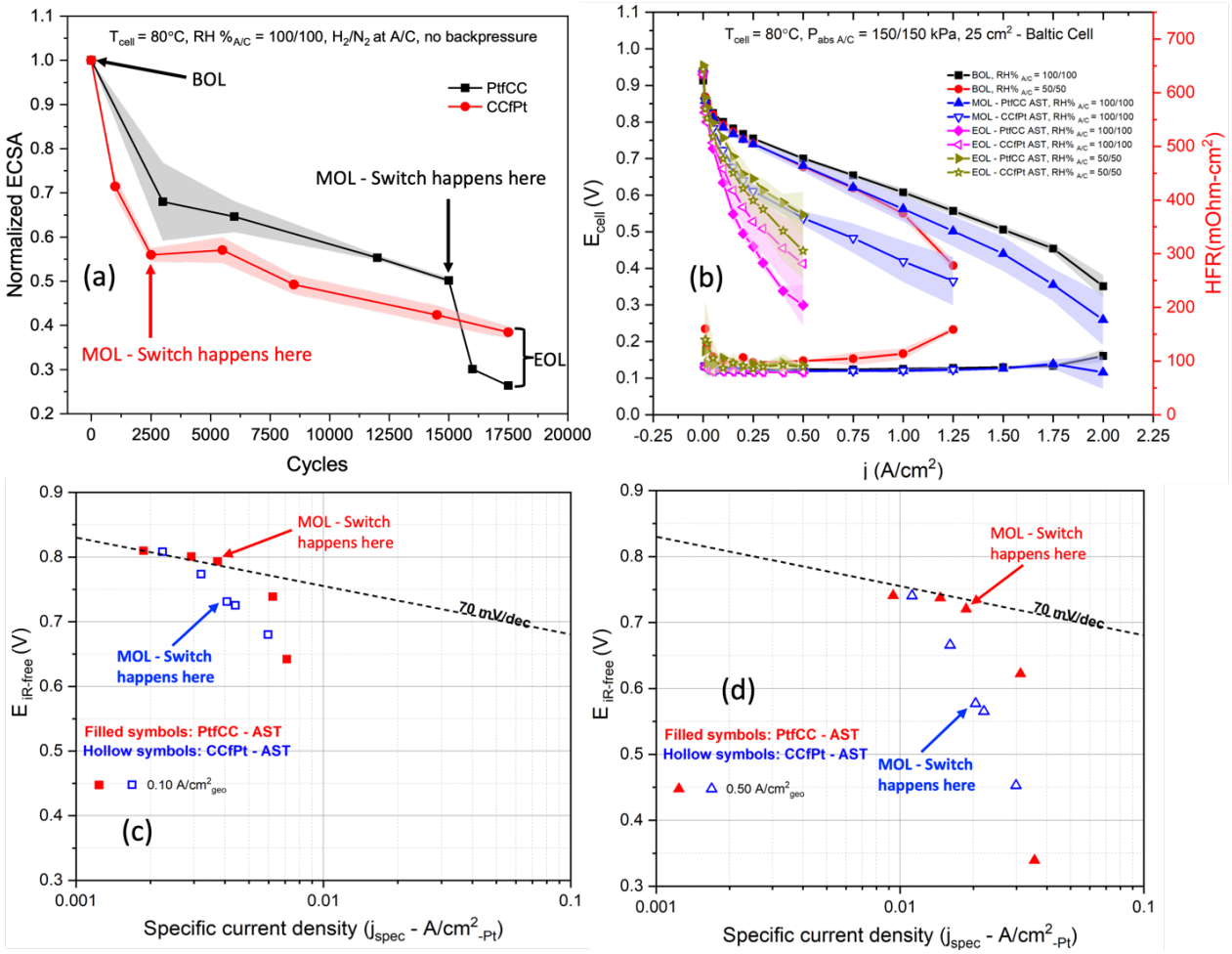


Figure 4.2. (a) Normalized ECSA versus number of AST cycles for PtfCC and CCfPt ASTs measured under fully humified ($RH\%_{A/C}$ = 100/100) H_2/N_2 (anode/cathode) atmosphere at a cell temperature (T_{cell}) of 80 °C with no backpressure. (b) Polarization curves of the MEAs at the BOL, MOL, and EOL for both the AST combinations used in this study. Panels (c) and (d) show the iR-free cell voltage as a function of specific current density at the geometric current densities of 0.1 A/cm^2 and 0.5 A/cm^2, respectively. Polarization conditions include T_{cell} = 80 °C, H_2/air stoichiometry ($\lambda_{H_2}/\lambda_{Air}$) of 1.5/2, $RH\%_{A/C}$ = 100/100 and 50/50 with a backpressure ($P_{abs\,A/C}$) of 150 kPa (absolute) on both the anode and cathode.

In the PtfCC AST, an initial rapid ECSA loss of approximately 32% compared to the BOL value occurs within 2,500 cycles. This loss is attributed to intensified electrochemical Ostwald ripening, wherein smaller Pt nanoparticles dissolve due to high surface energy (Gibbs-Thomson effect) and redeposit on larger particles or precipitate in the ionomer/membrane phase [8,48,49]. Although dissolution and redeposition of Pt ions may dominate ECSA loss in the early cycling phases, direct migration and coalescence of Pt nanoparticles cannot be ruled out [8]. Between 2,500 and 15,000 cycles, ECSA loss stabilizes, likely because a "quasi" stable average particle size is attained, resisting further dissolution. However, after 15,000 cycles (Middle-of-life, MOL), a sudden increase in ECSA loss occurs, likely due to carbon support corrosion within the voltage cycling window of 1.0 V to 1.5 V vs. RHE. Carbon support corrosion can cause Pt nanoparticle detachment from the support, rendering them electrochemically inactive [41,42,70,71]. Therefore, the primary reason for the sudden ECSA loss after 15,000 cycles in the PtfCC AST is likely Pt nanoparticle detachment, despite the particles reaching a relatively stable size.

In contrast, for the CCfPt AST, an initial rapid ECSA loss of approximately 43% compared to BOL occurs within the first 2,500 triangular-wave cycles. This loss is likely due to rapid oxidation of the amorphous carbon support, leading to Pt particle detachment [41,42]. Subsequently, after 2,500 cycles (MOL), when voltage cycling transitions to square-wave (0.6 V to 0.95 V vs. RHE), ECSA loss stabilizes, reaching a cumulative loss of approximately 61% at the EOL.

Interestingly, the ECSA loss during the carbon corrosion phase (1.0 V to 1.5 V vs. RHE) of PtfCC AST (~47% compared to MOL) is comparable to the ECSA loss during the same phase in CCfPt AST (~43% compared to BOL). However, the catalyst corrosion phase (0.6 V to 0.95 V vs. RHE) in PtfCC AST is more aggressive, resulting in approximately 50% ECSA loss compared to BOL, while CCfPt AST shows around 31% ECSA loss compared to MOL in the same phase. We hypothesize that since the "orphaned" Pt nanoparticles due to carbon support corrosion are electrochemically inactive, the electrochemical Ostwald ripening process is drastically slowed down or even eliminated in some cases [8,48]. The extent of electrochemical Ostwald ripening is influenced by factors such as particle size and distribution, the conductivity of the catalyst support in the catalyst layer, and the ionic conductivity of the ionomer in the catalyst layer [8,46,48,49,78,177,178]. Following carbon corrosion, the redistribution of ionomer may leave some particles either uncovered or excessively covered, leading to an increase in ionic resistance within the catalyst layer. Hence, the ECSA loss due to the catalyst corrosion phase in CCfPt AST is less

aggressive than in the PtfCC case. These observations highlight the complex interplay of degradation mechanisms in determining the overall ECSA loss.

Figure 4.2(b) illustrates the polarization performance with H_2/air at the BOL, MOL, and EOL stages for AST cases under wet (100% RH) and dry (50% RH) conditions. Detailed polarization curves during various intermediate aging stages for both AST cases are provided in Figure S4.16 of the Supporting Information for Chapter 4. From Figure 4.2(b), noticeable differences in wet and dry polarization performance at the EOL are observed for both PtfCC and CCfPt AST cases. For instance, at 0.5 A/cm^2 under wet conditions, MEAs subjected to PtfCC AST experienced a voltage loss of approximately 400 mV at the EOL, whereas those subjected to CCfPt AST had a loss of about 290 mV. Interestingly, under dry conditions, the performance loss trend is reversed, with a higher voltage loss (~230 mV) observed for the CCfPt AST case compared to the PtfCC case (~130 mV loss). These differences under wet and dry operating conditions are consistent across various geometric current densities. A comparison is made at 0.5 A/cm^2 because the MEAs did not exhibit stable polarization performance beyond this point at the EOL, especially under wet conditions.

In the PtfCC AST, voltage losses after the catalyst corrosion phase, i.e., the initial 15,000 cycles, can be primarily attributed to the reduction in ECSA due to potential cycling. With the MEAs losing approximately 50% of ECSA compared to BOL at this stage, there is likely a corresponding increase in Pt area-specific mass transport overpotential. This increase in mass transport overpotential is exacerbated at higher geometric current densities, where voltage losses are limited by reactant and product transport rather than purely kinetic losses. This trend in performance loss has been reported in previous studies [56,115,130,153]. Once the voltage cycling in the PtfCC AST shifts to the carbon corrosion phase, a significant voltage loss (~380 mV) at 0.5 A/cm^2 at the EOL compared to MOL under wet conditions is observed. This dramatic loss is likely due to flooding in the catalyst layer caused by pore structure collapse and decreased hydrophobicity. Carbon corrosion leads to Pt particle detachment from the support, rendering them inactive electrochemically. Additionally, due to aggressive voltage cycling, carbon corrosion causes pore structure collapse in the catalyst layer, making it difficult for liquid water to be removed from the catalyst layer. A notably better performance (~250 mV higher than the wet condition at 0.5 A/cm^2) under dry conditions at the EOL for PtfCC AST supports the flooding hypothesis of the catalyst layer. Under dry conditions, water retention in the catalyst layer keeps

the membrane hydrated, preventing excessive ohmic losses. It is important to note that Pt area-specific mass transport losses are further exacerbated during the carbon corrosion phase of PtfCC AST, as there is approximately a 47% further loss in ECSA during this phase [38,167].

During the carbon corrosion phase of CCfPt AST, the voltage drop (compared to BOL) under wet conditions is approximately 2.2 times smaller than in the PtfCC case (compared to MOL) during the same phase. This significant difference in performance under wet conditions could likely be attributed to flooding in the catalyst layer combined with an increase in Pt-area specific mass transport resistance during PtfCC AST. Although the primary nature of losses during the carbon corrosion phase of CCfPt AST is still predominantly due to mass transport resulting from the oxidation of the carbon support, these losses are exacerbated to a lesser extent compared to PtfCC AST at the EOL. Given that the cumulative number of cycles remains the same in both AST cases, the differences in polarization performance at the EOL suggest the interaction of different degradation modes, specifically electrochemical Ostwald ripening during the catalyst corrosion phase versus catalyst support corrosion during the carbon corrosion phase in both AST cases. When carbon corrosion follows catalyst corrosion AST, as is the case in PtfCC AST, the overall voltage losses at the EOL are exacerbated due to the reasons outlined above.

To further probe the nature of polarization losses in both AST cases, the iR-free voltage is plotted against the specific current density (j_{spec}) in Figure 4.2(c) and (d). Panel (c) presents the data at a geometric current density of 0.1 A/cm^2, while panel (d) shows it at 0.5 A/cm^2. The specific current density (j_{spec}) is defined as the ratio of geometric current density to the product of ECSA and Pt loading at a given aging stage, which is also known as the roughness factor. Mathematically, j_{spec} takes the following form [130]:

$$j_{spec}\ (A/cm^2_{Pt}) = \frac{j_{geo}(A/cm^2)}{ECSA\ (m^2_{Pt}/g_{Pt})\times L_{Pt}(mg_{Pt}/cm^2)\times 10} \quad (1)$$

where j_{geo} is the geometric current density, ECSA is the electrochemically active surface area, and L_{Pt} is the Pt loading in the cathode electrode, assuming minimal change in Pt loading during aging, and the performance loss follows Tafel kinetics. The change in oxygen reduction reaction (ORR) overpotential at any given geometric current density can be estimated using the equation [130]:

$$\Delta\eta_{ORR} = \frac{2.303\times RT}{\alpha F} \times log\left\{\frac{(i_o\times ECSA)_{BOL}}{(i_o\times ECSA)_{EOL}}\right\} \quad (2)$$

where i_o is the exchange current density, R is the universal gas constant, T is the temperature, F is Faraday's constant, and α is the cathodic charge transfer coefficient. This equation predicts a kinetic voltage loss of roughly 70 mV at 80 °C for every 10-fold decrease in ECSA. However, additional losses such as mass transport (local oxygen transport resistance and/or ionic resistance through thin ionomer films) can significantly deviate the experimentally measured slope from the purely kinetic Tafel prediction of 70 mV/decade [56,130].

It is worth mentioning that Tafel analysis is typically performed under differential conditions with pure oxygen flow, but the usage of stoichiometric air flow rates over a large active area is not uncommon [92,130,153,155]. In this study, stoichiometric hydrogen and air flow rates are used over a large active area. The validity of this analysis is confirmed by observing the slope of PtfCC AST at geometric current densities of 0.1 and 0.5 A/cm^2 during the catalyst corrosion phase, where losses can be assumed to be mostly kinetic in nature, showing a close proximity to the theoretical value of approximately 70 mV/decade. Moreover, while correcting the cell voltages in Figure 4.2 (c) and (d) for oxygen transport resistance through limiting current measurements would lead to a more accurate comparison, no such correction was made in this study. However, the validity of the Tafel analysis with stoichiometric air flow is already established.

In Figure 4.2(c), prior to transitioning to the carbon corrosion phase in PtfCC AST, the voltage losses primarily stem from kinetic factors due to ECSA loss. The Tafel slope closely aligns with the theoretical 70 mV/decade prediction, indicating minimal mass transport losses. However, significant mass transport losses are observed once the transition occurs, even at a low geometric current density of 0.1 A/cm^2. This observation corresponds with the substantial performance loss observed at the EOL for PtfCC AST, attributed to a combination of catalyst layer flooding and increased Pt area-specific mass transport resistance.

For CCfPt AST, while an initial deviation from the Tafel prediction is seen, the slope remains consistent after transitioning from the carbon corrosion phase to the catalyst corrosion phase. This observation suggests that the mass transport losses incurred during the initial carbon corrosion phase do not worsen in the subsequent catalyst corrosion phase of CCfPt AST. As mentioned earlier, initiating carbon corrosion first leads to Pt nanoparticle detachment from the carbon support and a reduction in pore space for effective water removal from the catalyst layer. Notably, these particles are smaller in size than those in the PtfCC case at MOL, as electrochemical Ostwald ripening is not the primary mechanism of Pt particle size growth in carbon corrosion [41,42].

This argument is supported by a recent study by Sharma et al. [153] where a 35% increase in the average Pt particle size compared to pristine samples was observed for an MEA subjected to carbon corrosion AST. Furthermore, Pt particles after the carbon corrosion phase of CCfPt AST may not have achieved a quasi-stable average size distribution, unlike in PtfCC AST. Therefore, upon transitioning to the catalyst corrosion phase in CCfPt AST, mass transport losses are not exacerbated, and the electrochemical Ostwald ripening of Pt nanoparticles is significantly slowed down. This observation is confirmed by detailed spatially-resolved Pt particle size mapping presented later in this chapter.

In Figure 4.2(d), similar trends in performance loss are observed at a geometric current density of 0.5 A/cm^2 compared to those at 0.1 A/cm^2, albeit with higher overall losses. This increase in losses at higher current densities is attributed to the greater electrochemically generated water, which exacerbates mass transport losses if not promptly removed from the cell.

Figure 4.3(a) and (b) shows the Nyquist impedance spectra for both AST cases at 0.1 and 0.2 A/cm^2. These spectra were recorded at the BOL and EOL for each AST case. These spectra are presented at low geometric current densities due to unstable cell performance at higher current densities at the EOL. To analyze the spectra and extract kinetic (K or R2), ohmic (R1), and mass transport (MT or R3) resistances, an equivalent circuit model was fitted, as illustrated in Figure 4.3(c). More details on this equivalent circuit model can be found in previous publications [72,153]. The individual resistance values extracted through the model fit are provided in Table S4.1 of the Supporting Information for Chapter 4. In Figure 4.3(a) and (b), the kinetic and mass transport resistances are combined and presented as a ratio between the EOL and BOL. This ratio is denoted as $(K + MT)_{EOL}/(K + MT)_{BOL}$. By combining these resistances, a comparison of the relative increase in cell impedance across different AST cases with respect to the BOL can be made.

From Figure 4.3(a) and (b), it can be seen that there is minimal change in the HFR at the EOL compared to the BOL for both AST cases. This observation is consistent with the single-frequency HFR values shown in Figure 4.2(b) alongside the polarization data. At a geometric current density of 0.1 A/cm^2, the lumped kinetic and mass transport (K+MT) impedance increased approximately 3 times for the PtfCC AST case compared to BOL. In contrast, for the CCfPt case, this impedance increased by approximately 1.7 times after the same cumulative cycles.

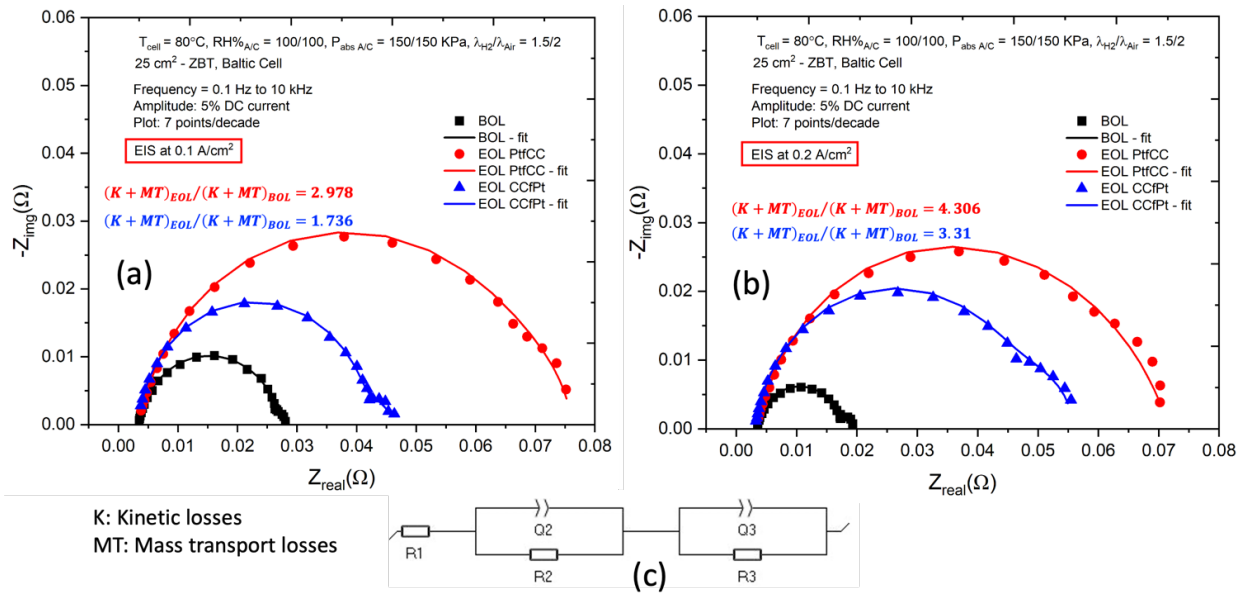


Figure 4.3. EIS spectra measured at the BOL and EOL for PtfCC and CCfPt ASTs at the current densities of (a) 0.1 A/cm^2, and (b) 0.2 A/cm^2. A small current perturbation (5% of DC) was imposed, and the frequency was swept from 0.1 Hz to 10 kHz. Panel (c) shows the equivalent circuit used for fitting the EIS spectra. The ratio of $(K + MT)_{EOL}$ to $(K + MT)_{BOL}$ can be noted from (a) and (b). The EIS spectra were recorded at T_{cell} = 80 °C, $\lambda_{H_2}/\lambda_{Air}$ = 1.5/2, and $RH\%_{A/C}$ = 100/100 with $P_{abs\ A/C}$ = 150/150 kPa.

At 0.2 A/cm^2, these losses exacerbate, with the ratio increasing to approximately 4.3 for PtfCC AST and around 3.3 for CCfPt AST. As the spectra were recorded under fully humidified conditions (100% inlet RH), the increase in lumped resistance aligns with the observed polarization performance loss trends in Figure 4.2(b), where the PtfCC AST case exhibited higher voltage losses at EOL compared to the CCfPt case after the same cumulative cycles. At such low geometric current densities (0.1 and 0.2 A/cm^2), where kinetic losses likely dominate, the higher lumped resistance ratio for the PtfCC AST case compared to the CCfPt case can be attributed to flooding in the catalyst layer caused by pore structure collapse and decreased hydrophobicity. Carbon corrosion induces Pt particle detachment from the support, rendering them electrochemically inactive. Additionally, aggressive voltage cycling during carbon corrosion leads to pore structure collapse in the catalyst layer, hindering liquid water removal from the catalyst layer.

Before discussing the CDDs for AST cases, it is crucial to understand that local current distributions are primarily influenced by factors such as relative humidity, reactant concentration, and liquid water distribution within the cell at a given voltage [95,171]. When air and hydrogen inlets are fully humidified, in-plane current gradients may arise due to oxygen depletion along the cathode flow field channels. Severe current gradients can develop if local flooding occurs at the cathode outlet or in colder spots. Moreover, if the inlets are underhumidified or relatively dry, current distributions are controlled by anode relative humidity. The maximum current is typically generated at locations where the membrane is optimally hydrated, due to the balance between the electroosmotic drag and back diffusion of water [95,171]. In this study, CDDs were captured at the BOL, MOL, and EOL. These distributions are compared at equivalent geometric current densities, ensuring that the electrochemically generated water remains consistent across all cases, with all other operating conditions being identical. It is important to note that the current distributions are shown as deviations from the mean current to highlight areas producing higher or lower currents than the mean.

Figure 4.4 illustrates the CDDs for the PtfCC AST at the BOL, MOL, and EOL. At the BOL (panels (a) to (e) in Figure 4.4), as the current density increases from 0.2 to 1.5 A/cm^2, current gradients emerge from the air inlet to the outlet. Smooth distributions at 0.2 and 0.5 A/cm^2 transition to higher current near the air inlet compared to regions near the outlet. Since these distributions were recorded under fully humidified conditions, they follow the oxygen

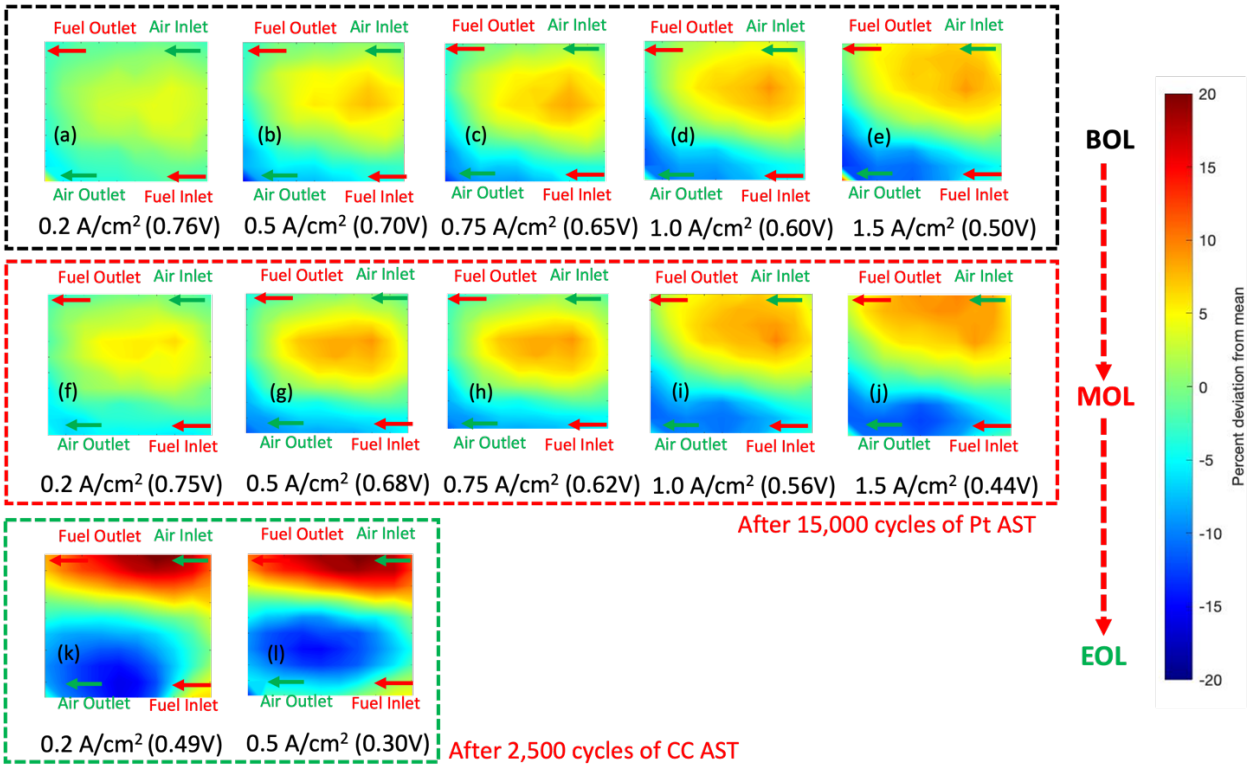


Figure 4.4. CDDs measured for PtfCC AST at different stages during aging. Panels (a) to (e) represent CDDs at the BOL, panels (f) to (j) represent MOL, and panels (k) and (l) represent EOL. All the distributions were recorded at T_{cell} = 80 °C, $\lambda_{H_2}/\lambda_{Air}$ = 1.5/2, and $RH\%_{\,A/C}$ = 100/100 with $P_{abs\ A/C}$ = 150/150 kPa. The cell operating current densities and voltages are marked under each distribution. The color scale bar on the right represents the percentage deviation of the local current from the mean.

depletion path down the cathode channel, where areas closer to the air inlet produce higher currents due to increased oxygen consumption. Accumulation of liquid water near the air outlet impedes oxygen supply to the catalyst layer, resulting in lower current production in areas near the outlet.

At the MOL (panels (f) to (j) in Figure 4.4), minor changes in current distributions are observed despite higher overpotential resulting from accelerated aging. Around 50% of ECSA is lost during this phase of catalyst corrosion, but significant changes in local current distributions are not observed. Sharma et al. [153] reported similar observations, where minor variations in current distributions were observed post-aging despite significant ECSA loss for Pt AST-Wet. However, dramatic changes occur when cycling switches to the carbon support corrosion phase. Panels (k) and (l) in Figure 4.4 depict the CDDs at the EOL for PtfCC AST, showing strong current gradients even at low geometric current densities. Specifically, the current gradients range from approximately +20% to about -15% from the mean. These gradients are likely due to flooding in the catalyst layer caused by pore structure collapse and decreased hydrophobicity. Pooling of liquid water blocks oxygen supply to reaction sites, increasing oxygen transport resistance [38]. Additionally, Pt area-specific mass transport overpotential is exacerbated during the carbon corrosion phase, with a 47% further reduction in ECSA.

CDDs recorded at a lower inlet relative humidity (panel (c) in Figure S4.17 of Supporting Information for Chapter 4) of 50% confirm flooding in the catalyst layer, with current gradients ranging from approximately $\pm$10% from the mean. Better performance under dry conditions at the EOL for PtfCC AST suggests that water retention in the catalyst layer keeps the membrane hydrated, preventing excessive ohmic losses (see Figure 4.2(b)). The drastic current gradients observed at the EOL for PtfCC AST resemble those of the CC AST case in the study by Sharma et al. [153].

Figure 4.5 shows the CDDs for the CCfPt AST at the BOL, MOL, and EOL. At the BOL (panels (a) to (e) in Figure 4.5), the CDDs are comparable to those of PtfCC AST in panels (a) to (e) in Figure 4.4. As the current density increases from 0.2 to 1.5 A/cm^2, current gradients develop from the air inlet to the outlet, following the oxygen depletion path down the cathode channels. At the MOL (after 2,500 cycles of carbon corrosion) for CCfPt AST, significant current gradients emerge, even at relatively low geometric current densities of 0.2 and 0.5 A/cm^2 (panels (f) and (g) in Figure 4.5). At the BOL, the CDDs at these current densities were smooth with only minor spatial variations. The strong current gradients (±15% from the mean) observed after an initial

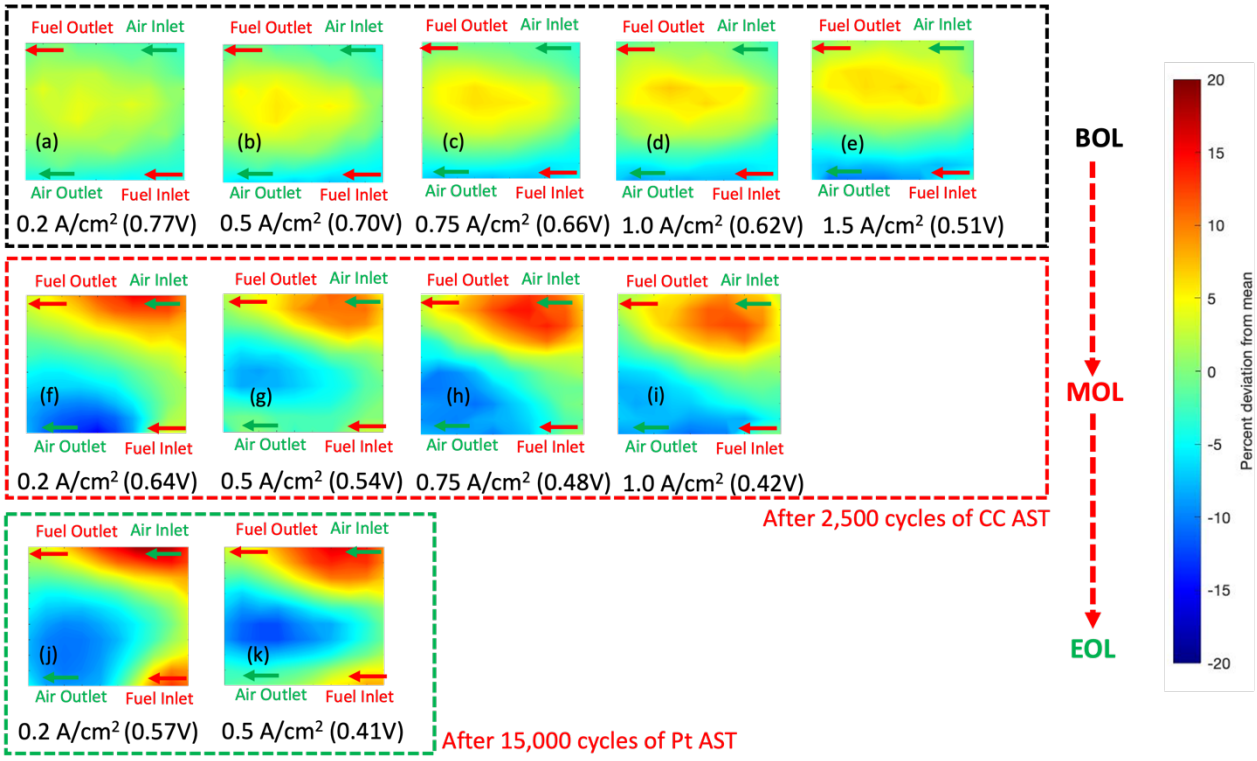


Figure 4.5. CDDs measured for CCfPt AST at different stages during aging. Panels (a) to (e) represent CDDs at the BOL, panels (f) to (i) represent MOL, and panels (j) and (k) represent EOL. All the distributions were recorded at T_{cell} = 80 °C, $\lambda_{H_2}/\lambda_{Air}$ = 1.5/2, and $RH\%_{\,A/C}$ = 100/100 with $P_{abs\ A/C}$ = 150/150 kPa.

rapid ECSA loss of approximately 43% compared to the BOL are likely due to the rapid oxidation of the amorphous carbon support, leading to Pt particle detachment. At the EOL of CCfPt AST, after 15,000 cycles of catalyst corrosion, these strong current gradients persist at geometric current densities of 0.2 and 0.5 A/cm^2 (panels (j) and (k) in Figure 4.5), with an increased overpotential. The cell did not operate stably beyond a geometric current density of 0.5 A/cm^2 at the EOL, so the CDDs for higher current densities are not presented in Figure 4.5. The current gradients at the EOL for CCfPt AST are less severe than those for PtfCC AST after the same number of cumulative cycles. As previously mentioned, upon switching to the catalyst corrosion phase in CCfPt AST, mass transport losses are likely not exacerbated, and the electrochemical Ostwald ripening of Pt nanoparticles is significantly slowed down.

These spatial current distributions correspond to the performance loss trends observed in Figure 4.2. Furthermore, the CDDs recorded at a lower inlet relative humidity (panel (d) in Figure S4.17 of Supporting Information for Chapter 4) of 50% exhibit better performance under dry conditions at the EOL and correlate well with the trends observed in Figure 4.2(b).

Figure 4.6 shows the one-dimensional current distributions at the BOL, MOL, and EOL for both AST cases at an average current density of 0.5 A/cm^2. These distributions are obtained by averaging the raw current data row-wise from the air inlet to the outlet, with each data point representing an average of 10 segments in a row. Presenting data this way helps provide a more comprehensive comparison between different AST cases. At the BOL, the distribution is relatively uniform, with the averaged currents in the segments varying between approximately 0.11 and 0.13 A. At the MOL, the PtfCC AST shows only minor variations in current distribution compared to the BOL. In contrast, the CCfPt AST at the MOL exhibits significant current deviations from the BOL, with average current in the segments ranging from about 0.15 A at the inlet to 0.12 A at the outlet. Lower average current can be observed in the segments closer to the air outlet. At the EOL, the current deviation profile for CCfPt AST is maintained but with a higher overpotential. For the PtfCC AST case, once cycling switches to the carbon corrosion phase, the previously uniform distribution at the MOL shows substantial deviation at the EOL, similar to those of the CCfPt AST. The overpotential is higher for PtfCC AST than for CCfPt AST at the EOL. Previous paragraphs discussed the reasons for these strong current deviations at different stages of the ASTs. Sharma et al. [153] reported similar distribution profiles in a recent publication on catalyst corrosion and carbon support corrosion ASTs.

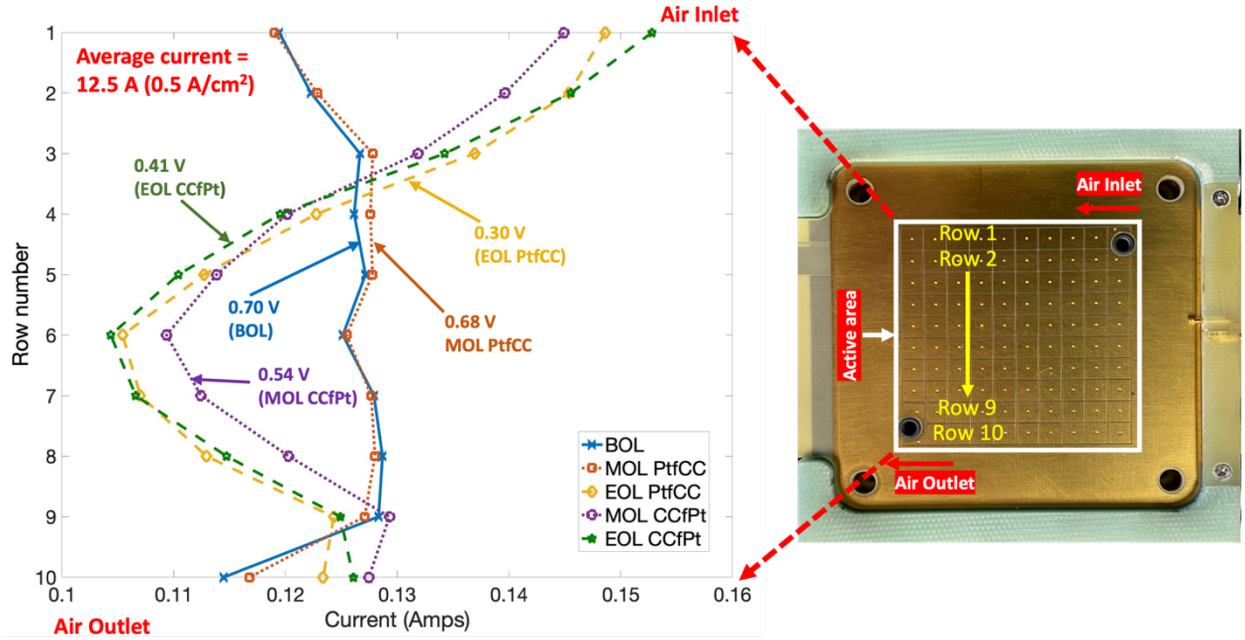


Figure 4.6. One-dimensional (1-D) current distributions at the BOL, MOL, and EOL for PtfCC and CCfPt ASTs at the average current density of 0.5 A/cm^2. Each point on the figure is a row-wise average of 10 current segments on the CDD board. The cell voltages at the BOL and EOL for different ASTs at 0.5 A/cm^2 are marked with the arrows. All the distributions were recorded at T_{cell} = 80 °C, $\lambda_{H_2}/\lambda_{Air}$ = 1.5/2, and $RH\%_{\,A/C}$ = 100/100 with $P_{abs\,A/C}$ = 150/150 kPa.

Figure 4.7 shows the micro-XRD maps of Pt particle size distribution over a 5 cm × 5 cm area for the MEAs aged with different ASTs. Panel (a) depicts the pristine sample, while panels (b) and (c) show MEAs aged with PtfCC and CCfPt ASTs, respectively. Due to the large active area of the MEAs, each sample was divided into four 5 cm^2 sections for the micro-XRD measurements. Each section was scanned individually in a 2 mm grid pattern using a 500 μm × 500 μm spot size. These sections were then combined to create the complete active area maps shown in Figure 4.7. The 7-channel serpentine flow field used in this study is overlaid on the maps to highlight areas of uneven catalyst growth. Although the 2 mm × 2 mm resolution was insufficient to distinguish Pt particle growth within the flow field channels and lands, it was adequate to detect variations from the cathode inlet to the outlet across the large active area.

The pristine sample has an average Pt particle size of 5.53 nm, with a mostly uniform distribution. Minor spatial variations at the BOL are likely due to the conditioning process. At the EOL, MEAs aged with PtfCC and CCfPt ASTs show an increase in average Pt particle size. Specifically, PtfCC AST shows an increase of about 94%, while CCfPt AST exhibits an increase of about 77%. The more significant Pt particle size growth in the PtfCC AST case is likely due to intensified electrochemical ripening during the catalyst corrosion phase compared to the CCfPt AST. In the CCfPt AST case, "orphaned" Pt nanoparticles resulting from carbon support corrosion become electrochemically inactive, significantly slowing down or even eliminating the electrochemical Ostwald ripening process during the catalyst corrosion phase. As previously discussed in this chapter, the extent of electrochemical Ostwald ripening is influenced by factors such as particle size and distribution, the conductivity of the catalyst support, and the ionic conductivity of the ionomer in the catalyst layer. Following carbon corrosion, the redistribution of ionomer may leave some particles either uncovered or excessively covered, leading to an increase in ionic resistance within the catalyst layer [8,46,48,49,78,177,178]. These differences in average Pt particle size growth also correspond to the cumulative ECSA loss observed in the two cases: PtfCC AST loses about 74% ECSA at the EOL, whereas CCfPt AST loses about 61% ECSA.

When the combined ASTs used in this study are compared to previous work by Sharma et al. [153] in Figure 4.7(d), it is evident that the PtfCC and CCfPt AST cases result in more significant catalyst degradation compared to standalone carbon corrosion ASTs and catalyst corrosion AST executed under drier (50% inlet RH) conditions (Pt AST-Dry). The catalyst corrosion AST executed under fully humidified inlet conditions (Pt AST-Wet) shows maximum catalyst growth.

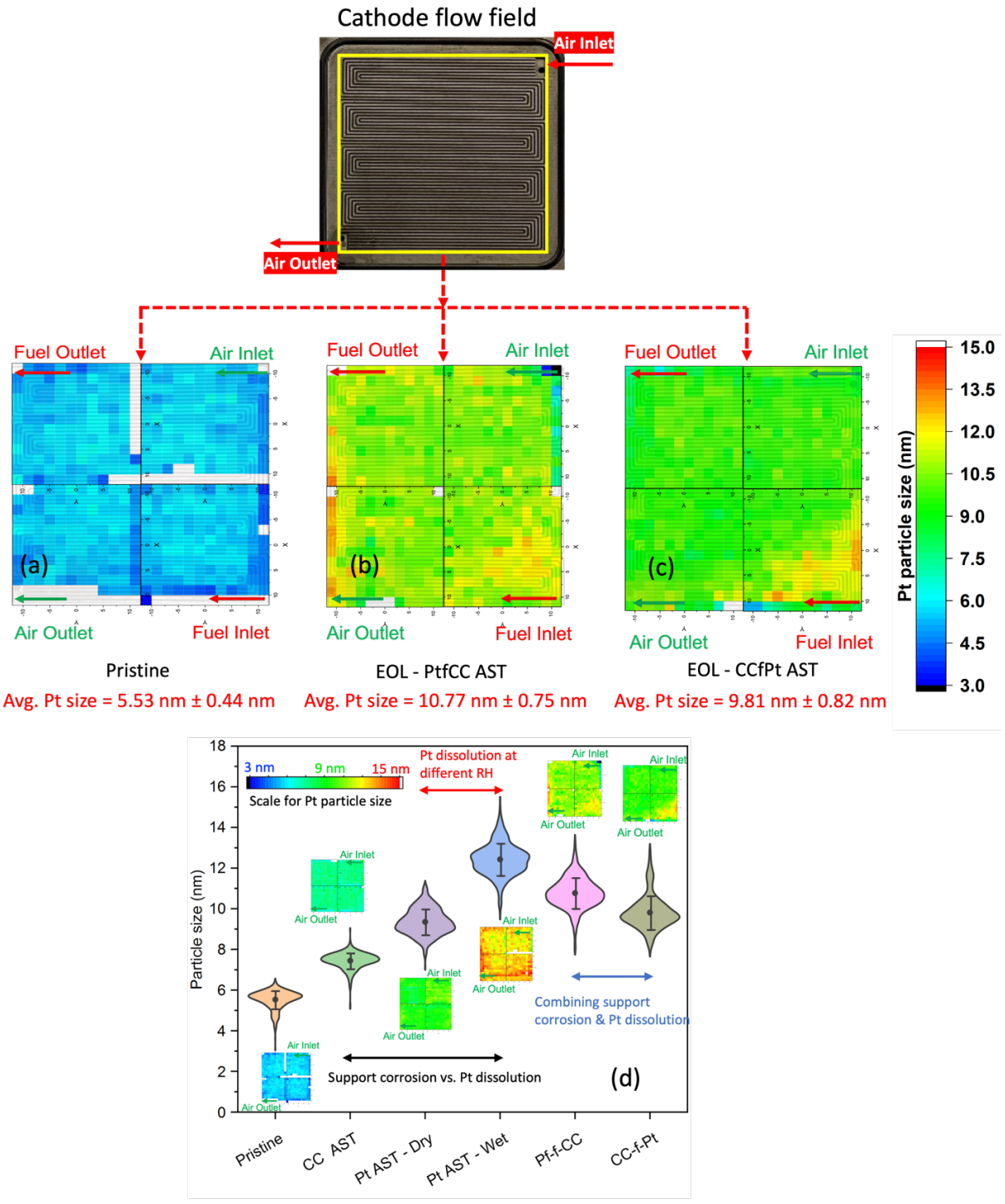


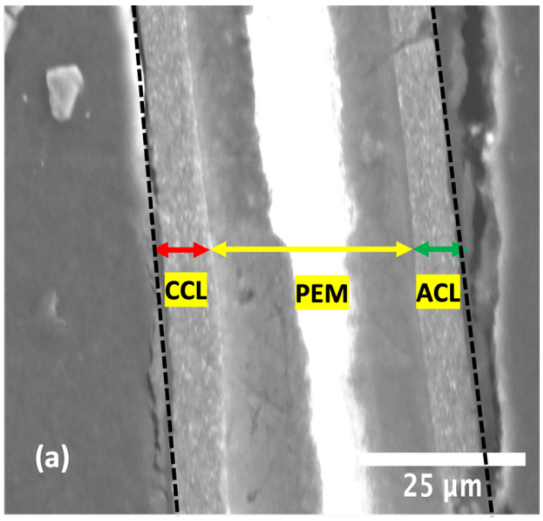
Figure 4.7. Full active area (5 cm x 5 cm) micro-XRD maps for the (a) pristine, (b) EOL PtfCC AST, and (c) EOL CCfPt AST. The average Pt particle size is reported with the standard deviation. Each full active map is constructed by stitching individual 5 cm^2 quadrants that were raster scanned separately. (d) Violin plots of Pt particle size distributions for the pristine and aged samples with different ASTs derived from their respective micro-XRD maps. The data for CC AST, Pt AST-Dry, and Pt AST-Wet is extracted from Sharma et al. [153], and plotted for comparison with PtfCC and CCfPt ASTs studied in this work. The inset micro-XRD maps serve as a guide to the eye.

Figure 4.7(d), summarizes the data from the two-dimensional particle size data into violin plots, fitted with kernel-smooth function. Pristine sample shows a mostly unimodal distribution, whereas all the aged MEAs exhibit multimodal distributions, due to varying degree of catalyst growth from cathode inlet to the outlet. It is important to note that only about 17,500 cycles of PtfCC and CCfPt ASTs were conducted, compared to 30,000 cycles for the standalone catalyst corrosion ASTs and 5,000 cycles for the catalyst support corrosion ASTs in the study by Sharma et al. [153].

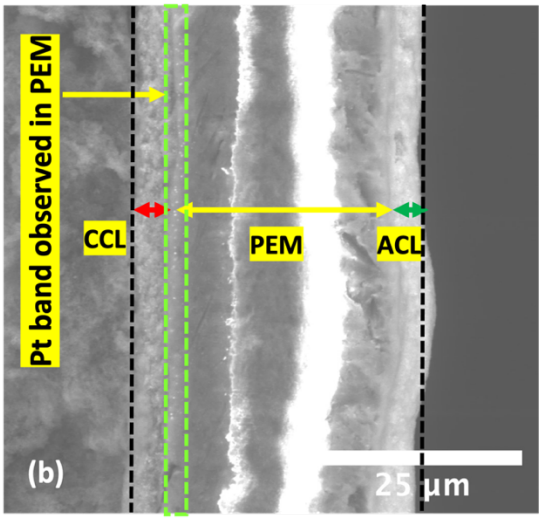
An interesting observation is the higher Pt particle size growth around the serpentine flow field bends in the PtfCC AST case (see Figure 4.7(d)). This more significant catalyst growth could be due to liquid water accumulation around these bends. Sharma et al. [153] also reported similar Pt particle growth around serpentine bends in a catalyst corrosion AST conducted under fully humidified conditions (Pt AST-Wet). In contrast, such heterogeneity in Pt growth is not observed in the CCfPt case, except for a narrow area near the fuel inlet. Since the fuel inlet is fully humidified and water tends to accumulate near the air outlet, this area near the fuel inlet likely experiences higher local humidity than the rest, leading to intensified electrochemical Ostwald ripening [8,48,92,115,153].

Figure 4.8 shows SEM cross-sectional images of MEAs aged with different ASTs used in this study. Panel (a) depicts the pristine sample, while panels (b) and (c) depict MEAs aged with PtfCC and CCfPt ASTs, respectively. In all images, a reinforced polymer electrolyte membrane (approximately 27 μm thick) is clearly visible with the cathode and anode catalyst layers on the left and right sides, respectively.

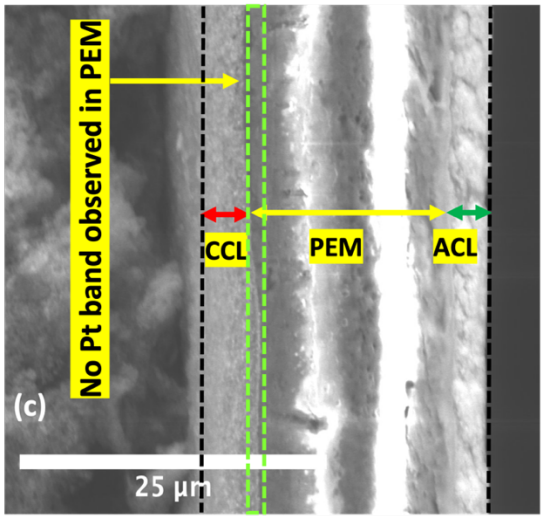
The pristine sample has an average cathode catalyst layer (CCL) thickness of approximately 6.98 μm ± 0.81 μm. Since the anode and cathode catalyst layers were identical in this study, the anode catalyst layer (ACL) has a similar thickness. Furthermore, under the AST conditions chosen in this study, anode degradation is expected to be negligible as the voltage cycling was performed with nitrogen at the cathode and pure hydrogen at the anode. At the EOL, the MEA aged with PtfCC AST shows an approximately 20% reduction in CCL thickness, whereas the MEA aged with CCfPt AST shows negligible changes in CCL thickness within measurement accuracy. The thinning of the CCL in the PtfCC AST case is likely due to aggressive carbon corrosion cycling following the catalyst corrosion phase. This carbon corrosion phase results in pore structure collapse and leads to flooding in the catalyst layer, causing Pt particle detachment from the support and rendering them electrochemically inactive.



Pristine
Avg. CCL thickness = 6.98 µm ± 0.81 µm



EOL – PtfCC AST
Avg. CCL thickness = 5.57 µm ± 1.72 µm



EOL – CCfPt AST
Avg. CCL thickness = 6.37 µm ± 1.15 µm

Figure 4.8. Cross-sectional SEM images for the (a) pristine, (b) EOL PtfCC AST, and (c) EOL CCfPt AST. The average CCL thickness is marked for each case. In all the images, CCL is on the left, and the anode catalyst layer (ACL) is on the right of the polymer membrane (PEM).

The significant performance loss (~380 mV at 0.5 A/cm^2) observed in the PtfCC AST case when voltage cycling shifts to the carbon corrosion phase at EOL, compared to MOL under wet conditions (sown in Figure 4.2(b)), can be linked to flooding resulting from CCL thinning. Additionally, better performance (~250 mV higher than the wet condition at 0.5 A/cm^2) under dry conditions at EOL for the PtfCC AST supports this flooding hypothesis. The steeper current gradients observed in panels (k) and (l) of Figure 4.4 for PtfCC AST, compared to the gradients in panels (j) and (k) of Figure 4.5 for CCfPt AST, also suggest flooding in the catalyst layer due to thinning.

Another interesting feature in Figure 4.8 is the presence of a distinct Pt band near the CCL-membrane interface in the PtfCC AST case. The location of this Pt band within the membrane is influenced by the partial pressures of oxygen at the cathode and hydrogen at the anode [174]. Since the PtfCC AST was conducted in a fully humidified H_2/N_2 environment, the partial pressure of oxygen at the cathode was 0 kPa during the AST, resulting in the Pt band forming adjacent to the CCL-membrane interface. This Pt band formation is attributed to the reduction of dissolved Pt ions by crossover hydrogen from the anode. The high flux of hydrogen crossover, which exceeds the flux of dissolved Pt species, leads to a nearly complete reduction of Pt ionic species at the CCL-membrane interface [49]. In the PtfCC AST, the catalyst corrosion phase precedes the carbon corrosion phase, leading to Pt dissolution and redeposition, which contribute to the heterogeneous distribution of Pt in the membrane. This redistribution of Pt explains the higher ECSA loss at the EOL for PtfCC AST compared to CCfPt AST. Conversely, no such Pt band is observed in the CCfPt AST case, indicating less Pt dissolution and redeposition during the catalyst corrosion phase that follows the carbon corrosion phase.

4.4 Conclusions

In this study, path-dependent degradation in polymer electrolyte fuel cells (PEFCs) was explored using two distinct accelerated stress test (AST) combinations derived from the U.S. Department of Energy (DOE) aging protocols. The first combination, PtfCC AST, involved 15,000 cycles of a square-wave voltage profile from 0.6 to 0.95 V vs. reversible hydrogen electrode (RHE), followed by 2,500 cycles of a triangular-wave voltage profile from 1.0 to 1.5 V vs. RHE. The second combination, CCfPt AST, reversed the sequence. Both combinations totaled 17,500 cycles. Multimodal characterization techniques, such as spatially resolved current distribution and

post-mortem micro-XRD platinum (Pt) particle size maps, were used to establish the path dependency of degradation modes.

The results revealed that PtfCC AST leads to about 74% electrochemically-active surface area (ECSA) loss at the end-of-life (EOL) compared to the beginning-of-life (BOL), while CCfPt AST shows around 61% ECSA loss. During the carbon corrosion phase, ECSA loss in PtfCC AST (~47% compared to middle-of-life, MOL) was similar to CCfPt AST (~43% compared to BOL). However, the catalyst corrosion phase in PtfCC AST was more aggressive, resulting in approximately 50% ECSA loss compared to BOL, while CCfPt AST showed around 31% loss compared to MOL. These findings suggest that "orphaned" Pt nanoparticles, rendered electrochemically inactive due to carbon support corrosion, slow down or eliminate the electrochemical Ostwald ripening process, highlighting the interplay between different degradation modes.

Polarization performance of membrane electrode assemblies (MEAs) under wet and dry conditions showed distinct characteristics. Under wet conditions at EOL, MEAs subjected to PtfCC AST experienced a significant voltage loss (~400 mV at 0.5 A/cm^2), whereas those subjected to CCfPt AST had a smaller loss (~290 mV at 0.5 A/cm^2). Under dry conditions, the trend reversed: CCfPt AST showed a higher voltage loss (~230 mV at 0.5 A/cm^2) compared to PtfCC AST (~130 mV at 0.5 A/cm^2). These differences are attributed to flooding and increased mass transport overpotential in PtfCC AST due to carbon corrosion, which leads to pore structure collapse and Pt particle detachment, whereas CCfPt AST experienced less severe degradation.

The current density distribution (CDD) maps showed that at the MOL, the PtfCC AST case showed minor changes in current density distributions (CDDs) despite significant ECSA loss. However, at EOL, PtfCC AST exhibited significant current gradients due to flooding and pore structure collapse, with gradients ranging from +20% to -15% from the mean, indicating severe performance degradation. In contrast, CCfPt AST showed strong gradients at MOL due to rapid carbon support oxidation but less severe gradients at EOL. The better performance of PtfCC AST under dry conditions at EOL suggests reduced flooding, while CCfPt AST maintained smoother CDDs, highlighting different degradation impacts.

Two-dimensional micro-XRD maps showed that the pristine sample had an average Pt particle size of 5.53 nm with a mostly uniform distribution. At EOL, PtfCC AST showed a significant increase in Pt particle size by about 94%, while CCfPt AST showed an increase of

about 77%. This more significant growth in PtfCC AST is attributed to intensified electrochemical ripening during the catalyst corrosion phase. The CCfPt AST exhibited smaller average Pt particle growth due to "orphaned" Pt nanoparticles becoming electrochemically inactive. Additionally, higher Pt particle size growth was observed around serpentine flow field bends in PtfCC AST, likely due to liquid water accumulation, a heterogeneity not seen in CCfPt AST except near the fuel inlet.

The scanning electron microscopy (SEM) images revealed that the pristine sample had a cathode catalyst layer (CCL) thickness of approximately 6.98 μm ± 0.81 μm, with a similar thickness for the anode catalyst layer (ACL). At EOL, the CCL of the MEA aged with PtfCC AST showed a 20% reduction in thickness, likely due to aggressive carbon corrosion, resulting in pore collapse and flooding, leading to significant performance loss (~380 mV at 0.5 A/cm^2) under wet conditions. In contrast, the MEA aged with CCfPt AST showed negligible changes in CCL thickness. Additionally, a distinct Pt band near the CCL-membrane interface was observed in the PtfCC AST case, attributed to Pt ion reduction by crossover hydrogen, whereas no such band was present in the CCfPt AST case, indicating less Pt dissolution and redeposition.

Overall, this study established the path dependency between different degradation modes (catalyst growth and carbon support corrosion) in a PEFC under equal cumulative stress. Understanding these interactions is crucial as real-world applications exhibit irregular cycling patterns with path-dependent behavior. These findings will aid in improving fuel cell durability and predictive state-of-health monitoring.

Chapter 5: Correlating Catalyst Growth with Liquid Water Distribution in Polymer Electrolyte Fuel Cells (PEFCs)

This chapter will not be published as a stand-alone article prior to submission of my ETD; therefore, a publication statement is not included. The content of this chapter (full or in part) will be submitted for a publication authored by Preetam Sharma, Douglas Aaron, Pierre Boillat, Lei Cheng, Christina Johnston, and Matthew M. Mench.

My contributions to this work include conceptualization of the idea, collection, reduction, and analysis of the data and manuscript preparation. Lei helped with synchrotron micro-XRD measurements. Pierre helped with the neutron imaging experiments at the Paul Scherrer Institut (PSI), Switzerland. Other authors assisted with data curation, review and editing of the manuscript.

5.1 Abstract

This study investigates the impact of liquid water distribution in a polymer electrolyte fuel cell (PEFC) on the spatially heterogeneous platinum (Pt) catalyst degradation. The membrane electrode assemblies (MEAs) are aged using accelerated stress tests (ASTs) in varied cathode gas environments (N_2 and air) to instigate Pt catalyst degradation. The study employs high-resolution neutron imaging and synchrotron micro-X-Ray diffraction (micro-XRD) to map liquid water distribution and Pt particle size, respectively. Neutron radiographs reveal liquid water accumulation primarily within the diffusion media, especially under flow field lands, due to thermal resistance differences between channels and lands. Aged MEAs exhibit increased water retention, likely due to increased hydrophilicity of the diffusion media with aging. Synchrotron micro-XRD maps unveil significant heterogeneity in Pt particle size distribution in the aged MEAs, correlated with preferential liquid water accumulation under flow field lands. This study highlights the critical role of flow field design and water distribution in catalyst degradation, underscoring the need for innovative strategies to enhance fuel cell durability and performance.

5.2 Introduction

Energy production is at the heart of the climate challenge because burning fossil fuels to generate electricity and heat contributes to approximately 75% of global greenhouse gas emissions, which are responsible for trapping heat in the Earth's atmosphere. To mitigate the adverse effects of climate change, emissions must be reduced by nearly half by 2030 and reach net-zero by 2050 [4]. Addressing this challenge requires transitioning from fossil fuels to clean, accessible, affordable, sustainable, and reliable alternative energy sources. The U.S. Department of Energy (U.S. DOE) aims to reduce emissions and decarbonize various sectors through four key technological strategies: improving energy efficiency, promoting industrial electrification,

developing low-carbon fuels, and advancing carbon capture, utilization, and storage technologies [179].

Hydrogen polymer electrolyte fuel cells (PEFCs) offer numerous advantages compared to traditional internal combustion engines in vehicles. Fuel cell electric vehicles (FCEVs) are known for their exceptional operating efficiency (over 60%), impressive driving range (more than 400 miles), and quick refueling times (under 5 minutes) [180]. Light-duty FCEVs have been in the works for more than a decade now and have captured global attention. However, there are still significant hurdles to overcome, particularly regarding vehicle cost and durability, before we can see widespread adoption. Recently, the focus has shifted from the use of fuel cells in light-duty vehicles (LDVs) to heavy-duty vehicles (HDVs) due to the unique scalability of fuel cells in terms of both power and energy, as opposed to battery-operated electric vehicles (BEVs). However, this shift in focus comes with a demand for substantial improvements in cost (targeting $80 per kilowatt), durability (aiming for 25,000 hours of operation), and peak efficiency (targeting 68%) in HDVs, compared to their LDV counterparts, by 2030 [6].

Automotive PEFCs undergo extensive load cycling, often reaching hundreds of thousands of cycles in regular use [46]. However, the dissolution of platinum (Pt) catalyst and carbon-support oxidation under these conditions are significant barriers to their widespread adoption. Consequently, PEFC electrocatalyst degradation has received significant attention in the past decade. In a typical PEFC, catalyst layers play a pivotal role in facilitating electrochemical reactions, with Pt or Pt-alloy nanoparticles supported on carbon-based materials. Among various carbon supports, high surface area carbon (HSAC) is preferred due to its ability to effectively disperse Pt nanoparticles, thereby enhancing the electrochemically active surface area (ECSA). However, the higher defect rates of HSAC render it more susceptible to corrosion, particularly under high potential excursions (> 1 V vs. reversible hydrogen electrode, RHE) during start-up/shutdown cycling and anode fuel starvation conditions [41,42,70]. Carbon corrosion not only affects the structural integrity of the catalyst layer but also orphans Pt nanoparticles, decreasing the overall electrochemical activity of the catalyst layer. Moreover, gradual oxidation of amorphous carbon can result in pore structure collapse and compaction, further exacerbating performance degradation. In addition to carbon corrosion, Pt catalyst degradation is a major concern during PEFC operation. Mechanisms such as Pt dissolution, redeposition, migration, and

agglomeration contribute to the loss of ECSA, ultimately impacting cell performance. These mechanisms are well documented in the literature [8,46,49,57,58,130].

To evaluate the durability of PEFC components, accelerated stress tests (ASTs) are commonly employed, simulating various operating conditions. These tests involve cycling between specific voltage limits (typically between 0.6 V and 1.0 V vs. RHE) under controlled environments, such as hydrogen and nitrogen atmospheres at the anode and cathode, respectively [55]. Through tailored conditions, ASTs aim to induce nearly homogeneous degradation, thereby establishing direct links between applied stressors - such as relative humidity (RH), temperature, reactant flow rates, and voltage cycling profiles - and performance deterioration.

Recent studies have unveiled the inherently heterogeneous nature of catalyst degradation within PEFCs [92,115,153,155,156,181]. The complexity arises from multifaceted interactions among the flow field architecture, materials employed, and local transport phenomena. Furthermore, recent investigations [92,115,153,155,156,181] have highlighted heterogeneous growth patterns in Pt particle size across different regions of the catalyst layer, spanning from flow field channels to lands and from cathode inlet to outlet. Particularly interesting is more significant Pt particle size growth observed underneath cathode flow field lands compared to channels and towards the flow field outlet [92,155]. This heterogeneity is believed to originate from the localized variations in water content within the catalyst layer underneath the cathode flow field lands. However, a direct link between the liquid water accumulation under the flow field lands and preferential growth of Pt particles is yet to be established. The present study establishes and quantifies this link between the preferential Pt nanoparticle size growth and liquid water distribution in a PEFC. This study deepens our understanding of how flow field design impacts catalyst degradation and opens avenues for exploring innovative designs to enhance PEFC durability.

The operating conditions of a fuel cell stack vary with the vehicle state, such as acceleration, deceleration, idling, start, and stop. Consequently, the in-plane (i.e. inlet-to-outlet) water content in the membrane electrode assembly (MEA) fluctuates accordingly. Typically, water content increases during acceleration and decreases during deceleration [182]. Given that these stacks utilize plates with large active areas (> 300 cm^2), gradients in water distribution across the plane can develop, influencing local impedance and affecting performance. Vehicle manufacturers aim to control in-plane water content within specified upper and lower bounds to enhance durability and performance. In addition, a more uniform in-plane water distribution could expand

the range for control [182]. Furthermore, storage of liquid water in the GDL and catalyst layer can lead to cold temperature performance issues [82,83]. As this study will demonstrate, flow field design strongly influences in-plane water content, affecting the catalyst degradation and resulting in power loss.

In this study, MEAs were aged in varied cathode gas environments (N_2 and air) using the ASTs recommended by the U.S. DOE in a specially designed cell. The AST conditions were chosen to induce Pt catalyst degradation. High-resolution neutron imaging was performed at the Paul Scherrer Institut (PSI), Switzerland, and the liquid water distribution in the pristine and aged samples was mapped. These samples were then used for ex-situ post-mortem characterization, including Pt particle size mapping through synchrotron micro-X-Ray diffraction (micro-XRD), performed at Beamline 12.3.2 of the Advanced Light Source (ALS) at Lawrence Berkeley National Laboratory. Quantification of in-plane liquid water distribution in the GDLs and MEAs, specifically in the cathode land/channel (L/C) regions and at the inlet/outlet, enabled correlation with observed spatially heterogeneous Pt nanoparticle size growth via ex-situ synchrotron micro-XRD. Extensive electrochemical characterization was also performed in addition to water and Pt particle size maps. This comprehensive approach provides insights into the relationship between water distribution, Pt particle size, and electrochemical performance in fuel cell systems.

5.3 Method of Approach

5.3.1 Materials and test equipment

The test cell used in the present study was machined out of aluminum and has an active area of 20 cm^2 (8 cm X 2.5 cm). A high aspect ratio (AR = 3.2) cell enabled high-resolution neutron imaging with minimum blurring. The anode and the cathode flow fields were identical and had a single serpentine flow channel, as shown in Figure 5.1. These flow field plates were gold coated with a thin nickel sublayer. The flow channels were 1 mm deep and wide, with a landing width of 1 mm. For superior and differential cell temperature control, two independent coolant plates were placed on either side of the flow field plates. These coolant plates were supplied with deionized water from a precisely temperature-controlled refrigerated circulator in the co-flow direction. High coolant flow rate ensured nearly uniform temperature distribution across the cell. The flow field and coolant plate assembly were compressed using 20 mm-thick stainless-steel compression plates. For electrical isolation of the flow field and coolant plate assembly from the stainless-steel compression plates, incompressible polytetrafluoroethylene (PTFE) coated fiberglass plates with

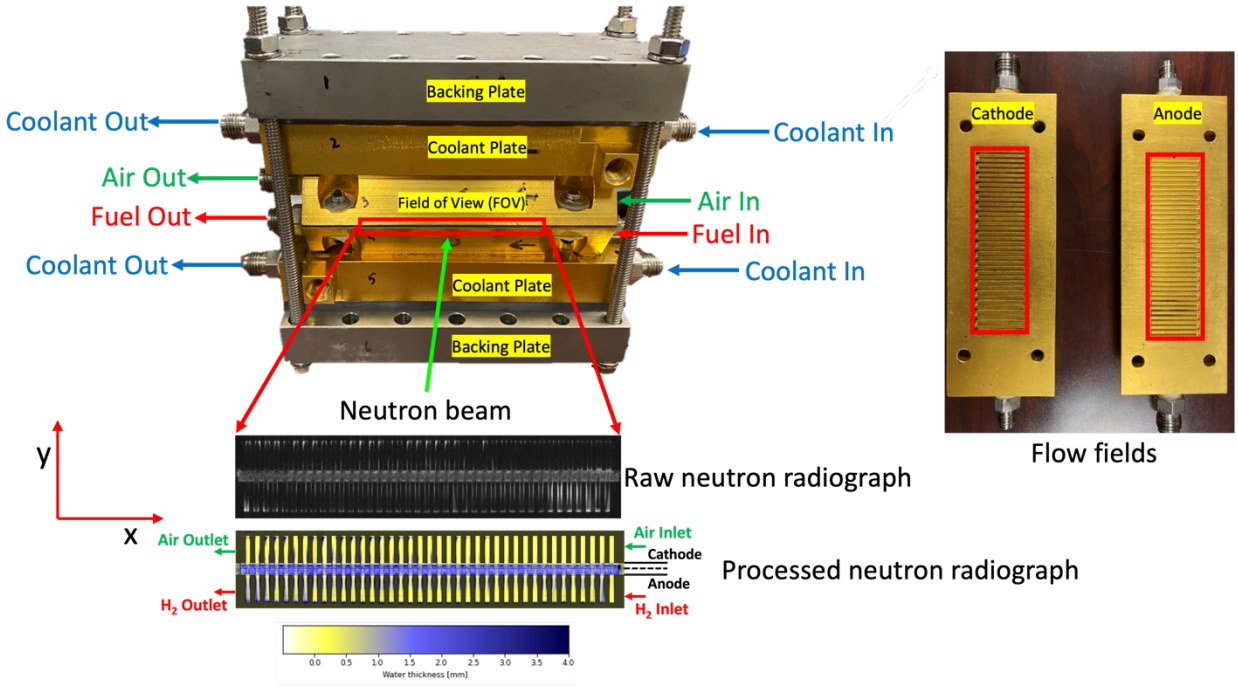


Figure 5.1. Schematics of the cell hardware to quantify in-plane liquid water distribution using neutron imaging. The complete field-of-view (FOV) is marked, along with the anode and cathode single-serpentine flow fields shown on the right.

fiberglass washers were used. Uniform compression (approximately 20% of GDL thickness) throughout the cell was verified by placing Fujifilm Prescale Super Low-pressure measurement films between different layers in the cell. The air and hydrogen were supplied in a co-flow arrangement. Similar test cells have been used for high-resolution neutron imaging in previously published studies [18,28,143,183].

The MEAs used in the present study consisted of catalyst-coated (40 wt.% Pt on Vulcan carbon) Nafion XL membrane (thickness ≈ 27.5 μm) sandwiched between Sigracet SGL 22BB GDLs. The catalyst layers (cathode and anode) had an identical Pt loading of ~0.3 mg-Pt/cm^2, and were each approximately 7 μm thick (characterized by SEM in a previous study [153]). All the MEAs, including the GDLs, were purchased from the Fuel Cell Store in Bryan, Texas, and are commercially available.

5.3.2 Catalyst AST and in-situ electrochemical characterization

The voltage cycle profiles for the ASTs used in the present study are summarized in Figure 5.2. Two different ASTs recommended by the U.S. DOE [55] were performed at a cell temperature of 80 °C. The first AST, referred to as N_2 AST, was executed under an H_2/N_2 (anode/cathode) atmosphere in the cell with atmospheric back pressure. The cell voltage was controlled in a square-wave format using an external potentiostat (Biologic SP-240) between 0.6 V and 0.95 V vs. RHE, and 30,000 cycles were executed. The cell voltage was held constant for 3 seconds at each step. Note that a voltage ramp rate of 500 mV/s was applied during this AST, leading to a total cycle time of about 7.4 seconds. During the N_2 AST, fully humidified (100% inlet RH) H_2/N_2 reactant streams with constant flow rates of 100/200 sccm were used. The second AST, referred to as Air AST, was executed under an H_2/air atmosphere in the cell with a backpressure of 150 kPa (absolute) at the anode and cathode. The cell voltage was cycled between 0.6 V and open circuit voltage (OCV), which was approximately 0.925 V for the given MEA samples and test conditions. A total of 30,000 cycles of this square-wave AST were executed, with a 3-second hold at each voltage step (total cycle time of 6 seconds). Constant flow rates of 280 sccm and 850 sccm were maintained at the anode (H_2) and cathode (air), respectively, with 100% RH at the cell inlet. These flow rates were selected by assuming a maximum operating current density of 1.5 A/cm^2 at 0.6 V with an H_2/air stoichiometry of 1.5/2. Furthermore, these constant flow rates ensured that there was no additional degradation in the cell related to reactant starvation during load switching. It is important to mention that under these conditions, there was a negligible drop in OCV of the MEAs

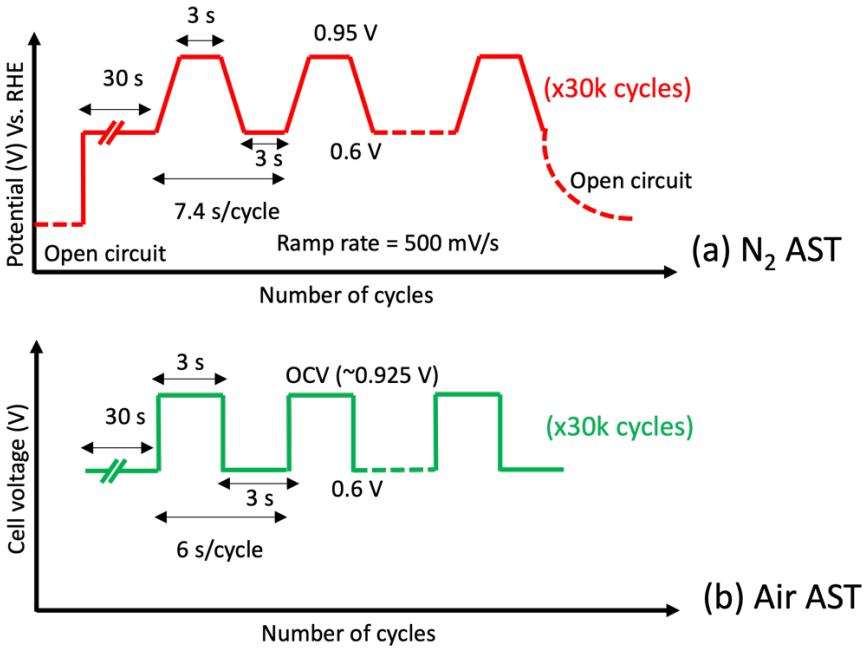


Figure 5.2. U.S. DOE [55] voltage cycling profiles used in the present study for (a) N_2 AST, and (b) Air AST.

over the course of 30,000 AST cycles; hence, the cell voltage was reliably controlled. A drop in OCV most likely occurs due to the membrane degradation and concomitant increase in hydrogen crossover in the cell. No such increase in the hydrogen crossover was observed in the current study, as indicated by crossover measurements in Figure S5.20 of Supporting Information for Chapter 5.

To estimate the electrochemically-active surface area (ECSA), cyclic voltammograms (CVs) were collected under a fully humidified H_2/N_2 (anode/cathode) atmosphere at 80 °C. The cell potential was cycled from 0.1 V to 0.9 V vs. RHE at 50 mV/s. Constant flow rates of 100 and 200 sccm were used at the anode and cathode, respectively. After correcting the CVs for double-layer capacitance, hydrogen desorption peaks were numerically integrated to compute the ECSA. Linear sweep voltammograms (LSVs) were executed under identical cell operating conditions as CVs, except for the voltage range and scan rate. During LSVs, the cell voltage was swept from 0.1 V to 0.7 vs. RHE at 2 mV/s. The polarization curves (H_2/air) were recorded at a cell temperature of 80 °C and two different inlet RH conditions, i.e., 100% and 50%. These humidity conditions were chosen to study the impact of different ASTs on the wet and dry performances at the EOL. During polarization curves, an H_2/air stoichiometry was maintained constant at 1.5 and 2 at the anode and cathode, respectively, with minimum flows of 100 sccm (H_2) and 300 sccm (air) and 150 kPa (absolute) backpressure. The cell current decreased from 1.5 A/cm^2 to 0 A/cm^2, with each galvanostatic hold lasting for 4 minutes. The data were then averaged over the last 30 seconds of each galvanostatic hold. Identical starting conditions for polarization curves were ensured to avoid the hysteresis effects due to in membrane hydration variation. Also, sweeping the cell current from high to low ensured optimum membrane hydration and performance. High frequency resistance (HFR) was measured at a single frequency of 3,800 kHz (determined from independent EIS measurements) in parallel with the galvanostatic holds during the polarization curves. All the MEAs were subjected to an identical break-in or conditioning procedure [115,153,165] before performing the ASTs and other in-situ electrochemical measurements. The conditioning procedure involved cycling the cell voltage between 0.8, 0.6, and 0.3 V with a 30-second hold at each potential. During the conditioning procedure, the cell temperature, H_2/air stoichiometry, and backpressure were held constant at 80 °C, 1.5/2, and 150 kPa (absolute), respectively. Also, for all the MEAs, the sequence of electrochemical characterization from the beginning-of-life (BOL) to end-of-life (EOL) was consistent. After the conditioning procedure, polarization curves were recorded at the specified conditions, followed by the CVs and LSVs. Then, the ASTs were

executed. CVs were collected at regular intervals during the ASTs to estimate the ECSA. At least three different MEA samples were tested for each AST case.

The aged samples, carefully disassembled from the cell, were stored for in-situ neutron imaging at PSI, Switzerland. Before mapping water in these aged samples, a short activation/recovery procedure was executed to ensure nearly identical polarization performance at the EOL. The cell compression remained consistent during the reassembly for neutron imaging experiments. The error bars in the polarization curves shown in the present study account for minor differences in performance observed after the reassembly. These samples were then used for ex-situ post-mortem characterization. It is important to mention that the ASTs were performed at the University of Tennessee, Knoxville, due to limited beam-time availability at PSI.

5.3.3 In-situ neutron imaging

Neutron imaging experiments were conducted at the SINQ-NEUTRA beam-line [184] at Paul Scherrer Institut (PSI), Switzerland, to quantify in-plane liquid water distribution in fresh and aged samples. All the images were acquired with an exposure time of 30 seconds and a field-of-view (FOV) measuring 83.2 mm X 4 mm, as illustrated in Figure 5.1. For each AST case, various current densities (0.1, 0.2, 0.5, 0.75, and 1.0 A/cm^2) were chosen for imaging while maintaining a cell temperature of 80 °C and fully humidified H_2/air flows (100% inlet RH) at both the anode and cathode. H_2/air stoichiometry remained constant at 1.5 and 2 at the anode and cathode, respectively, with minimum flow rates of 100 sccm (H_2) and 300 sccm (air) and a backpressure of 150 kPa (absolute). Before image acquisition at each condition, steady-state operation was obtained. Imaging parameters were selected to achieve adequate spatial resolution for resolving liquid water distribution in the diffusion media, particularly under the flow field lands. Additionally, a large FOV facilitated the quantification of in-plane liquid water distribution from the cell inlet to the outlet. Anisotropic pixel sizes of 40 μm in the flow direction (x) and 7 μm perpendicular to it (y, through the plane of MEA layers) were realized due to detector tilt, resulting in an overall spatial resolution of approximately 25 μm. To be concise, neutron radiographs at only 0.1 and 0.5 A/cm^2 are discussed in this study.

Quantification of in-plane liquid water distribution in the MEAs and GDLs, specifically in the land/channel (L/C) regions and at the inlet/outlet, enabled correlation with observed spatially heterogeneous Pt nanoparticle size growth via ex-situ synchrotron micro-XRD. After completing all experiments for a given MEA, the cell was dried out by purging it with dry nitrogen, and a

reference image was obtained. Raw neutron radiographs were processed to quantify water thicknesses (integrated in the direction of beam travel). This processing involved pixel-wise referencing by dividing the acquired raw radiographs by corresponding dry images, thus obtaining beam attenuation due to liquid water in the cell. Before referencing, necessary corrections were made regarding detector background, neutron scattering, and changes in beam intensity. The water thickness (δ_w) in the sample was calculated using the Lambert-Beer law [185]:

$$\delta_w = \frac{-ln(I/I_o)}{\Sigma}$$

where I is the pixel intensity in the raw image, I_o is the pixel intensity in the reference image, and Σ is the attenuation coefficient of neutrons in liquid water. For the imaging setup at NEUTRA, the value of Σ is 0.35 mm^{-1}.

Although the flow field channel width, depth, and land width were all 1 mm, the processed neutron radiographs are presented asymmetrically to better differentiate liquid water distribution in the flow field channels and underneath the lands for a given MEA and operating condition. Additional details on the neutron imaging setup, measurement uncertainties, and image processing algorithm can be found in previous publications [185–188].

5.3.4 Post-mortem synchrotron micro-X-ray diffraction

The synchrotron X-ray micro-diffraction mapping/imaging experiments were conducted at Beamline 12.3.2 of the Advanced Light Source (ALS) at Lawrence Berkeley National Laboratory. A 10 keV X-ray beam was focused to approximately 2×5 μm^2 using a set of Kirkpatrick−Baez mirrors. The CCM sample was positioned on a high-resolution x−y scan stage tilted at 25° relative to the incident X-ray beam. Two-dimensional X-ray diffraction mapping was performed in reflection mode using a two-dimensional Pilatus-1 M detector, positioned at an angle of 60° to the incoming X-ray beam and located approximately 150 mm from the probe spot. The exposure time at each scan location was set to 10 seconds. Prior to the measurements, calibrations for distance, center channel position, and detector tilt were conducted using a reference Al_2O_3 powder diffraction pattern taken under the same experimental geometry. For each MEA sample, which covered an area of 35×20 cm^2, a 2-D scan consisting of 175×20 points was carried out. The step size was set to 200 μm on the x-axis and 1000 μm on the y-axis. Subsequently, the obtained X-ray diffraction data was processed using XMAS. Debye-Scherrer rings were integrated along the

azimuthal direction, and the resulting peak widths were determined by fitting a 2d Lorentzian function with an angular resolution of approximately 0.02°.

5.4 Results and Discussion

Figure 5.3(a) shows the normalized ECSA loss as a function of AST cycles. The ECSA is calculated from the hydrogen desorption regions shown in Figure S5.18(a) and (b), Supporting Information for Chapter 5. At the EOL, MEAs aged with Air and N_2 AST lost about 56% and 70% of the initial ECSA, respectively. Specific ECSA values at the BOL, during ASTs, and at EOL are detailed in Figure S5.18(c) of the Supporting Information for Chapter 5. These trends align with existing literature on ASTs conducted in air and N_2 environments [92,153,189]. For instance, Khedekar et al. [92] observed the highest ECSA loss (~75% at EOL) for MEAs subjected to N_2-Wet AST, compared to a 52% ECSA loss for the Air-Wet case. This difference was attributed to lower UPL values in the Air-Wet case, where UPL dropped below 0.9 V.

During H_2-air voltage cycling, the choice of gas flow rates can influence aging within the cell. Differential flow conditions (very high stoichiometry) minimize in-plane temperature and humidity gradients, resulting in more uniform aging throughout the cell. Conversely, stoichiometric flow conditions may lead to the development of temperature and humidity gradients, resulting in non-uniform aging. A recent study by Astudillo et al. [190] reported that while ECSA loss decreased with decreasing RH, it remained independent of gas feeds (N_2 and air) for typical voltage cycling ASTs. The authors attributed this discrepancy between their findings and other published studies to differential flows during H_2-air cycling protocols. In the present study, flow rates were determined assuming a maximum operating current density of 1.5 A/cm^2 at 0.6 V with an H_2/air stoichiometry of 1.5/2. Therefore, there exists the possibility of heterogeneous catalyst degradation due to humidity and temperature gradients from the flow field inlet to the outlet. This phenomenon of inhomogeneous degradation has been extensively documented in previous studies [92,115,153,155,181].

Figure 5.3(a) shows a rapid ECSA decline in early phases of cycling, particularly for N_2 AST. After the first 5,000 cycles, N_2 AST lost about 52% of the initial ECSA, while Air AST only experienced a 25% loss. This rapid decline likely results from intensified electrochemical Ostwald ripening of small Pt nanoparticles [8,48]. Chemical potential for Pt dissolution and agglomeration inversely correlates with Pt particle size (Gibbs-Thomson effect); smaller particles dissolve rapidly and redeposit onto adjacent larger Pt nanoparticles to minimize surface energy [8,48]. Note that Pt

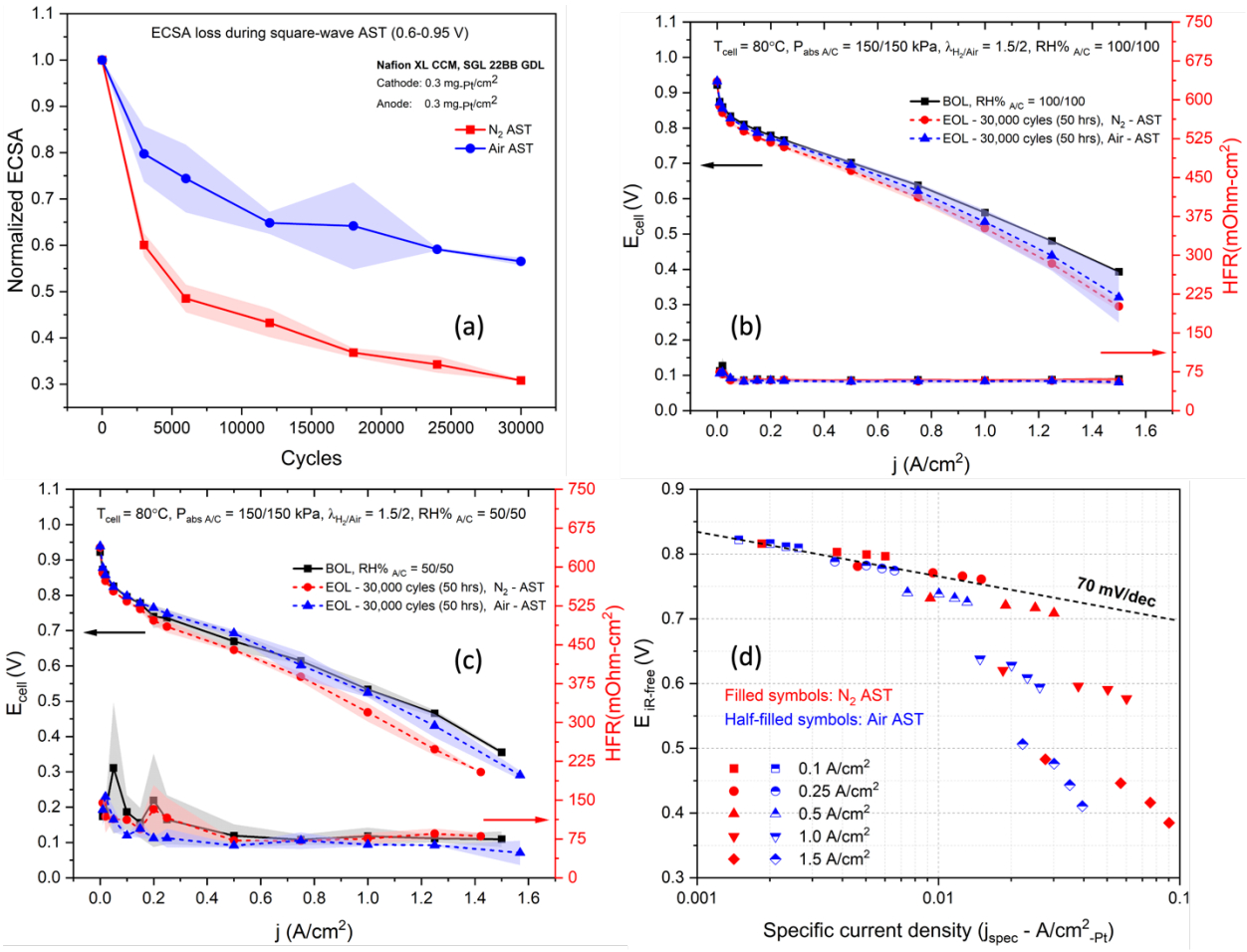


Figure 5.3. (a) Normalized ECSA versus number of AST cycles for N_2 and Air ASTs measured under fully humified ($RH\%_{A/C}$ = 100/100). H_2/N_2 (anode/cathode) environment at T_{cell} = 80 °C with no backpressure. (b) Polarization curves of the MEAs before and after aging for N_2 and Air AST at fully humidified cell inlets ($RH\%_{A/C}$ = 100/100). (c) Polarization curves at partially humidified cell inlets ($RH\%_{A/C}$ = 50/50). Other conditions during polarization curves include cell temperature (T_{cell}) of 80 °C, H_2/air stoichiometry ($\lambda_{H_2}/\lambda_{Air}$) of 1.5/2 with a backpressure ($P_{abs\ A/C}$) of 150 kPa (absolute) on both the anode and cathode. (d) iR-free cell voltage versus specific current density for different ASTs used in the present study. A Tafel slope of 70 mV/decade is marked as a reference. This plot is generated by plotting the iR-free cell voltage from polarization curves collected at T_{cell} = 80 °C, $RH\%_{A/C}$ = 100/100, $\lambda_{H_2}/\lambda_{Air}$ = 1.5/2 with $P_{abs\ A/C}$ = 150 kPa/150 kPa on both the anode and cathode.

nanoparticle migration on the carbon support is also possible during the early phases of cycling. However, this mechanism is proposed to be responsible for ECSA loss in the fuel cell cathode at low voltages since the solubility of Pt nanoparticles is believed to be negligible below 0.7 V vs. RHE [8]. The voltage cycling in all the experiments in the present study was performed above 0.6 V vs. RHE. Therefore, the contributions of direct crystal migration and coalescence is expected to be small compared to Ostwald ripening. Moreover, due to a slightly higher upper potential limit (UPL) in the case of N_2 AST (0.95 V vs. RHE) compared to Air AST (~0.925 V), there is likely a higher amount of Pt being dissolved, and hence, a higher initial ECSA loss in 5,000 cycles [56–58,191]. For both the AST cases, as the cycling continues, the Pt particles likely attain a quasi-stable average size that is less susceptible to further dissolution. Hence, the ECSA loss slows down in the later phases of cycling. It is important to mention that there was a negligible drop in OCV for the MEAs subjected to Air-AST throughout 30,000 cycles. A drop in OCV most likely occurs due to membrane degradation and a concomitant increase in hydrogen crossover [63,64,67,68,192]. No such increase in the hydrogen crossover was observed in the current study, as indicated by crossover measurements in Figure S5.20 of Supporting Information for Chapter 5. Moreover, the HFR for both the AST cases did not change appreciably at the EOL (Figure 5.3(b) and (c)), indicating no damage to the polymer membrane.

Figure 5.3(b) and (c) show the polarization curves for MEAs aged with N_2 and Air AST at BOL and EOL under different relative humidity conditions. Regardless of humidity levels, a consistent performance loss trend is observed at EOL, with N_2 AST-aged MEAs exhibiting higher losses across all current densities. For instance, at 1.0 A/cm^2 under wet conditions (100% inlet RH), Air AST-aged MEAs lost approximately 30 mV, whereas N_2 AST-aged MEAs lost around 50 mV. Under dry conditions (50% inlet RH), the performance decline was more pronounced, with N_2 AST-aged MEAs exhibiting a loss of about 70 mV compared to 10 mV for Air AST-aged MEAs at 1.0 A/cm^2. Detailed polarization curves for both ASTs at various cycling stages are provided in Figure S5.19 of the Supporting Information for Chapter 5. Voltage losses in both ASTs primarily stem from ECSA decrease with voltage cycling, with the disparity in overall ECSA loss (approximately 70% for N_2 AST vs. 56% for Air AST at EOL) explaining higher voltage losses in N_2 AST case [57,92,130,153,191].

For a deeper understanding of the nature of polarization losses in both AST cases, Figure 5.3(d) shows the iR-free voltage against specific current density (j_{spec}). The data covers geometric

current densities ranging from 0.1 A/cm^2 to 1.5 A/cm^2. The specific current density (j_{spec}) is defined as the ratio of geometric current density to the product of ECSA and the Pt loading at a given aging stage. Note that this product of ECSA and the Pt loading is also known as the roughness factor. As per the definition, j_{spec} takes the following form [130]:

$$j_{spec}\,(A/cm^2_{Pt}) = \frac{j_{geo}(A/cm^2)}{ECSA\,(m^2_{Pt}/g_{Pt})\times L_{Pt}(mg_{Pt}/cm^2)\times 10} \quad (1)$$

Here, j_{geo} is the geometric current density, ECSA is the electrochemically active surface area, and L_{Pt} is the Pt loading in the cathode electrode. Assuming minimal change in Pt loading during aging and performance loss following Tafel kinetics, the change in ORR overpotential at any given geometric current density can be expressed as [130]:

$$\Delta\eta_{ORR} = \frac{2.303\times RT}{\alpha F} \times log\left\{\frac{(i_o\times ECSA)_{BOL}}{(i_o\times ECSA)_{EOL}}\right\} \quad (2)$$

In this equation, i_o is the exchange current density, R is the universal gas constant, T is the temperature, F is Faraday's constant, and α is the cathodic charge transfer coefficient. However, additional losses such as mass transport (local oxygen transport resistance and/or ionic resistance through thin ionomer films) can significantly deviate the experimentally measured slope from the purely kinetic Tafel prediction of 70 mV/decade [130]. It is worth noting that Tafel analysis is typically performed under differential conditions with pure oxygen flow. However, the use of stoichiometric air flow rates over a large active area is not uncommon and has been used in previous studies [92,130,153,155].

Figure 5.3(d) shows that for both AST cases, the voltage losses align with Tafel prediction up to a geometric current density of 0.5 A/cm^2, indicating predominantly kinetic control. However, at higher geometric current densities of 1.0 and 1.5 A/cm^2, there is a departure from the expected 70 mV/decade Tafel prediction. This deviation suggests the presence of additional mass transport losses. These additional losses may stem from local oxygen transport resistance at catalyst sites or proton conduction through thin ionomer or water films covering these sites. Notably, the deviation from Tafel prediction begins around a j_{spec} of approximately $0.02 A/cm^2_{Pt}$. Previous studies have also reported similar j_{spec} values marking the onset of deviation from Tafel prediction, especially in electrodes with low Pt loading or small roughness factors [92,130,136,153,167]. Correcting the voltage losses for oxygen transport resistance using limiting current measurements could yield a more accurate comparison in Figure 5.3(d). However, this correction was not made in the current study because limiting current measurements were not performed.

As previously mentioned, the aged samples were carefully disassembled from the cell and then stored for in-situ neutron imaging at PSI, Switzerland. Before analyzing the water distribution in these aged samples, a brief activation/recovery procedure was carried out to ensure optimal polarization performance. It was ensured that the compression of the cell remained consistent during reassembly for the neutron imaging experiments. Due to the limited spatial resolution of about 25 µm for imaging, differentiating the water content in the membrane from other layers was not feasible, given the membrane thickness of 27.5 µm used in this study. Various interfaces in the neutron radiographs, such as the cathode channel/GDL interface, anode channel/GDL interface, and anode and cathode GDL interfaces, were approximately identified based on visible features in the image data. It is important to note that in this study, the cathode water content includes the total water content in the cathode GDL (with a microporous layer, MPL), cathode catalyst layer, and the polymer membrane. Similarly, the anode water content encompasses the total water content in the anode GDL (with an MPL) and the anode catalyst layer. The water content in the cathode and anode gas channels was not factored into the calculations.

Figure 5.4 presents neutron radiographs of both pristine and aged samples at a geometric current density of 0.1 A/cm^2 at T_{cell} = 80 °C and fully humidified conditions (100% inlet RH on both the anode and cathode). These radiographs provide a quantification of the in-plane water content, integrated in the direction of the neutron beam. In our study, the active area width of the neutron imaging cell is 25 mm. Hence, a water thickness of 4 mm corresponds to 16% of the path length occupied by liquid water.

At 0.1 A/cm^2, both pristine and aged samples show liquid water primarily within the MEA and GDLs. However, liquid water is also observed accumulating in the anode gas channels, particularly near the flow field inlet. At low geometric current densities, water and heat generation are minimal, and the primary mechanism for water removal is through the path of least resistance, namely the anode flow channels. Since the inlet streams are fully humidified (100% RH) and the membrane is optimally hydrated, back diffusion of water from the cathode to the anode can outweigh electroosmotic drag, shifting the water balance towards the anode. This mechanism of water removal through anode gas channels has been observed in previous studies utilizing similar cells [18,28,143,183]. A notable feature in both pristine and aged samples is the accumulation of liquid water under the flow field lands. During regular operation of a PEFC with H_2/air, liquid water can accumulate under the flow field lands in diffusion media. This accumulation is primarily due to

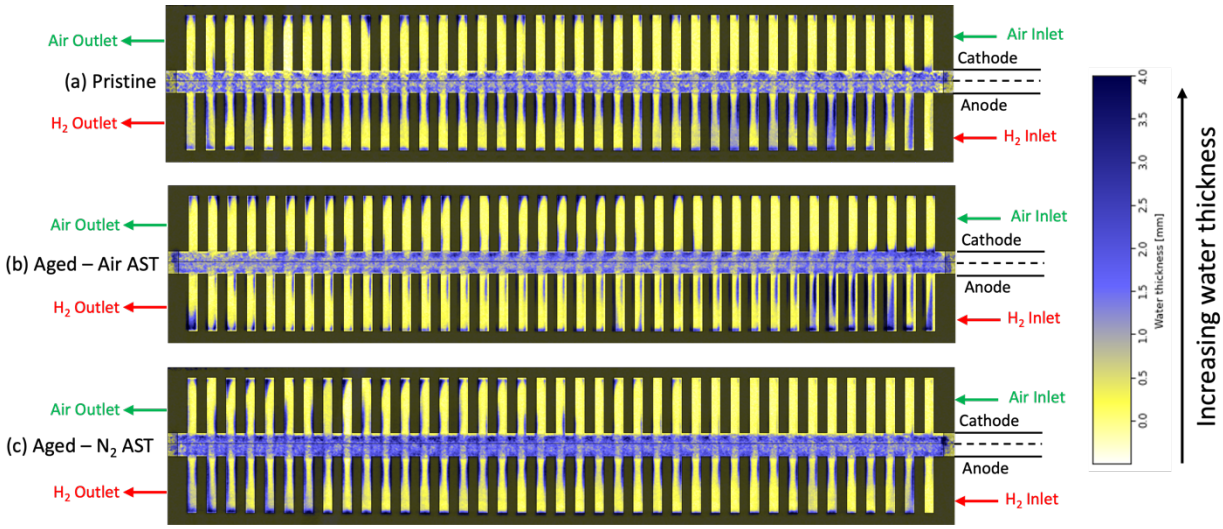


Figure 5.4. Neutron images/radiographs (anisotropic scale) of the test cell with (a) pristine MEA, (b) MEA aged with Air AST, and (c) MEA aged with N_2 AST at a current density of 0.1 A/cm^2. In all the images, cathode is shown at the top and anode is at the bottom. The scale on the right shows the measured water thickness (mm) along in-plane direction. Other operating conditions include T_{cell} = 80 °C, $RH\%_{\,A/C}$ = 100/100, $\lambda_{H_2}/\lambda_{Air}$ = 1.5/2 with $P_{abs\,A/C}$ = 150 kPa/150 kPa on both the anode and cathode.

the difference in thermal resistance between the flow field land/GDL interface and the channel/GDL interface. The land/GDL interface offers lower thermal resistance, resulting in colder lands compared to the channels. Consequently, water vapor condenses under the colder lands and accumulates over time until enough capillary pressure buildup pushes the liquid water into the flow field channels [17,24,28,147,193,194] .

The temperature gradient between the channels and lands can be exacerbated at higher current densities and with aging [148,195]. The flow field channel-to-land ratio (L/C) is known to impact the amount of liquid water stored in the diffusion media, with a higher ratio resulting in a more significant accumulation of liquid water [17]. In our study, a ratio of 1 was utilized.

To further quantify the liquid water accumulation under the flow field channels and lands in both pristine and aged samples, pixel-wise averaging (perpendicular to MEA plane) of the water content in the MEA and GDLs was performed. This data is plotted from the flow field inlet to the outlet in Figure 5.5, separately for both the anode and cathode. The plot clearly indicates a bias in liquid water accumulation between the channels and lands along this direction. Spikes or increases in liquid water content, or saturation, are correlated with the presence of flow field lands. Notably, there is higher overall water accumulation under the cathode flow field lands than under the anode. Additionally, higher water content is observed at the cathode flow field outlet than at the inlet for all samples. This preferential accumulation from the flow field inlet to the outlet aligns with observations from previous studies and can be attributed to spatial temperature and humidity gradients. Notably, the MEAs aged with N_2-AST exhibit higher liquid water saturation under the lands towards the cathode flow field outlet than the inlet, in contrast to the pristine and Air AST-aged MEA samples.

With aging, fuel cell components, especially GDLs, tend to become more hydrophilic. Although ex-situ measurements were not conducted to confirm the increase in hydrophilicity in our study, similar trends have been reported in other studies [77,81,196,197]. For example, Liu et al. [196] observed a decrease in surface contact angle for GDLs subjected to ex-situ accelerated aging, with a more significant increase in hydrophilicity observed for GDL substrates without PTFE treatment. The increased overall water retention (discussed later in this chapter) supports the assertion of increased hydrophilicity. All other operating parameters remained identical during imaging between the pristine and aged samples. Galvanostatic operation during imaging ensured that the electrochemically generated water was consistent across all samples. Given the identical

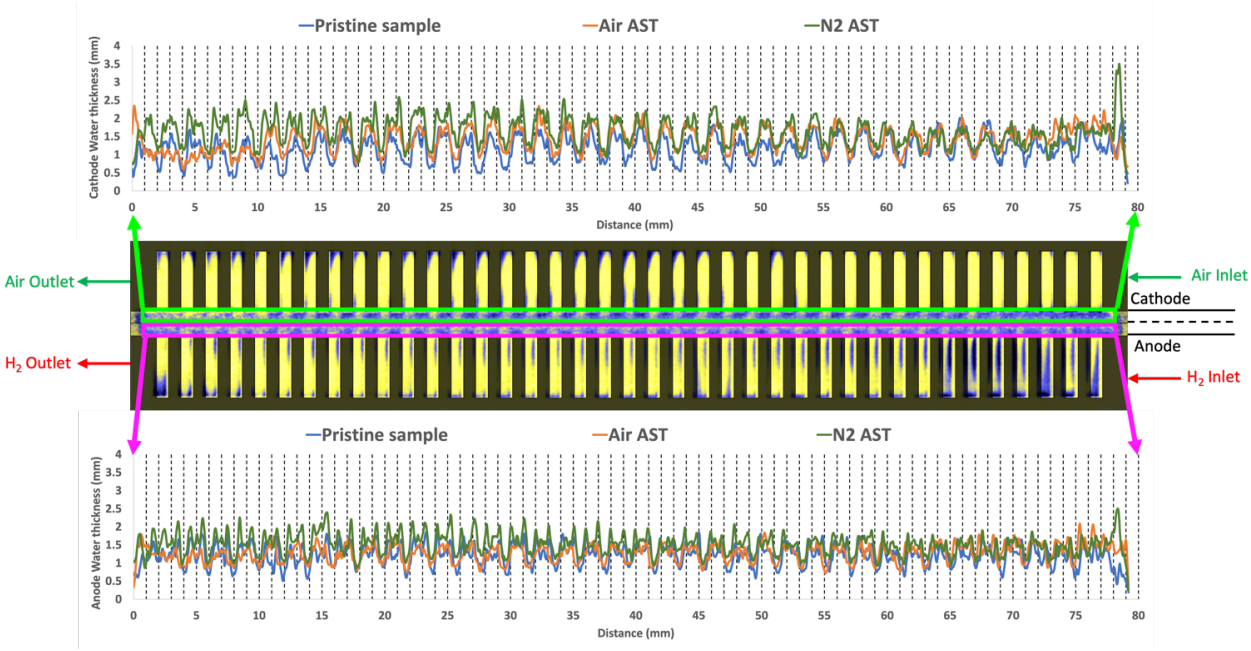


Figure 5.5. Averaged water thickness (mm) in the MEA along the cell inlet to the outlet (from right to left) for the pristine and aged MEAs at a current density of 0.1 A/cm^2. In this image, cathode is shown at the top and anode is at the bottom. Other operating conditions include T_{cell} = 80 °C, $RH\%_{\,A/C}$ = 100/100, $\lambda_{H_2}/\lambda_{Air}$ = 1.5/2 with $P_{abs\,A/C}$ = 150 kPa/150 kPa on both the anode and cathode. Note that the neutron radiograph is just a representative image to show where the liquid water distribution is calculated from.

and precisely controlled operating conditions, the difference in overall water content can be attributed to different aging protocols.

In Figure 5.6, neutron radiographs of both pristine and aged samples are depicted at a geometric current density of 0.5 A/cm^2 at T_{cell} = 80 °C and fully humidified conditions (100% inlet RH on both the anode and cathode). Similar to observations at 0.1 A/cm^2, clear channel/land bias in liquid water saturation is evident. The dominant mechanism for water removal remains through the anode, as indicated by the presence of liquid water in the anode gas channels. Notably, at 0.5 A/cm^2, higher heat and water generation occur. Consequently, there is a greater degree of liquid water evaporation and removal through the vapor phase compared to 0.1 A/cm^2. Additionally, due to higher overpotential in the aged samples (voltage loss of 40 and 30 mV for N_2 AST and Air AST, respectively, compared to BOL), there is increased waste heat generation compared to the pristine sample at the same current density.

In Figure 5.7, pixel-wise averaged (in the direction perpendicular to the plane of the MEA) water content profiles for both pristine and aged samples are presented. Similar to trends observed at 0.1 A/cm^2 in Figure 5.5, a distinct channel/land bias in liquid water accumulation is observed from the flow field inlet to the outlet. Moreover, increases in liquid water content or saturation correlate with the presence of flow field lands. However, unlike at 0.1 A/cm^2, the saturation profiles near the outlet for aged samples match those of the pristine samples, although the overall water content is higher. This difference may be attributed to increased waste heat generation due to higher overpotential in the aged samples, leading to partial water removal in the vapor phase [28,109,110].

Overall, at both geometric current densities (0.1 and 0.5 A/cm^2), a distinct bias towards liquid water saturation in the channel/land regions is evident in both aged and pristine samples. Particularly noteworthy is the higher liquid water retention observed in the aged samples. Additionally, greater water saturation near the cathode flow field outlet compared to the inlet is observed in the aged samples, particularly noticeable at 0.1 A/cm^2 compared to the pristine sample. This channel/land bias in liquid water storage, especially in the aged samples, is crucial for understanding its correlation with the preferential Pt nanoparticle size growth discussed subsequently.

Figure 5.8 illustrates the averaged water mass (in mg) for both pristine and aged MEAs at current densities of 0.1 and 0.5 A/cm^2. The water mass within the cathode or anode of each MEA

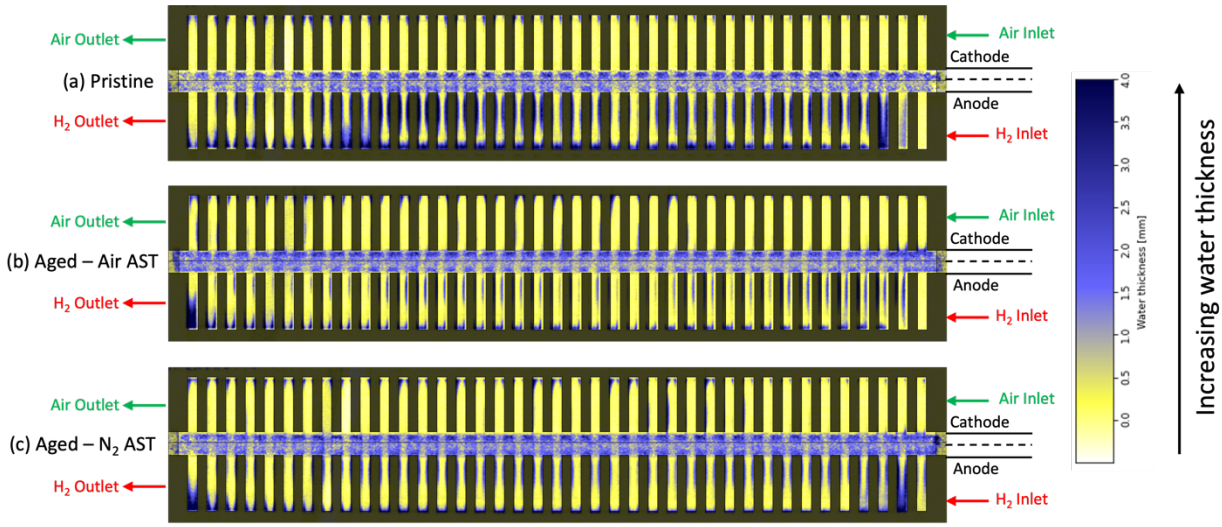


Figure 5.6. Neutron images/radiographs (anisotropic scale) of the test cell with (a) pristine MEA, (b) MEA aged with Air AST, and (c) MEA aged with N_2 AST at a current density of 0.5 A/cm^2. In all the images, cathode is shown at the top and anode is at the bottom. The scale on the right shows the measured water thickness (mm) along in-plane direction. Other operating conditions include T_{cell} = 80 °C, $RH\%_{\,A/C}$ = 100/100, $\lambda_{H_2}/\lambda_{Air}$ = 1.5/2 with $P_{abs\,A/C}$ = 150 kPa/150 kPa on both the anode and cathode.

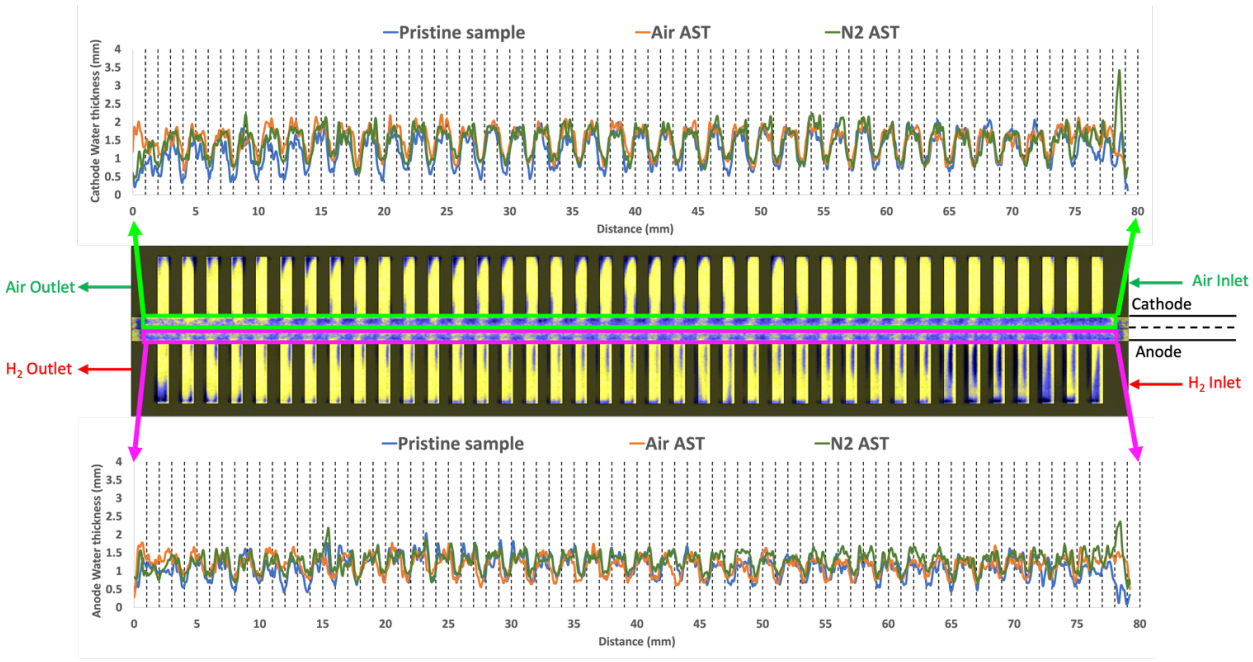


Figure 5.7. Averaged water thickness (mm) in the MEA along the cell inlet to the outlet (from right to left) for the pristine and aged MEAs at a current density of 0.5 A/cm^2. In this image, cathode is shown at the top and anode is at the bottom. Other operating conditions include T_{cell} = 80 °C, $RH\%_{\,A/C}$ = 100/100, $\lambda_{H_2}/\lambda_{Air}$ = 1.5/2 with $P_{abs\,A/C}$ = 150 kPa/150 kPa on both the anode and cathode. Note that the neutron radiograph is just a representative image to show where the liquid water distribution is calculated from.

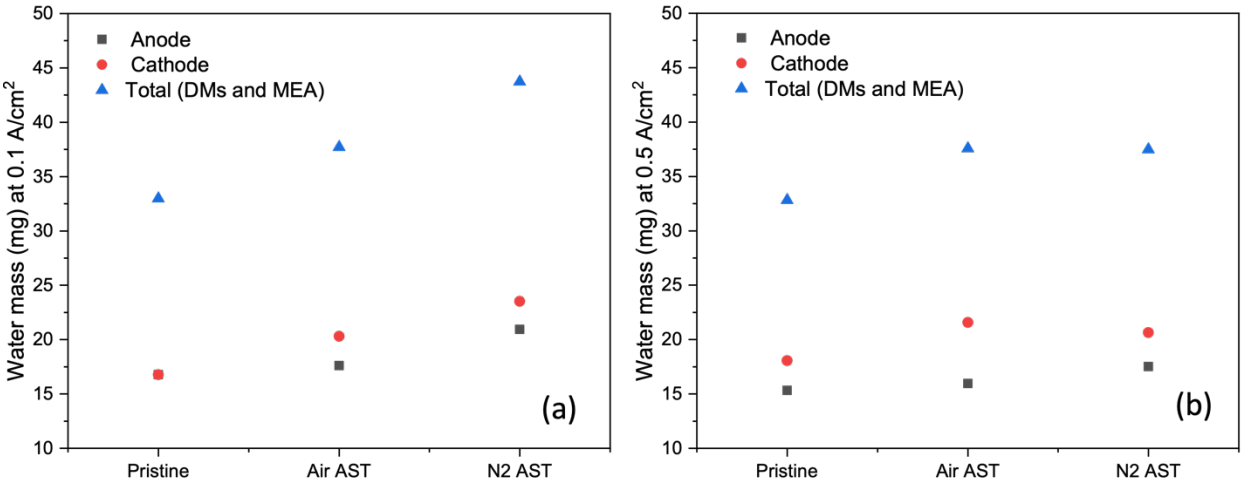


Figure 5.8. Averaged water mass (mg) in the pristine and aged MEAs with different ASTs used in this study at (a) 0.1 A/cm^2, and (b) 0.5 A/cm^2. The water mass in the cathode or anode for a particular MEA is calculated by averaging water thickness from the cell inlet to the outlet in the diffusion media and catalyst layers alone. In all the images, cathode is shown at the top and anode is at the bottom. This calculation does not include water thickness in the flow field channels at the cathode or anode. Other operating conditions include T_{cell} = 80 °C, $RH\%_{\ A/C}$ = 100/100, $\lambda_{H_2}/\lambda_{Air}$ = 1.5/2 with $P_{abs\ A/C}$ = 150 kPa/150 kPa on both the anode and cathode.

is determined by averaging water thickness from the cell inlet to the outlet in the diffusion media and catalyst layers alone, excluding water accumulated in the anode and cathode gas channels. Notably, at 0.1 A/cm^2, the total water mass in the Air AST-aged sample increased by approximately 14% compared to the pristine sample, while in the MEA aged with N_2 AST, the increase was approximately 33%. Furthermore, a slightly higher overall water mass is observed in the cathode than in the anode, consistent with water being electrochemically generated at the cathode. At low geometric current densities, where water and heat generation are minimal, primary water removal occurs through the anode flow channels. Given fully humidified inlet streams and optimally hydrated membranes, back diffusion of water from the cathode to the anode can outweigh electroosmotic drag, shifting the water balance towards the anode [147,194]. The increased water retention in aged MEAs is likely due to the enhanced hydrophilicity of MEA components, especially the GDLs, post-aging [77,81,196,197].

Interestingly, at a current density of 0.5 A/cm^2, MEAs aged with Air and N_2 AST exhibit a similar increase in overall water mass, approximately 14% compared to the pristine sample. This higher current density leads to increased heat and water generation, resulting in greater liquid water evaporation and removal through the vapor phase compared to 0.1 A/cm^2. Note that waste heat scales as the square of the operating current while the water generation scales linearly. Additionally, the increased waste heat generation in aged samples due to higher overpotential contributes to this phenomenon. The higher overpotential for N_2 AST-aged MEAs at the EOL compared to Air AST likely explains the decreased water retention at 0.5 A/cm^2.

Figure 5.9 presents synchrotron micro-XRD maps for pristine and aged samples, covering approximately 70% of the total active area (70 mm X 20 mm). Including the cathode flow field image in Figure 5.9 allows correlation between the Pt particle size maps at the inlet and outlet. Step sizes of 0.2 mm in the x-direction and 1 mm in the y-direction were chosen for Pt nanoparticle size mapping to resolve 1 mm-wide channels and lands. Additionally, areas closer to the inlet and outlet of the MEAs were examined to understand the impact of preferential water accumulation. The data from the 2-D Pt maps in Figure 5.9(a) and (b) are plotted as histograms in Figure 5.9(c).

The pristine MEA exhibits an average Pt particle size of approximately 5.1 nm, consistent with a previous study [153]. Minor channel/land bias in Pt particle size is observed, with differences of less than 5% between channels and lands at both the inlet and outlet, likely resulting from the conditioning process and intentional design of the neutron imaging cell with wider lands.

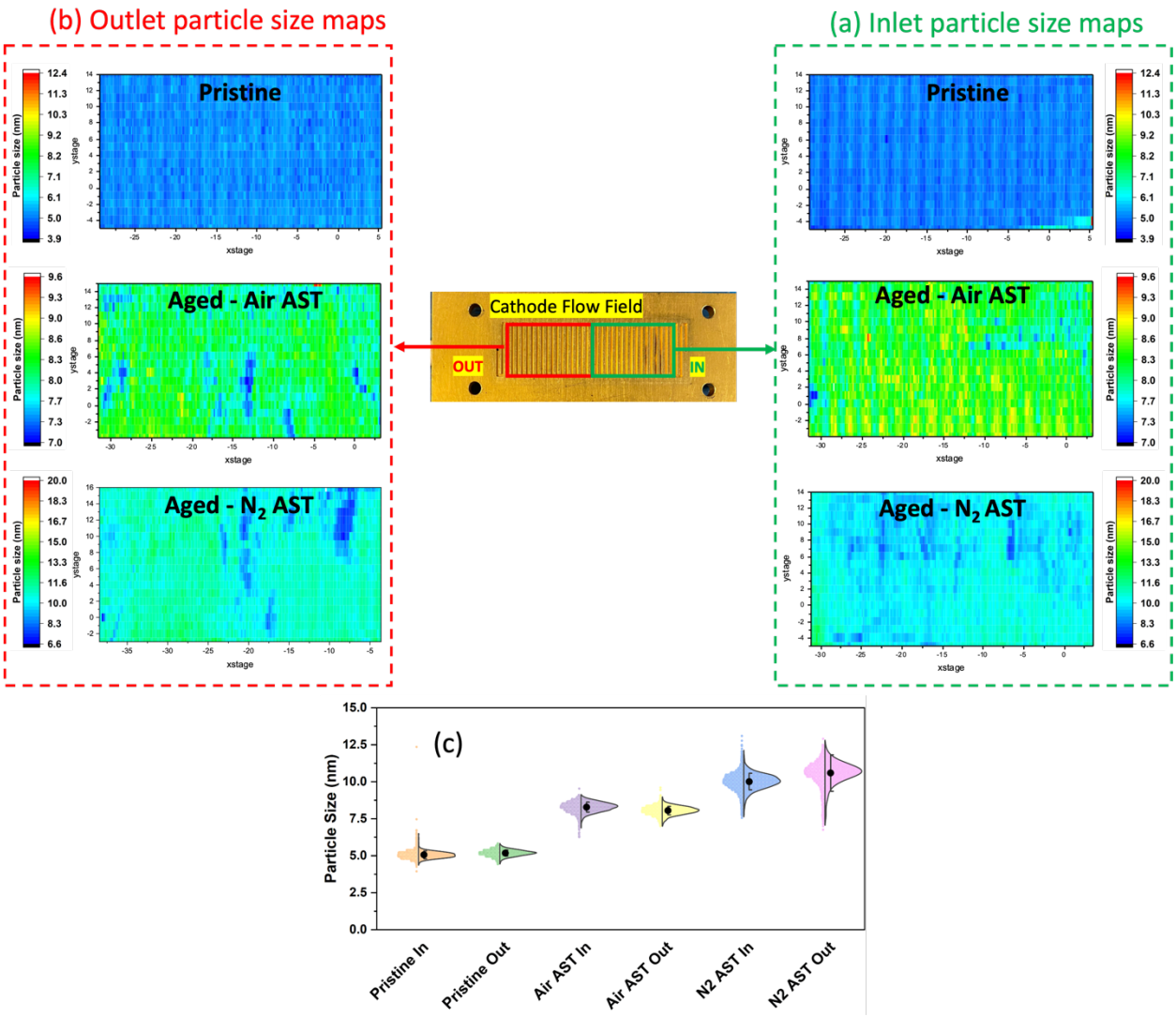


Figure 5.9. Synchrotron micro-XRD maps for the pristine and aged samples with N_2 and Air ASTs at the (a) inlet and the (b) outlet of the cathode flow field. The color bars for the maps represent Pt particle sizes in nm. Panel (c) shows the particle size distributions derived from the spatial micro-XRD maps for the pristine and aged samples at the inlet and outlet.

In contrast, aged samples display a non-uniform Pt particle size distribution. The Air AST-aged MEA shows a clear channel/land bias in Pt particle size growth, especially near the flow field inlet, with an average (over the entire mapped area) Pt particle size of around 8.2 nm. Variations up to 15 to 20% in Pt particle size growth between lands and channels are observed, suggesting highly non-uniform aging. Certain patches in the outlet Pt particle size maps exhibit significantly lower average Pt particle sizes. Previous studies have also observed such spots mapping the heterogeneous Pt particle size growth [92,153,181]. For N_2 AST-aged MEAs, channel/land bias is still present but to a lesser extent than in Air AST-aged MEAs. The average Pt particle size for N_2 AST-aged MEAs is approximately 10.3 nm (over the entire mapped area). Slight variations in average Pt particle sizes between the inlet and outlet areas are observed, likely attributed to higher water accumulation near the flow field outlet (discussed earlier in Figure 5.5 and Figure 5.7).

The channel/land bias observed in Pt particle size growth in the aged samples can be directly linked to the preferential accumulation of liquid water under the flow field lands, as discussed in Figure 5.5 and Figure 5.7. The increased saturation underneath the lands is expected to elevate the local liquid water content in the catalyst layer below the landing area [17,194]. This increased presence of liquid water over the voltage cycling period enhances the effective mobility of dissolved Pt species, thereby intensifying Ostwald ripening in the catalyst layer beneath the flow field lands. Consequently, more pronounced Pt particle size growth occurs in these areas compared to the channels. This preferential degradation of the catalyst underneath the lands, in contrast to the channels, likely contributes significantly to the overall power loss.

In previous studies [92,155] where this bias in Pt particle size growth between channels and lands was observed, it was hypothesized that it might be due to the preferential accumulation of liquid water underneath the flow field lands. Our study confirms and quantifies this relationship between preferential liquid water accumulation and Pt particle size growth. It is worth noting that during the N_2 AST, even though the inlet reactant streams (H_2/N_2) were fully humidified (100% RH), some water condensation can still occur under the flow field lands due to thermal gradients. With this link between preferential liquid water accumulation and heterogeneous degradation established and quantified for typical voltage cycling protocols, enhancing the durability of PEFCs could involve reducing the landing area in contact with the diffusion media to lower overall water storage underneath the colder lands. This correlation between the L/C ratio and total liquid water storage is explored comprehensively in a previous study. However, reducing landing width should

be approached cautiously to avoid increased contact resistance. Additionally, minimizing the number of switchbacks in a serpentine flow field design is crucial, as liquid water tends to accumulate preferentially around these areas. A recent study by Sharma et al. [153] demonstrated that these switchbacks become sites of heightened Pt particle size growth compared to other flow field areas. This research highlights the significant impact a flow field design can have on catalyst degradation and opens avenues for exploring innovative designs to enhance PEFC durability.

5.5 Conclusions

In this study, membrane electrode assemblies (MEAs) were subjected to accelerated stress tests (ASTs) in varied cathode gas environments (N_2 and air) to simulate Pt catalyst degradation. High-resolution neutron imaging and synchrotron micro-XRD were employed to map liquid water distribution and Pt particle size, respectively. At the end of life (EOL), MEAs aged with N_2 and Air AST showed substantial losses in electrochemically-active surface area (ECSA), with approximately 70% and 56% reductions, respectively. Slightly higher upper potential limit (UPL) in the N_2 AST (0.95 V vs. RHE) compared to Air AST (~0.925 V) resulted in a higher cumulative ECSA loss. Polarization losses correlated with ECSA reduction, with N_2 AST-aged MEAs exhibiting higher losses across all current densities. A deviation from Tafel prediction indicated additional mass transport losses at higher geometric current densities (1.0 and 1.5 A/cm^2).

Neutron radiographs revealed liquid water accumulation primarily within the MEA and gas diffusion layers (GDLs), with some in the anode gas channels, especially near the inlet, where the primary water removal mechanism was through these channels. A notable feature in both pristine and aged samples was the accumulation of liquid water under the flow field lands, primarily due to the difference in thermal resistance between the flow field land/GDL interface and the channel/GDL interface. Furthermore, higher saturation was observed at the cathode flow field outlet than at the inlet. Aged MEAs showed increased water retention, attributed to increased hydrophilicity of diffusion media post-aging. At 0.1 A/cm^2, the total water mass increased by approximately 14% for Air AST-aged MEAs and 33% for N_2 AST-aged MEAs compared to pristine samples. Similarly, at 0.5 A/cm^2, both aged MEAs exhibited approximately a 14% increase in overall water mass compared to pristine samples, attributed to increased heat and water generation, with N_2 AST-aged MEAs experiencing decreased water retention due to higher overpotential (portion of water removed in vapor phase).

Synchrotron micro-XRD revealed significant heterogeneity in Pt particle size distribution, particularly in aged samples subjected to Air and N_2 ASTs. Air AST-aged MEAs exhibited a distinct channel/land bias, with an average Pt particle size of approximately 8.2 nm, and variations of up to 15 to 20% between lands and channels. Similarly, N_2 AST-aged MEAs exhibited a channel/land bias, with an average Pt particle size of approximately 10.3 nm, albeit to a lesser extent. This non-uniform growth pattern correlated with the preferential accumulation of liquid water under the flow field lands. The increased saturation under the lands intensified Pt particle growth through Ostwald ripening, leading to more pronounced growth than the channels and significantly impacting overall power loss in the MEAs. These findings underscore the critical role of flow field design and water distribution in catalyst degradation, emphasizing the need for innovative strategies which limit any liquid water accumulation near catalysts to enhance fuel cell durability.

Chapter 6: Conclusions and Future Work

Automotive PEFCs undergo extensive load cycling, often reaching hundreds of thousands of cycles in regular use. However, the dissolution of platinum (Pt) catalyst and carbon-support oxidation under these conditions are significant barriers to their widespread adoption. The U.S. Department of Energy (DOE) has set durability benchmarks at 8,000 hours for light-duty vehicles and 30,000 hours for heavy-duty vehicles. Consequently, PEFC electrocatalyst degradation has received significant attention in the past decade. Still, our understanding of electrocatalyst degradation remains incomplete, particularly regarding heterogeneity in catalyst growth and its localized performance impact. Based on these gaps in the literature, this dissertation thoroughly investigated the following research questions (objectives):

1. Impact of cathode gas flow rate on catalyst degradation during an accelerated stress test (AST), a parameter often overlooked in PEFC degradation research.
2. Effects of heterogeneous catalyst degradation on localized electrochemical performance loss in a PEFC
3. Interaction between various degradation modes or path-dependent degradation in PEFCs
4. Correlation between heterogeneous catalyst growth and liquid water distribution in a PEFC

A deeper understanding of local performance responses to aging and the interactions of different degradation mechanisms explored in this study will enable the design of highly durable fuel cells capable of withstanding thousands of load/unload, start-up/shutdown cycles.

Major conclusions from the studies in Chapters 2 through 5 are outlined below.

6.1 Impact of cathode gas flow rate on catalyst degradation in polymer electrolyte fuel cells

This study (Chapter 2) quantified spatially heterogeneous electrocatalyst degradation at the cathode (Pt particle size growth and distribution) in a PEFC as a function of fully humidified N_2 flow rate during a U.S. DOE square-wave AST (0.6 V to 0.95 V vs. RHE, 30,000 cycles) with H_2/N_2 on the anode/cathode, respectively. The current density peaks associated with different facets of polycrystalline Pt nanoparticles in the hydrogen desorption region of the CVs of low (4 sccm/cm^2), medium (8 sccm/cm^2), and high (16 sccm/cm^2) N_2 flow rates decreased at different rates, highlighting possible changes in Pt crystal structure with aging. As the AST progressed, the ECSA loss at each sampling interval was inversely proportional to N_2 flow rate. Interestingly, at the EOL, irrespective of the N_2 flow rates and influence on ECSA loss rate, the MEAs ended up

having similar overall ECSA loss (~65 % from the BOL). This can be attributed to the fact that Pt particles attain a "quasi" stable average size which resists further dissolution and impedes Pt degradation rate.

A first-order rate model for ECSA loss predicted a linear dependence of the rate constant on N_2 flow rate. The rate constant increased by ~57% for an increase in N_2 flow rate from 4 sccm/cm^2 to 16 sccm/cm^2 at the CCL during the AST. The 2D (2 cm x 2 cm) micro-XRD maps of the pristine and the aged MEAs revealed striking differences; Pt particle size distribution for the pristine MEA sample was largely uniform with an average of 3.5 nm, whereas the MEAs aged with different N_2 flow rates exhibited spatial heterogeneity in Pt particle size growth and distribution. In general, a higher Pt particle size growth was observed near the flow field outlet than the inlet. Although micro-XRD could not resolve channel-land differences in Pt particle sizes, this is an important finding as the ASTs used for studying Pt dissolution in PEFCs with N_2 are usually intended to achieve nearly homogenous Pt particle size growth throughout the CCL. However, an implicit assumption that Pt particle size growth is homogeneous is not supported by this work. It is hypothesized that non-uniform humidification from the flow field inlet to the outlet (outlet more humidified than the inlet) could be responsible for heterogeneous Pt particle size growth at high temperature and humidity AST conditions. This non-uniform humidification across the cell active area results from the increase in water-carrying capacity of N_2 due to the local heating in the inlet lines to the cell. This humidity gradient is expected to be smaller for higher N_2 flow rate, likely offset by its overall increase in water removal capacity from the cell. Thus, overall humidification in the cell (in the absence of Faradaic reactions) is a delicate balance between the humidity gradient at the cell inlet and water removal capacity of the purge gas which directly depends on its flow rate in the channels. Since the humidity gradient and overall water mass is expected to be smaller for high N_2 flow rate, we would expect smaller average Pt particle size and "tighter" Pt particle size distribution compared to low N_2 flow rate as Pt particle size growth is supported by water content. This hypothesis is supported by our data. Furthermore, the non-uniform humidification impacts local chemical gradients (concentration and the mobility of the soluble Pt species) inside the cell, leading to the patterned or heterogenous Pt particle size growth. The hydration levels are further exacerbated by increased strength of cross-flow under the lands for higher N_2 flow rates in a serpentine flow field.

The histograms of Pt particle sizes followed a Gaussian distribution with the mean Pt particle sizes of 10.4 nm, 10.1 nm, and 9.1 nm for 4, 8, and 16 sccm/cm^2 N_2 flow rates, respectively. The histograms for 4 and 8 sccm/cm^2 N_2 flow rates, however, exhibited a larger fraction of Pt particles with sizes greater than 11 nm compared to 16 sccm/cm^2 N_2 flow, corroborated by the TEM measurements. The voltage loss (ΔV) analysis with H_2/air revealed greater losses for higher N_2 flow rates at most of the operating current densities; higher polarization losses occurred at moderate-to-high current densities, most likely due to the heterogeneous nature of the Pt particle size growth.

Overall, it can be concluded that the catalyst aging inside the cell with fully humidified N_2 flow subjected to an AST is spatially heterogeneous, even though there is negligible heat and water generation (absence of Faradaic currents). The flow field architecture cannot be neglected as it strongly influences thermal and mass transport inside the cell due to the channel-land bias. An important outcome of this study is the call for inclusion of N_2 flow rate as a stressor for Pt degradation along with the usual ones during an AST for a holistic assessment of the performance and durability of the state-of-the-art Pt catalysts in PEFCs. Determination of the role of architecture is critical in understanding local degradation behavior.

6.2 Effects of heterogeneous catalyst degradation on the localized electrochemical performance loss of polymer electrolyte fuel cells

This study (Chapter 3) examined heterogeneous aging patterns in current, Pt particle size, and temperature distributions after ASTs. The chosen conditions simulated carbon corrosion (CC AST) and Pt particle size growth in both fully humidified (Pt AST-Wet) and underhumidified (Pt AST-Dry) H_2/N_2 environments. Multimodal characterization techniques such as in-situ current and temperature mapping, along with full active area micro-XRD maps, enabled the study of the impact of accelerated aging on local cell performance and morphological changes.

At the EOL, ECSA losses occurred in all MEAs, with differing rates and mechanisms. The ECSA losses ranged from about 25% for Pt AST-Dry to roughly 60% for Pt AST-Wet. With regard to polarization performance loss at EOL, the most significant performance degradation was evident in the CC AST case, where nearly ~250 mV loss at a low geometric current density of 0.25 A/cm^2 occurred, mainly due to mass transport restrictions. The Pt AST-Dry case experienced a lower performance loss than the Pt AST-Wet case, likely owing to a smaller cumulative ECSA loss.

Interestingly, while the CC AST demonstrated considerable changes in current distributions and strong current gradients, the Pt AST-Wet and Pt AST-Dry cases showed only minor variations, despite substantial ECSA loss. This finding challenges the conventional belief that ECSA alone can indicate fuel cell health. This investigation also revealed that carbon corrosion in a fully humidified H_2/N_2 environment proceeds relatively uniformly, and mass transport properties significantly shape the local current distributions post-AST. Furthermore, supporting these observations, SEM cross-sectional measurements revealed substantial catalyst layer thinning in the MEAs exposed to CC AST, while others showed negligible thinning. A distinct Pt band near the CCL-membrane interface was visible in the Pt AST-Wet case but absent in the other AST cases. The average Pt particle size after aging for CC AST, Pt AST-Dry, and Pt AST-Wet increased by around 35%, 69%, and 124%, respectively, as determined from the full active area micro-XRD maps. Notably, the larger average Pt particle size in the Pt AST-Wet and Pt AST-Dry cases did not result in significant variations in current distributions. This finding re-emphasizes the need to consider additional factors beyond ECSA for fuel cell health assessment. Moreover, a higher particle size growth under the serpentine flow field bends in the Pt AST-Wet case was observed, possibly due to liquid water accumulation. This study is the first to report such a preferential growth of Pt particles under bends for large active areas. Despite the smallest average Pt particle size at EOL in the CC AST case, this case demonstrated strong gradients in current distributions compared to the other cases.

Lastly, at EOL, the Pt AST-Wet and Pt AST-Dry cases showed only minor changes in spatial temperature distributions compared to the BOL. The CC AST case presented a shift in the hotter region closer to the air inlet. However, the absolute temperature variation stayed within ~2°C of the set value of 80°C.

Overall, this study provides critical insights into the heterogeneous aging patterns of a PEFC under different ASTs. It is evident that mass transport properties, morphological changes, and humidity conditions significantly influence fuel cell performance following the ASTs. Our research indicates that the degradation in the performance of aged MEAs is more closely tied to species distribution than to the growth of Pt particle size. While the ECSA loss has been recognized as an important contributor to fuel cell aging, this study underscores that ECSA loss is not the sole determinant of fuel cell health; instead, a complex interplay of several aspects shapes a PEFC's

overall performance and durability. For enhanced durability and uniform current distributions in a PEFC, it is crucial to avoid high potential excursions (>1 V vs. RHE).

6.3 Path-dependent degradation in high-performance polymer electrolyte fuel cells

In this study (Chapter 4), path-dependent degradation in PEFCs was explored using two distinct AST combinations derived from the U.S. DOE aging protocols. The first combination, PtfCC AST, involved 15,000 cycles of a square-wave voltage profile from 0.6 to 0.95 V vs. RHE, followed by 2,500 cycles of a triangular-wave voltage profile from 1.0 to 1.5 V vs. RHE. The second combination, CCfPt AST, reversed the sequence. Both combinations totaled 17,500 cycles. Multimodal characterization techniques, such as spatially resolved current distribution and post-mortem micro-XRD platinum (Pt) particle size maps, were used to establish the path dependency of degradation modes.

The results revealed that PtfCC AST leads to about 74% ECSA loss at the EOL compared to the BOL, while CCfPt AST shows around 61% ECSA loss. During the carbon corrosion phase, ECSA loss in PtfCC AST (~47% compared to middle-of-life, MOL) was similar to CCfPt AST (~43% compared to BOL). However, the catalyst corrosion phase in PtfCC AST was more aggressive, resulting in approximately 50% ECSA loss compared to BOL, while CCfPt AST showed around 31% loss compared to MOL. These findings suggest that "orphaned" Pt nanoparticles, rendered electrochemically inactive due to carbon support corrosion, slow down or eliminate the electrochemical Ostwald ripening process, highlighting the interplay between different degradation modes.

Polarization performance of MEAs under wet and dry conditions showed distinct characteristics. Under wet conditions at EOL, MEAs subjected to PtfCC AST experienced a significant voltage loss (~400 mV at 0.5 A/cm^2), whereas those subjected to CCfPt AST had a smaller loss (~290 mV at 0.5 A/cm^2). Under dry conditions, the trend reversed: CCfPt AST showed a higher voltage loss (~230 mV at 0.5 A/cm^2) compared to PtfCC AST (~130 mV at 0.5 A/cm^2). These differences are attributed to flooding and increased mass transport overpotential in PtfCC AST due to carbon corrosion, which leads to pore structure collapse and Pt particle detachment, whereas CCfPt AST experienced less severe degradation.

The current density distribution (CDD) maps showed that at the MOL, the PtfCC AST case showed minor changes in CDDs despite significant ECSA loss. However, at EOL, PtfCC AST exhibited significant current gradients due to flooding and pore structure collapse, with gradients

ranging from +20% to -15% from the mean, indicating severe performance degradation. In contrast, CCfPt AST showed strong gradients at MOL due to rapid carbon support oxidation but less severe gradients at EOL. The better performance of PtfCC AST under dry conditions at EOL suggests reduced flooding, while CCfPt AST maintained smoother CDDs, highlighting different degradation impacts.

Two-dimensional micro-XRD maps revealed that the pristine sample had an average Pt particle size of 5.53 nm with a mostly uniform distribution. At EOL, PtfCC AST showed a significant increase in Pt particle size by about 94%, while CCfPt AST showed an increase of about 77%. This more significant growth in PtfCC AST is attributed to intensified electrochemical ripening during the catalyst corrosion phase. The CCfPt AST exhibited smaller average Pt particle growth due to "orphaned" Pt nanoparticles becoming electrochemically inactive. Additionally, higher Pt particle size growth was observed around serpentine flow field bends in PtfCC AST, likely due to liquid water accumulation, a heterogeneity not seen in CCfPt AST except near the fuel inlet.

The SEM cross-sectional images showed that the pristine sample had a CCL thickness of approximately 6.98 μm ± 0.81 μm, with a similar thickness for the anode catalyst layer. At EOL, the CCL of the MEA aged with PtfCC AST showed a 20% reduction in thickness, likely due to aggressive carbon corrosion, resulting in pore collapse and flooding, leading to significant performance loss (~380 mV at 0.5 A/cm^2) under wet conditions. In contrast, the MEA aged with CCfPt AST showed negligible changes in CCL thickness. Additionally, a distinct Pt band near the CCL-membrane interface was observed in the PtfCC AST case, attributed to Pt ion reduction by crossover hydrogen, whereas no such band was present in the CCfPt AST case, indicating less Pt dissolution and redeposition. Note that there was no change in the anode catalyst layer thickness of different samples at the EOL.

Overall, this study established the path dependency between different degradation modes (catalyst growth and carbon support corrosion) in a PEFC under equal cumulative stress. Understanding these interactions is crucial as real-world applications exhibit irregular cycling patterns with path-dependent behavior. These findings will aid in improving fuel cell durability and predictive state-of-health monitoring. Gaining a deeper understanding of local performance responses to aging and the interplay of various degradation mechanisms explored in this study will enable the design of highly durable fuel cells.

6.4 Correlating catalyst growth with liquid water distribution in polymer electrolyte fuel cells

In this study (Chapter 5), MEAs were subjected to ASTs in varied cathode gas environments (N_2 and air) to simulate Pt catalyst degradation. High-resolution neutron imaging and synchrotron micro-XRD were employed to map liquid water distribution and Pt particle size, respectively. At the EOL, MEAs aged with N_2 and Air AST showed substantial losses in ECSA, with approximately 70% and 56% reductions, respectively. Slightly higher upper potential limit (UPL) in the N_2 AST (0.95 V vs. RHE) compared to Air AST (~0.925 V) resulted in a higher cumulative ECSA loss. Polarization losses correlated with ECSA reduction, with N_2 AST-aged MEAs exhibiting higher losses across all current densities. A deviation from Tafel prediction indicated additional mass transport losses at higher geometric current densities (1.0 and 1.5 A/cm^2).

Neutron radiographs revealed liquid water accumulation primarily within the MEA and GDLs, with some in the anode gas channels, especially near the inlet, where the primary water removal mechanism was through these channels. A notable feature in both pristine and aged samples was the accumulation of liquid water under the flow field lands, primarily due to the difference in thermal resistance between the flow field land/GDL interface and the channel/GDL interface. Furthermore, higher saturation was observed at the cathode flow field outlet than at the inlet. Aged MEAs showed increased water retention, attributed to increased hydrophilicity of diffusion media post-aging. At 0.1 A/cm^2, the total water mass increased by approximately 14% for Air AST-aged MEAs and 33% for N_2 AST-aged MEAs compared to pristine samples. Similarly, at 0.5 A/cm^2, both aged MEAs exhibited approximately a 14% increase in overall water mass compared to pristine samples, attributed to increased heat and water generation, with N_2 AST-aged MEAs experiencing decreased water retention due to higher overpotential (portion of water removed in vapor phase).

Synchrotron micro-XRD revealed significant heterogeneity in Pt particle size distribution, particularly in aged samples subjected to Air and N_2 ASTs. Air AST-aged MEAs exhibited a distinct channel/land bias, with an average Pt particle size of approximately 8.2 nm, and variations of up to 15 to 20% between lands and channels. Similarly, N_2 AST-aged MEAs exhibited a channel/land bias, with an average Pt particle size of approximately 10.3 nm, albeit to a lesser extent. This non-uniform growth pattern correlated with the preferential accumulation of liquid

water under the flow field lands. The increased saturation under the lands intensified Pt particle growth through Ostwald ripening, leading to more pronounced growth than the channels and significantly impacting overall power loss in the MEAs. These findings underscore the critical role of flow field design and water distribution in catalyst degradation, emphasizing the need for innovative strategies which limit any liquid water accumulation near catalysts to enhance fuel cell durability.

6.5 Future work and recommendations

6.5.1 Novel catalyst layer architectures to mitigate degradation

Conventional PEFC catalyst layers are usually 10 – 20 μm thick and consist of Pt/Pt-alloy nanoparticles (2 – 5 nm) dispersed on the surface of primary carbon particles (40 – 90 nm) for electrical contact and an impregnated ion conducting phase (ionomer), forming a highly porous three-dimensional structure. Electrochemical reactions occur at triple phase boundaries (TPB) with an open pore volume for reactant delivery and product removal, electrical contact with the support for electron transfer, and ionomer coverage for ion transport. A high number of TBPs is necessary for optimal performance, which translates to a high ECSA. However, the random mixing and deposition processes used to manufacture these electrodes often lead to limited catalyst utilization, suboptimal oxygen reduction reaction (ORR) activity, and complex, inefficient pathways for species transport. Additionally, these conventional catalyst layers are prone to various forms of degradation, as discussed extensively in this dissertation.

To address these issues, novel electrode architectures are being developed to eliminate unstable materials like carbon supports and to optimize catalyst dispersion [45,198,199]. One approach involves manufacturing macro-patterned electrodes through techniques such as inkjet printing, allowing structural control at scales ranging from millimeters to hundreds of microns. These designs can mimic the geometries of flow field channels, thereby enhancing catalyst utilization and durability.

Chapter 5 of this dissertation showed that liquid water accumulation under the flow field lands leads to heterogeneous catalyst growth. Specifically, catalysts under the flow field lands experience more significant growth than those in the flow field channels. Consequently, the catalysts within the channel areas are likely the primary contributors to power output in an aged cell. Therefore, novel designs where the catalyst dispersion follows the channel geometry can significantly reduce Pt loading. Another innovative strategy is the development of micro-patterned

electrodes using microfabrication techniques like lithography [45]. This method achieves micron-scale structural control by patterning the membrane surface or electrode, creating non-tortuous pathways for species transport and ensuring uniform reaction rates across the electrode thickness. Additionally, other advanced manufacturing techniques are being explored, such as electrospinning, enhanced-porosity fabrication, and the development of catalyst film electrodes through chemical and physical vapor deposition [45]. These methods aim to improve species transport and durability by precisely controlling electrode architecture at various length scales. These novel electrode designs promise to enhance the performance and durability of PEFCs by overcoming the limitations of traditional catalyst layers.

6.5.2 Flow field architectures that eliminate land/channel bias (porous flow fields)

In Chapters 2 and 5 of this dissertation, it was demonstrated that the performance degradation of aged MEAs is more closely related to species distribution than to the catalyst growth. Although ECSA loss is an important factor in fuel cell aging, it is not the sole determinant of fuel cell health. Instead, a complex interplay of various factors influences the overall performance and durability of PEFCs. Furthermore, the studies highlighted the critical role of flow field design and water distribution in catalyst degradation, emphasizing the need for innovative strategies to limit liquid water accumulation near catalysts to enhance fuel cell durability. One promising approach involves using porous materials (e.g., metal/carbon foam, sinters, porous plates, and 3D mesh) as alternative flow fields [21]. These highly porous (>90%) materials substantially increase the reactant supply to the catalyst layer, improve electron conduction pathways, and enhance contact stress distribution. Such flow fields have demonstrated improved high current density performance in PEFCs, particularly under wet conditions [21]. Another interesting approach involves integrating bipolar plate-MEA structures, where the flow channels are incorporated into the GDLs [200]. This design reduces cell/stack volume and minimizes ohmic and concentration losses. Overall, these novel designs enhance species transport and heat removal by eliminating the conventional channel/land bias, thereby improving catalyst durability.

A natural extension of this dissertation could be to explore the impact of these porous flow fields on the durability of the catalyst and its support, particularly under conditions relevant to heavy-duty vehicle applications. Compared to conventional flow fields, catalyst growth is expected to be more uniform from the cathode inlet to the outlet.

6.5.3 Polymer electrolyte membrane degradation under heavy-duty vehicle-relevant operating conditions

Per-fluorinated sulfonic acid (PFSA) – based membranes are used in light-duty vehicles (LDVs) due to their high ionic conductivity and inherent chemical and mechanical stability. These state-of-the-art membranes typically have intramembrane reinforcement for mechanical support. To mitigate chemical degradation when attacked by free radicals such as hydroxyl radical (*OH), hydroperoxyl radical (*OOH), and hydrogen radical (*H), these membranes have dopants such as oxides of cerium and manganese to scavenge free radicals [46]. The chemical and mechanical stability of PFSA based membranes becomes even more critical for heavy-duty vehicle (HDV) applications due to the longer required lifetime (~25,000 hours), higher operating temperatures (> 100 °C), and minimizing hydrogen and oxygen crossover [6]. Membrane thickness could become another design parameter for simultaneous optimization of performance and durability.

Another important research area is the impact of other cell components on membrane durability. For example, corrosion of the bipolar plates can lead to cation leaching into the membrane, which reduces proton conductivity. Additionally, the membrane can suffer structural damage from the penetration of carbon fibers from the gas diffusion layers (GDLs). Although membrane durability was not the focus of this dissertation, as the test conditions did not cause significant membrane degradation, it is crucial to consider in HDV applications. Understanding and mitigating membrane degradation will be essential for developing more durable fuel cells for HDVs.

6.5.4 System level mitigation strategies

Various system level mitigation strategies such as limiting the upper potential limit during cycling, including idling can significantly mitigate degradation. Most FCEVs have a battery to load share during voltage transients. While the system level mitigation strategies prevent catalyst degradation, these are usually expensive and limit the fuel cell power output. Furthermore, it is important to understand the impact of voltage clipping on the degradation of other cell components and overall system efficiency.

6.6 Broader impact of this dissertation

This dissertation enhances the understanding of spatial heterogeneity in Pt loss within the cathode catalyst layer and identifies the operating conditions that influence it. By examining how cell architecture and flow fields impact heterogeneous catalyst degradation, this research offers

valuable insights for designing and engineering PEFC components that improve durability and reduce costs for vehicle applications. Gaining a deeper understanding of local performance responses to aging and the interplay of various degradation mechanisms explored in this dissertation will enable the design of highly durable fuel cells. These fuel cells will be capable of enduring thousands of load/unload and start-up/shutdown cycles, which are essential for the practical use of PEFCs in vehicles. Furthermore, the novel insights from this study will support the development of ultra-low Pt-loaded electrodes (< 0.125 mg_{-Pt}/cm^2) and MEAs that align with the U.S. DOE's long-term (2050) targets for cost and durability. Meeting these targets is critical because Pt is a scarce and expensive resource, as most of the world's Pt supply comes from mines in South Africa, with Russia, Zimbabwe, and a few other countries contributing smaller amounts.

By addressing these challenges, this research has the potential to play a pivotal role in developing cost-effective and durable fuel cell technologies. This, in turn, can pave the way for broader adoption of clean energy solutions and contribute to global efforts towards sustainable and ethical resource utilization.

References

[1] Hannah Ritchie, Max Roser, Pablo Rosado, "https://ourworldindata.org/co2-and-greenhouse-gas-emissions," **2020**.

[2] "https://www.un.org/en/climatechange/raising-ambition/renewable-energy," **2023**.

[3] Hannah Ritchie and Pablo Rosado, "https://ourworldindata.org/energy-mix," **2020**.

[4] "https://www.un.org/en/climatechange/net-zero-coalition," **2023**.

[5] "https://www.energy.gov/eere/fuelcells/h2scale," **2016**.

[6] D. A. Cullen, K. C. Neyerlin, R. K. Ahluwalia, R. Mukundan, K. L. More, R. L. Borup, A. Z. Weber, D. J. Myers, A. Kusoglu, *Nat Energy* **2021**, *6*, 462.

[7] "https://millionmilefuelcelltruck.org/about-us," **2023**.

[8] Y. Shao-Horn, W. C. Sheng, S. Chen, P. J. Ferreira, E. F. Holby, D. Morgan, *Top Catal* **2007**, *46*, 285.

[9] M. M. Mench, *Fuel Cell Engines*, John Wiley & Sons, Inc., **2008**.

[10] S. Litster, G. McLean, *J Power Sources* **2004**, *130*, 61.

[11] W. Yuan, Y. Tang, X. Yang, Z. Wan, *Appl Energy* **2012**, *94*, 309.

[12] R. Taherian, *J Power Sources* **2014**, *265*, 370.

[13] H. Wang, J. A. Turner, *Fuel Cells* **2010**, *10*, 510.

[14] P. Chen, F. Fang, Z. Zhang, W. Zhang, Y. Wang, *Int J Hydrogen Energy* **2017**, *42*, 12593.

[15] A. E. Fetohi, R. M. Abdel Hameed, K. M. El-Khatib, E. R. Souaya, *Int J Hydrogen Energy* **2012**, *37*, 10807.

[16] C. Rocha, T. Knöri, P. Ribeirinha, P. Gazdzicki, *Renewable and Sustainable Energy Reviews* **2024**, *192*, DOI 10.1016/j.rser.2023.114198.

[17] A. Turhan, K. Heller, J. S. Brenizer, M. M. Mench, *J Power Sources* **2008**, *180*, 773.

[18] A. Turhan, S. Kim, M. Hatzell, M. M. Mench, *Electrochim Acta* **2010**, *55*, 2734.

[19] A. K. Srouji, L. J. Zheng, R. Dross, A. Turhan, M. M. Mench, *J Power Sources* **2012**, *218*, 341.

[20] A. K. Srouji, L. J. Zheng, R. Dross, A. Turhan, M. M. Mench, *J Power Sources* **2013**, *239*, 433.

[21] G. Zhang, Z. Qu, W. Q. Tao, X. Wang, L. Wu, S. Wu, X. Xie, C. Tongsh, W. Huo, Z. Bao, K. Jiao, Y. Wang, *Chem Rev* **2023**, *123*, 989.

[22] M. M. Mench, *Fuel Cell Engines*, John Wiley & Sons, Inc., **2008**.

[23] A. Ozden, S. Shahgaldi, X. Li, F. Hamdullahpur, *Prog Energy Combust Sci* **2019**, *74*, 50.

[24] J. J. Kowal, A. Turhan, K. Heller, J. Brenizer, M. M. Mench, *J Electrochem Soc* **2006**, *153*, A1971.

[25] P. Satjaritanun, S. Hirano, A. D. Shum, I. V. Zenyuk, A. Z. Weber, J. W. Weidner, S. Shimpalee, *J Electrochem Soc* **2018**, *165*, F1115.

[26] K. Jiao, X. Li, *Prog Energy Combust Sci* **2011**, *37*, 221.

[27] M. Khandelwal, M. M. Mench, *J Power Sources* **2006**, *161*, 1106.

[28] S. Kim, M. M. Mench, *J Electrochem Soc* **2009**, *156*, B353.

[29] A. D. Shum, D. Y. Parkinson, X. Xiao, A. Z. Weber, O. S. Burheim, I. V. Zenyuk, *Electrochim Acta* **2017**, *256*, 279.

[30] R. W. Atkinson, Y. Garsany, B. D. Gould, K. E. Swider-Lyons, I. V. Zenyuk, *ACS Appl Energy Mater* **2018**, *1*, 191.

[31] G. Xu, J. M. Lamanna, J. T. Clement, M. M. Mench, *J Power Sources* **2014**, *256*, 212.

[32] A. Z. Weber, J. Newman, *Modeling Transport in Polymer-Electrolyte Fuel Cells*, **2004**.

[33] A. Kusoglu, A. Z. Weber, *Chem Rev* **2017**, *117*, 987.

[34] T. A. M. Suter, K. Smith, J. Hack, L. Rasha, Z. Rana, G. M. A. Angel, P. R. Shearing, T. S. Miller, D. J. L. Brett, *Adv Energy Mater* **2021**, *11*, DOI 10.1002/aenm.202101025.

[35] N. Nonoyama, S. Okazaki, A. Z. Weber, Y. Ikogi, T. Yoshida, *J Electrochem Soc* **2011**, *158*, 416.

[36] T. A. Greszler, D. Caulk, P. Sinha, *J Electrochem Soc* **2012**, *159*, F831.

[37] D. R. Baker, D. A. Caulk, K. C. Neyerlin, M. W. Murphy, *J Electrochem Soc* **2009**, *156*, DOI 10.1149/1.3152226.

[38] J. P. Owejan, T. A. Trabold, M. M. Mench, *Int J Heat Mass Transf* **2014**, *71*, 585.

[39] Y. C. Park, H. Tokiwa, K. Kakinuma, M. Watanabe, M. Uchida, *J Power Sources* **2016**, *315*, 179.

[40] J. You, Z. Zheng, X. Cheng, H. Li, C. Fu, L. Luo, G. Wei, S. Shen, X. Yan, J. Zhang, *ACS Appl Mater Interfaces* **2023**, *15*, 21457.

[41] N. Macauley, D. D. Papadias, J. Fairweather, D. Spernjak, D. Langlois, R. Ahluwalia, K. L. More, R. Mukundan, R. L. Borup, *J Electrochem Soc* **2018**, *165*, F3148.

[42] P. Saha, K. Khedekar, H. Wang, P. Atanassov, L. Cheng, S. Stewart, C. Johnston, I. V. Zenyuk, *J Mater Chem A Mater* **2022**, *10*, 12551.

[43] U. Martinez, S. Komini Babu, E. F. Holby, H. T. Chung, X. Yin, P. Zelenay, *Advanced Materials* **2019**, *31*, 1.

[44] Y. Shao, J. P. Dodelet, G. Wu, P. Zelenay, *Advanced Materials* **2019**, *1807615*, 1.

[45] G. Yang, C. Lee, X. Qiao, S. K. Babu, U. Martinez, J. S. Spendelow, *Electrochemical Energy Reviews* **2024**, *7*, 9.

[46] P. Ren, P. Pei, Y. Li, Z. Wu, D. Chen, S. Huang, *Prog Energy Combust Sci* **2020**, *80*, 100859.

[47] E. Zhu, M. Wu, H. Xu, B. Peng, Z. Liu, Y. Huang, Y. Li, *Adv Funct Mater* **2022**, *32*, DOI 10.1002/adfm.202203883.

[48] P. J. Ferreira, G. J. la O', Y. Shao-Horn, D. Morgan, R. Makharia, S. Kocha, H. A. Gasteiger, *J Electrochem Soc* **2005**, *152*, A2256.

[49] P. J. Ferreira, Y. Shao-Horn, *Electrochemical and Solid-State Letters* **2007**, *10*, 63.

[50] H. Yano, M. Watanabe, A. Iiyama, H. Uchida, *Nano Energy* **2016**, *29*, 323.

[51] M. Wakisaka, S. Asizawa, H. Uchida, M. Watanabe, *Physical Chemistry Chemical Physics* **2010**, *12*, 4184.

[52] M. Shao, A. Peles, K. Shoemaker, *Nano Lett* **2011**, *11*, 3714.

[53] T. Lazaridis, B. M. Stühmeier, H. A. Gasteiger, H. A. El-Sayed, *Nat Catal* **2022**, *5*, 363.

[54] **2022**.

[55] S. Stariha, N. Macauley, B. T. Sneed, D. Langlois, K. L. More, R. Mukundan, R. L. Borup, *J Electrochem Soc* **2018**, *165*, F492.

[56] A. Kneer, N. Wagner, *J Electrochem Soc* **2019**, *166*, F120.

[57] A. Kneer, N. Wagner, C. Sadeler, A.-C. Scherzer, D. Gerteisen, *J Electrochem Soc* **2018**, *165*, F805.

[58] A. Kneer, J. Jankovic, D. Susac, A. Putz, N. Wagner, M. Sabharwal, M. Secanell, *J Electrochem Soc* **2018**, *165*, F3241.

[59] M. Alsabet, M. Grden, G. Jerkiewicz, *Journal of Electroanalytical Chemistry* **2006**, *589*, 120.

[60] N. P. Subramanian, T. A. Greszler, J. Zhang, W. Gu, R. Makharia, **2012**, *159*, DOI 10.1149/2.088205jes.

[61] Y. Shao-Horn, W. C. Sheng, S. Chen, P. J. Ferreira, E. F. Holby, D. Morgan, *Top Catal* **2007**, *46*, 285.

[62] J. C. Meier, C. Galeano, I. Katsounaros, J. Witte, H. J. Bongard, A. A. Topalov, C. Baldizzone, S. Mezzavilla, F. Schüth, K. J. J. Mayrhofer, *Beilstein Journal of Nanotechnology* **2014**, *5*, 44.

[63] M. Inaba, T. Kinumoto, M. Kiriake, R. Umebayashi, A. Tasaka, Z. Ogumi, *Electrochim Acta* **2006**, *51*, 5746.

[64] S. Zhang, X. Z. Yuan, J. N. C. Hin, H. Wang, J. Wu, K. A. Friedrich, M. Schulze, *J Power Sources* **2010**, *195*, 1142.

[65] B. Wu, M. Zhao, W. Shi, W. Liu, J. Liu, D. Xing, Y. Yao, Z. Hou, P. Ming, J. Gu, Z. Zou, in *Int J Hydrogen Energy*, Elsevier Ltd, **2014**, pp. 14381–14390.

[66] W. Liu, D. Qiu, L. Peng, X. Lai, *Fuel Cells* **2023**, *23*, 170.

[67] X. Z. Yuan, S. Zhang, H. Wang, J. Wu, J. C. Sun, R. Hiesgen, K. A. Friedrich, M. Schulze, A. Haug, *J Power Sources* **2010**, DOI 10.1016/j.jpowsour.2010.06.023.

[68] Y. Singh, R. T. White, M. Najm, T. Haddow, V. Pan, F. P. Orfino, M. Dutta, E. Kjeang, *J Power Sources* **2019**, *412*, 224.

[69] O. V. Cherstiouk, A. N. Simonov, N. S. Moseva, S. V. Cherepanova, P. A. Simonov, V. I. Zaikovskii, E. R. Savinova, *Electrochim Acta* **2010**, *55*, 8453.

[70] Y. Qi, Y. Huang, Z. Gao, C. H. Chen, A. Perego, H. Yildirim, M. Odgaard, T. Asset, P. Atanassov, I. V. Zenyuk, *J Power Sources* **2022**, *551*, DOI 10.1016/j.jpowsour.2022.232209.

[71] Y. C. Park, K. Kakinuma, M. Uchida, D. A. Tryk, T. Kamino, H. Uchida, M. Watanabe, *Electrochim Acta* **2013**, *91*, 195.

[72] D. Spernjak, J. Fairweather, R. Mukundan, T. Rockward, R. L. Borup, *J Power Sources* **2012**, *214*, 386.

[73] T. Mittermeier, A. Weiß, F. Hasché, H. A. Gasteiger, *J Electrochem Soc* **2018**, *165*, F1349.

[74] S. Ghosh, H. Ohashi, H. Tabata, Y. Hashimasa, T. Yamaguchi, *J Power Sources* **2017**, *362*, 291.

[75] C. A. Reiser, L. Bregoli, T. W. Patterson, J. S. Yi, J. D. Yang, M. L. Perry, T. D. Jarvi, *Electrochemical and Solid-State Letters* **2005**, *8*, 273.

[76] M. M. Mench, E. C. Kumbur, T. N. Veziroglu, *Polymer Electrolyte Fuel Cell Degradation*, Academic Press - Elsevier, **2012**.

[77] F. Lapicque, M. Belhadj, C. Bonnet, J. Pauchet, Y. Thomas, *J Power Sources* **2016**, *336*, 40.

[78] A. P. Young, J. Stumper, S. Knights, E. Gyenge, *J Electrochem Soc* **2010**, *157*, B425.

[79] M. Chandesris, R. Vincent, L. Guetaz, J. S. Roch, D. Thoby, M. Quinaud, *Int J Hydrogen Energy* **2017**, *42*, 8139.

[80] H. Liu, M. G. George, N. Ge, D. Muirhead, P. Shrestha, J. Lee, R. Banerjee, R. Zeis, M. Messerschmidt, J. Scholta, P. Krolla, A. Bazylak, *J Electrochem Soc* **2018**, *165*, F3271.

[81] H. Liu, M. G. George, R. Banerjee, N. Ge, J. Lee, D. Muirhead, P. Shrestha, S. Chevalier, J. Hinebaugh, R. Zeis, M. Messerschmidt, J. Scholta, A. Bazylak, *J Electrochem Soc* **2017**, *164*, F704.

[82] S. Kim, B. K. Ahn, M. M. Mench, *J Power Sources* **2008**, *179*, 140.

[83] S. Kim, M. M. Mench, *J Power Sources* **2007**, *174*, 206.

[84] Y. Pan, H. Wang, N. P. Brandon, *J Power Sources* **2021**, *513*, DOI 10.1016/j.jpowsour.2021.230560.

[85] R. A. Antunes, M. C. L. Oliveira, G. Ett, V. Ett, *Int J Hydrogen Energy* **2010**, *35*, 3632.

[86] J. D. Fairweather, D. Spernjak, A. Z. Weber, D. Harvey, S. Wessel, D. S. Hussey, D. L. Jacobson, K. Artyushkova, R. Mukundan, R. L. Borup, *J Electrochem Soc* **2013**, *160*, F980.

[87] R. Lin, F. Xiong, W. C. Tang, L. Técher, J. M. Zhang, J. X. Ma, *J Power Sources* **2014**, *260*, 150.

[88] T. Lochner, L. Hallitzky, M. Perchthaler, M. Obermaier, J. Sabawa, S. Enz, A. S. Bandarenka, *Appl Energy* **2020**, *260*, 114291.

[89] R. T. White, S. H. Eberhardt, Y. Singh, T. Haddow, M. Dutta, F. P. Orfino, E. Kjeang, *Sci Rep* **2019**, *9*, DOI 10.1038/s41598-018-38464-9.

[90] J. Hack, L. Rasha, P. L. Cullen, J. J. Bailey, T. P. Neville, P. R. Shearing, N. P. Brandon, D. J. L. Brett, *Electrochim Acta* **2020**, *352*, 136464.

[91] L. Cheng, K. Khedekar, M. Rezaei Talarposhti, A. Perego, M. Metzger, S. Kuppan, S. Stewart, P. Atanassov, N. Tamura, N. Craig, I. V. Zenyuk, C. M. Johnston, *Adv Energy Mater* **2020**, *2000623*, 1.

[92] K. Khedekar, M. R. Talarposhti, M. M. Besli, S. Kuppan, A. Perego, Y. Chen, M. Metzger, S. Stewart, P. Atanassov, N. Tamura, N. Craig, L. Cheng, C. M. Johnston, I. V Zenyuk, *Adv Energy Mater* **2021**, *11*, 2101794.

[93] J. Stumper, S. A. Campbell, D. P. Wilkinson, M. C. Johnson, M. Davis, *Electrochim Acta* **1998**, *43*, 3773.

[94] S. J. C. Cleghorn, C. R. Derouin, M. S. Wilson, S. Gottesfeld, *J Appl Electrochem* **1998**, *28*, 663.

[95] M. M. Mench, C. Y. Wang, M. Ishikawa, *J Electrochem Soc* **2003**, *150*, A1052.

[96] C. Kalyvas, A. Kucernak, D. Brett, G. Hinds, S. Atkins, N. Brandon, *Wiley Interdiscip Rev Energy Environ* **2014**, *3*, 254.

[97] C. Wieser, A. Helmbold, E. Gülzow, *J Appl Electrochem* **2000**, *30*, 803.

[98] L. C. Pérez, L. Brandão, J. M. Sousa, A. Mendes, *Renewable and Sustainable Energy Reviews* **2011**, *15*, 169.

[99] R. Lin, F. Xiong, W. C. Tang, L. Técher, J. M. Zhang, J. X. Ma, *J Power Sources* **2014**, *260*, 150.

[100] H. Wang, X.-Z. Yuan, H. Li, *PEM Fuel Cell Diagnostic Tools*, CRC Press, Taylor & Francis Group, Boca Raton, FL, **2011**.

[101] R. Mosdale, G. Gebel, M. Pineri, *J Memb Sci* **1996**, *118*, 269.

[102] R. J. Bellows, M. Y. Lin, M. Arif, A. K. Thompson, D. Jacobson, *J Electrochem Soc* **1999**, *146*, 1099.

[103] R. Satija, D. L. Jacobson, M. Arif, S. A. Werner, *J Power Sources* **2004**, *129*, 238.

[104] I. A. Schneider, D. Kramer, A. Wokaun, G. G. Scherer, *Electrochem commun* **2005**, *7*, 1393.

[105] U. Beuscher, *J Electrochem Soc* **2006**, *153*, A1788.

[106] T. A. Trabold, J. P. Owejan, D. L. Jacobson, M. Arif, P. R. Huffman, *Int J Heat Mass Transf* **2006**, *49*, 4712.

[107] J. Zhang, D. Kramer, R. Shimoi, Y. Ono, E. Lehmann, A. Wokaun, K. Shinohara, G. G. Scherer, *Electrochim Acta* **2006**, *51*, 2715.

[108] A. Turhan, K. Heller, J. S. Brenizer, M. M. Mench, *J Power Sources* **2006**, *160*, 1195.

[109] M. A. Hickner, N. P. Siegel, K. S. Chen, D. S. Hussey, D. L. Jacobson, M. Arif, *J Electrochem Soc* **2008**, *155*, B294.

[110] M. A. Hickner, N. P. Siegel, K. S. Chen, D. S. Hussey, D. L. Jacobson, M. Arif, *J Electrochem Soc* **2008**, *155*, B427.

[111] A. Turhan, K. Heller, J. S. Brenizer, M. M. Mench, *J Power Sources* **2008**, *180*, 773.

[112] C. Hartnig, I. Manke, N. Kardjilov, A. Hilger, M. Grünerbel, J. Kaczerowski, J. Banhart, W. Lehnert, *J Power Sources* **2008**, *176*, 452.

[113] P. Boillat, E. H. Lehmann, P. Trtik, M. Cochet, *Curr Opin Electrochem* **2017**, *5*, 3.

[114] V. Manzi-Orezzoli, M. Siegwart, M. Cochet, T. J. Schmidt, P. Boillat, *J Electrochem Soc* **2020**, *167*, 054503.

[115] P. Sharma, B. Bera, D. Aaron, M. M. Besli, S. Kuppan, L. Cheng, J. Braaten, N. Craig, S. Stewart, M. Metzger, C. Johnston, M. M. Mench, *J Electrochem Soc* **2022**, *169*, 114506.

[116] P. Ren, P. Pei, Y. Li, Z. Wu, D. Chen, S. Huang, *Prog Energy Combust Sci* **2020**, *80*, 100859.

[117] R. K. Ahluwalia, X. Wang, J.-K. Peng, V. Konduru, S. Arisetty, N. Ramaswamy, S. Kumaraguru, *J Electrochem Soc* **2021**, *168*, 044518.

[118] M. Breitwieser, M. Klingele, S. Vierrath, R. Zengerle, S. Thiele, *Adv Energy Mater* **2018**, *8*, DOI 10.1002/aenm.201701257.

[119] J. Hack, L. Rasha, P. L. Cullen, J. J. Bailey, T. P. Neville, P. R. Shearing, N. P. Brandon, D. J. L. Brett, *Electrochim Acta* **2020**, *352*, 136464.

[120] I. Martens, A. Vamvakeros, N. Martinez, J. Pusa, M. V. Blanco, E. A. Fisher, T. Asset, S. Escribano, F. Micoud, T. Starr, A. Coelho, V. Honkim, D. Bizzotto, D. P. Wilkinson, S. D. M. Jacques, L. Dubau, S. Lyonnard, A. Morin, J. Drnec, *ACS Energy Lett* **2021**, DOI 10.1021/acsenergylett.1c00718.

[121] R. L. Borup, A. Kusoglu, K. C. Neyerlin, R. Mukundan, R. K. Ahluwalia, D. A. Cullen, K. L. More, A. Z. Weber, D. J. Myers, *Curr Opin Electrochem* **2020**, *21*, 192.

[122] P. Sharma, B. Bera, D. Aaron, M. M. Besli, Z. Taie, L. Cheng, S. Stewart, S. Kuppan, C. Johnston, M. Metzger, M. M. Mench, *{ECS} Meeting Abstracts* **2020**, *{MA}2020-0*, 2345.

[123] R. N. Carter, S. S. Kocha, F. Wagner, M. Fay, H. A. Gasteiger, **2007**, 403.

[124] T. R. Garrick, T. E. Moylan, M. K. Carpenter, A. Kongkanand, *J Electrochem Soc* **2017**, *164*, F55.

[125] B. H. Toby, R. B. Von Dreele, *J Appl Crystallogr* **2013**, *46*, 544.

[126] I. E. L. Stephens, A. S. Bondarenko, U. Grønbjerg, J. Rossmeisl, I. Chorkendorff, *Energy Environ Sci* **2012**, *5*, 6744.

[127] S. Mukerjee, *J Appl Electrochem* **1990**, *20*, 537.

[128] A. A. Topalov, S. Cherevko, A. R. Zeradjanin, J. C. Meier, I. Katsounaros, K. J. J. Mayrhofer, *Chem Sci* **2014**, *5*, 631.

[129] K. Yu, D. J. Groom, X. Wang, Z. Yang, M. Gummalla, S. C. Ball, D. Myers, P. J. Ferreira, *Microscopy and Microanalysis* **2014**, *20*, 482.

[130] P. Zihrul, I. Hartung, S. Kirsch, G. Huebner, F. Hasché, H. A. Gasteiger, *J Electrochem Soc* **2016**, *163*, F492.

[131] H. Yu, A. Baricci, A. Bisello, A. Casalegno, L. Guetaz, L. Bonville, R. Maric, *Electrochim Acta* **2017**, *247*, 1155.

[132] M. K. Debe, A. K. Schmoeckel, G. D. Vernstrom, R. Atanasoski, *J Power Sources* **2006**, *161*, 1002.

[133] W. Bi, Thomas. F. Fuller, *J Electrochem Soc* **2008**, *155*, B215.

[134] M. Messing, E. Kjeang, *J Power Sources* **2020**, *451*, 227750.

[135] M. Moein-Jahromi, M. J. Kermani, S. Movahed, *J Power Sources* **2017**, *359*, 611.

[136] G. S. Harzer, J. N. Schwämmlein, A. M. Damjanović, S. Ghosh, H. A. Gasteiger, *J Electrochem Soc* **2018**, *165*, F3118.

[137] K. Khedekar, M. R. Talarposhti, M. M. Besli, S. Kuppan, A. Perego, Y. Chen, M. Metzger, S. Stewart, P. Atanassov, N. Tamura, N. Craig, L. Cheng, C. M. Johnston, I. V Zenyuk, *Adv Energy Mater* **2021**, DOI 10.1002/aenm.202101794.

[138] C. Takei, K. Kakinuma, K. Kawashima, K. Tashiro, M. Watanabe, M. Uchida, *J Power Sources* **2016**, *324*, 729.

[139] N. Macauley, D. D. Papadias, J. Fairweather, D. Spernjak, D. Langlois, R. Ahluwalia, K. L. More, R. Mukundan, R. L. Borup, *J Electrochem Soc* **2018**, *165*, F3148.

[140] M. Inaba, T. Kinumoto, M. Kiriake, R. Umebayashi, A. Tasaka, Z. Ogumi, *Electrochim Acta* **2006**, *51*, 5746.

[141] M. Chandesris, R. Vincent, L. Guetaz, J. S. Roch, D. Thoby, M. Quinaud, *Int J Hydrogen Energy* **2017**, *42*, 8139.

[142] A. Turhan, S. Kim, M. Hatzell, M. M. Mench, *Electrochim Acta* **2010**, *55*, 2734.

[143] M. C. Hatzell, A. Turhan, S. Kim, D. S. Hussey, D. L. Jacobson, M. M. Mench, *J Electrochem Soc* **2011**, *158*, B717.

[144] S. Kim, M. M. Mench, *J Memb Sci* **2009**, *328*, 113.

[145] S. Kim, M. M. Mench, *J Electrochem Soc* **2009**, *156*, B353.

[146] P. A. García-Salaberri, D. G. Sánchez, P. Boillat, M. Vera, K. A. Friedrich, *J Power Sources* **2017**, *359*, 634.

[147] J. M. LaManna, D. S. Aaron, M. M. Mench, *J Electrochem Soc* **2020**, *167*, 104504.

[148] Y. Wang, C. Y. Wang, *J Power Sources* **2006**, *153*, 130.

[149] A. D. Santamaria, M. K. Becton, N. J. Cooper, A. Z. Weber, J. W. Park, *J Power Sources* **2015**, *293*, 162.

[150] W. Bi, Q. Sun, Y. Deng, T. F. Fuller, *Electrochim Acta* **2009**, *54*, 1826.

[151] Q. Wang, B. Li, D. Yang, H. Dai, J. P. Zheng, P. Ming, C. Zhang, *J Power Sources* **2021**, *492*, 229613.

[152] S. Shimpalee, P. Satjaritanun, S. Hirano, N. Tippayawong, J. W. Weidner, *J Electrochem Soc* **2019**, *166*, F534.

[153] P. Sharma, L. Cheng, D. Aaron, S. Mehrazi, J. Braaten, N. Craig, C. Johnston, M. M. Mench, *Small* **2023**, DOI 10.1002/smll.202306433.

[154] C. G. Chung, L. Kim, Y. W. Sung, J. Lee, J. S. Chung, *Int J Hydrogen Energy* **2009**, *34*, 8974.

[155] L. Cheng, K. Khedekar, M. Rezaei Talarposhti, A. Perego, M. Metzger, S. Kuppan, S. Stewart, P. Atanassov, N. Tamura, N. Craig, I. V. Zenyuk, C. M. Johnston, *Adv Energy Mater* **2020**, *2000623*, 1.

[156] I. Martens, A. Vamvakeros, N. Martinez, R. Chattot, J. Pusa, M. V. Blanco, E. A. Fisher, T. Asset, S. Escribano, F. Micoud, T. Starr, A. Coelho, V. Honkimäki, D. Bizzotto, D. P. Wilkinson, S. D. M. Jacques, F. Maillard, L. Dubau, S. Lyonnard, A. Morin, J. Drnec, *ACS Energy Lett* **2021**, *6*, 2742.

[157] T. V. Reshetenko, G. Bender, K. Bethune, R. Rocheleau, *Electrochim Acta* **2013**, *88*, 571.

[158] I. Alaefour, G. Karimi, K. Jiao, X. Li, *Appl Energy* **2012**, *93*, 80.

[159] H. Shao, D. Qiu, L. Peng, P. Yi, X. Lai, *J Power Sources* **2019**, *412*, 717.

[160] L. Peng, H. Shao, D. Qiu, P. Yi, X. Lai, *J Power Sources* **2020**, *453*, 227836.

[161] R. Eckl, R. Grinzinger, W. Lehnert, *J Power Sources* **2006**, *154*, 171.

[162] J. T. Clement, D. S. Aaron, M. M. Mench, *J Electrochem Soc* **2016**, *163*, A5220.

[163] K. Shinozaki, H. Yamada, Y. Morimoto, *J Electrochem Soc* **2011**, *158*, B467.

[164] R. N. Carter, S. S. Kocha, F. Wagner, M. Fay, H. A. Gasteiger, *ECS Trans* **2007**, *11*, 403.

[165] S. Kabir, D. J. Myers, N. Kariuki, J. Park, G. Wang, A. Baker, N. Macauley, R. Mukundan, K. L. More, K. C. Neyerlin, *ACS Appl Mater Interfaces* **2019**, DOI 10.1021/acsami.9b11365.

[166] X. Wang, S. DeCrane, T. Nowicki, N. N. Kariuki, S. C. Ball, D. J. Myers, *J Electrochem Soc* **2021**, *168*, 054516.

[167] J. P. Owejan, J. E. Owejan, W. Gu, *J Electrochem Soc* **2013**, *160*, F824.

[168] A. Orfanidi, P. Madkikar, H. A. El-Sayed, G. S. Harzer, T. Kratky, H. A. Gasteiger, *J Electrochem Soc* **2017**, *164*, F418.

[169] G. S. Harzer, A. Orfanidi, H. El-Sayed, P. Madkikar, H. A. Gasteiger, *J Electrochem Soc* **2018**, *165*, F770.

[170] M. Belhadj, A. Aquino, J. Heng, S. Kmiotek, S. Raël, C. Bonnet, F. Lapicque, *Chem Eng Sci* **2018**, *185*, 18.

[171] Q. Dong, M. M. Mench, S. Cleghorn, U. Beuscher, *J Electrochem Soc* **2005**, *152*, A2114.

[172] S. Enz, T. A. Dao, M. Messerschmidt, J. Scholta, *J Power Sources* **2015**, *274*, 521.

[173] N. Linse, L. Gubler, G. G. Scherer, A. Wokaun, *Electrochim Acta* **2011**, *56*, 7541.

[174] J. Zhang, B. A. Litteer, W. Gu, H. Liu, H. A. Gasteiger, *J Electrochem Soc* **2007**, *154*, B1006.

[175] K. Yoshizawa, K. Ikezoe, Y. Tasaki, D. Kramer, E. H. Lehmann, G. G. Scherer, *J Electrochem Soc* **2008**, *155*, B223.

[176] D. Spernjak, S. G. Advani, A. K. Prasad, *J Electrochem Soc* **2009**, *156*, B109.

[177] Y. Yin, R. Li, F. Bai, W. Zhu, Y. Qin, Y. Chang, J. Zhang, M. D. Guiver, *Electrochem commun* **2019**, *109*, 106590.

[178] K. Nagamori, S. Aoki, M. Ikegawa, K. Tamoto, Y. Honda, Y. Seki, H. Igarashi, M. Uchida, *ACS Appl Energy Mater* **2023**, DOI 10.1021/acsaem.3c01706.

[179] "https://www.energy.gov/industrial-technologies/doe-industrial-decarbonization-roadmap," **2022**.

[180] Z. P. Cano, D. Banham, S. Ye, A. Hintennach, J. Lu, M. Fowler, Z. Chen, *Nat Energy* **2018**, *3*, 279.

[181] K. Khedekar, A. Zaffora, M. Santamaria, M. Coats, S. Pylypenko, J. Braaten, P. Atanassov, N. Tamura, L. Cheng, C. Johnston, I. V. Zenyuk, *Nat Catal* **2023**, DOI 10.1038/s41929-023-00993-6.

[182] S. Tanaka, K. Nagumo, M. Yamamoto, H. Chiba, K. Yoshida, R. Okano, *eTransportation* **2020**, *3*, DOI 10.1016/j.etran.2020.100046.

[183] M. P. Manahan, M. C. Hatzell, E. C. Kumbur, M. M. Mench, *J Power Sources* **2011**, *196*, 5573.

[184] E. H. Lehmann, P. Vontobel, L. Wiezel, in *Nondestructive Testing and Evaluation*, Gordon And Breach Science Publishers Inc., **2001**, pp. 191–202.

[185] P. Boillat, A. Iranzo, J. Biesdorf, *J Electrochem Soc* **2015**, *162*, F531.

[186] P. Boillat, **n.d.**, DOI 10.3929/ethz-a-005911827.

[187] P. Boillat, D. Kramer, B. C. Seyfang, G. Frei, E. Lehmann, G. G. Scherer, A. Wokaun, Y. Ichikawa, Y. Tasaki, K. Shinohara, *Electrochem commun* **2008**, *10*, 546.

[188] A. Iranzo, G. M. Cabello González, B. Toharias, P. Boillat, F. Rosa, *Int J Hydrogen Energy* **2024**, *50*, 221.

[189] K. Khedekar, P. Satjaritanun, S. Stewart, J. Braaten, P. Atanassov, N. Tamura, L. Cheng, C. M. Johnston, I. V. Zenyuk, *Small* **2022**, 2201750.

[190] L. I. Astudillo, H. A. Gasteiger, *J Electrochem Soc* **2023**, *170*, 124512.

[191] R. K. F. Della Bella, B. M. Stühmeier, H. Gasteiger, *J Electrochem Soc* **2022**, DOI 10.1149/1945-7111/ac67b8.

[192] C. Lim, L. Ghassemzadeh, F. Van Hove, M. Lauritzen, J. Kolodziej, G. G. Wang, S. Holdcroft, E. Kjeang, *J Power Sources* **2014**, *257*, 102.

[193] A. Turhan, K. Heller, J. S. Brenizer, M. M. Mench, *J Power Sources* **2006**, *160*, 1195.

[194] J. M. Lamanna, S. Chakraborty, J. J. Gagliardo, M. M. Mench, *Int J Hydrogen Energy* **2014**, *39*, 3387.

[195] P. Satjaritanun, S. Shimpalee, I. V. Zenyuk, *Acc Mater Res* **2022**, DOI 10.1021/accountsmr.1c00125.

[196] H. Liu, M. G. George, M. Messerschmidt, R. Zeis, D. Kramer, J. Scholta, A. Bazylak, *J Electrochem Soc* **2017**, *164*, F695.

[197] J. Sim, J. Kim, H. Chun, J. Chang, Y. Kim, B. Kim, S. Kang, K. Min, *J Power Sources* **2024**, *595*, DOI 10.1016/j.jpowsour.2023.234026.

[198] C. H. Lee, W. J. M. Kort-Kamp, H. Yu, D. A. Cullen, B. M. Patterson, T. A. Arman, S. Komini Babu, R. Mukundan, R. L. Borup, J. S. Spendelow, *Nat Energy* **2023**, DOI 10.1038/s41560-023-01263-2.

[199] G. Yang, S. K. Babu, W. P. R. Liyanage, U. Martinez, D. Routkevitch, R. Mukundan, R. L. Borup, D. A. Cullen, J. S. Spendelow, *Advanced Materials* **2023**, DOI 10.1002/adma.202301264.

[200] J. P. Owejan, S. G. Goebel, *J Power Sources* **2021**, *494*, DOI 10.1016/j.jpowsour.2021.229740.

Appendices

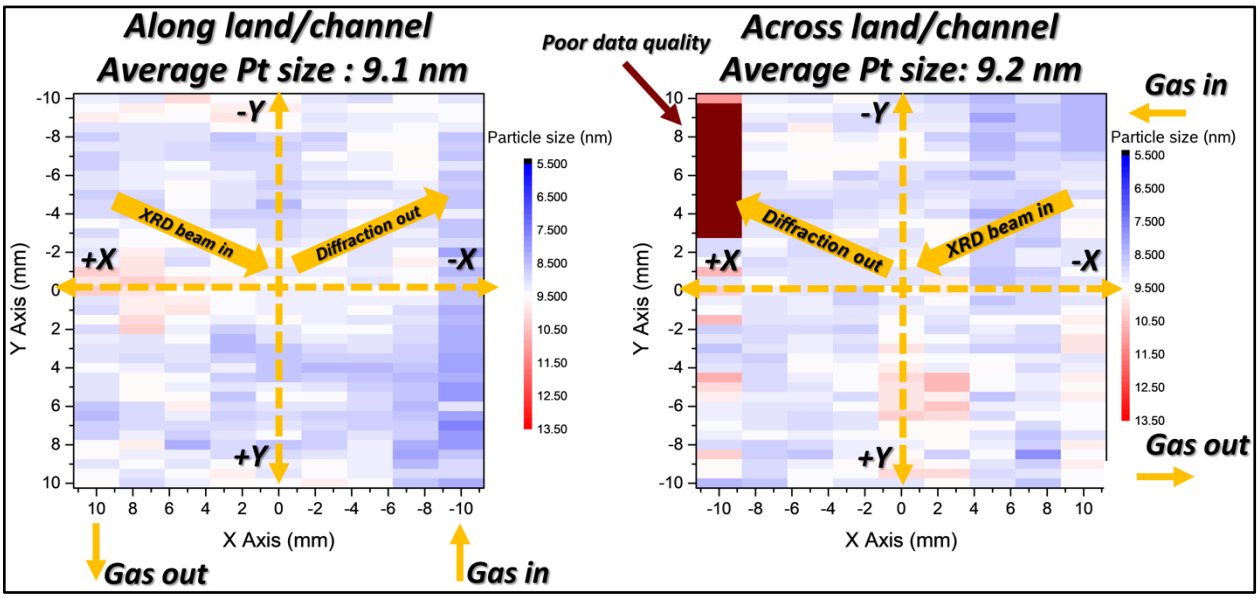


Figure S2.1. No difference in the average Pt particle size was observed when measuring the sample in a different direction, i.e., when resolving along the land and channels as opposed to across.

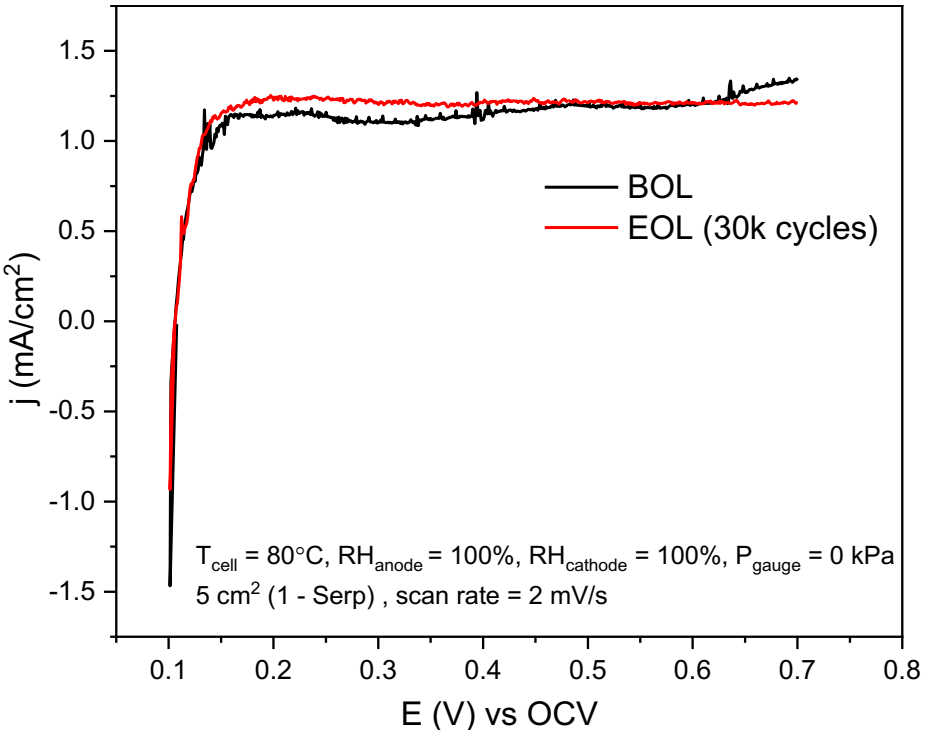


Figure S2.2. Linear scan voltammograms (LSVs) of a sample MEA (subjected to 16 sccm/cm^2 N_2 flow rate during the AST) at the BOL and EOL, recorded in H_2/N_2 atmosphere at 2 mV/s, 80 °C cell temperature, 100 % relative humidity on both sides and at atmospheric backpressure.

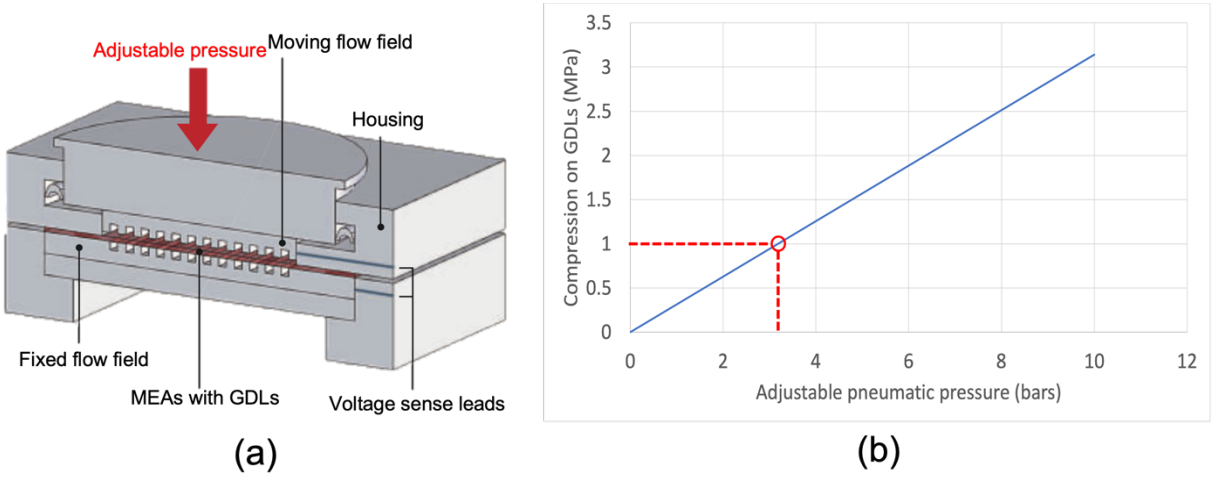
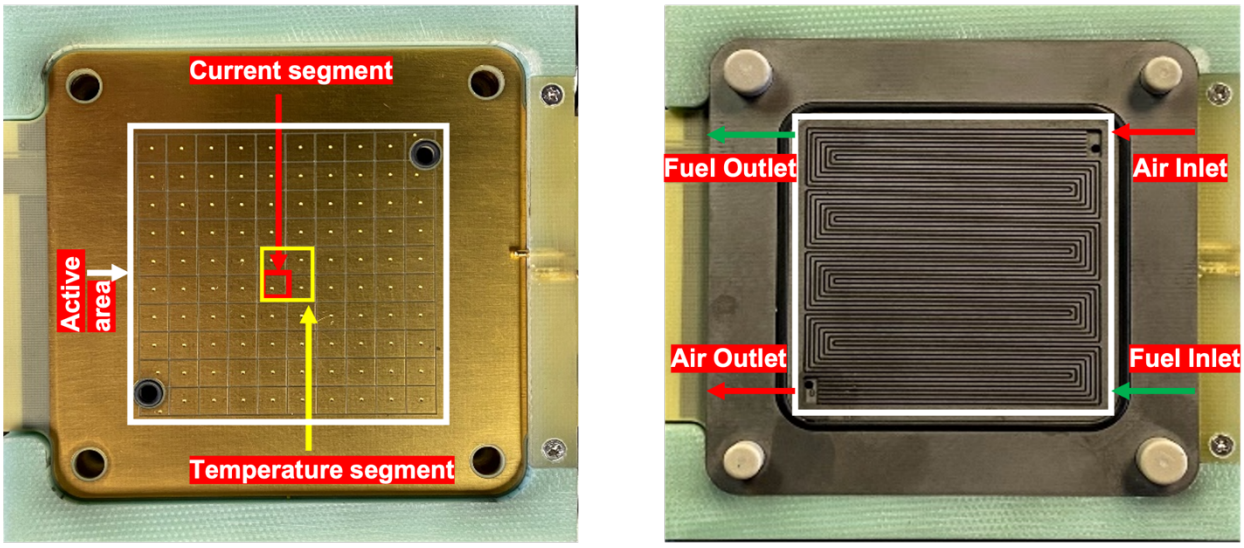


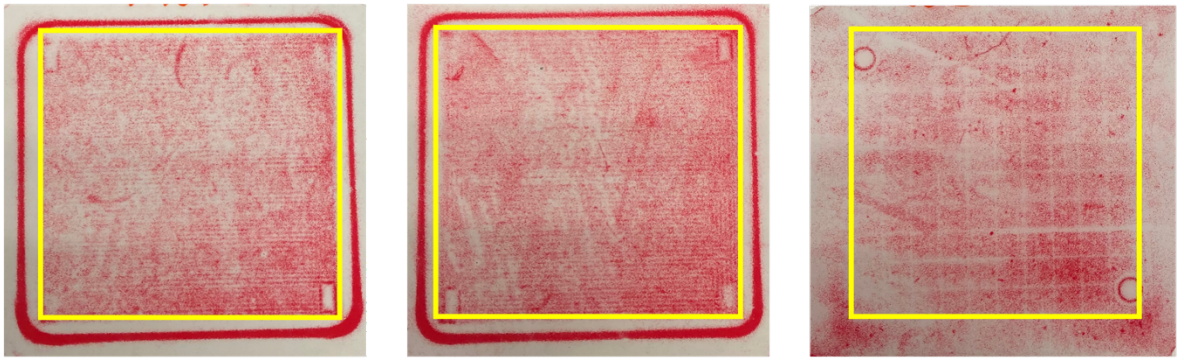
Figure S3.3. (a) Schematic of Baltic cell fixture, (b) compression pressure on the gas diffusion layers (GDLs) (in MPa) vs. adjustable pneumatic pressure. In the present study, a pneumatic pressure of ~3.2 bars was applied to achieve a compression pressure of ~1 MPa on the GDLs.



(a) Current distribution board

(b) Cathode flow field bolted on top of the current distribution board

Figure S3.4. Images of (a) current distribution board with current and temperature measurement segments, (b) cathode flow field bolted on top of the current distribution board. The air and fuel inlet/outlet are marked. The anode flow field is identical to the cathode flow field and the fuel i.e., hydrogen enters at the bottom and leaves at the top. The air enters at the top and leaves at the bottom.



(a) Pressure film between cathode flow field and GDL

(b) Pressure film between anode flow field and GDL

(c) Pressure film between cathode flow field and CDD board

Figure S3.5. Compression paper (Fujifilm Prescale® Super Low film) images showing uniform compression between (a) cathode flow field and the GDL, (b) anode flow field and the GDL, and (c) cathode flow field and the current density distribution (CDD) board. The yellow square in the images depicts the active area (25 cm^2). The impression of the flow fields can be clearly seen in (a) and (b). Also, the air inlet and the outlet O-rings can be identified in (c).

Data reduction procedure for current and temperature distributions

The data reduction procedure involves several stages to analyze the current distribution at a particular operational condition. The raw current distribution is initially smoothed and plotted as a percentage deviation from the average current at that operating condition (see panels (a) and (b) in Figure S3.6). This representation of the current distribution facilitates the identification of regions with low or high currents. Subsequently, these distributions are adjusted for minor ohmic variations, as shown in Figure S3.7.

Next, the percentage deviation maps from the mean current at geometric current densities of 0.01 A/cm^2, 0.02 A/cm^2, 0.05 A/cm^2, and 0.1 A/cm^2 for any specific cell build are averaged to produce a distribution (Figure S3.7 (e)). The average is performed assuming that current distributions at such low geometric current densities should be relatively uniform. Any variations observed in the current distributions can be attributed to minor ohmic variations inherent to a particular cell build. The very low geometric current density distributions are essentially identical, as observed from panels (a) to (d) in Figure S3.7, thus confirming their likely derivation from minor ohmic variations. The averaged distribution from Figure S3.7 (e) is then subtracted from the uncorrected distributions at higher geometric current densities to correct for minor ohmic variations. The resulting distribution at 1 A/cm^2 is depicted in Figure S3.7 (h).

For further validation of this correction method, a test was conducted with a configuration where the air inlet and the outlet were reversed, but the fuel inlet and outlet remained unchanged. The resulting distributions are displayed in Figure S3.8. Notably, the averaged distributions used for the correction in both unflipped and flipped cases are identical (see panels (a) and (e) in Figure S3.8). This observation supports the assumption that at such low geometric current densities, any fluctuations noticed in current distributions are mainly due to minor ohmic variations. The corrected distributions, ranging from 0.5 to 1.5 A/cm^2, indicate regions of high and low current near the air inlet and outlet, respectively. The correction methodology is further exemplified for a case with lower inlet relative humidity (RH of 50% at the anode and cathode), keeping all other parameters constant from Figure S3.8. The resulting distributions are demonstrated in Figure S3.9. To summarize, the flipping of the air inlet and outlet and the operation under lower inlet relative humidity illustrate the robustness of the correction methodology applied to current distributions in this study.

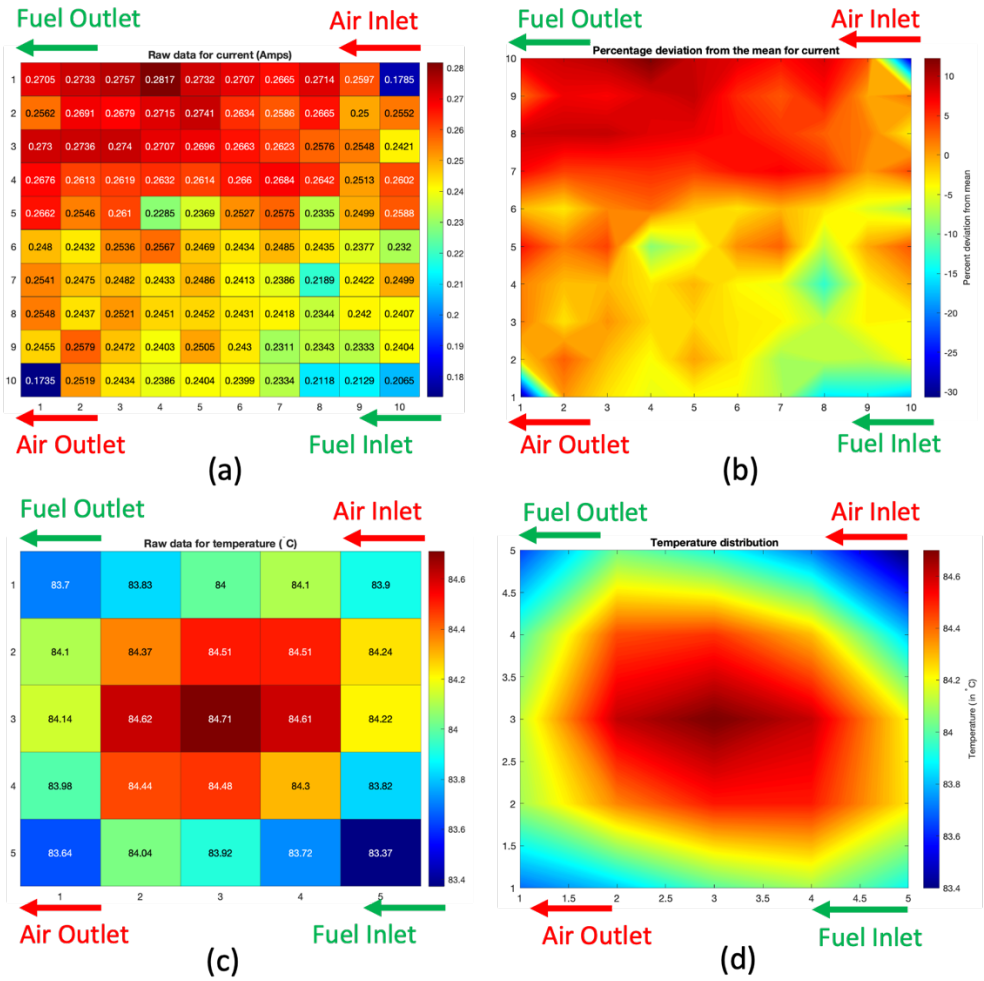


Figure S3.6. (a) Raw current (amps) in the 100 segments at the average cell current of 25 A (1 A/cm^2), (b) smoothed contours of percentage deviation from the mean current measured in (a), (c) raw temperature data (in °C) in the 25 segments at 25 A (1 A/cm^2), and (d) smoothed contours of raw temperature data measured in (c). All the distributions were recorded at T_{cell} = 80 °C, $\lambda_{H_2}/\lambda_{Air}$ = 1.5/2, and $RH\%_{\,A/C}$ = 100/100 with $P_{abs\,A/C}$ = 150/150 kPa.

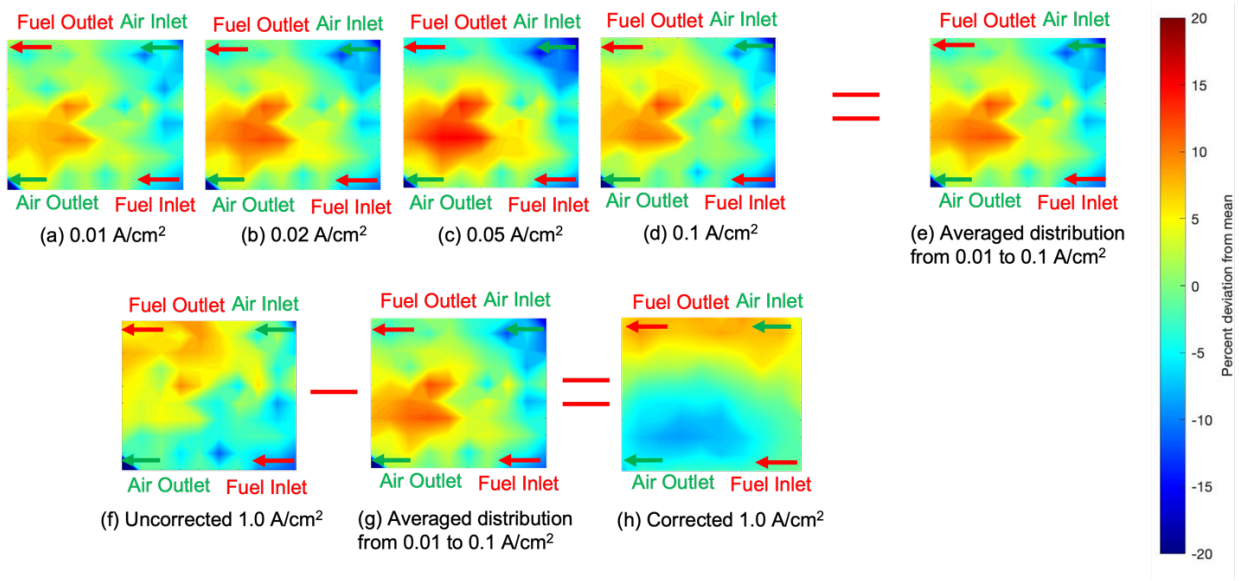


Figure S3.7. Correction methodology for current density distributions (CDD). Raw current distributions plotted as the percentage deviation from mean at low geometric current densities (a) to (d) are averaged to obtain distribution in (e). This distribution is then subtracted from a distribution at high geometric current density (f) to obtain a corrected distribution in (h). All the distributions were recorded at T_{cell} = 80 °C, $\lambda_{H_2}/\lambda_{Air}$ = 1.5/2, and $RH\%_{\,A/C}$ = 100/100 with $P_{abs\,A/C}$ = 150/150 kPa.

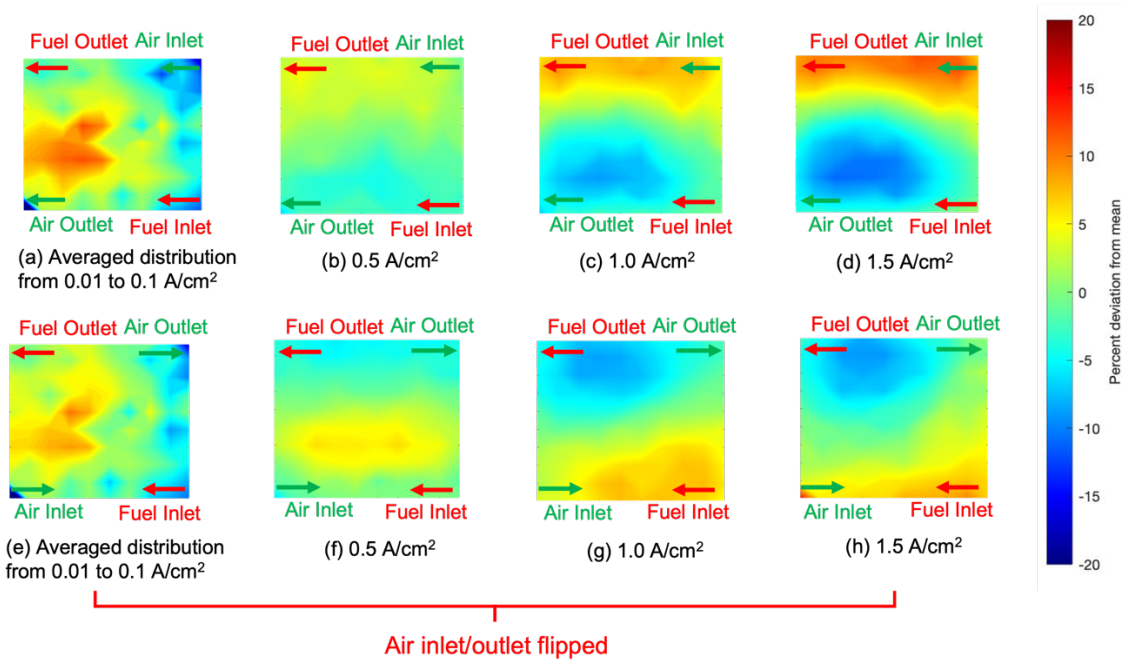


Figure S3.8. (b) to (d) are corrected distributions obtained from subtracting the averaged distribution in (a) at high geometric current densities. (f) to (h) are corrected distributions obtained from subtracting the averaged distribution in (e) at high geometric current densities with the flipped air inlet and outlet as compared to distributions in (a) to (d) to verify the robustness of the correction approach. All the distributions were recorded at T_{cell} = 80 °C, $\lambda_{H_2}/\lambda_{Air}$ = 1.5/2, and $RH\%_{\,A/C}$ = 100/100 with $P_{abs\,A/C}$ = 150/150 kPa.

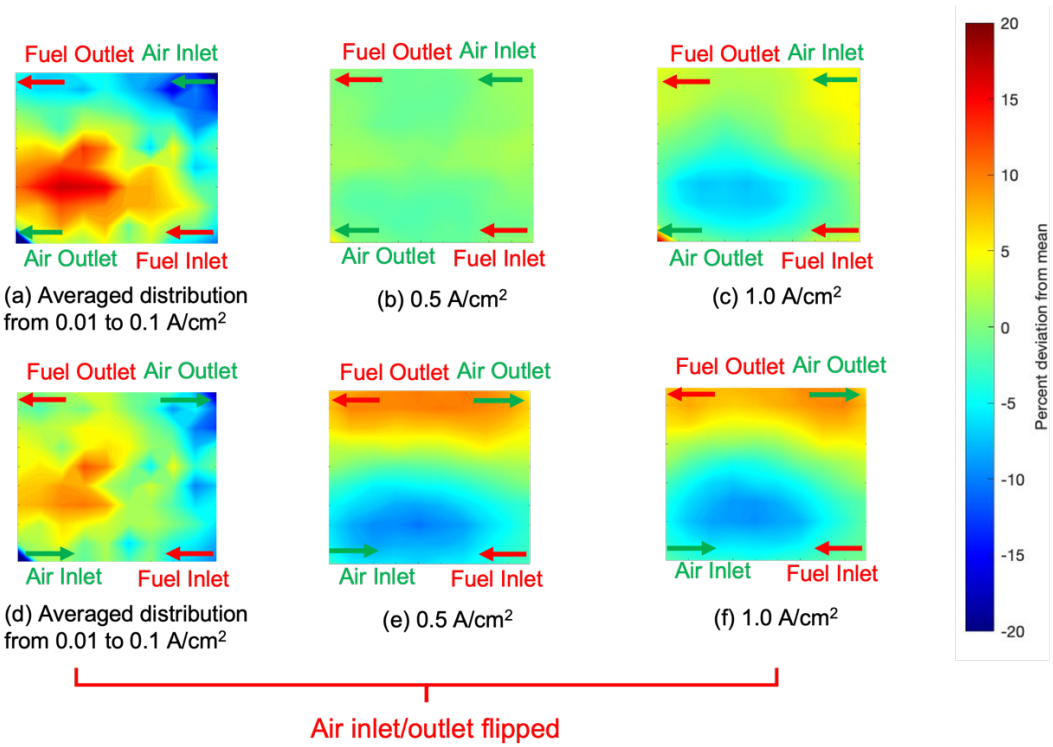


Figure S3.9. (b) and (c) are corrected distributions obtained from subtracting the averaged distribution in (a) at high geometric current densities under dry inlet conditions ($RH\%_{A/C}$ = 50/50). (e) and (f) are corrected distributions obtained from subtracting the averaged distribution in (d) at high geometric current densities with the flipped air inlet and outlet as compared to distributions in (a) to (c), to test the robustness of the correction approach at dry inlet conditions ($RH\%_{A/C}$ = 50/50). All the distributions were recorded at T_{cell} = 80 °C, $\lambda_{H_2}/\lambda_{Air}$ = 1.5/2, and $RH\%_{A/C}$ = 50/50 with $P_{abs\ A/C}$ = 150/150 kPa.

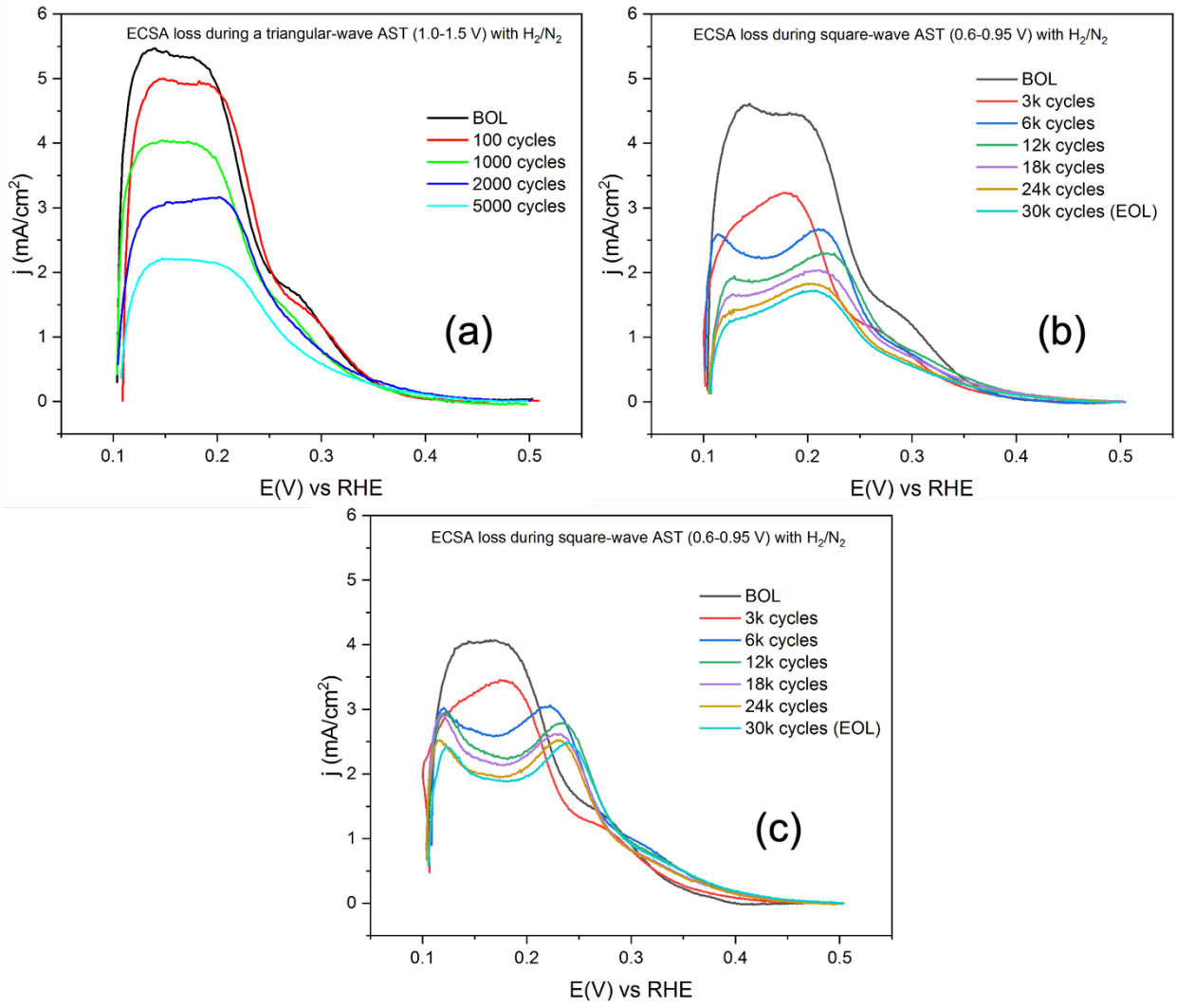


Figure S3.10. Cyclic voltammograms (CVs) of the hydrogen desorption region after baseline correction for double-layer capacitance at the beginning-of-life (BOL) and different stages during the accelerated stress tests (ASTs) for (a) CC AST and (b) Pt AST-Wet, and (c) Pt AST-Dry measured under H_2/N_2 atmosphere at $T_{cell} = 80$ °C, $RH\%_{A/C} = 100/100$ with no backpressure.

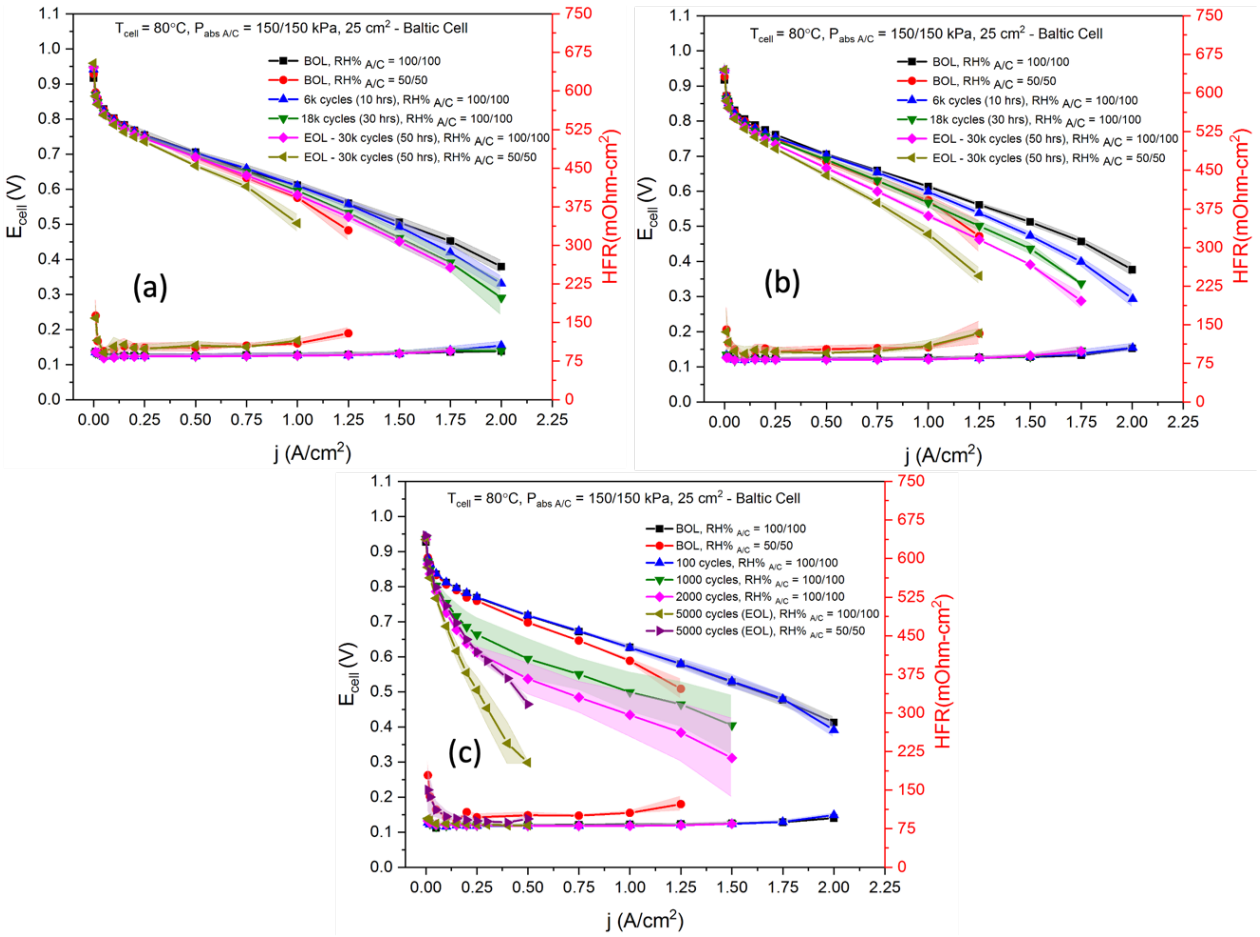


Figure S3.11. (a) Polarization performance of the membrane electrode assemblies (MEAs) at the BOL and different stages of the ASTs for (a) Pt AST-Dry, (b) Pt AST-Wet, and (c) CC AST. Polarization curves were recorded at T_{cell} = 80 °C, $\lambda_{H_2}/\lambda_{Air}$ = 1.5/2, inlet $RH\%_{A/C}$ = 100/100 and 50/50 with $P_{abs\ A/C}$ = 150/150 kPa.

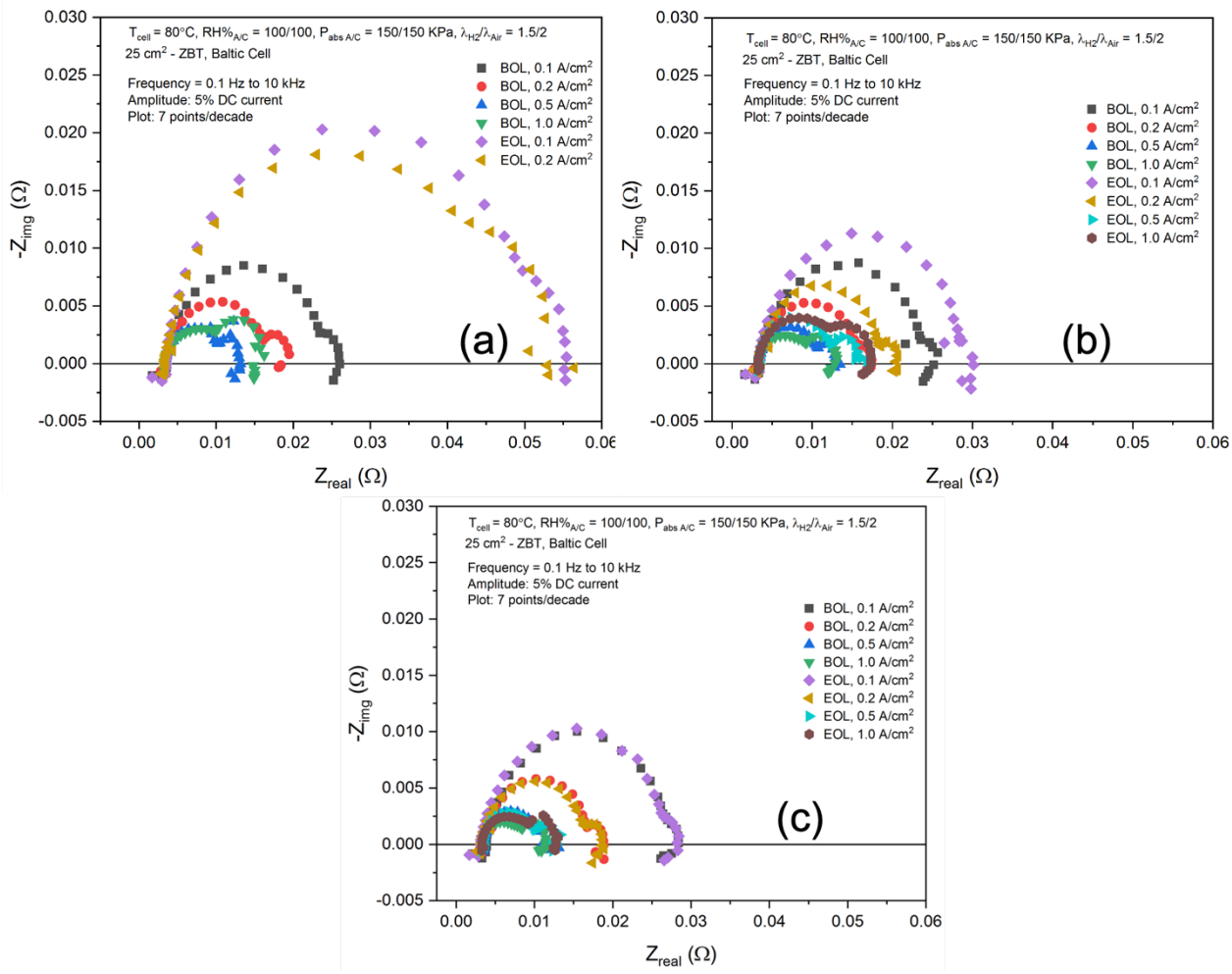


Figure S3.12. Electrochemical impedance spectroscopy (EIS) spectra (0.1 Hz to 10 kHz, 5 % DC current amplitude, 7 points/decade) measured at the BOL and end-of-life (EOL) for (a) CC AST, (b) Pt AST-Wet, and (c) Pt AST-Dry at different geometric current densities. The spectra were recorded at T_{cell} = 80 °C, $\lambda_{H_2}/\lambda_{Air}$ = 1.5/2, and $RH\%_{\,A/C}$ = 100/100 with $P_{abs\ A/C}$ = 150/150 kPa.

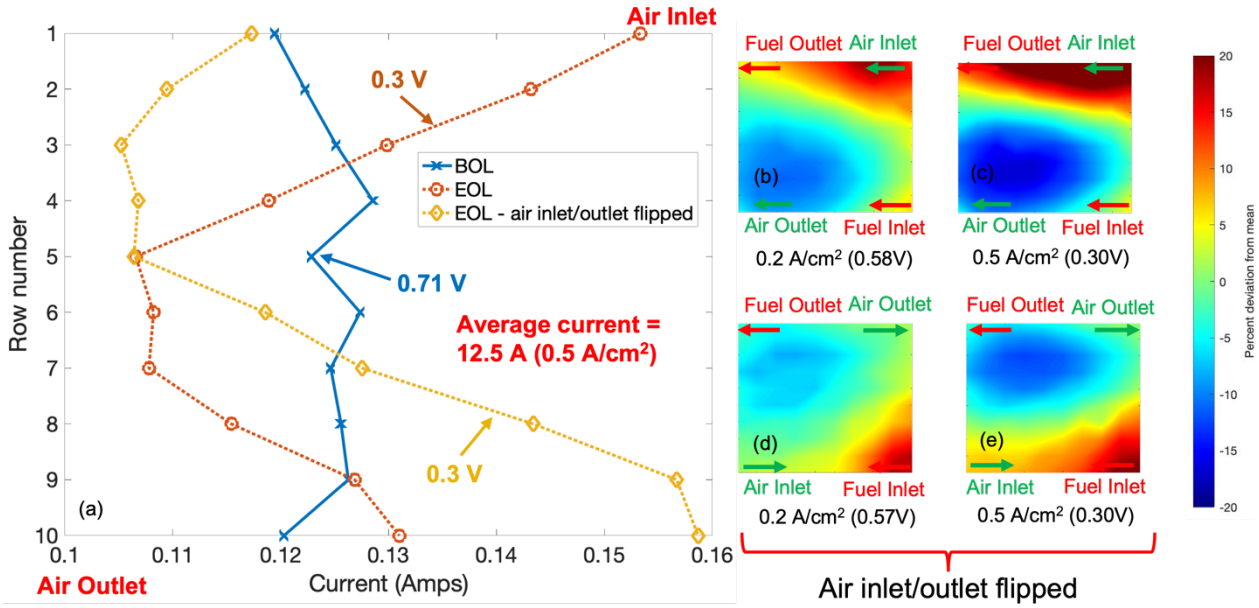


Figure S3.13. One dimensional (1-D) current distributions at the BOL and EOL for CC AST at the average current density of 0.5 A/cm^2. All the distributions were recorded at T_{cell} = 80 °C, $\lambda_{H_2}/\lambda_{Air}$ = 1.5/2, and $RH\%_{\ A/C}$ = 100/100 with $P_{abs\ A/C}$ = 150/150 kPa. Each point on the plot (row number ss. current) from the air inlet (top-right) to outlet (bottom-left) is a row-wise average of 10 current segments. (b) to (e) are the CDD distributions at the EOL for CC AST. The cell voltages at the BOL and EOL at 0.5 A/cm^2 are marked with the arrows.

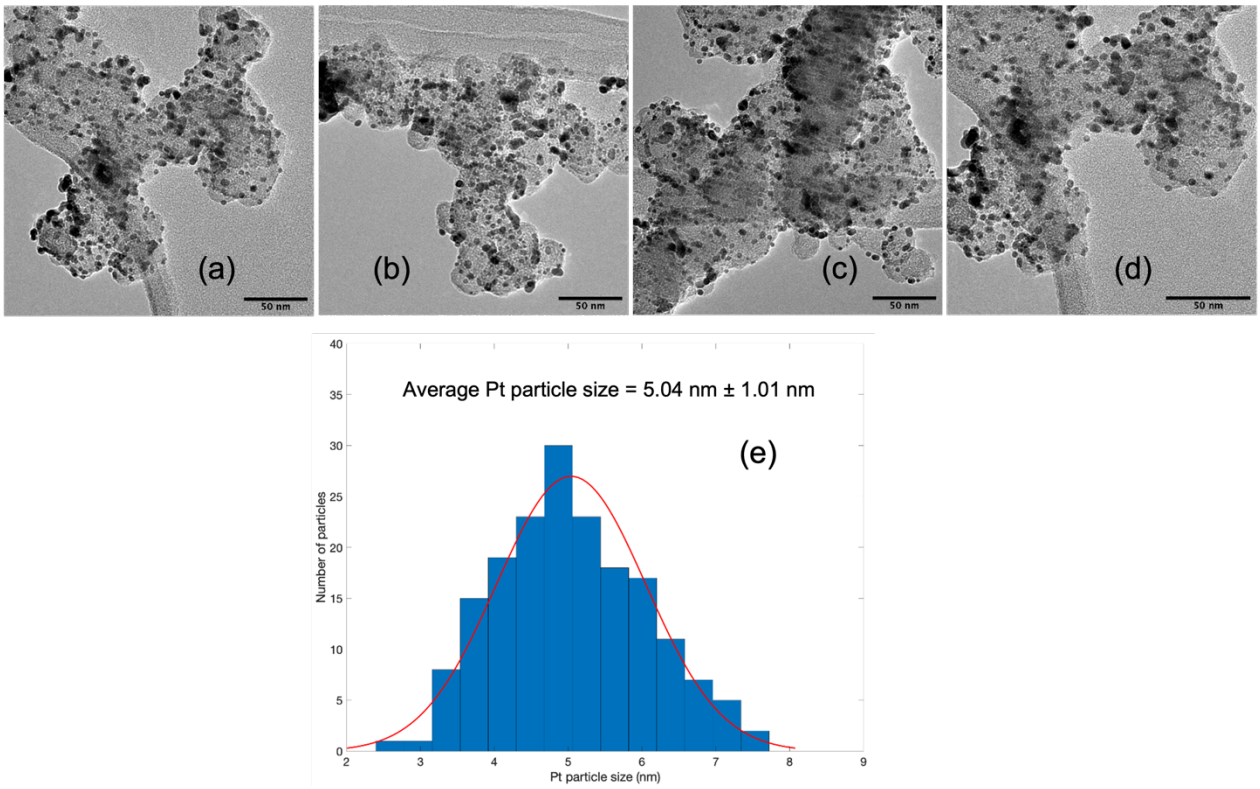


Figure S3.14. (a) to (d) are the TEM images from different locations of the cathode catalyst layer of the pristine MEA sample. (e) Particle size distribution obtained by analyzing particles from the images in (a) to (d) using ImageJ along with a Gaussian fit to the distribution.

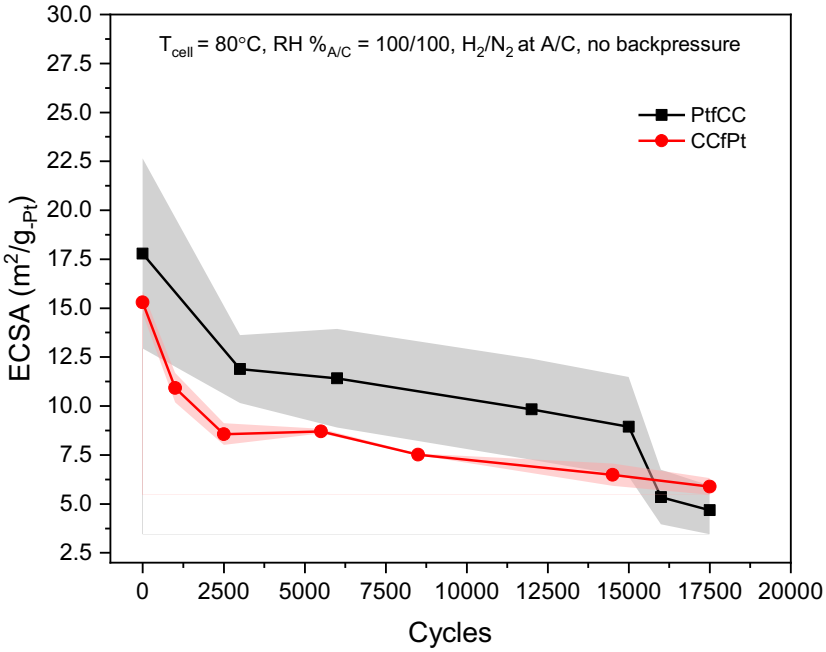


Figure S4.15. Absolute ECSA ($m^2/g_{\text{-Pt}}$) versus number of AST cycles for PtfCC and CCfPt ASTs measured under fully humified ($RH\%_{A/C} = 100/100$), H_2/N_2 (anode/cathode) atmosphere at a cell temperature (T_{cell}) of 80 °C with no backpressure.

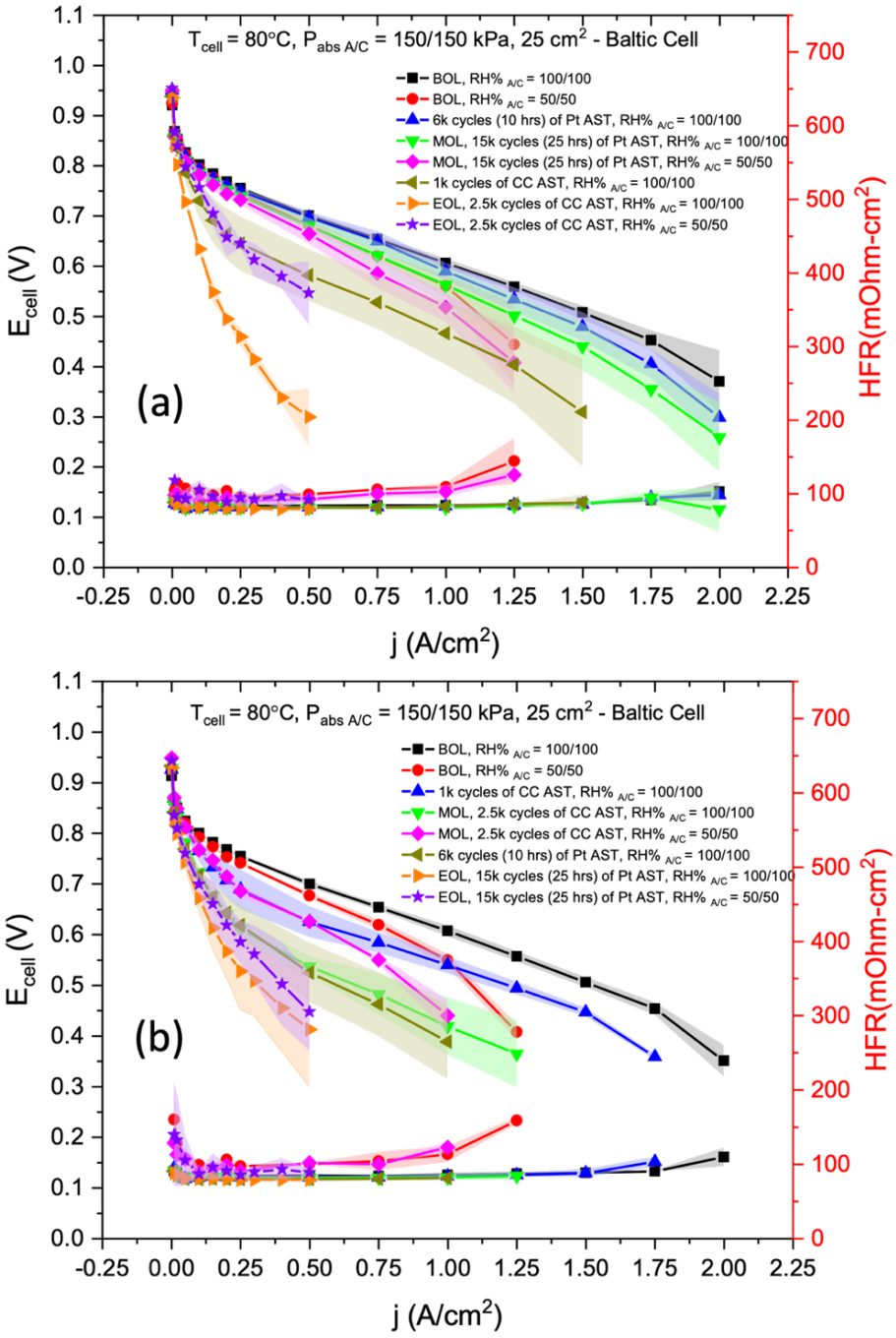


Figure S4.16. Polarization curves for MEAs at different stages during aging for (a) PtfCC AST, and (b) CCfPt AST. Polarization conditions include T_{cell} = 80 °C, H_2/air stoichiometry ($\lambda_{H_2}/\lambda_{Air}$) of 1.5/2, $RH\%_{A/C}$ = 100/100 and 50/50 with a backpressure ($P_{abs\ A/C}$) of 150 kPa (absolute) on both the anode and cathode.

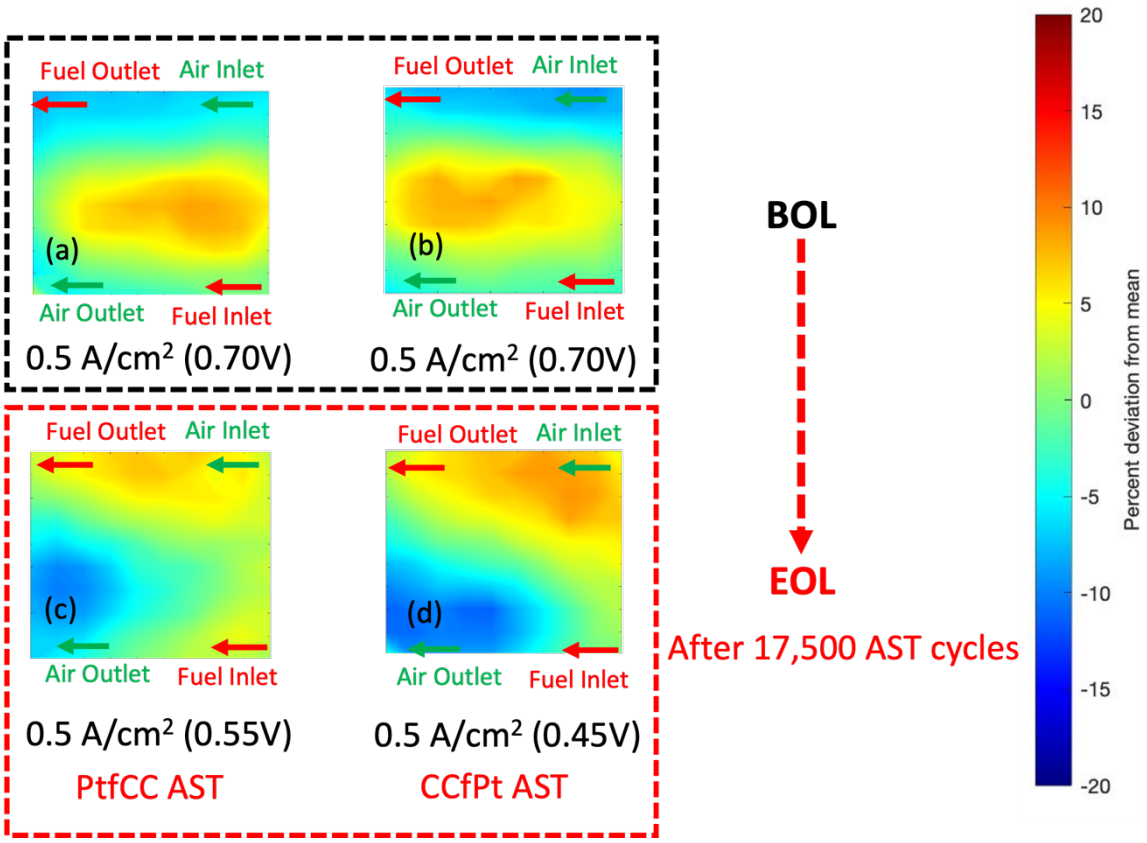


Figure S4.17. Panels (a) and (b) represent CDDs measured at the BOL for PtfCC and CCfPt AST, respectively. Panels (c) and (d) represent CDDs measured at the EOL for PtfCC and CCfPt AST, respectively. All the distributions were recorded at T_{cell} = 80 °C, $\lambda_{H_2}/\lambda_{Air}$ = 1.5/2, and $RH\%_{\ A/C}$ = 50/50 with $P_{abs\ A/C}$ = 150/150 kPa.

Table S4.1. Fitted EIS parameters from the equivalent circuit for PtfCC and CCfPt ASTs at the BOL and EOL.

Current density during EIS	AST type	State of health	R1 (Ω) - Ohmics	R2 (Ω) - Kinetics	R3 (Ω) - Mass transport
0.1 A/cm^2		BOL	3.43x10^{-3}	0.02365	0.755x10^{-3}
	PtfCC AST	EOL	3.45x10^{-3}	0.06805	4.635x10^{-3}
	CCfPt AST	EOL	3.43x10^{-3}	0.03852	3.863x10^{-3}
0.2 A/cm^2		BOL	3.53x10^{-3}	0.01373	2.147x10^{-3}
	PtfCC AST	EOL	3.26x10^{-3}	0.02191	0.04647
	CCfPt AST	EOL	3.19x10^{-3}	0.04448	8.155x10^{-3}

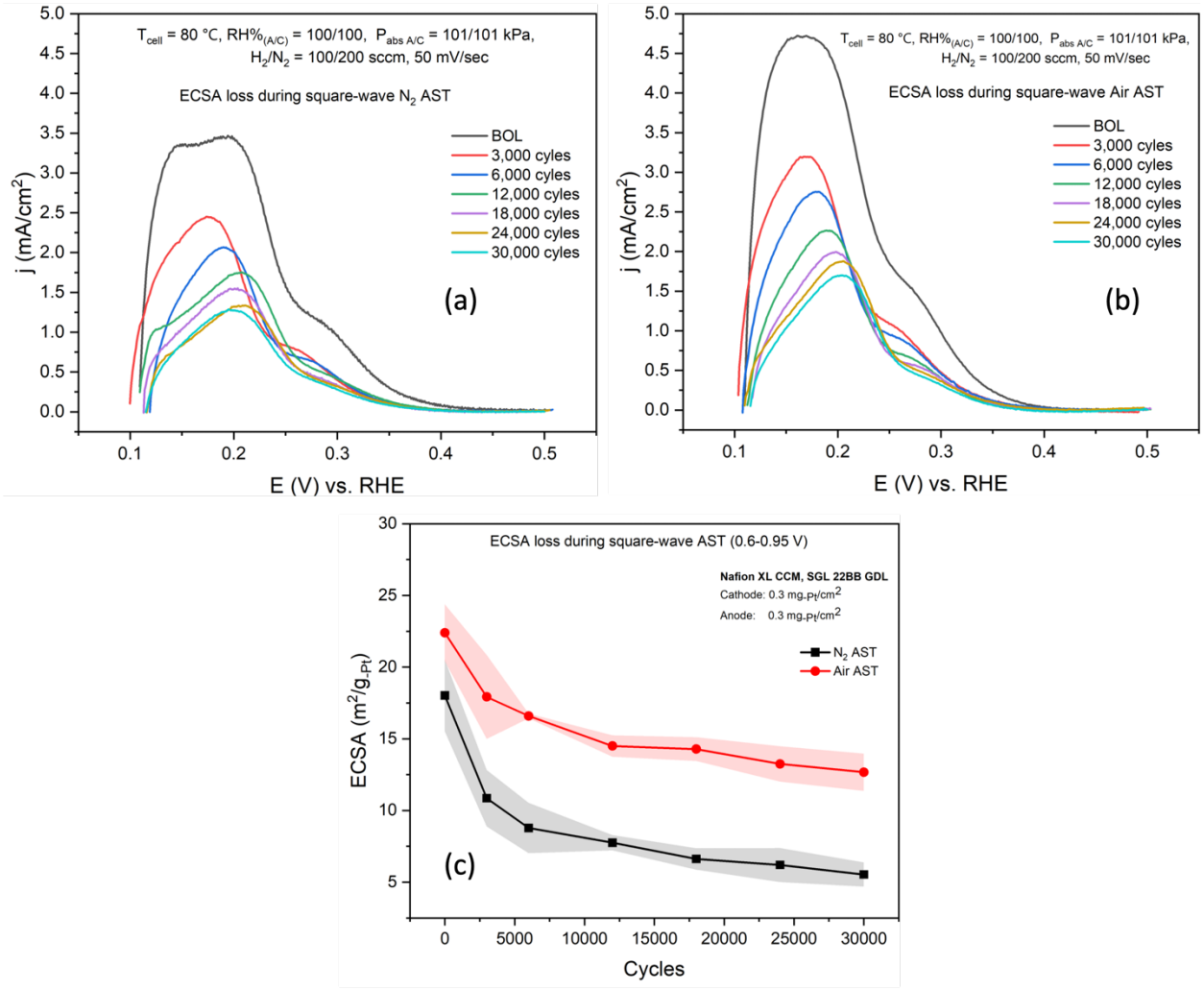


Figure S5.18. Hydrogen desorption regions of the cyclic voltammograms (CVs) collected under H_2/N_2 atmosphere at anode/cathode for the MEAs aged with (a) N_2 AST, and (b) Air AST. These CVs are corrected for the double-layer capacitance, and are used for calculating the electrochemically active surface area (ECSA) during different stages of the aging. Other conditions during the CVs include a scan rate of 50 mV/s, T_{cell} = 80 °C, and $RH\%_{A/C}$ = 100/100 with no backpressure. Panel (c) shows the absolute ECSA ($m^2/g_{\text{-Pt}}$).

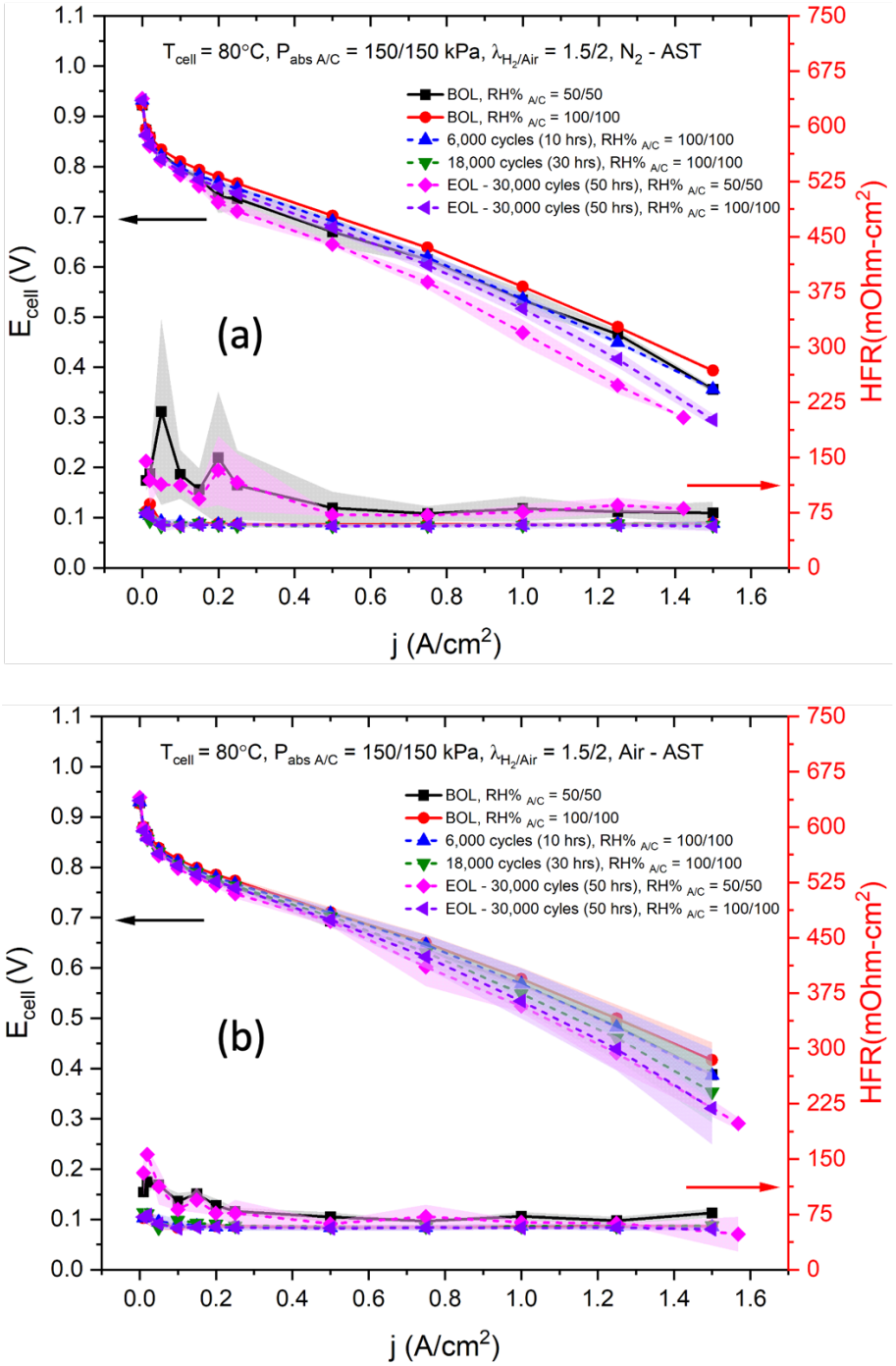


Figure S5.19. Polarization curves of the MEAs during different aging stages for (a) N_2 AST, and (b) Air AST. Polarization curves were collected T_{cell} = 80 °C, $RH\%_{A/C}$ = 100/100 or 50/50, $\lambda_{H_2}/\lambda_{Air}$ = 1.5/2 with $P_{abs\ A/C}$ = 150 kPa/150 kPa on both the anode and cathode.

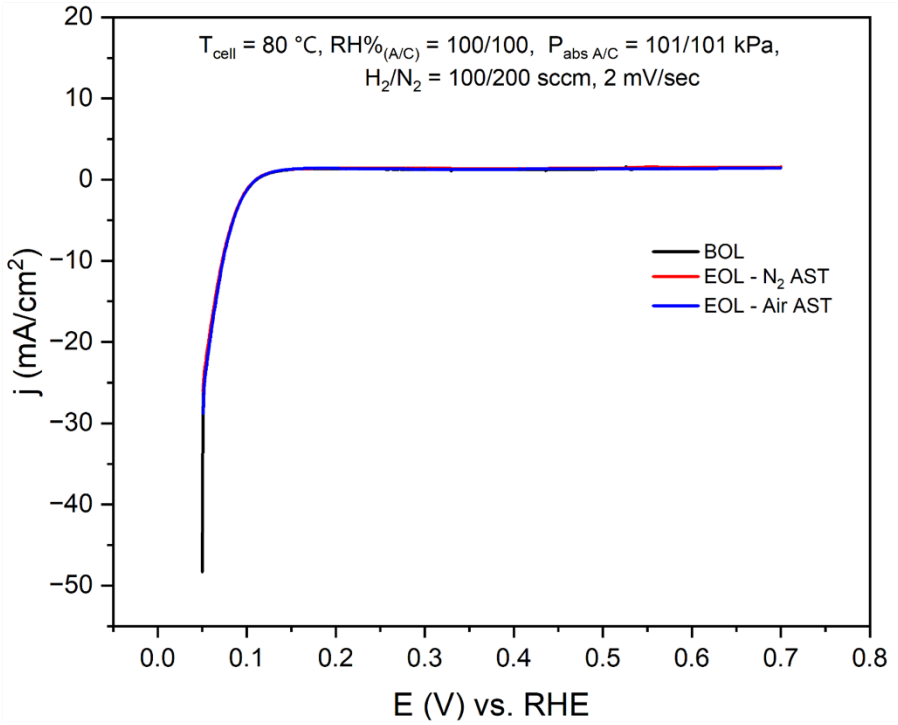


Figure S5.20. Linear sweep voltammograms (LSVs) collected under H_2/N_2 atmosphere at anode/cathode for the pristine and aged MEAs aged with N_2 and Air ASTs. These LSVs are used for calculating the hydrogen crossover currents for the pristine and aged sample. Other conditions during the LSVs include a scan rate of 2 mV/s, T_{cell} = 80 °C, and $RH\%_{A/C}$ = 100/100 with no backpressure.

Vita

Preetam Sharma was born in Haryana, India, in 1993. He earned a Bachelor of Engineering (B.E.) degree in Aeronautical Engineering from Anna University - Chennai, India, in 2015. Subsequently, he pursued a Master of Technology (M.Tech.) degree in Aerospace Engineering at the Indian Institute of Technology Kanpur (IIT Kanpur), graduating in June 2017. After graduation, he worked as a Project Engineer with Prof. Vaibhav Arghode's research group at the Advanced Combustion and Acoustics Laboratory, IIT Kanpur, for over a year. In pursuit of further academic endeavors, he then moved to the University of Tennessee, Knoxville, USA, in the summer of 2019 where he pursued a Ph.D. in Mechanical Engineering under the guidance of Dr. Matthew M. Mench. He is a Tennessee Fellow, recipient of the prestigious Tennessee Fellowship for Graduate Excellence. He successfully completed his Ph.D. in the summer of 2024.